Towards controlled mesomorphic phase behaviour of lipid bilayers

Niek de Lange

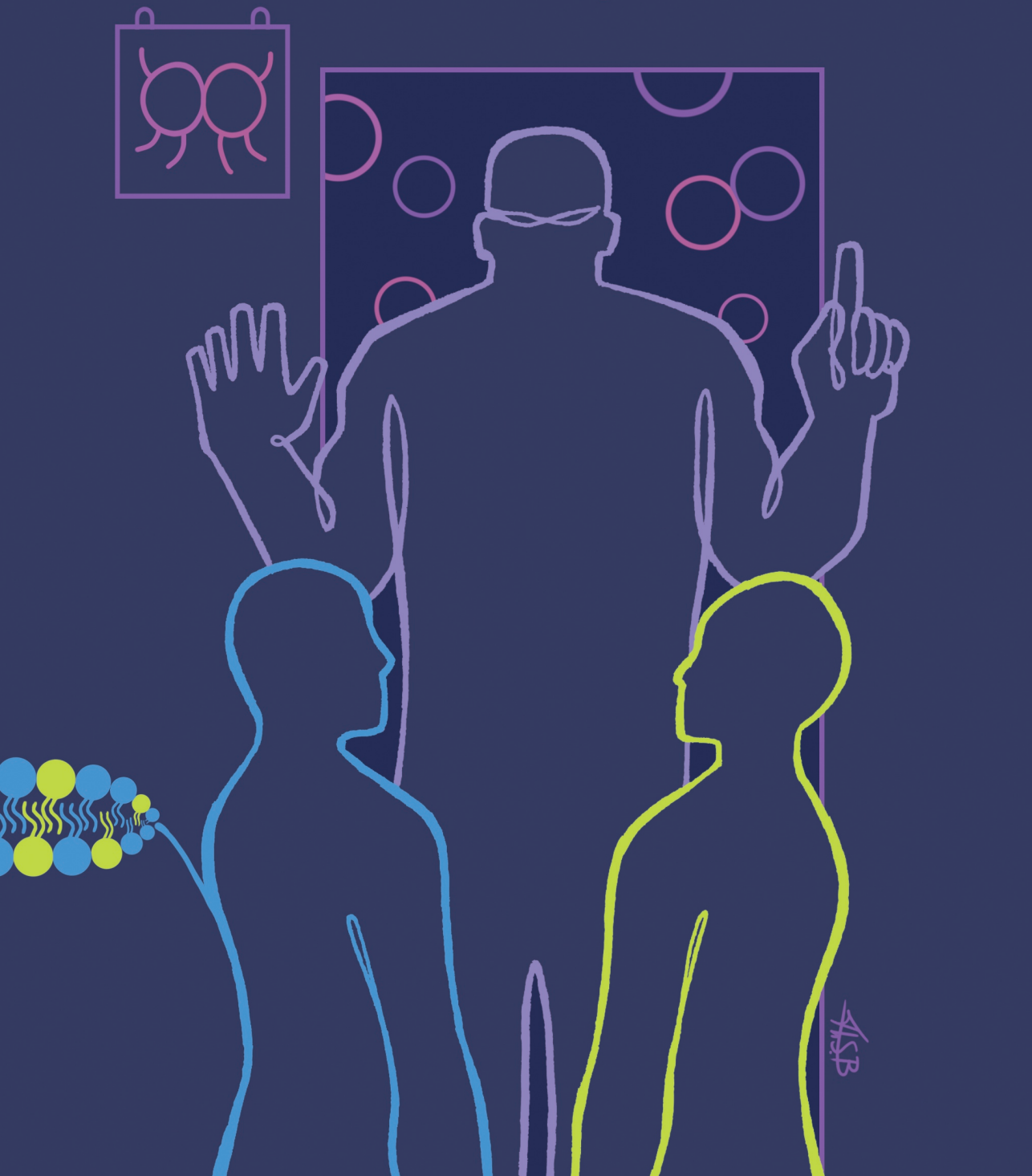

Propositions

1. The lateral mobility of bilayer constituents is key for limited aggregation of vesicles.
   (*this thesis*)
2. A sign-switch of the Gaussian bending rigidity induces topological phase transitions of lipid membranes.
   (*this thesis*)
3. The diagnostic potential of magnetic resonance imaging (MRI) increases when combined with magnetic resonance spectroscopy (MRS).
4. The COVID-19 pandemic is yet another way of Nature to say earth is overpopulated.
   (Gatti, R.C, et al., *Science of The Total Environment* (2021))
5. Playing strategic board games is not wasted time.
6. Wikipedia is an excellent fact-checking tool for the general public.

Propositions belonging to the thesis, entitled

Towards controlled mesomorphic phase behaviour of lipid bilayers

Niek de Lange
Wageningen, 14 May 2021

Towards controlled mesomorphic phase behaviour of lipid bilayers

Niek de Lange

Thesis committee

Promotor:
Prof. Dr F. A. M. Leermakers
Personal chair, Physical Chemistry and Soft Matter
Wageningen University & Research

Co-promotors:
Dr J. M. Kleijn
Assistant professor, Physical Chemistry and Soft Matter
Wageningen University & Research

Other members:
Prof. Dr H. van Amerongen, Wageningen University & Research
Dr S. Lindhoud, University of Twente, Enschede
Prof. Dr R. Tuinier, Eindhoven University of Technology
Prof. Dr J. A. Killian, Utrecht University

This research was conducted under the auspices of the Graduate School VLAG
(Advanced studies in Food Technology, Agrobiotechnology, Nutrition and Health Sciences)

Towards controlled mesomorphic phase behaviour of lipid bilayers

Niek de Lange

Thesis

submitted in fulfilment of the requirements for the degree of doctor at
Wageningen University
by the authority of the Rector Magnificus
Prof. Dr A. P. J. Mol,
in the presence of the
Thesis Committee appointed by the Academic Board
to be defended in public
on Friday 14 May 2021
at 4 p.m. in the Aula.

Niek de Lange
Towards controlled mesomorphic phase behaviour of lipid bilayers
208 pages.

PhD thesis, Wageningen University, Wageningen, NL (2021)
With references, with summary in English

ISBN 978-94-6395-745-8
DOI: https://doi.org/10.18174/543240

Contents

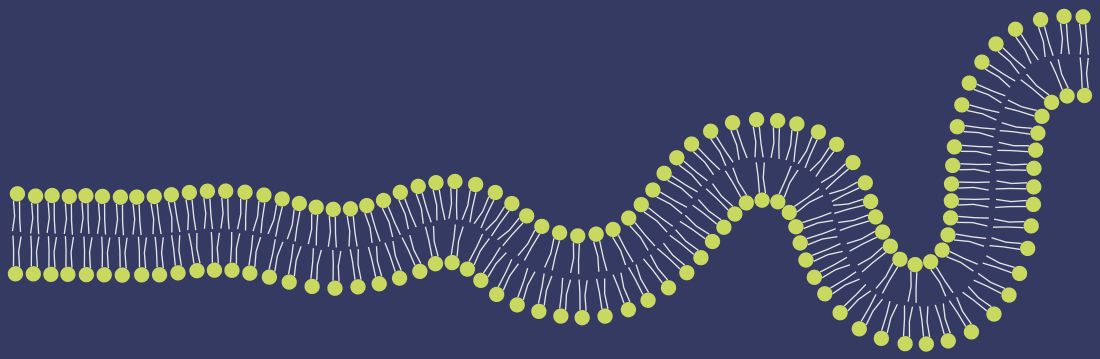

CHAPTER 1

Introduction

1.1 Scope of this thesis

Ever since the invention of the microscope in the 17^{th} century, our knowledge of life skyrocketed. Microscopic observations revealed the immense scope of the invisible microscopic universe. Most astoundingly was the discovery of small living cells. We now know that every living being on our planet consists of cells, and that these are the 'factories' of all life. Almost everybody by now has seen some type of drawing of a cell. Nowadays, the picture of the cell as seen in figure 1.1 is one of the first illustrations present in a biology textbook. A cell consists of many components: a nucleus and many other organelles such as the endoplasmic reticulum (ER), mitochondrion or the Golgi apparatus. However one thing in particular stands out when looking at this picture (or any other schematic picture of cells that you can find): membranes. What you mainly see are membranes. I subsequently realized that biological membranes must be one of the most, if not the most, important feature of the cell. First and foremost, there would be no cell or organelles if not for membranes as these define their boundaries. As such, the cell membrane acts as a barrier, protecting the cell from the often hostile outer environment. The barrier function additionally provides the opportunity for different micro-environments on either side of the membrane. This is essential for organelles as it allows them to perform specific and unique tasks within the cell. Next to this, biomembranes fulfil crucial functions in numerous processes like the cell metabolism and intercellular communication. But for this to happen, the cell membrane has to allow nutrients to enter the cell, and waste products to exit. Interestingly, this seems to contradict its primary role as a barrier. The cell membrane however seems to be able to manage the intricate balance between being a barrier while selectively allowing substances to go through.

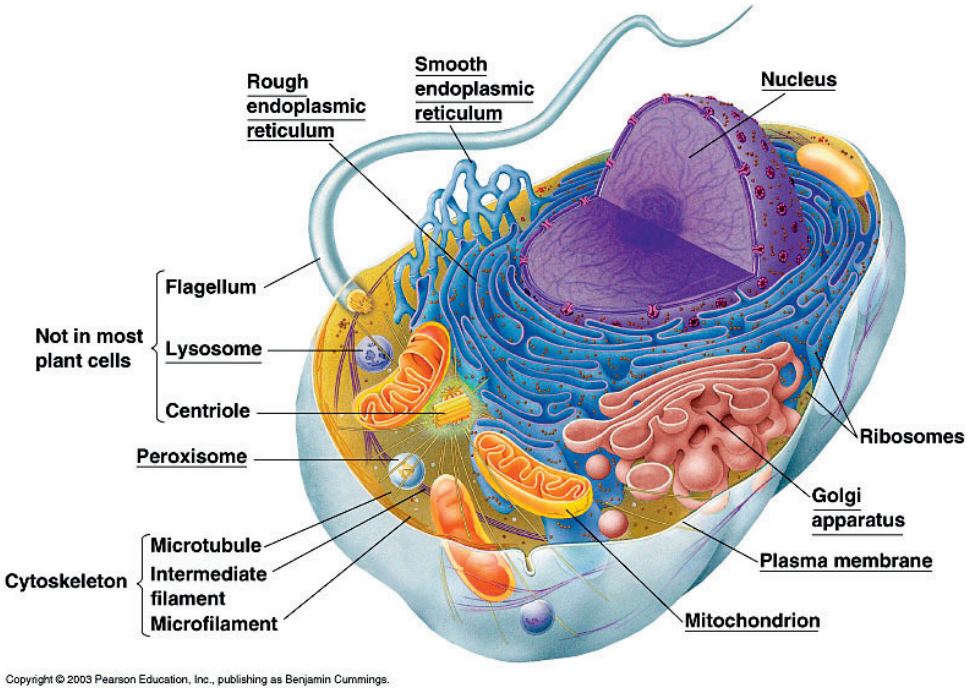

Figure 1.1: Graphical representation of a cell and its components.

In 1972 Singer and Nicolson [1] came up with a model that could capture the properties described above: the 'fluid-mosaic model', see figure 1.2A. In this model, two layers of (phospho)lipids, together the lipid bilayer, form the basic structure of the membrane. There exist many types of lipids. Most commonly, lipids consist of two apolar fatty acid 'tails' and a polar 'head'. For phospholipids, the headgroup consists of a negatively charged phosphate group which subsequently is connected to another R- (residual) group. The negative charge makes that biomembranes often are also negatively charged. The general phospholipid used in this thesis has a choline R-group, dioleoyl phosphatidylcholine (DOPC), see figure 1.2B for a coarse-grained schematic drawing. The nitrogen of the choline group is positively charged, making DOPC a zwitterionic phospholipid. The charges in the headgroup of the phospholipid make the headgroup hydrophilic (water loving), as opposed to its hydrophobic (water repulsing) tails. As such, the lipids are oriented in such a way that their hydrophobic tails face each other and their hydrophilic 'heads' face the water phase. The hydrophobic 'dry' core of this bilayer is ideally suited for the barrier function, even though it is only a few nanometers in width, because it is impermeable to most water-soluble molecules. All other components of the bilayer, e.g.

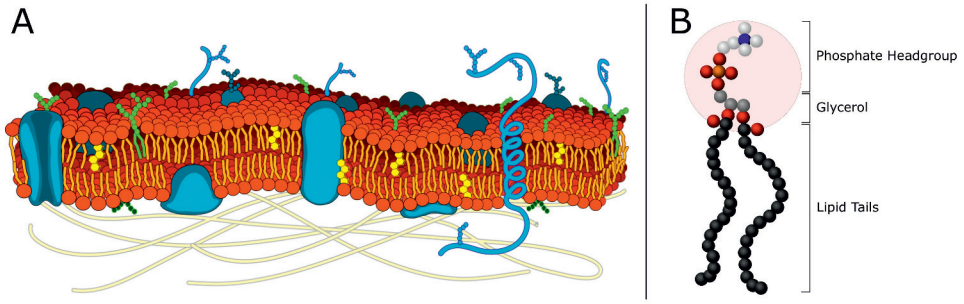

Figure 1.2: The fluid-mosaic model of a biological membrane (Copyright by LadyofHats Mariana Ruiz [Public domain], via Wikimedia Commons)) (A), and the basic (coarse-grained) structure of the phospholipid DOPC (B). The black, gray and white segments resemble carbon segments of the tail, glycerol and headgroup respectively. Red resembles oxygen, orange resembles phosphor and blue nitrogen.

cholesterol, proteins and saccharides, are embedded in this bilayer and provide further functionality, such as allowing the transport of selective substances across the bilayer. The overall composition is different for each membrane of a different cell type or organelle and is ultimately responsible for the unique functionality of each particular membrane. Another important aspect of the fluid-mosaic model is that each bilayer component is able to move laterally along the membrane. This 'fluid' part of lipid bilayers is a prime cause for membranes being so versatile in their function, as it allows for the diffusion of specific components, such as membrane proteins, towards the area where they can execute their task. This property of lipid membranes turned out to be crucial in my research as well, as will become clear in the experimental chapters of this thesis.

While the fluid-mosaic model is an ideal starting point to model biomembranes, it is arguably still too simplistic. For one, it does not explain how the bilayer on a mesoscopic scale - the scale between molecular and macroscopic - can take on many different shapes and forms. In other words, a bilayer membrane can exist in various mesomorphic phases. Take for example the nuclear envelope. As can be seen in figure 1.1, the nucleus is surrounded by a double bilayer that safeguards the DNA of a cell. Special pores, so-called nucleopores, form holes in this envelope allowing for the transport of RNA out of the nucleus and into the ER. In these nucleopores the bilayer is curved in such a way that the inner membrane and outer membrane are connected through handles, such as depicted in figure 1.3. Topologically speaking, the nuclear envelope can thus be seen as a single membrane where a lipid could diffuse to the other side through these handles. While large protein complexes facilitate the formation of nucleopores, the impact of the mechanical properties of the lipid bilayer itself is often overlooked. However, these are

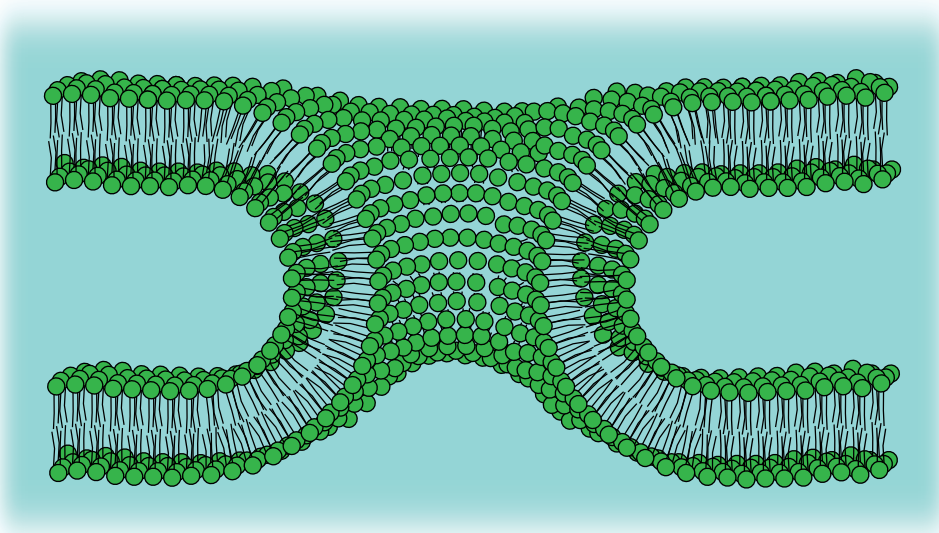

Figure 1.3: Close-up of a handle between two lipid bilayers.

crucial because they regulate the formation of complex structures such as bilayer handles. After all, if bending the bilayer would cost an excessive amount of energy, the formation of bilayer handles would not happen.

Apart from handles, as found in nucleopores, many more different shapes and forms can occur in membranes. An overview of different bilayer mesophases will be given later in this introduction, but to give a general idea, bilayers can be flat or curved, individual or stacked, separate or connected. The endoplasmic reticulum for example clearly exhibits a different membrane shape compared to the nuclear envelope, or the outer cell membrane, see figure 1.1. While on the mesoscopic scale these membrane structures are highly different from one another, on a molecular level they all show the same configuration: the bilayer membrane. It should be clear that membranes can do much more than expected based on the fluid-mosaic model.

We know that the packing of lipids within the bilayer affects its mechanical properties, including its resistance to stretching and bending, and that these properties determine what shape the bilayer can adopt. However, many questions remain as to what bilayer composition (types of lipids and additives) causes the formation of specific mesomorphic bilayer structures. For example, what composition of the bilayer is required to allow for the formation of nucleopores? Which bilayer properties are the reason bilayers undergo mesoscopic phase transitions such as fusion? Can we control this behaviour? In this

thesis, I try to solve a piece of this complex puzzle by exploring how bilayers respond and interact with each other through the addition of specific additives.

1.2 Phase separation and self-assembly

To figure out what aspects of a phospholipid bilayer are responsible for the specific mesoscopic structure of a bilayer, we must understand why a bilayer is formed in the first place. For this, let's start with the very basics of bilayer formation: phase separation.

When enough of a hydrophobic substance is put into a hydrophilic solvent such as water, phase separation occurs. The best known example is that of oil in water. After mixing, phase separation results in an oil-rich phase and a water-rich phase. In a pure oil-water system the interface between the two phases is sharp, in the order of a single molecule width, to limit the contact of oil with water as much as possible. Following the same logic, the area of the interface becomes as small as possible as well. In such a system, increasing the interfacial area costs energy as this implies that more oil will come in contact with water. In other words, the interfacial tension γ, which is defined as the amount of energy necessary to increase the interfacial area by a certain amount, has a finite value.

When instead of purely hydrophobic molecules, amphiphilic molecules (molecules with both hydrophilic and hydrophobic groups), such as phospholipids, are mixed with water, fascinating behaviour is observed as these molecules self-assemble into specific mesoscopic structures above a certain concentration, generally dubbed the critical micelle concentration (CMC). The driving force for self-assembly is the same as the driving force that initiates phase separation in an oil-water system: reduction of the contact of the hydrophobic parts with water. However, the situation is different as the transition of hydrophilic to hydrophobic occurs within the same molecule. Although the force minimizing the area of the interface is still present, this now causes the amphiphiles to be pushed towards each other, creating a 'local' pressure that pushes back. In equilibrium, both forces are equal and as a result $\gamma = 0$. In other words, for such systems, the interfacial surface area is not minimized anymore (like with the oil-water interface) but becomes proportional to the number of amphiphilic molecules present in the interface. This leaves the door open for amphiphilic molecules to self-assemble into various structures.

One of the commonly known structures that amphiphiles self-assemble into is the bilayer. However, aside from the bilayer, many other forms exist as well. A good first-order prediction of the type of self-assembled structure can be made based on the effective shape of the molecule. Israelachvili and coworkers were one of the first to realize this and published their theory in 1976. [2] Here they described the effective shape of a

amphiphile or surfactant with the dimensionless critical packing parameter P. It combines the (average) length (l) and the effective volume of the hydrophobic chain(s) (v) with the cross sectional area of the hydrophilic-hydrophobic interface in the surfactant molecule (a_0) in a dimensionless number,

$$P = \frac{v}{la_0} \tag{1.1}$$

which value is indicative of how the amphiphiles would preferentially self-assemble. For $P < 1/3$, the surfactant has a cone-like shape, see figure 1.4. As such it prefers to pack in the form of spherical micelles. When $1/3 < P < 1/2$ the surfactant appears to have a wedge-like shape and tends to pack in the form of cylindrical micelles. When $1/2 < P < 1$ the surfactant appears to have a cylindrical shape and in this case a bilayer is the preferred self-assembled structure. Lastly, when $P > 1$ various inverted structures such as an inverted hexagonal phase or inverted micelles can occur. Phospholipids, consisting of a hydrophilic headgroup and two relatively long hydrophobic tails generally have a packing parameter of $P \approx 1$ [3, 4] and as such they tend to pack in the form of a bilayer. An example of such a phospholipid is dioleoyl phosphatidylcholine (DOPC), the main lipid used in this thesis.

1.3 Bilayer mesophases

The effective shape of phospholipids thus explains that they self-assemble into bilayers. But to understand or predict which mesomorphic structure a bilayer adopts, we should look at the physics of bilayers themselves. For this, it is convenient to first provide an overview of the various bilayer mesophases and topologies that can happen.

First of all, there is the planar bilayer. However, individual planar bilayers are generally not stable as they have an energetically unfavourable edge. The edge-energy increases with increasing bilayer surface area and at a certain moment is larger than the energy-cost to curve the bilayer into closed spherical structures, so-called vesicles or liposomes, in which no unfavourable edge exist. As such, planar bilayers at concentrations above their CMC take on the appearance of vesicles. In addition, bilayers can be both attractive ('sticky') or repulsive. As bilayers are generally negatively charged, planar bilayers and vesicles generally repel each other. However bilayers without negatively charged lipids can become attractive or 'sticky' because of electrostatic attraction (dipole-dipole attraction) or with the addition of linker molecules (we will discuss these later in the introduction as well). As a result, vesicles aggregate together or form stacks of flat bilayers, the so-called lamellar phase. They subsequently phase separate into a bilayer-rich phase and a water-rich phase, similar to the case of oil in water. Various lamellar phases with different

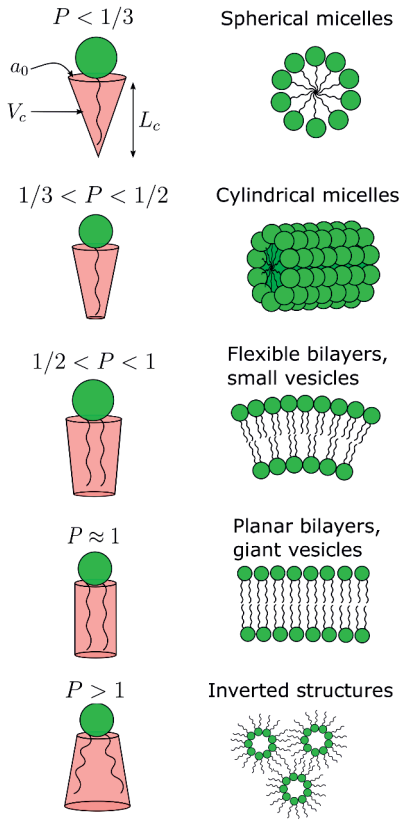

Figure 1.4: Schematic representation of the shape of surfactants and lipids with corresponding critical packing parameter P (see equation 1.1) and the structures in which they self-assemble.

bilayer properties can be distinguished depending on temperature and other factors such as saturation (presence of double bonds) in the lipid tails. A schematic drawing of two main types of lamellar phases is given in figure 1.5. Apart from these general phases, various subphases exist as well. For example, lipid tails ordering as found in the gel phases can be tilted, inter-digitated or in any phase in between the gel and fluid lamellar phase. In this thesis we do not go into detail on these different phases and operate mainly in conditions in which the lipid bilayer exists in the fluid lamellar phase (L_α) where the lipid tails are disorderly oriented in the bilayer core. This phase is characterized by a high lateral fluidity of the bilayer components.

Apart from lamellar phases, in which bilayers are stacked but not connected, bilayers can be connected through handles, effectively resulting into one single bilayer. If this happens

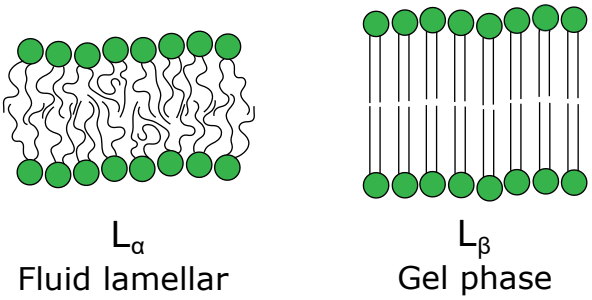

Figure 1.5: Schematic representation of two main types of lamellar bilayers.

disorderly we refer to this phase as a sponge phase (L_3), while if this happens periodically we call this a cubic phase. Cubic phases can have different forms of periodicity, giving rise to different mesomorphic structures. An overview of the sponge phase and various cubic phases is given in figure 1.6.

While lamellar phases subdivide a volume in many different compartments, the cubic or sponge phase subdivides the solvent in only two volumes that both span the whole system. To visualize such a bicontinuous phase, one can imagine a swimmer on one side of the system. To get to the other side of the system, this swimmer has to cross several bilayers in a lamellar phase system, whereas he could 'swim' all the way to the other side without crossing a single bilayer in a cubic/sponge phase system. These topological differences have severe consequences for the physical properties of such a system. The conductivity of a cubic phase system is, for example, much higher compared to a lamellar system. Nature has found a way to utilize the properties of these different mesomorphic phases to its own benefit. Cubic-like phases have been observed in various organelles such as chloroplasts, mitochondria and the endoplasmic reticulum (ER) [5], which benefit enormously from having a greatly enlarged membrane surface area that divides their volume into just two different compartments.

1.4 Elastic properties of the lipid bilayer

To understand why bilayers form cubic/sponge phases over flat bilayers, we have to go further than electrostatic and dipolar interactions and look into the elastic properties of these bilayers. To do so, we have to start with curvature itself. The curvature of any interface at a specific spot is generally described by the two principal curvatures, R_x and R_y. The curvature in the x-direction is then given by $c_x = 1/R_x$ and similarly the curvature in the y-direction is $c_y = 1/R_y$. However, instead of using c_x or c_y, it turns out to be more elegant to use the mean (J) and Gaussian (K) curvatures which are

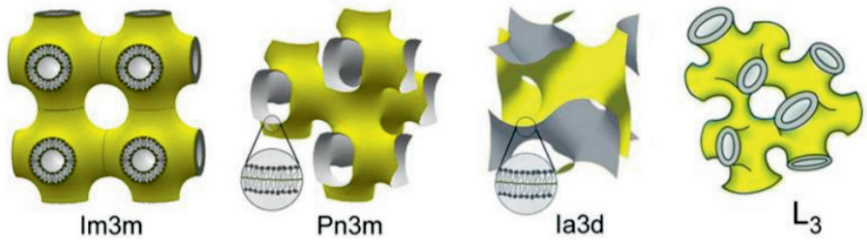

Figure 1.6: Schematic representation of various cubic phases (Im3m, Pn3m, Ia3d) and the sponge phase (L_3) of lipid bilayers. Adapted from Koynova et al. [6] with permission.

combinations of these two:

$$J = c_x + c_y \tag{1.2}$$

$$K = c_x \times c_y \tag{1.3}$$

To make this a bit less abstract, let me give some relevant examples for this thesis: for a spherical vesicle we have $c_x = c_y = 1/R$ and thus $J = 2/R$ and $K = 1/R^2$. A cylindrically shaped bilayer has $c_x = 1/R_x$ and $c_y = 0$, which gives $J = 1/R$ and $K = 0$. A membrane handle between bilayers, such as seen in a nucleopore, has a very interesting shape, where the two circles describing the curvature lay at opposite sides of the interface, see figure 1.3. For these so-called saddle shapes, $c_x = 1/R_x$ and $c_y = -1/R_y$, which makes $K < 0$. This negative sign for K is important to remember.

The origin of the current theory on membrane elasticity stems from the work of Helfrich in 1973 [7]. Helfrich suggested to consider a Taylor series expansion of the interfacial tension (γ) in the curvatures J and K up to second order in $1/R$. This equation bears his name:

$$\gamma(J, K) = \gamma(0, 0) + \frac{\partial \gamma}{\partial J} J + \frac{1}{2} \frac{\partial^2 \gamma}{\partial J^2} J^2 + \frac{\partial \gamma}{\partial K} K \tag{1.4}$$

Here, $\gamma(0, 0)$ is the surface tension in the planar state. In equilibrium its value equals zero. The tensionless planar bilayer can be seen as the ground state from which the curvature energy is counted. The term $\partial\gamma/\partial J$ is related to the spontaneous curvature of the interface (J_0), which due to the symmetry of the bilayer equals zero as well. Note that the spontaneous curvature of a single leaflet (J_0^m), which follows from the same Helfrich equation for a monolayer, does not have to be zero. In fact, J_0^m can be related to the critical packing parameter [8] where $J_0^m >> 0$ corresponds to $P < 1/2$, in which lipids self-assemble into micellar structures, and $J_0^m << 0$ corresponds to $P > 1$, indicative of inverted self-assembled structures.

By defining two bending rigidities: $\kappa = \partial^2\gamma/\partial J^2$ and $\bar{\kappa} = \partial\gamma/\partial K$ we can write equation 1.4 as:

$$\gamma(J, K) = \frac{1}{2}\kappa J^2 + \bar{\kappa}K \tag{1.5}$$

These rigidities effectively quantify the amount of energy required to bend the bilayer in a certain way. In physical terms, you can think of κ as related to the stiffness of the membrane: the 'stiffer' the membrane, the higher κ and the more energy is required for bending the membrane. Quantitatively, κ is always positive. This is not the case for $\bar{\kappa}$, which can have both positive and negative values. $\bar{\kappa}$ is related to the tendency of bilayers to form saddles. A positive $\bar{\kappa}$ means that the saddle shape, for which K is negative, lowers the surface tension of the bilayer. In simpler words, when $\bar{\kappa}$ is positive, the membrane has the tendency to form saddle shapes, corresponding to sponge and cubic phases. The opposite is true for a negative $\bar{\kappa}$, which supports the formation of non-saddle shaped bilayers, like vesicles. We therefore hypothesize that a sign-switch in $\bar{\kappa}$ for bilayers as a result of a change in conditions (e.g. temperature, concentration, ionic strength or addition of specific additives) can be interpreted as a topological or mesomorphic phase transition.

To provide a deeper insight into why the formation of saddle shapes can be related to topological transitions, we generally refer to the Gauss-Bonnet theorem, which relates curvature of an interface to topology. This theorem states that the total Gaussian curvature of a closed surface M is equal to 2π times the Euler characteristic of that surface (χ_M).

$$\int_M K\, dA = 2\pi\chi_M \tag{1.6}$$

For bilayer structures, the Euler characteristic is given by $\chi_M = 2 - 2g$ where g is the genus of the structure, which effectively is a measure for how many 'holes' or handles are present in the membrane. A vesicle for example does not have a hole and the Euler characteristic $\chi_\mathrm{v} = 2$, whereas a bilayer torus (donut shape), does have a hole and the Euler characteristic $\chi_\mathrm{t} = 0$. The total Gaussian curvature for a vesicle and torus are subsequently $K_\mathrm{tot,v} = 2\pi \times 2 = 4\pi$ and $K_\mathrm{tot,t} = 2\pi \times 0 = 0$, regardless of their size or how many dents or protrusions are present. Different surfaces are topologically seen as different if the total Gaussian curvature is different. All vesicles, no matter their shape or size, can therefore topologically be seen as similar objects, but they are topologically different from donut-shaped vesicles. Topological transitions also occur during vesicle fusion, although the begin and end state topologies of the structures remain the same, i.e. vesicles. However, in order for vesicles to fuse the bilayers need to connect, which they do through intermediate structures such as a stalk [9] where the outer leaflets of both vesicles are connected in a handle, but the inner leaflets remain separated. Both

the fusion of vesicles and the formation of holes and handles are associated with the formation of saddle-shaped curvatures. This is why the sign-switch of $\bar{\kappa}$, indicative of whether saddle-shaped curvatures naturally occur or not, can be a good prediction of a topological transition.

1.5 Aims of this thesis

Let us summarize the previous sections before we highlight the aims of this thesis. There are quite a number of variables that are responsible for the mesomorphic phase behaviour of self-assembled lipid structures. This thesis focuses on the phase behaviour of (phospho)lipid bilayers, which under general circumstances exist in lamellar, usually non-aggregated phases, such as lipid vesicles. The stability of these phases however is rather intricate: a small amount of 'sticky' molecules can already disturb the colloidal stability of the vesicles. Additionally, the bilayer itself can be disturbed through the addition of surfactants with a low packing parameter ($P < 1/2$) or a high packing parameter ($P > 1$). In these cases, the spontaneous curvature of the monolayer goes far from 0, which pushes the self-assembly of the surfactants into micellar structures ($J_0^m >> 0$) or inverted structures ($J_0^m << 0$). Lastly, the change in various conditions such as temperature, concentration, ionic strength or addition of specific additives can alter the lamellar stability through the formation of saddles (when $\bar{\kappa} > 0$). Exerting control on the phase behaviour of lipid bilayers is a daunting task, for which many questions need to be addressed. To name a few: which lipid properties are responsible for the corresponding mechanical properties of the bilayer? How can we change the properties of stable lipid bilayers to trigger a mesomorphic phase change? Which additives can help to do this?

The main goal of this thesis is to provide the tools and insight necessary to obtain control on the mesomorphic phase behaviour of lipid bilayers. To do so, we have chosen to combine experimental work with theoretical modelling and have defined a number of objectives for both routes.

Experimentally, we have focused on obtaining methods to bring lipid bilayers in close proximity of one another, as this is an ideal starting point to induce phase changes like the formation of membrane handles or membrane fusion. Additionally, our goal was to establish a method that allows to check whether the formation of such a phase change, or any other process like membrane fusion, has occurred. Theoretical modelling should provide insight into how the mechanical (bending) properties of the lipid bilayer depend on the molecular structure of the lipids. It should also address the question as to what bilayer composition is needed to potentially allow formation of saddle shapes, i.e., what

type of additives we can use to stimulate this mesomorphic phase change in lipid bilayer systems.

1.6 Approach

In this section we describe our approaches to reach these objectives in some more detail. Let's start with our experimental approaches first.

1.6.1 Experimental

The most important experimental challenge was to develop methods that could bring membranes together in a controlled manner and allowed us to check the occurrence of a mesomorphic phase change such as the formation of membrane handles or membrane fusion. The two routes that have been followed in this work are creating supported double lipid bilayers (SDLBs) and making small vesicle aggregates. Both are explained in some detail below.

Perhaps the most straightforward method to bring two bilayers in close proximity, is the formation of a double bilayer onto a surface, a so-called supported double lipid bilayer (SDLB). The first supported lipid bilayer (SLB) is generally deposited via adhesion, rupture and fusion of lipid vesicles on a clean substrate, usually silica or glass [10, 11]. The second bilayer can be deposited on top of the first following a similar process of vesicle adhesion, rupture and fusion, but for this to happen the adhesion force between the supported bilayer and the vesicles should be strong enough. This can be achieved through electrostatic interactions, i.e. depositing negatively charged vesicles on top of a positively charged SLB [12], by covalently binding lipids together that can act as linkers between the bilayers [13] or by using other linker systems, such as biotinylated lipids in combination with streptavidin [14], polycationic polymers such as poly-L-lysine [15] to connect negatively charged bilayers or complementary DNA strands attached to lipids [16]. An advantage of using SDBLs to study the interaction between two lipid bilayers is the possibility to use analytical surface techniques such as atomic force microscopy (AFM), total internal reflection fluorescence (TIRF) microscopy and reflectometry.

My initial PhD work was focused on producing SDLBs, but in a later stage I switched to creating small vesicle aggregates, which is another straightforward method to bring membranes close together. The same linker systems as mentioned above for SDLB production can be used to link vesicles together, as is evidenced by the shear amount of literature [17–22] available. An advantage of making vesicle aggregates instead of SDLBs, is that the contact area between vesicles represents an ideal double membrane, free in solution.

In SDLBs the first supported membrane is in close contact with and adheres to the substrate surface, which might prevent topological shape changes like saddle formation. In addition, within vesicle pairs or other small aggregates, formation of handles or vesicle fusion would result into lipid and content exchange between vesicles, which both can be used in an assay to monitor such events. Within this thesis I tested a lipid exchange assay based on Förster resonance energy transfer (FRET) to report the mixing of fluorescently labelled lipids.

While much literature on vesicle aggregation is available, the frontier research in this area is now on controlling this process and directing it to formation of vesicle aggregates of specific shapes or sizes. Small, stable vesicle aggregates can for example be used as a model for primitive cell assemblies, or as multi-compartment drug delivery tool. For our research, obtaining stable vesicle aggregates of limited size is highly preferred as well, as our long term goal is to induce intermembrane handles using additives. As such, additives should be able to reach the contact areas between vesicles. For large vesicle aggregates, a major part of these areas will however be unreachable for these additives and moreover results from e.g. FRET assays would be hard to interpret.

Complete control on size of the vesicle aggregates however remains a challenge. By making clever use of different types of linkers, including a novel thermo-reversible linker (C18-pNIPAm), and taking into account the timescales for vesicle collision and linker diffusion laterally along the membranes, we provide a solid new strategy for the production of vesicle pairs and small stable vesicle aggregates.

1.6.2 Theoretical modelling

Above we have highlighted the fact that the mean and Gaussian bending rigidity control much of the physics of tensionless bilayers, including its mesomorphic phase behaviour. Is it therefore important to gain more knowledge on how these mechanical parameters follow from the properties of the membrane constituents. However, while various experimental methods are available to determine κ of model lipid bilayers [23–26], determining $\bar{\kappa}$ is much more difficult and currently no experimental method exist that can quantify it directly. We can only gain insight in trends of this parameter by correlating (topological) phase changes upon the change of the molecular composition, the temperature or pressure. In this thesis we explore theoretical modelling as an alternative to deepen our insight in the relation between the molecular structure of bilayers and the mechanical parameters.

Various modelling methods exist. The one with perhaps most appeal is molecular dynamics (MD), which has been successfully used to predict various self-assembled structures and has even been applied to follow complex processes such as protein folding [27, 28].

With this technique one follows the dynamics of a system over time on a molecular or even atomistic scale. It does so by applying Newton's laws of motion for each particle in the system. For this, the mass, initial position and velocity of each particle are required as input values. In addition, the interaction forces between all particles need to be defined and these follow from the pair potentials. These potentials are collected in so-called force fields, which from time to time are being fine-tuned to improve the accuracies of the predictions. The molecularly detailed 'movie' of the system subsequently provides detailed structural and dynamical information. The main caveat of this technique is that it is computational very demanding. The larger and more complex the system, the more computation time is required to follow the system even for a short amount of simulation time (typically tens of nanoseconds is doable). Although the computational strength of computers has increased immensely over the last couple of decades, the simulation of biological processes that involve many molecules and require simulation times in the order of a couple of microseconds is far from routine (realistically out of reach). The simulation of protein folding has therefore been limited to small, fast-folding proteins [28, 29]. Simulations of biological membranes, which are per definition ensembles of many molecules, have mostly been limited to obtaining structural information on equilibrium bilayers, following relatively simple and fast processes such as the transport of small molecules across the membrane [30, 31], or membrane-peptide interactions [32]. Many biological processes, such as topological phase transitions of bilayers, occur on timescales of milliseconds, if not seconds [33], making it hard to use MD simulations. The few researchers who have reported on these processes [34, 35], used the MARTINI model, a coarse-grained MD simulation model which effectively sacrifices molecular detail in favour of computation time.

In addition, we are interested in determining thermodynamic and mechanical properties of the bilayer. According to the laws of statistical thermodynamics this calls for the evaluation of so-called partition functions, which can be described as the sum of the statistical weights over all possible and allowed configurations of a system. For MD simulations, finding all possible configurations is nigh impossible. In addition, the system needs to be very large in order to be (thermodynamically) meaningful in terms of the mesoscale morphology. This once again increases the already extensive computation time. As an alternative one can use Monte Carlo simulations, but these simulations run into similar problems in estimating partition functions and other thermodynamic quantities.

When molecular detailed simulations do not readily give answers, mean-field calculations can be the way to go. Mean-field modelling effectively solves the problem of one molecule in an external mean force field, which represents the average interactions with all other molecules. Compared to the many-body problems of MD and MC simulations, the mean-

field approach is much less computational demanding. For bilayers, it turns out that the mean-field approach tends to give very reasonable results despite that it disregards fluctuations in the system. This is because in large and densely packed systems, such as bilayers, fluctuations are relatively inconsequential. We therefore choose to use a mean-field approach as both structural and thermodynamic properties can be evaluated while using a reasonably detailed molecular model.

In this thesis, we make use of Scheutjens-Fleer self-consistent field (SF-SCF) theory [36, 37]. At the base of this mean-field theory is a (mean-field) free energy functional. This free energy functional is written in terms of volume fractions profiles (dimensionless concentrations) of the segments (molecules are composed of strings of segments) and segment potential profiles. The segment potentials are characteristic for SCF theory and quantify the amount of (potential) energy that is required to transfer a certain segment from the bulk to a specified location. These potentials feature in Boltzmann-like statistical weights and are instrumental to evaluate the volume fraction distributions. These volume fraction distributions are subsequently used to compute the segment potentials. Hence, the segment volume fraction distributions and the segment potentials mutually depend on each other. Importantly the SCF machinery calls for an optimisation of the mean-field free energy functional. Characteristic for such optimised free energy is the so-called self-consistent field situation: the segment potentials both follow from and determine the volume fraction profiles and *vice versa*. [38] This 'fixed point', better known as the self-consistent field solution, is found numerically by iterations.

In order to execute the above procedure, various input variables need to be provided. These include how many lipids one has per unit membrane area, the molecular architecture of the molecules (lipid, water) and a set of interaction parameters that specify how the segments of the molecules interact with each other (hydrophobic versus hydrophilic).

As soon as the self-consistent field solution is available, we can evaluate the mean-field free energy and extract other thermodynamic quantifies, such as the membrane tension γ. In general, this membrane tension will not be zero, as it would be a very lucky guess that exactly the correct number of lipids per unit membrane area was chosen as input. Consequently, the number of molecules per unit membrane area has to be adjusted and the optimisation of the free energy functional is repeated. This cycle is repeated until the membrane is free of tension. Once this is done we can implement the Helfrich analysis and obtain estimates for the mechanical parameters of the membranes (more about this below).

As mentioned, the SF-SCF model makes use of computer algorithms to optimise the mean-field free energy. The implementation of such algorithms requires some sort of

discretisation scheme. The SF-SCF theory makes use of a lattice (a regular set of coordinates) to discretize space. On top of this, the method considers that the molecules are composed of strings of discrete segments (in our case coarse-grained atoms). In the classical approach [8, 39] one segment fits exactly on one lattice site. Hence, there is only one length scale in the discretisation protocol. A disadvantage of this method is that all information on a length scale smaller than one lattice site, or (in this case) one segment, is lost. As a consequence, in systems in which gradients in densities (volume fractions) are steep, such as for lipid bilayer membranes, lattice artefacts develop and the method becomes inaccurate.

To solve this problem, we report on a variation on the discretisation strategy in this thesis. Here, each lattice site is a discrete number of times smaller than a segment. We refer to this approach as the lattice-refined SF-SCF theory. In doing so, we are able to eliminate the lattice artefacts, which subsequently allows us to evaluate the bending rigidities for the first time in the grand canonical ensemble (μVT ensemble), as will be explained below.

In order to correctly evaluate the free energy functional, it is important to make some assumptions and decisions. First of all, we have to choose the lattice and the lattice refinement. Secondly, we have to implement the chain model. We use the freely-jointed chain (FJC) model. In this model, consecutive segments in a molecule are put in adjacent lattice sites, but there is no long-distance correlation that would limit in which direction a consecutive segment is positioned. Thirdly, we have to characterize the interactions between the segments. This is done with a mean-field approach and quantified using so-called Flory-Huggins χ-parameters [40, 41], where a $\chi > 0$ stands for repulsion and $\chi < 0$ for attraction. The higher the absolute value of χ, the stronger the attraction/repulsion. In our models, we only take interactions between neighbouring segments into account and neglect longer distance interactions. The final choice we have to make is what type of molecules we put into the system and in what quantities. For a lipid bilayer system, this involves lipid molecules and water. In chapter 5 we also consider additives in the membranes.

The lattice-refined SF-SCF machinery provides two types of outputs. First of all there are the volume fraction profiles per segment type. For a system of phospholipids in water, in which the interaction parameters of the tail segments with water are higher than those of the headgroup segments with water (tail is more hydrophobic than the headgroups), this results in a bilayer. In figure 1.7 an example volume fraction profile of such a bilayer is given. As can be seen from such a profile, we find the lipid tails in the centre of the bilayer, and the hydrophilic headgroups at the outer sides. Water, i.e. the solvent, resides

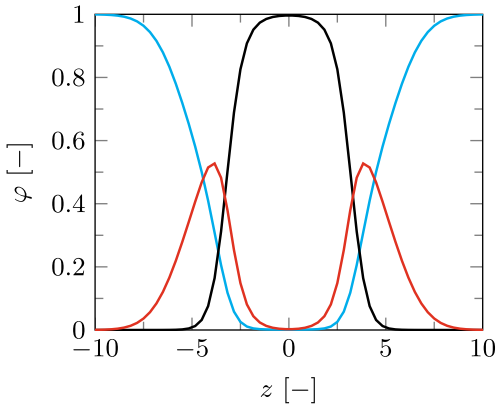

Figure 1.7: A typical cross-sectional volume fraction profile of a tensionless lipid bilayer. Here, the volume fractions (φ) of the lipid tails (black), the lipid headgroup (red) and the solvent (blue) are given as a function of the z coordinate, with $z = 0$ at the mid-plane of the bilayer.

partly in the headgroup areas but is expelled from the bilayer core. On top of the volume fraction profiles, we can extract thermodynamic quantities such as the grand potential Ω. The grand potential per unit area is identified as the membrane tension.

Using the lattice-refined SF-SCF approach, we are able to model a planar bilayer for the first time without large lattice artefacts and therefore unambiguously find the tensionless lipid bilayer, i.e. the number of lipids per unit area for which the membrane tension $\gamma = 0$. We also obtain information on the concentration of lipids in the aqueous solution which is in equilibrium with the bilayer. Next, we do similar calculations in a spherical lattice geometry. The bilayer in such a system is homogeneously curved in a vesicle type structure. The grand potential of the resulting vesicles is found to be completely determined by the curvature energy: $\Omega = 4\pi(2\kappa+\bar{\kappa})$. This remarkable result indicates that the curvature energy of a vesicle does not depend on its radius and thus is scale invariant. The natural consequence is that the chemical potential of the lipids in the vesicle system must be the same as the chemical potential of the lipids in the tensionless planar bilayer. In other words, the planar bilayer and the spherical vesicle are considered in one and the same grand canonical ensemble (chemical potentials μ fixed, same lipid bulk concentrations). To cut a long story short, it is therefore possible to correlate the thermodynamic quantities found in the two geometries and accurately extract the bilayer mechanical parameters such as the bending rigidity. With the mechanical parameters known, we can subsequently correlate molecular properties of the lipids to existing mesomorphic phase behaviour of lipid bilayers and are able to identify groups of additives that may induce a specific mesomorphic phase change such as the formation of a bilayer handle.

1.7 Thesis outline

This thesis is structured as follows. In **chapters 2 and 3** I show our experimental efforts and results on the controlled production of stable vesicle pairs **(chapter 2)** and small vesicle aggregates **(chapter 3)** using several linker systems: (i) vesicles containing biotinylated lipids are coupled together with streptavidin, (ii) cationic polymers (polylysine) are used to link negatively charged vesicles, and (iii) temperature as a control parameter is used for the aggregation of vesicles using the thermo-sensitive surfactant C18-pNIPAm. We show that a key characteristic allowing for "self-limiting aggregation" is that the membrane-bound linker molecules can diffuse to the contact area between two vesicles, depleting the rest of the membrane, before collision with another vesicle occurs. We further demonstrate that by combining the reversible 'switch-like' aggregation properties of C18-pNIPAm with the irreversible linkage between biotinylated lipids and streptavidin, it is possible to control the size of the aggregates step by step using a simple temperature program. In **chapter 3**, we additionally introduce and apply a lipid-exchange assay to identify whether lipids exchange between vesicles as a result of the linking process, something that will happen if vesicles fuse or form intermembrane handles. In **chapters 4 and 5** we discuss SCF calculations on lipid bilayers. To be specific, in **chapter 4** we introduce a lattice refinement to the existing SF-SCF framework that allowed us to revise and follow the correct protocols to estimate the bending rigidities of phospholipid bilayers. We then used this protocol to gain insight on the effects of several lipid properties, for example headgroup hydrophilicity and tail length on these bending rigidities. In **chapter 5** we expand on the work of chapter 4 by introducing various additives in the system to stimulate changes in bending rigidities and identify groups of additives that could potentially induce mesomorphic phase changes. The final chapter **(chapter 6)** of this thesis provides a general discussion, where I put our results in a wider context, discuss aspects and results that have not yet been addressed and provide an overview of the challenges that still remain and what direction future research may take.

References

[1] S Jonathan Singer and Garth L Nicolson. The fluid mosaic model of the structure of cell membranes. *Science*, 175(4023):720–731, 1972.

[2] Jacob N Israelachvili, D John Mitchell, and Barry W Ninham. Theory of self-assembly of hydrocarbon amphiphiles into micelles and bilayers. *Journal of the Chemical Society, Faraday Transactions 2: Molecular and Chemical Physics*, 72:1525–1568, 1976.

[3] Derek Marsh. Intrinsic curvature in normal and inverted lipid structures and in membranes. *Biophysical journal*, 70(5):2248–2255, 1996.

[4] Leonie van't Hag, Sally L Gras, Charlotte E Conn, and Calum J Drummond. Lyotropic liquid crystal engineering moving beyond binary compositional space–ordered nanostructured amphiphile self-assembly materials by design. *Chemical society reviews*, 46(10):2705–2731, 2017.

[5] Zakaria A Almsherqi, Sepp D Kohlwein, and Yuru Deng. Cubic membranes: a legend beyond the flatland* of cell membrane organization. *The Journal of cell biology*, 173(6):839–844, 2006.

[6] Rumiana Koynova and Boris Tenchov. Mesomorphic phases and phase transitions in membranes, biomechanical aspects. *Series on Biomechanics*, 2017.

[7] Wolfgang Helfrich. Elastic properties of lipid bilayers: theory and possible experiments. *Zeitschrift für Naturforschung C*, 28(11-12):693–703, 1973.

[8] H Pera, JM Kleijn, and FAM Leermakers. Linking lipid architecture to bilayer structure and mechanics using self-consistent field modelling. *The Journal of chemical physics*, 140(6):02B606_1, 2014.

[9] AF Smeijers, Albert J Markvoort, K Pieterse, and PAJ Hilbers. A detailed look at vesicle fusion. *The Journal of Physical Chemistry B*, 110(26):13212–13219, 2006.

[10] Lukas K Tamm and Harden M McConnell. Supported phospholipid bilayers. *Biophysical journal*, 47(1):105, 1985.

[11] Ralf P Richter, Rémi Bérat, and Alain R Brisson. Formation of solid-supported lipid bilayers: an integrated view. *Langmuir*, 22(8):3497–3505, 2006.

[12] Yoshihisa Kaizuka and Jay T Groves. Structure and dynamics of supported intermembrane junctions. *Biophysical journal*, 86(2):905–912, 2004.

[13] Xiaojun Han, Ammathnadu S Achalkumar, Matthew R Cheetham, Simon DA Connell, Benjamin RG Johnson, Richard J Bushby, and Stephen D Evans. A self-assembly route for double bilayer lipid membrane formation. *ChemPhysChem*, 11(3):569–574, 2010.

[14] David H Murray, Lukas K Tamm, and Volker Kiessling. Supported double membranes. *Journal of structural biology*, 168(1):183–189, 2009.

[15] George R Heath, Mengqiu Li, Isabelle L Polignano, Joanna L Richens, Gianluca Catucci, Paul O'Shea, Sheila J Sadeghi, Gianfranco Gilardi, Julea N Butt, and Lars JC Jeuken. Layer-by-layer assembly of supported lipid bilayer poly-l-lysine multilayers. *Biomacromolecules*, 17(1):324–335, 2016.

[16] Minsub Chung, Randall D Lowe, Yee-Hung M Chan, Prasad V Ganesan, and Steven G Boxer. Dna-tethered membranes formed by giant vesicle rupture. *Journal of structural biology*, 168(1):190–199, 2009.

[17] ET Kisak, MT Kennedy, D Trommeshauser, and JA Zasadzinski. Self-limiting aggregation by controlled ligand- receptor stoichiometry. *Langmuir*, 16(6):2825–2831, 2000.

[18] Scott A Walker and Joseph A Zasadzinski. Electrostatic control of spontaneous vesicle aggregation. *Langmuir*, 13(19):5076–5081, 1997.

[19] Maik Hadorn and Peter Eggenberger Hotz. Dna-mediated self-assembly of artificial vesicles. *PLoS One*, 5(3):e9886, 2010.

[20] Guilherme Volpe Bossa, Tereza Pereira de Souza, and Sylvio May. Adhesion of like-charged lipid vesicles induced by rod-like counterions. *Soft matter*, 14(19):3935–3944, 2018.

[21] Jingxia Yao, Yuan Feng, Ying Zhao, Zichen Li, Jianbin Huang, and Honglan Fu. Vesicle aggregation in aqueous mixtures of negatively charged polyelectrolyte and conventional cationic surfactant. *Journal of colloid and interface science*, 314(2):523–530, 2007.

[22] Dmitry Volodkin, Vincent Ball, Pierre Schaaf, Jean-Claude Voegel, and Helmuth Mohwald. Complexation of phosphocholine liposomes with polylysine. stabilization by surface coverage versus aggregation. *Biochimica et Biophysica Acta (BBA)-Biomembranes*, 1768(2):280–290, 2007.

[23] Rumiana Dimova. Recent developments in the field of bending rigidity measurements on membranes. *Advances in colloid and interface science*, 208:225–234, 2014.

[24] C Monzel and K Sengupta. Measuring shape fluctuations in biological membranes. *Journal of Physics D: Applied Physics*, 49(24):243002, 2016.

[25] Thomas Portet, Sharona E Gordon, and Sarah L Keller. Increasing membrane tension decreases miscibility temperatures; an experimental demonstration via micropipette aspiration. *Biophysical journal*, 103(8):L35–L37, 2012.

[26] G Pabst, N Kučerka, M-P Nieh, MC Rheinstädter, and J Katsaras. Applications of neutron and x-ray scattering to the study of biologically relevant model membranes. *Chemistry and Physics of Lipids*, 163(6):460–479, 2010.

[27] David E Shaw, Paul Maragakis, Kresten Lindorff-Larsen, Stefano Piana, Ron O Dror, Michael P Eastwood, Joseph A Bank, John M Jumper, John K Salmon, Yibing Shan, et al. Atomic-level characterization of the structural dynamics of proteins. *Science*, 330(6002):341–346, 2010.

[28] Kresten Lindorff-Larsen, Stefano Piana, Ron O Dror, and David E Shaw. How fast-folding proteins fold. *Science*, 334(6055):517–520, 2011.

[29] Ken A Dill and Justin L MacCallum. The protein-folding problem, 50 years on. *science*, 338(6110): 1042–1046, 2012.

[30] D Bemporad, C Luttmann, and JW Essex. Computer simulation of small molecule permeation across a lipid bilayer: dependence on bilayer properties and solute volume, size, and cross-sectional area. *Biophysical journal*, 87(1):1–13, 2004.

[31] Siewert-Jan Marrink and Herman JC Berendsen. Simulation of water transport through a lipid membrane. *The Journal of Physical Chemistry*, 98(15):4155–4168, 1994.

[32] Jakob P Ulmschneider and Martin B Ulmschneider. Molecular dynamics simulations are redefining our view of peptides interacting with biological membranes. *Accounts of chemical research*, 51(5): 1106–1116, 2018.

[33] Julian C Shillcock and Reinhard Lipowsky. The computational route from bilayer membranes to vesicle fusion. *Journal of Physics: Condensed Matter*, 18(28):S1191, 2006.

[34] Siewert-Jan Marrink and D Peter Tieleman. Molecular dynamics simulation of spontaneous membrane fusion during a cubic-hexagonal phase transition. *Biophysical journal*, 83(5):2386–2392, 2002.

[35] Hari Leontiadou, Alan E Mark, and Siewert J Marrink. Molecular dynamics simulations of hydrophilic pores in lipid bilayers. *Biophysical journal*, 86(4):2156–2164, 2004.

[36] JMHM Scheutjens and GJ Fleer. Statistical theory of the adsorption of interacting chain molecules. 1. partition function, segment density distribution, and adsorption isotherms. *Journal of Physical Chemistry*, 83(12):1619–1635, 1979.

[37] J M H M Scheutjens and G J Fleer. Statistical theory of the adsorption of interacting chain molecules. 2. train, loop, and tail size distribution. *J. Phys. Chem.*, 84(2):178–190, 1980. URL `http://pubs.acs.org/doi/abs/10.1021/j100439a011`.

[38] O. A. Evers, J. M. H. M. Scheutjens, and G. J. Fleer. Statistical thermodynamics of block copolymer adsorption. 1. formulation of the model and results for the adsorbed layer structure. *Macromolecules*, 23(25):5221–5233, 1990.

[39] F A M Leermakers. Bending rigidities of surfactant bilayers using self-consistent field theory. *J. Chem. Phys.*, 138(15):04B610, 2013. URL `https://doi.org/10.1063/1.4801327`.

[40] Paul J Flory. Thermodynamics of high polymer solutions. *The Journal of chemical physics*, 10(1): 51–61, 1942.

[41] Maurice L Huggins. Solutions of long chain compounds. *The Journal of chemical physics*, 9(5): 440–440, 1941.

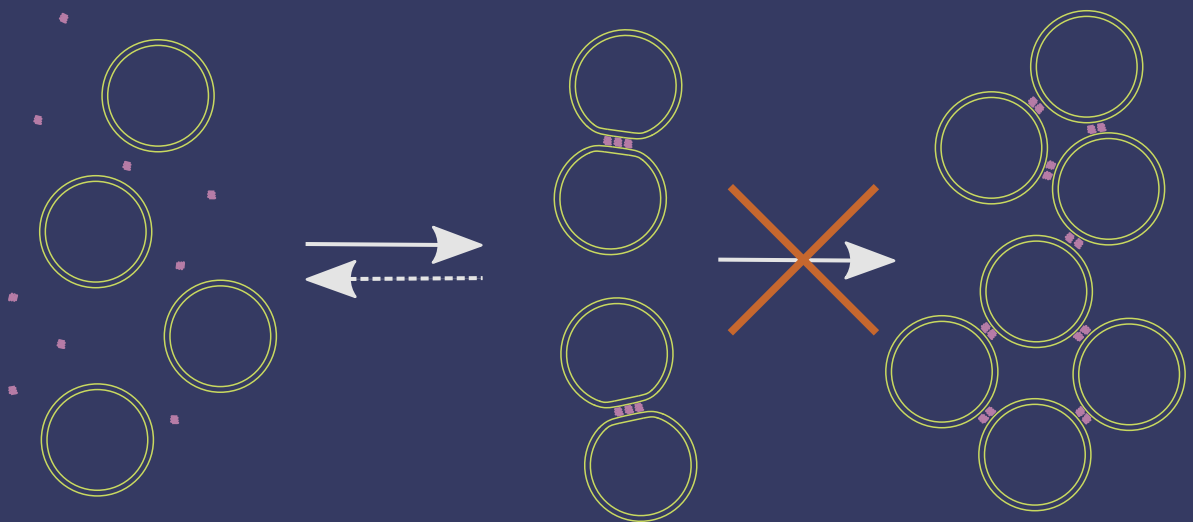

CHAPTER 2

Self-limiting aggregation of phospholipid vesicles

Lipid vesicles are widely used as model systems to study biological membranes. Self-assembly of such vesicles into vesicle pairs provides further opportunity to study interactions between membranes. However, formation of vesicle pairs, while subsequently keeping their colloidal stability intact, is challenging. Here we report on three strategies that lead to stable finite-sized aggregates of phospholipid vesicles: (i) vesicles containing biotinylated lipids are coupled together with streptavidin, (ii) bridging attraction is exploited by adding cationic polymers (polylysine) to negatively charged vesicles, and (iii) temperature as a control parameter is used for aggregation of vesicles mixed with a thermo-sensitive surfactant. While each strategy has its own advantages and disadvantages for vesicle pair formation, the latter strategy additionally shows reversible limited aggregation: above the LCST of pNIPAm, vesicle pairs are formed, while below the LCST single vesicles prevail. Mixing protocols were assessed by dynamic and static light scattering as well as fluorescence correlation spectroscopy to determine under which conditions vesicle pairs dominate the aggregate size distribution. We have strong indications that without subsequent perturbation, the individual vesicles remain intact and no fusion or leakage between vesicles occurs after vesicle pairs have formed.

This chapter has been published as: De Lange, N., F. A. M. Leermakers, and J. M. Kleijn. *Soft Matter* **16**(9) (2020): 2379-2389.

2.1 Introduction

The biological membrane is a cornerstone of life. Not only are cells surrounded by such a double leaflet of lipids, but their interior is also packed with it. Where the primary function of the outer cell membrane is that of a barrier, membranes, in particular intracellular membranes, have a wide variety of different tasks. It is well known that the composition of membranes is tactically adjusted to suit these tasks [1–3]. This is evidenced by an extraordinary variety of shapes, structures and even topologies of the membrane present in the cell, each of which is accompanied by a distinct, complex and dynamic composition of the membrane.

Changes in shape or topology of the membrane, like membrane fusion or the formation of handles between membranes occur often within cells [4]. This allows for content exchange across membranes which is vital for the cell that needs to transport materials to and from organelles or in and out of the cell. However, the physics behind these membrane interactions remains poorly understood.

Model membrane systems like lipid vesicles, or liposomes, are widely used to study the membrane. They consist of some liquid enclosed by a lipid bilayer and naturally occur within the cell for transport of material across the cell. Lipid vesicles have been used for various applications like drug delivery [5, 6], bioreactors [7, 8] or to study chemical reactions under confinement and biologically relevant conditions [9]. Liposomes can easily be generated in vitro when carefully selected lipids are dispersed in an aqueous solution. This 'bottom-up' approach allows for control over the membrane composition. Liposomes, therefore, are ideally suited to study membranes including various inter-membrane interactions like adhesion [10] or (hemi-) fusion as was shown using lipid-anchored DNA [11] and SNARE proteins [12].

A natural starting point for studying membrane (hemi-)fusion are small aggregates of liposomes, ideally limited to vesicle pairs. To obtain such systems, one has to first start the self-assembly of liposomes and stop further self-assembly at a very early stage. We will refer to such arrested aggregation as limited aggregation.

Aggregation of colloidal particles, such as lipid vesicles, has been a popular research field since the publishing of the DLVO theory [13, 14]. For charged colloids, the colloidal stability is governed by a balance of electrostatic repulsion and van der Waals attraction. The DLVO theory explains the loss of colloidal stability through its dependence on ionic strength as an 'all or nothing' process. To control the aggregation, by limiting the aggregation or directing the assembly into specific shapes and structures, several strategies can be applied. Particles of specific shapes [15, 16], with symmetrically arranged

patches [17, 18], or with functionalized surfaces [19, 20] have been successfully used. In particular, DNA sticky ends are widely used on numerous colloidal particles such as solid metal nanoparticles [21, 22], polystyrene microparticles [23] and emulsion droplets [24]. The aforementioned strategies have provided a rich variety of advanced colloidal materials with various functions [18, 25].

For vesicles, aggregation needs to be induced by additives as van der Waals attraction is negligible. Additives that can do this may be referred to as 'linkers'. This approach is not new, as is evidenced by the amount of literature available. Different types of linkers include the previously mentioned tethered DNA strands with complementary sticky ends [26–28], the protein streptavidin which links to biotinylated lipids [29–31] or using charged polymers and oppositely charged vesicles [32, 33]. Other methods include the use of univalent or divalent counterions [34, 35]. A linker binds vesicles together which usually leads to large multivesicular aggregates. While such aggregates are easy to obtain, achieving control on the aggregation to get vesicle aggregates of a given size vastly expands possible applications, for example multicompartment drug delivery [6]. Several strategies have been applied to control the aggregation. This includes introducing charge in vesicles to slow down the aggregation rate [29]. The electrostatic repulsion between vesicles obtained through the charge creates an energy barrier for aggregation, which reduces the amount of successful vesicle collisions. The range of electrostatic repulsion is governed by the Debye length which can be controlled using salt or other electrolytes [36]. The specific properties of biotin and streptavidin can also be used to control vesicle aggregation. As streptavidin is able to bind 2 biotin on either side of the molecule, it is able to bridge vesicles. A prerequisite for this is that a bound streptavidin is able to find a free biotinylated lipid on another vesicle. If however the biotin is already bound to another streptavidin, which happens often if the amount of streptavidin present exceeds the amount of biotin present (biotin-starved regime), bridging between vesicles does not occur. This limitation can be exploited for the formation small vesicle aggreggates [30].

An aspect of the liposome that can be exploited for limited aggregation is the lateral mobility of the lipids and subsequent linker molecules inserted in the membrane. Upon binding of two vesicles an adhesion patch is formed. Through the lateral mobility of other linker molecules to this adhesion patch, the strength of the adhesion between two vesicles increases in time [37]. A consequence of the local enrichment of linker molecules in an adhesion patch is that these linkers are no longer available to link to other vesicles and that the parts of the vesicles outside the adhesion zone are depleted of the linkers. This intra-aggregate binding is the hallmark for limited aggregation, as was previously shown [26, 38].

Our aim is to stop the assembly of vesicles as good as possible on the pair level. For this, we have to obtain the optimal relation between the time scale for vesicle-vesicle collision and the time scale for the lateral mobility of linkers towards the adhesion patches. In short, the vesicle concentration should be low enough so that the characteristic collision time is large compared to the maximum lateral diffusion time. Of course, the number of linkers per vesicle should remain under a threshold value so that a sufficient part of them can be hidden in the adhesion patches. Ideally, we would like to obtain multiple orthogonal approaches to extend the possibilities of manipulating vesicle associates. With an extended toolbox, one can, for example, bring two bilayers together by one of the linkers and compromise the topological stability of such a bilayer pair by another.

We have tested several types of linkers for their capability of linking vesicles to form small stable aggregates. Aggregation of the vesicles was studied using static and dynamic light scattering, with fluorescent correlation spectroscopy and with electrophoretic mobility measurements. We found three scenarios in which the self-limiting association could be established: (1) biotinylated lipids act as receptors on the vesicles with streptavidin as ligand coupling the vesicles together. This method was shown before to give finite sized aggregates [30]. (2) Cationic polymers (polylysine, or PLL) are added to a solution with anionic vesicles. Because of the strong cooperative binding of the polymer onto the vesicle, we can induce bridging flocculation. When we limit the number of polymers per vesicle to (close to) unity, the assembly is naturally limited. (3) Thermo-sensitive surfactants containing a C18 tail and a poly-NIPAm headgroup (C18-pNIPAm) allow for the formation of stable small liposome aggregates by a temperature switch: pNIPAm exhibits LCST behaviour and thus the aggregation is triggered by bringing the vesicles to a temperature above $T \approx 32$ °C. While this method has not been used for vesicle aggregation before, it has been shown that this thermosensitive surfactant can initiate aggregation of polystyrene particles into small crystallites (order of 100 particles) in a matter of minutes or to destabilize droplet suspensions triggering phase separation using a simple temperature switch [39]. For each system, we explore the effects of the relevant physical conditions on the self-assembly of vesicles and discuss in which way vesicle pair formation can be further optimized.

Our working hypothesis is that the ability to fabricate small clusters of vesicles, or more specifically, vesicle pairs, is a useful step to start studying the physical properties of membrane pairs. Combining different attraction strategies systematically with variations in the lipid composition of vesicles may prove to be crucial to alter the topological stability of bilayer pairs and induce membrane (hemi-)fusion or the formation of handles between the vesicles which could be checked with lipid mixing assays or content mixing assays [40, 41].

2.2 Materials and Methods

2.2.1 Materials

All chemicals are analytical grade and were used without further purification. Chloroform solutions of the phospholipids 1,2-dioleoyl-sn-glycero-3-phosphocholine (DOPC), 1,2-dioleoyl-sn-glycero-3-phosphoethanolamine-N-(cap biotinyl) (DOPE-biotin), 1,2-dioleoyl-sn-glycero-3-phosphoglycerol (DOPG) and 1,2-dioleoyl-sn-glycero-3-phosphoethanolamine-N-(7-nitro-2-1,3-benzoxadiazol-4-yl) (NBD-PE) were purchased from Avanti Polar Lipids Inc. Streptavidin was purchased from Jackson ImmunoResearch. N-isopropylacrylamide (NIPAm) was obtained from TCI Europe N.V. Other analytical grade chemicals were acquired from Sigma-Aldrich. This includes 1-octadecatonethiol, 2,2'-azobis(2-methylpropionitrile (AIBN), 0.1% (w/v) poly-L-lysine solution in H_2O ($M_w \approx 1.5 \times 10^5 - 3.0 \times 10^5$ g/mol), poly-L-lysine hydrobromide ($M_w \approx 1000 - 5000$ g/mol) and all chemicals used to make the buffer solutions.

Buffer solutions were prepared using ultrapure water (resistivity > 18 MΩ cm). All buffer solutions contained 10 mM Tris (2-amino-2-(hydroxymethyl)propane-1,3-diol) and 50 mM NaCl and the pH was adjusted to 7.5 unless otherwise mentioned. Adjusting the pH was done by adding 1 M HCl or 1 M NaOH. All buffers were filtered through 0.2μm pores before use.

2.2.2 Vesicle preparation

Vesicle preparation was performed similarly to previous work [42, 43]. In short, we mixed phospholipids together in the desired ratio in a round bottom flask, evaporated the chloroform under a stream of nitrogen and dried the lipid film under vacuum for at least 2 h. After drying, the lipids were resuspended in the appropriate buffer to a final lipid concentration ($C_l \approx 2.0\text{e}{-2}$ M) and hydrated for about 1 h in a rotary evaporator (no vacuum, 323 K, 100 rpm). This resulted in multilamellar vesicles. Subsequently, four freeze-thaw steps were applied using liquid nitrogen and a 40 °C water bath to obtain unilamellar vesicles. After this, the vesicles were extruded 21 times using a mini-extruder (Avanti Polar Lipids, Inc) equipped with a polycarbonate membrane with 0.2μm pore sizes, to obtain vesicles of approximately 75 nm in radius. The vesicles were subsequently collected and stored in the fridge until further use. The maximum storage time was 5 days. Characterization of the vesicles was performed using dynamic and static light scattering (DLS and SLS) [44, 45]. A cumulant analysis [46], see Supplementary information (SI), showed the vesicles to be spherical, with hydrodynamic radius $R_h \approx$ 65-80 nm and polydispersity index (PDI) ≈ 0.1. An overview of all vesicles used can be found in the SI,

table 2.2.

2.2.3 C18-pNIPAm surfactant synthesis

Synthesis of the C18-pNIPAm surfactant was done following the protocol previously described [39]. It involves a free radical chain-transfer polymerization of 1-octadecanethiol and NIPAm using AIBN as the initiator. 1.03 g of 1-octadecanethiol ($\sim$ 3.5 mmol), 29.36 g NIPAm ($\sim$ 262.5 mmol) and 1.14 g AIBN ($\sim$ 7.0 mmol) were dissolved in a 250 ml round bottom flask with THF (100ml). This corresponds to molar ratios thiol/NIPAm/AIBN of 1:75:2. The solution was bubbled with nitrogen for 30 minutes after which the reaction was run overnight at 55°C. Purification was done by precipitation into cold hexane, with subsequent centrifugation. The precipitate was dried under vacuum, collected and stored for further use. The molecular weight of the surfactant was characterized by gel permeation chromatography (GPC) with HFIP (hexafluoro-2-propanol) as the running solvent; $\langle M_n \rangle = 5708$, PDI = 2.8, degree of polymerization approximately 50.

2.2.4 Aggregation experiments

For aggregation experiments vesicles were diluted in buffer to a final lipid concentration $C_l \approx 1.0\text{e}{-4}$ M, unless specified otherwise. After measuring the size, mass or electrophoretic mobility of the vesicles, a small amount of linkers, i.e. streptavidin, polylysine (PLL) or C18-pNIPAm surfactants, was added to the sample. Streptavidin was added to vesicles containing biotin (B vesicles or NBD vesicles), PLL was added to vesicles containing DOPG (PG vesicles) and C18-pNIPAm was added to pure DOPC vesicles (S-0 vesicles); see table 2.2 (SI). After adding the linkers, the sample was mixed gently and measured for the new size and mass. Subsequently, the amount of linkers in the sample was doubled, mixed and measured once again. This cycle was repeated until the molar streptavidin/biotin ratio (N_s/N_b) was 2.4, the molar C18-pNIPAm / DOPC ratio ($N_{\mathrm{C18}}/N_{\mathrm{DOPC}}$) was 0.32, or when uncontrolled aggregation of the vesicles was observed. The latter happened at high PLL amounts and could be recognized by an indefinite increase in hydrodynamic radius (R_h) over time.

For DOPG vesicles with PLL, reverse aggregation experiments were carried out as well. For this, stable aggregates of vesicles at fixed PLL per vesicle ratio were subjected to an increasing amount of salt (NaCl) in the solution.

The size and mass of the vesicles and vesicle aggregates were measured using dynamic and static light scattering (DLS and SLS). For NBD vesicles fluorescent correlation spectroscopy (FCS) was applied.

2.2.5 Light scattering

All light scattering experiments were performed using an ALV instrument equipped with an ALV5000/60×0 external correlator and a 300 mW Cobolt Samba-300 DPSS laser operating at a wavelength $\lambda = 532$ nm.

For aggregation with streptavidin and biotin or with PLL, standard DLS experiments involve 45-100 measurements of 10 s recorded at a 90° angle. The diffusion coefficient D and subsequently the R_h were calculated similarly to previous work [47]. Once D was steady over time, the average D was determined and this value was used to obtain a normalised diffusion coefficient D_0/D or hydrodynamic radius R/R_0, with D_0 and R_0 the diffusion coefficient and hydrodynamic radius of single vesicles. SLS experiments were only carried out after DLS experiments showed a steady D over time. Standard SLS experiments consist of measurements performed at scattering angles (θ) ranging from 30° to 55° with steps of 1°. For each θ, three measurements were recorded of 10 s. To calculate the absolute Rayleigh scattering (R_θ), a similar SLS experiment was performed on buffer solution (10 mM Tris-HCl, 50 mM NaCl, pH 7.5) and on toluene as reference. The molar mass of the aggregates (M_v) and the radius of gyration (R_g) were estimated using a Guinier analysis [48]. From M_v we can calculate the mean aggregate number (M), which is defined as the average number of single vesicles per aggregate. See SI for a detailed explanation on the data analysis of DLS and SLS.

For samples in which C18-pNIPAm surfactants were added to the vesicles, a standard DLS measurement consists of 1000 measurements of 10 s recorded at a 90° angle. During the recording, the vesicles underwent a temperature program. This involved 10 minutes at 25 °C, 30 minutes at 40 °C and the remainder of the experiment back at 25 °C. In repeat experiments, vesicles were subjected to an extensive temperature program. Here, 30-minute cycles at various temperatures (27.5 °C, 30 °C, 31 °C, 32 °C, 33 °C, 34 °C, 35 °C, 37.5 °C and 40 °C) were alternated with 60 min cycles at 25 °C. SLS experiments were performed similarly as for the other vesicles, both at 25 °C and at 40 °C.

2.2.6 Fluorescent correlation spectroscopy

FCS measurements were performed as an extra check for the size and aggregation number of the vesicles containing biotin, before and after self-assembly with streptavidin. For these experiments, vesicles were fluorescently labelled with NBD (NBD vesicles).

Comparable to DLS, FCS uses the intensity fluctuations of the detected fluorescent light caused by the diffusion of fluorescent particles in and out of the confocal volume, to determine the diffusion coefficient of the fluorescent particles [47, 49, 50]. For this, the

dimensions of the confocal spot have to be known. Therefore, Rhodamine 110 (R110), of which the diffusion coefficient is known (D = 4.3e−10 m^2/s), was used to calibrate the setup. We found a diffusion time of 18 μs and a structural parameter a (= ω_z/ω_{xy}, i.e. the ratio of the equatorial and axial radii of the detection volume) between 5 and 10. From this, the confocal volume was found to be approximately 0.2 fL.

To perform FCS experiments, a Leica TCS SP8 X microscope equipped with a 63× 1.20 NA water immersion objective and a super continuum laser or White light laser (SLL) selecting the 488 nm laser line was used. NBD was excited at 488 nm wavelength with a pulse frequency of 40 MHz. The fluorescence signal was detected through a pinhole, set at 90 μm, and filtered using a 495-550 nm spectral filter. The signal was recorded with the internal hybrid detector, coupled to a PicoHarp 300 TCSPC module (PicoQuant). Measurements were performed in 8-well chamber slides from Nunc^{TM} Lab-Tek^{TM} (Thermo Fischer Scientific). For each sample that contained vesicles, 15 or more measurements were recorded of 4 minutes. For the R110 samples, 20 measurements of 30 seconds each were recorded.

For FCS data analysis, the FFS-data processor version 2.3 (Scientific Software Technologies Software Centre) was used [50]. With the program, the average number of particles in the confocal volume ($\langle N \rangle$), their diffusion coefficient (D_f) and corresponding R_h were calculated. See SI for a detailed explanation of the data analysis.

2.2.7 Electrophoretic mobility

The electrophoretic mobility of DOPG vesicles with added PLL were measured by laser microelectrophoresis on a zetasizer Nano ZS with a dip cell (Malvern Instruments). See section 1.4 for the procedure of sample preparation.

2.2.8 Simple model of vesicle pairs

We model the translational diffusion behaviour of the vesicle pairs as if they are prolate ellipsoids. For such objects the diffusion coefficient is given by Kuipers et al [51]. In DLS and FCS the diffusion coefficient is experimentally determined and using the Stokes-Einstein equation an effective hydrodynamic radius, R_h, is calculated. It can be shown (see SI) that for pairs of monodisperse vesicles, R_h is expected to be between 1.32 R_0 and 1.15 R_0: the first value refers to the case that the vesicles have a very small contact area ($\ll R_0^2$), the second value is for an extensive contact area causing the vesicle pair to be perfectly spherical.

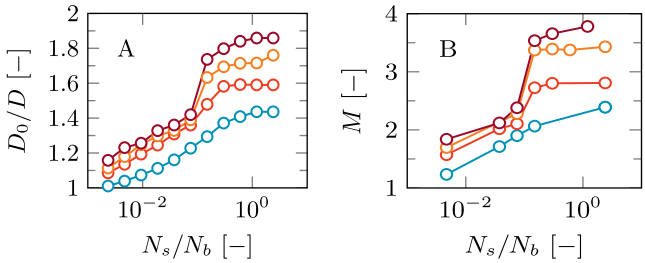

Figure 2.1: A) Normalized diffusion coefficient (D_0/D) as measured using DLS, B) the aggregation number (M), as a function of the logarithm of the streptavidin/biotin ratio (N_s/N_b). Experiments were carried out for different fractions of biotinylated DOPE phospholipids (f_b). The results are shown for vesicles containing $f_b = 0.0004$ (blue), $f_b = 0.002$ (red), $f_b = 0.004$ (orange) and $f_b = 0.006$ (purple). All experiments are performed with a lipid concentration $C_l = 0.1$ mM.

2.3 Results and discussion

Using the extrusion method as described in the materials and methods section with 21 push-throughs we produce monodisperse unilamellar vesicles with an average radius of 65-80 nm, as determined using SLS and DLS (see SI, table 2.2).

2.3.1 Vesicle aggregation using biotin and streptavidin

Streptavidin has four binding sites for biotin, two on opposite sides of the protein molecule. If streptavidin is added to vesicles that contain biotin, it acts as a cross-linker between the vesicles, inducing vesicle aggregation. For all measurements reported here, after a short incubation period, the aggregate size, or diffusion coefficient, proved to be stable over time and the aggregation was regarded as limited. The size and aggregate number (M) were subsequently determined from DLS and SLS measurements. Figure 2.1 shows D_0/D and M as a function of the streptavidin/biotin molar ratio (N_s/N_b) for vesicles with different fractions of biotinylated lipids.

In figure 2.1 two regimes can be distinguished. In the first regime, at relative small amounts of streptavidin ($N_s/N_b < 0.1$), D_0/D increases logarithmically ($D_0/D \propto \log(N_s/N_b)$. A transition to the second regime occurs between $0.1 < N_s/N_b < 0.2$. Here, R_h/R_0 increases more or less sharply depending on the experimental conditions. In the second regime, for $N_s/N_b > 0.2$, D_0/D is practically constant. We find that at the end of the first region $M \approx 2$, suggesting a population of mainly vesicle pairs. In the second regime, $M > 2$ for the samples containing a fraction of biotinylated DOPE phospholipids $f_b > 0.0004$, implying aggregation beyond vesicle pairs.

To further verify the formation of vesicle pairs, FCS measurements were performed. Sim-

Table 2.1: Comparison between DLS/SLS and FCS results for the B-0.4% vesicles. Normalization of diffusion coefficients and aggregate numbers were done using vesicles without added streptavidin ($N_s/N_b = 0$), see SI (table 2.2).

N_s/N_b [-]	D_0/D **DLS** [-] ± **St. Dev.**	D_0/D **FCS** [-] ± **St. Dev.**	M **SLS** [-] ± **St. Dev.**	M **FCS** [-]± **St. Dev.**
0	1 ±0.02	1 ±0.08	1 ±0.03	1 ±0.07
1/25.6	1.47 ±0.03	1.56 ±0.17	2.47 ±0.23	2.11 ±0.35

ilar to DLS, from the intensity fluctuations due to the movement of fluorescent particles in and out of the confocal volume the hydrodynamic radius is obtained. In addition, the average number of particles ($\langle N \rangle$) in the (known) confocal volume can be determined. Comparing the concentration of fluorescent particles in the confocal volume with the known total (original) concentration of single vesicles allows to distinguish between the cases of aggregation in mainly vesicle pairs or having a few larger aggregates with many single vesicles. In the first case the concentration of fluorescent particles is half the total concentration of single vesicles, in the latter the concentration fluorescent particles is only slightly lower compared to that of the single vesicles. Based on the $\langle N \rangle$ values we calculated the aggregation number M as well. The FCS results as compared with findings from DLS/SLS can be found in table 2.1.

According to our data, at the end of the first regime, D_0/D obtained through FCS is equal to D/D_0 as measured by DLS. In addition, FCS also gives an $M \approx 2$, verifying the formation of vesicle pairs (on average). In comparison, M obtained by SLS is slightly higher, which we attribute to the dominant contribution of larger particles to the scattering signal.

The vesicle preparation methods we perform yields polydisperse samples (PDI > 0.1) and the distributions of sizes and aggregate numbers are expected to widen upon aggregation. This is reflected by the somewhat higher standard deviations for the vesicle pairs compared to that of single vesicles, see table 2.1. In addition, we performed a CONTIN analysis [52–54] on the DLS results to follow the changes in particle distribution during the aggregation experiments (SI, figure 2.11). This reveals for the streptavidin-biotin linker system that broadening of the size distributions is quite limited. We will come back to this later in the discussion.

Streptavidin is a protein that can bind a maximum of four biotin moieties. Assuming that half of the biotinylated lipids in a vesicle are on the inner leaflet of the membrane, all the

available biotin can bind to streptavidin at $N_s/N_b \approx \frac{1}{8}$. Below this fraction, we have more biotin than biotin-binding sites. In other words, the amount of streptavidin is limiting the amount of connections that can be formed. We will therefore refer to regime 1 as the streptavidin-limited regime. At $N_s/N_b > \frac{1}{8}$ we have less biotin than biotin binding sites, and then the amount of biotin is limiting the amount of connections that can be formed. The second regime will therefore be referred to as the biotin-limited regime.

Streptavidin-limited regime.

Within this regime, adding streptavidin to the system directly increases the amount of links that can be established between vesicles. As a consequence, the total aggregation increases. Interestingly, this does not happen linearly, but the aggregation number M increases only logarithmically with the added amount of streptavidin. This behaviour can be explained by intra-aggregate binding (the binding of a biotin-streptavidin pair with another biotin of an already bound vesicle).

Intra-aggregate binding happens especially if the time required for a bound streptavidin to diffuse to the vesicle-vesicle contact zone (t_{diff}) is very low compared to the vesicle collision time (τ). We calculated that for a standard aggregation experiment with $C_l = 1.0\text{e}{-4}$ M and $R_v \sim 65-80$ nm), assuming each collision is successful and that a bound streptavidin has to diffuse the maximum distance, $t_{\text{diff}} \sim 1-2$ ms and $\tau \sim 80-130$ ms (see SI for the full calculation). So, for our standard experiments, $\tau/t_{\text{diff}} \approx 70$. That we are in the regime where $\tau \ll t_{\text{diff}}$ was confirmed by the observation that the concentration of vesicles has no effect on the results (see SI). This heavily favors intra-aggregate binding over coupling to new vesicles, not even taking into account steric hindrance and alignment effects during vesicle collision. As a consequence, although the total amount of links between vesicles increases with increasing amount of streptavidin, aggregation remains limited to mainly vesicle pairs.

At the end of the streptavidin-limited regime, the SLS and FCS measurements confirm a vesicle population of mainly vesicle pairs, as $M \approx 2$, see table 2.1. At this point, for vesicles with biotin fractions of 0.002, 0.004 and 0.006, the average hydrodynamic radius has increased to about 1.4 times the hydrodynamic radius of a single vesicle ($R_{vp}/R_0 = 1.4$, corresponding to a $D_0/D = 1.4$). Since we are dealing with mainly vesicle pairs, based on the model used for their diffusional behaviour (see SI) we conclude that the contact zones have to be small (i.e., patch radius significantly smaller than R_0).

The size of the contact zone is dependent on the balance between the adhesion strength and energy cost associated to the increased membrane curvature. The stronger the adhesion strength, the larger the contact zone, but the membrane curvature at the edges of the

contact zone increases as well. Biotin and streptavidin have a very high bond strength, on the order of 30 k_BT [55], which suggest the formation of large contact areas. This is however not the case. As the energy required to pull a phospholipid out of a bilayer is smaller, 16 k_BT [55], we can imagine that streptavidin attached to a single vesicle is able to pull out other biotinylated and more lipids to form micellar structures on the non-vesicle bound side of streptavidin. Other structural conformations might be possible as well. While bridge formation between two vesicles is the preferred conformation, the adhesion strength could be of much lower strength in comparison to the biotin-streptavidin bond strength. In addition, the energy required for deforming already highly curved membranes, which is the case for our small unilamellar vesicles (SUVs), is high as well. Finding the balance of these two forces as a function of vesicle size and adhesion strength is a highly interesting topic, for which further experiments and theoretical calculations are required, something we aspire to do ourselves.

Transition to the biotin-limited regime.

As the amount of streptavidin increases, so does the energy penalty associated with accommodating more streptavidin in the existing contact zones. This increases the chances of streptavidin linking with other not yet bound vesicles or vesicle aggregates. As a consequence, above a certain N_s/N_b ratio, vesicle pairs aggregate together to larger structures. However, above $N_s/N_b \approx 0.2$ the higher aggregates do not grow anymore. This is easily explained as from this point biotin becomes the limiting factor preventing the formation of new contacts. In line with this, the final mean aggregate number M increases with the biotin fraction in the vesicles: after the contact zones are saturated, for higher biotin fractions more biotin is left for connections with other vesicle pairs.

The sample with $f_b = 0.0004$ hardly shows aggregation beyond vesicle pairs. Apparently, at this low fraction of biotin, practically all biotin is already involved in the contact zones of vesicle pairs, leaving no biotin for further aggregation. We also performed the aggregation experiment for vesicles with relative high biotin fractions: $f_b = 0.02$ and higher (data not shown). In the streptavidin-limited region this resulted in similar results as obtained for the other biotin fractions. However, adding more streptavidin resulted in a continuing, unlimited aggregation.

Interestingly, for biotin fractions 0.002, 0.004 and 0.006 the transition to the streptavidin-limited regime seems to occur around the same N_s/N_b ratio (≈ 0.075). This suggests that saturation of the contact zones between vesicles occurs at a fixed N_s/N_b ratio, for vesicles of similar size. We however expect the transition to occur at higher N_s/N_b ratios for lower biotin fractions. For f_b in the range of 0.002 - 0.006 this is probably not visible

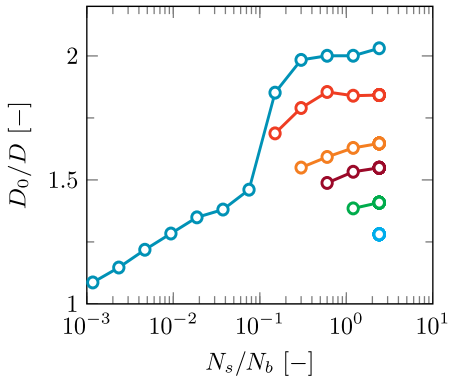

Figure 2.2: Normalized hydrodynamic radius of the vesicles found by DLS as a function of the N_s/N_b ratio in lin-log coordinates. The concentration of streptavidin was increased by subsequently adding an amount of streptavidin to a fixed concentration of vesicles ($C_l = 0.1$ mM) with biotin fraction $f_b = 0.004$. Each coloured series represent a new experiment in which the initial amount of streptavidin added to the sample is different. This amount corresponds to the N_s/N_b of the first (most left) data point of each series.

because of the limited experimental accuracy. However, as expected, for the sample with $f_b = 0.0004$ a much higher N_s/N_b fraction is necessary to get vesicle pairs.

Effect of overloading biotinylated vesicles with streptavidin.

In the experiments described above, streptavidin was added stepwise, exploring both the streptavidin-limited and the biotin-limited regime. In addition, we performed experiments in which the biotinylated vesicles were immediately overloaded with streptavidin. This is illustrated in figure 2.2 for the case of $f_b = 0.004$. For each series of measuring points the initial amount of streptavidin added to the single vesicle solution is different.

When the starting amount of streptavidin is low (red curve), the maximum hydrodynamic radius obtained is about twice the radius of a single vesicle. For all the cases with initial ratio N_s/N_b higher than 1/8, the final hydrodynamic radius is lower and drops down to about only 1.3 R_0 for an initial value $N_s/N_b \approx 2.5$ (red dot). This effect can be contributed to an overloading of streptavidin onto the biotin. If the initial amount of streptavidin is high, many of the biotinylated lipids in the vesicles immediately bind to a streptavidin molecule and the formation of links with free biotin on other vesicles is hampered, so that less aggregation will occur. The higher the initial amount of streptavidin, the stronger this effect. With proper tuning, vesicle aggregates of specific aggregate sizes could be achieved, including vesicle pairs (green curve, figure 2.2.

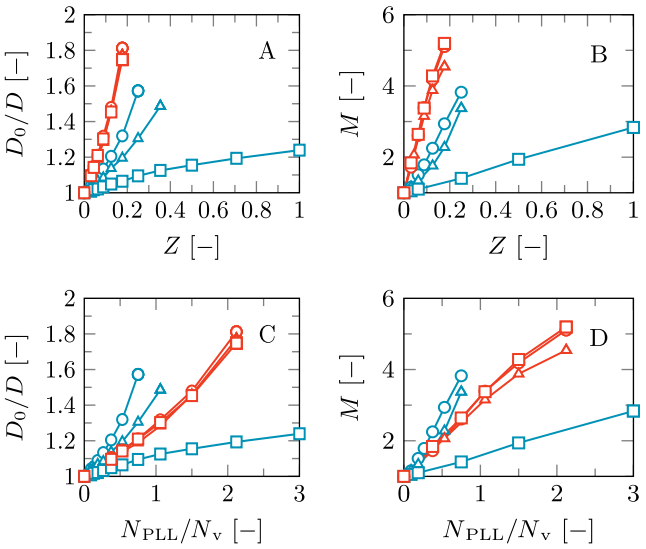

Figure 2.3: DLS results showing the normalized diffusion coefficients,D_0/D (A and C) and mean aggregation number,M (B and D) of PG vesicles as a function of the charge ratio between PLL and vesicles, Z (A and B), or the number of PLL molecules per vesicle, N_{PLL}/N_V (C and D). Blue: vesicles with a DOPG lipid fraction $f_{\mathrm{DOPG}} = 0.025$. Red: $f_{\mathrm{DOPG}} = 0.1$. Measurements were performed at three NaCl concentrations: 10 mM (circles), 50 mM (triangles) and 100 mM (squares).

2.3.2 Vesicle aggregation using polycations

Vesicle aggregation experiments using cationic polymers were performed in a similar way as those with biotin and streptavidin: we started with single vesicles and stepwise added linker molecules to induce aggregation. The linker molecule here is the polycation poly-L-lysine (PLL). We continued adding of PLL until unlimited aggregation was observed. In most cases this happened close to the point where the amount of positive charges on the added PLL equals the amount of negative charges of the DOPG in the vesicle ($Z = 1$). The results are presented in figure 2.3; for all measured points, D was constant on the time scale of the experiments (≈ 0.5 h)

All these aggregation experiments have in common that, no matter the DOPG content of the vesicles or the salt concentration, the finite aggregate size increases with addition of PLL, which is consistent with previous studies involving aggregation of charged vesicles and oppositely charged polymers [32, 56]. The extent of the exponential increase varies with salt concentration and vesicle charge density (σ) as will be discussed in the next paragraph. This is fundamentally different compared to aggregation with biotin and streptavidin, where we found a logarithmic relationship between size and amount of linkers. Apparently in this case newly added linkers form bridges with other vesicles rather

than diffusing to the adhesion zone. We contribute this effect to the repulsion between PLL molecules, which prevents accumulation of the polymer in an adhesion patch. As a consequence, when a second PLL molecule attaches to a vesicle, it will tend to attract another vesicle. As such, establishing (mainly) vesicle pairs is only possible if a very limited amount of linker molecules is added. This is reflected in figure 2.3D in which vesicle pairs ($M \approx 2$) are obtained at PLL/vesicle ratios (N_{PLL}/N_v) at 1.5 and below.

Another key difference with the biotin-streptavidin type of linkage is that all positive charges on PLL can interact with the negative charges on one single vesicle, while streptavidin only has four binding sites. As the bond between streptavidin and biotin is very strong [57] we expect that the lipid membrane of a vesicle adjusts it conformation to cover all four binding sites. However, as the binding sites are at opposite sides of the molecule, the conformation in which streptavidin bridges two vesicles is most stable. Furthermore, the bond between streptavidin and biotin is notoriously resilient and independent of experimental conditions [58]. In contrast, the strength of the interaction of PLL with the vesicles strongly depends on salt concentration and charge density σ. At low σ in combination with a high salt concentration, limited aggregation was obtained at $Z = 1$, whereas continuous aggregation was observed at lower Z for all other conditions, see figure 2.3.

Effect of salt concentration and vesicle charge density.

PLL binds to the vesicles as a result of electrostatic attraction. Therefore, it is no surprise that adding salt to the system, which screens the charges on both PLL and the vesicles, leads to a lower degree of aggregation. Interestingly, the effect of salt decreases at high σ, see red curves in figure 2.3. We correlate this effect to the extent to which polylysine binds to the vesicle surface. At low σ ($f_{\mathrm{DOPG}} = 0.025$), PLL binds only weakly to the vesicle surface. Further screening of these charges, at higher salt concentration, consequently has a strong effect on the binding of these PLL to the vesicles and thus on the extent of vesicle aggregation that follows. At low σ, in combination with a high $C_{\mathrm{NaCl}} = 100$ mM, vesicle aggregation could be reduced significantly. We expect that at higher salt concentrations, aggregation can be prevented all together. At high σ, PLL binds more strongly to the vesicle surface, and although at $C_{\mathrm{NaCl}} = 100$ mM, the salt does screen the charges considerably, this does not have a strong impact on the extent of the PLL adsorption on the vesicle surface and thus on the extent of vesicle aggregation. Our electrophoretic mobility (μ_e) measurements support this claim (see SI section 'Electrophoretic mobility of PG vesicles').

When comparing the extent of vesicle aggregation with the N_{PLL}/N_v ratio (figure 2.3),

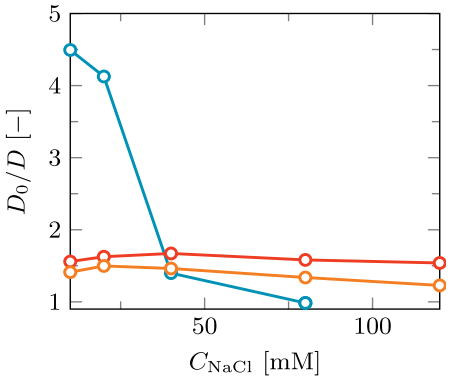

Figure 2.4: Normalized hydrodynamic radius of DOPC/DOPG vesicles measured by DLS as a function of the NaCl concentration obtained with stepwise adding NaCl to the solution. The results are shown for vesicles with $f_{\mathrm{DOPG}} = 0.025$ (blue), $f_{\mathrm{DOPG}} = 0.05$ (red) and $f_{\mathrm{DOPG}} = 0.1$ (orange).

we observe that at low salt concentrations (10 mM), vesicle aggregates with $M \approx 2$ are obtained at lower N_{PLL}/N_v for low σ (red circles) compared to high σ (red circles). We anticipate this because at low σ the charge of PLL is not easily compensated by binding to a single vesicle, and linkage with another vesicle therefore happens more frequently than for vesicles with a high charge density. Interestingly, for $Z \leq 1$, the electrophoretic mobility of stable vesicle aggregates remains constant with increasing PLL concentration and increasing aggregate size. This supports the idea that once PLL binds to a vesicle surface, it initiates aggregation with other vesicles, completely enclosing itself in the contact area.

Reversibility.

An additional feature offered by using polyelectrolytes for aggregation of charged vesicles, is reversibility. Increasing the salt concentration of a DOPC/DOPG vesicle solution in which limited aggregation has occurred by addition of PLL, can reverse the aggregation, as can be seen in figure 2.4.

The effect of increasing the salt concentration is strongest for vesicles with a low charge density ($f_{\mathrm{DOPG}} = 0.025$), where small vesicle aggregates break up completely into single vesicles. Also at higher f_{DOPG}, the average hydrodynamic radius could be reduced by increasing the salt concentration and possibly full reversal to single vesicles occurs at salt concentrations higher than explored in this experiment.

Reversible aggregation of vesicles is an important feature which may be useful in further research on lipid bilayer interactions and for application in controlled drug delivery strategies, where release may be triggered by aggregation and inhibited when reversed.

In practice, however, using variations in salt concentration to (repeatedly) induce aggregation and de-aggregation is not possible or at least complicated, since in many systems the salt concentration cannot be varied and otherwise decreasing the salt concentration while maintaining other conditions, such as the vesicle concentration, requires dialysis or other labour intensive techniques.

Effect of polylysine chain length.

All experiments with PLL shown thus far, were performed using PLL of molar mass M_n of 150 - 300 kg/mol. In addition, we performed the same aggregation experiments with much smaller PLL molecules (M_n of 1 - 5 kg/mol) (see SI). Interestingly, we found no aggregation at all up until unlimited aggregation occurs. Stable, small aggregates could not be obtained. We assume the cause for this behaviour is that for small PLL molecules at low concentrations the conformational and translational entropy penalty is too high to adsorb on the vesicles. As a consequence, the small PLL exist in large quantities solvated in the solution.

Above a threshold concentration, however, the PLL start to adsorb. Once adsorbed, the chains were also able to form bridges between vesicles, linking vesicles to each other. However, at these high PLL concentrations the adsorption is such that the equilibrium concentration of PLL in the bulk is hardly affected and therefore uncontrolled aggregation occurs.

2.3.3 Vesicle aggregation using thermoresponsive poly-NIPAm containing surfactants

The principle behind aggregation using C18-pNIPAm is that its carbon tail is inserted into the vesicle membrane while the pNIPAm part can link the vesicles together depending on temperature. Above its characteristic LCST (lower critical solution temperature), pNIPAm expels its hydration water, effectively becoming hydrophobic. It tries to form a condensed pNIPAm phase and it can do this better when pNIPAm of an opposite vesicle is also used. Hence the LCST-behaviour starts vesicle aggregation. This effect is reversible as once the temperature goes below the LCST, the pNIPAm polymers take up water again and swell, and as a result de-aggregation occurs.

To perform an aggregation experiment with C18-pNIPAm, we make a DOPC vesicle solution to which we add a certain amount of the surfactants. After mixing light scattering measurements are performed while the sample undergoes a temperature program. This involves a 10 minutes step at 25 °C, then half an hour at 40 °C and lastly another 10 minutes at 25 °C. The LCST of pNIPAm lies around 32 °C. In figure 2.5 a typical

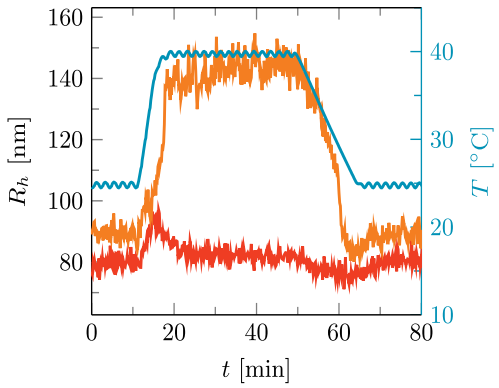

Figure 2.5: Hydrodynamic radius R_h over time for DOPC vesicles undergoing a standard temperature cycle of 10 min at 25 °C, 30 min at 40 °C and another 10 min at 25 °C. The blue curve represents the temperature at the given time. The hydrodynamic radius (R_h) is shown for vesicles without C18-pNIPAm (red) and for vesicles with a C18-pNIPAm/DOPC fraction of 0.08 (orange).

DLS result is displayed for vesicles with a C18-pNIPAm/DOPC ratio of 0.08. Control measurements on vesicles without surfactants are shown as well.

As can be seen from the figure, in the presence of C18-pNIPAm aggregation occurs above the LCST. Without vesicles, the surfactants aggregate very quickly and uncontrollably while vesicles without surfactants show no aggregation. For the mixture after increasing the temperature to 40 °C, a quick increase in size is observed after which the aggregation size stabilizes, indicating that the aggregation is limited. This process is fully reversible, as once the temperature drops below the LCST, the aggregates quickly disassemble into single vesicles again. Like for the streptavidin-biotin system, stabilizing of the aggregation size above the LCST is due to intra-aggregate binding of the linkers. Basically, C18-pNIPAm surfactants in the membrane of the vesicles diffuse towards the contact areas as they are attracted to the other C18-pNIPAm surfactants already lumped together there. As a result, within a short time, there are no remaining surfactants on the outer surface of the vesicles and therefore binding to other vesicles does not happen anymore.

Effect of C18-pNIPAm/DOPC ratio.

Control of the aggregation size is most easily obtained by tuning the C18-pNIPAm/DOPC ratio. The effect of this ratio on the aggregation size is shown in figure 2.6.

Each dot represents a standard aggregation experiment as explained earlier. The average size is calculated for both 25 °C and 40 °C. After each experiment, instead of making a new sample, more C18-pNIPAm surfactants are added to the initial sample, mixed

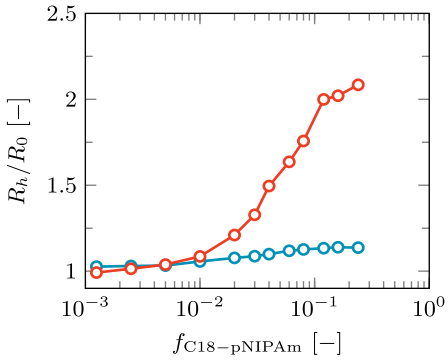

Figure 2.6: Normalized hydrodynamic radius of the vesicles as a result of stepwise adding C18-pNIPAm surfactant to the sample. The average size is shown for each sample at 25 °C (blue) and at 40 °C (red). Lipid concentration $C_l = 0.1$ mM in 10 mM Tris-HCl buffer.

and measured using DLS with the standard temperature program. The results clearly show a dependence of the aggregation size on C18-pNIPAm/DOPC ratio. A threshold ratio of around 0.01 has to be reached before aggregation occurs at all. Above this threshold ratio, the aggregation size scales logarithmically with the ratio, confirming accumulation of collapsed pNIPAm in contact zones (intra-aggregate binding, similar to what happens in the biotin-streptavidin system). Above the LCST and around a C18-pNIPAm/DOPC ratio of 0.04-0.08 the vesicles are mainly present in pairs. Our SLS results show $M = 2.62$ at 40 degrees at a C18-pNIPAm/DOPC ratio of 0.08. The presence of a threshold value is characteristic for phase separation. This can only set in when the concentration grows above the binodal. In this case the local pNIPAm concentration needs to be above a binodal value for the C18-pNIPAm anchored into the membrane. The binodal value appears at relatively high C18-pNIPAm/DOPC ratios, which we attribute to C18-pNIPAm being able to partition partly in the bilayer, near the interface between lipid head groups and tails, thus already avoiding contact with water to some extent. We anticipate that this binodal/threshold value further decreases with temperature, that is when the PNIPAm-water demixing is quenched deeper in the two-phase state we expect the threshold concentration to decrease. This threshold concentration may further be a function of the size of the PNIPAm block.

Effect of temperature.

Close to the LCST the aggregation size depends on the temperature, which is shown in figure 2.7. Slightly above the LCST, at 32 °C, some aggregation already occurs, but the aggregation size is substantially lower than at 40 °C . This phenomenon is due to the fact that there is no sharp transition in properties of pNIPAm at the LCST. Slightly

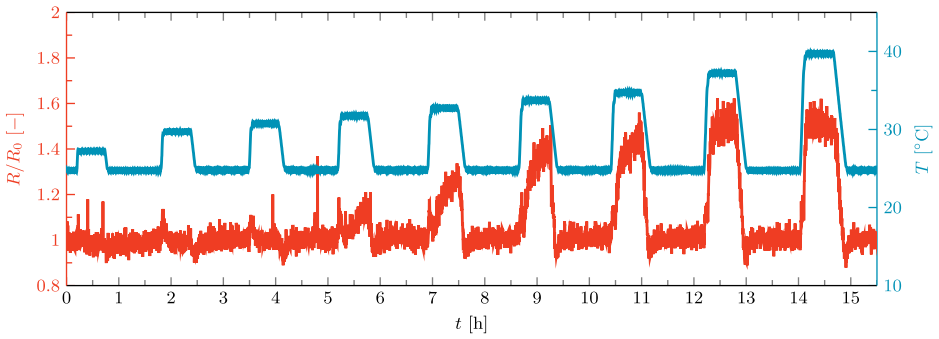

Figure 2.7: Normalized radius of vesicles containing C18-pNIPAM as they undergo a temperature program (red curve). The blue curve shows the temperature. C18-pNIPAM/DOPC ratio = 0.08.

above the LCST, pNIPAm does repel water, but not all of it yet. As a consequence, the hydrophobic attraction between the C18-pNIPAm molecules and thus the driving force for vesicle aggregation is still relatively low.

2.4 General discussion

Limited aggregation, i.e. the formation of stable, small aggregates, is a special feature in the assembly of vesicles triggered by additives. This is emphasized by the fact that not all approaches that we attempted to form stable vesicle pairs, were successful. Apart from the strategies reported here, we tried, for example, to induce limited aggregation using telechelic (triblock) copolymers, which combine a hydrophilic middle block and two short aliphatic end blocks. This type of molecule is used as associative thickener in paints [59, 60]. We used a variant with C18 tails in combination with a pEO middle block of nominal weight $M_w \approx 35000$ g/mol (~ 800 monomers) [61]. Already in dilute solutions, these molecules self-assemble and form flower-like micelles. In combination with phospholipid vesicles, we found that the telechelics partition between being assembled in such micelles and being inserted with their hydrophobic blocks in the vesicle membranes. Above a threshold concentration of the telechelics, aggregation of vesicles could be induced as expected. However, the aggregates kept growing in time. We assume that the cause of this unlimited association behaviour stems from the buffering capacity of the flower-like micelle population. Telechelics that were 'lost' in adhesion patches could be replenished by disintegrating of micelles. At ultra-low concentrations of the telechelics, one could imagine that they would be all vesicle-bound and no flowerlike micelles would exist. However, we found no association of vesicles below the CMC of the telechelics. Maybe the length of the PEO and hydrophobic blocks of the telechelics could be tuned such that limited

aggregation is possible, but we failed to hit on such an ideal species. As shown in this paper, a similar failure of limited aggregation was found when low molecular weight cationic polymer was used to link negatively charged vesicles together. Arguably, the failures to achieve limited aggregation are as instructive as the successes.

Based on both our successful and unsuccessful strategies, two routes can be distinguished that result into limited aggregation of vesicles. The most simple one is just limiting the amount of linkers. In principle, if the amount of linker molecules per vesicle is close to unity, aggregation will be limited and most of the vesicles will aggregate into stable vesicle pairs. For this to happen, the interaction between the linker and the vesicles and the tendency to bridge vesicles need to be strong. We observe this type of limited aggregation for negatively charged vesicles bridged by long PLL molecules. An additional feature is that the cationic polymers repel each other, resulting into only one polymer per adhesion patch. Optimization of the vesicle surface charge and salt concentration is a necessary requirement though.

The second route is to use membrane-bound linkers that attract each other. Limited aggregation then can be obtained provided that the timescale in which linkers diffuse along the membrane to the first formed adhesion patch between two vesicles (t_{diff}) is small compared to the vesicle collision time (τ). This implies that the vesicle concentration should be relatively low. Following this route we were able to arrest the aggregation of vesicles at pair level using biotinylated lipids that can couple by adding streptavidin to the vesicle solution, and by using C18-pNIPAm surfactants that couple above their LCST through hydrophobic interactions.

Each of the three suitable linker types that we used has its own advantages and drawbacks. Limited aggregation by adding an appropriate amount of long polyelectrolytes to charged vesicles, has the advantage that it is relatively cheap, simple and straightforward and that aggregation can be reversed by addition of salt. However, in practice repeatedly inducing aggregation and de-aggregation is not possible or complicated. In addition, even if the average aggregation number is two, a fairly broad distribution of single vesicles, vesicles pairs, trimers etc. is obtained. The strategies using biotin-streptavidin or C18-pNIPAm as linkers however can lead to a sharp distribution of aggregate sizes, with mainly vesicle pairs. This is supported by the development of the particle size distributions during the aggregation experiments with the various linkers, obtained from CONTIN analysis of the DLS results (figure 2.11, SI). The links between the vesicles are strong and very insensitive to experimental conditions, which may be advantageous in some cases, but can also be a drawback if reversibility is an issue. C18-pNIPAm surfactant molecules also robustly enable limited aggregation, similar to the streptavidin-biotin linkers. In

addition, complete reversibility can be achieved, which can be triggered multiple times by increasing and decreasing the temperature with respect to the LCST.

Possible applications for small vesicle aggregates or vesicle pairs involves research into inter-membrane interactions such as membrane (hemi-)fusion. The perfect example of a specific linker molecule that is able not only to connect vesicles but also to induce fusion is DNA [11, 26]. We aspire to find alternative linkers, such as the used in this work, that upon certain conditions could achieve similar results. Further experiments are necessary though as there are strong indications that the strategies used to induce limited aggregation of the vesicles occurred without subsequent fusion of the membranes. The reversibility of the aggregation of both vesicles attached by C18-pNIPAm (decreasing temperature) and vesicles attached by PLL (increasing salt concentration) already strongly points to this. A strong indication that fusion did also not occur in the vesicle pairs formed by biotin and streptavidin, was found by fitting the SLS data using the form factor of a spherical shell (SI figure 2.12). The presence of an adhesion patch in the vesicle pairs influenced the form factor enough to give a significantly worse fit than for single vesicles. For more direct proofs of fusion or the lack of it, we are planning to perform lipid mixing or content mixing experiments using fluorescent molecules in follow up experiments.

2.5 Conclusions

We have presented three successful strategies that lead to stable finite-sized vesicles aggregates. We showed that by tuning the experimental parameters it is possible to obtain an average aggregation number of 2. In addition we analysed vesicle aggregation on this average pair level under various relevant physico-chemical conditions. We distinguish two routes that lead to limited aggregation of vesicles: limiting the amount of linkers, or using membrane-bound linkers that upon contact with another vesicle are able to diffuse to the contact area, depleting the rest of the membrane of linker molecules to bind with other vesicles. It is expected that under well-chosen experimental conditions the latter route can provide a dominant population of vesicle pairs.

Amongst the successful strategies, the one involving C18-pNIPAm as a linker molecule shows an additional feature: the limited aggregation of vesicles is completely and repeatedly reversible using temperature as the trigger. We therefore anticipate that this system can serve as a base to study targeted and triggered interactions between membranes.

We envision that the ability to create stable vesicles pairs is an effective and useful way to study interactions between lipid membranes and the physical properties of membrane pairs. Combining different linker strategies in combination with variations in the lipid

Table 2.2: Properties of the various vesicles in 50 mM NaCl

Vesicle Code	**Membrane composition [DOPC/DOPE-Biotin/ DOPG/NBD-PE]**	**Radius [nm] ± St. Dev.**	**PDI [-] ± St. Dev.**
S-0	1 / 0 / 0 / 0	76.5 ± 2.8	0.16 ± 0.05
B-0.04%	999 / 1 / 0 / 0	75.6 ± 0.9	0.11 ± 0.04
B-0.2%	995 / 5 / 0 / 0	74.6 ± 1.1	0.11 ± 0.03
B-0.4%	990 / 10 / 0 / 0	73.5 ± 0.9	0.11 ± 0.04
B-0.6%	985 / 15 / 0 / 0	75.1 ± 1.1	0.10 ± 0.03
PG-2.5%	975 / 0 / 25 / 0	64.6 ± 1.4	0.10 ± 0.04
PG-10%	900 / 0 / 100 / 0	72.6 ± 1.7	0.09 ± 0.04
NBD-0.2%	980 / 10 / 0 / 10	69.6 ± 1.3	0.12 ± 0.04

composition of the vesicles, could be used to unravel the principles underlying the topological stability of bilayer pairs. Furthermore, it enables studies into the nature and time scales of lipid exchange between bilayers and the content exchange of vesicles with or without full scale fusion of the vesicles.

2.6 Supplementary Information

2.6.1 Overview of prepared vesicles

Vesicle preparation was performed as explained in the materials and methods section of the main document. In table 2.2 we present an overview of the properties of the vesicles. The S-0 vesicles are vesicles purely made from DOPC. These have been used during aggregation experiments involving C18-pNIPAm. DLS and SLS experiments involving biotin and streptavidin have been performed on B-n% samples. The FCS experiments involving biotin and streptavidin have been done using NBD-0.2% vesicles. Lastly, the PG-n% samples were used in aggregation experiments involving polylysine.

2.6.2 Simple model of vesicle pairs

We model the translational diffusion behaviour of the vesicle pairs as if they are prolate ellipsoids with axes a, b, with $a > b$. See figure 2.8. The translational diffusion coefficient

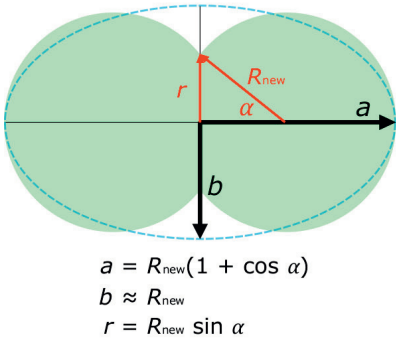

Figure 2.8: Vesicle pair modeled as a prolate ellipsoid with axes a, b, b with $a > b$, in order to estimate its diffusion coefficient.

D is given by Kuipers et al [51]

$$D = \frac{k_B T}{6\pi\eta b} \times S_{\text{prolate}} \tag{2.1}$$

with

$$S_{\text{prolate}} = \frac{2}{\sqrt{p^2-1}} \ln(p + \sqrt{p^2-1}) \tag{2.2}$$

where p is the aspect ratio: $p = a/b$. Note that S_{prolate} equals 1 in the limit of an aspect ratio of 1 and we obtain the Stokes-Einstein relation for spheres.

For the limiting case that the contact area between the two vesicles is extremely small, $a \approx 2R_0$ (R_0 being the radius of the single vesicles) and $b = R_0$, leading to $S_{\text{prolate}} = 0.76$. In other words, the diffusion coefficient D as measured with DLS would be equal to D_0/S_{prolate}. If one calculates the hydrodynamic radius from this value using the Stokes-Einstein equation (so, for a sphere with the same D), one obtains $R_{SE} = 1.32R_0$.

Generally, one can estimate the diffusion coefficient as a function of contact zone by assuming that the total area of lipid bilayer is constant:

$$A_{\text{bilayer}} = 2(4\pi R_{\text{new}}^2 - 2\pi R_{\text{new}}^2(1 - \cos\alpha) + \pi r^2) \tag{2.3}$$

Here, the first term of the equation gives the area of the spheres with new radius R_{new}, the second term withdraws the caps from these spheres "lost" in the contact zone, and the third represents two times the contact zone. See figure 2.8:

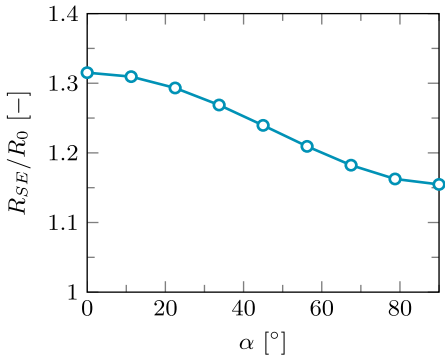

Figure 2.9: The Stokes-Einstein radius normalized by the radius of a single vesicle (R_{SE}/R_0) is plotted as a function of α as predicted using our simple model of vesicle pairs.

We can rewrite this as:

$$A_{\text{bilayer}} = 2\pi R_{\text{new}}^2(4 - (1 - \cos\alpha)^2) \tag{2.4}$$

This area should be equal to two times the surface area of a single vesicle, i.e.

$$A_{\text{bilayer}} = 8\pi R_0^2 \tag{2.5}$$

One then arrives at

$$R_{\text{new}} = \frac{2R_0}{\sqrt{4 - (1 - \cos\alpha)^2}} \tag{2.6}$$

From this, the diffusion coefficient, the Stokes-Einstein radius and the area of the contact zone can be calculated. For the case of a maximum contact zone ($\alpha = 90°$), $R_{SE}/R_0 = 1.15$ and when the contact zone is small ($\alpha = 0°$), $R_{SE}/R_0 = 1.32$, See figure 2.9. As our experiments show that $R_h/R_0 \approx 1.4$ for vesicle pairs we conclude that the contact areas are small.

2.7 Vesicle collision and lateral diffusion timescale calculations

The vesicle collision time can be calculated using the following equation:

$$\tau = d^2/6D_v \tag{2.7}$$

where D_v is the vesicle diffusion coefficient and d the average distance between vesicles. These parameters can be calculated as follows:

$$D_v = k_B T / 6\pi\eta R_v \tag{2.8}$$

and

$$d = \langle r \rangle - 2R_v \tag{2.9}$$

with k_B the Boltzmann constant, T the temperature in Kelvin, and R_v the vesicle radius; $\langle r \rangle$ is the mean center-to-center inter-particle distance, which in turn can be calculated using the molar vesicle concentration C_v:

$$\langle r \rangle = 1/C_v^{1/3} \tag{2.10}$$

With our experimental parameters, ($C_v \approx 5\text{e}{-10}$ M, $R_v \approx 65$ - 80 nm and $T = 298$ K we find a collision time of $\sim 80 - 130$ ms. The diffusion time for a biotinylated lipid to diffuse over the maximum distance d_b to the contact area of a vesicle pair is given by:

$$t_{\text{diff}} = d_b^2 / 4D_l \tag{2.11}$$

where D_l is the lateral diffusion coefficient of a lipid in the bilayer and d_b corresponds to half the circumference of a vesicle. Using the same experimental parameters and a $D_l \approx 8.25\text{e}{-12}$ m^2/s, we find diffusion times of $1 - 2$ ms.

2.7.1 DLS and SLS data analysis

The DLS and SLS data analysis has been previously described in literature [46–48]. The following sections provide a short overview of the equations used to calculate the main properties of our system including the fits of the correlation curves that correspond to values of table 1 in the main article.

Cumulant analysis of DLS data

The light scattering intensity as obtained with DLS or SLS can be described as a constant average scattering intensity I with a time-dependent part $I(t)$. The intensity autocorrelation function $G_2(\tau)$, correlating the scattering intensity at time t with the intensity at time $t + \tau$, can be described as follows:

$$G_2(\tau) = \frac{\langle I(t) \cdot I(t+\tau) \rangle}{\langle I(t) \rangle^2} \tag{2.12}$$

The corresponding field autocorrelation function $G_1(\tau)$ can be related to $G_2(\tau)$ using the Siegert equation and can be rewritten as follows:

$$G_1(\tau) = \frac{1}{\sqrt{\beta}}\sqrt{G_2(\tau) - 1} \tag{2.13}$$

where β is an experimental constant that depends on the DLS/SLS setup and has a value approximately equal to unity. $G_1(\tau)$ can also be written as a weighted average of all possible decays dependent on the correlation decay rate Γ, diffusion coefficient D of the particles and the wave vector q:

$$G_1(\tau) = \lim_{n\to\infty} \frac{1}{n} \sum_{i=1}^{n} w_i(\Gamma_i) e^{-\Gamma_i \tau} \tag{2.14}$$

with $\Gamma = q^2 D$ and $q = \frac{4\pi n}{\lambda_0} \sin\left(\frac{\theta}{2}\right)$. Here, λ_0 is the wavelength, n is the refractive index of the medium and θ is the detection angle.

For monodisperse spherical particles, the above equations can be combined, which leads to

$$\ln\sqrt{G_2(\tau) - 1} = \ln(A) - \Gamma\tau \tag{2.15}$$

with $A = \sqrt{\beta}$. By plotting the experimentally obtained $\ln\sqrt{G_2(\tau) - 1}$ as a function of τ, we obtain a linear relation from which Γ and ln(A) can be calculated.

For polydisperse samples, the size distribution can be fitted through the cumulant expansion [46]. As in our case the second order cumulant and third order cumulant fits resulted in similar results for the found diffusion coefficients, the second order cumulant was used to fit all the data presented in the article. This second order cumulant is expressed as:

$$\ln\sqrt{G_2(\tau) - 1} = \ln(A) - \Gamma\tau + \frac{\mu_2}{2!}\tau^2 \tag{2.16}$$

which is effectively is equation (15) but with an extra term $\frac{\mu_2}{2!}$. We calculated D from Γ and subsequently used the Stokes-Einstein relation for spherical particles to calculate the hydrodynamic radius (R_h):

$$R_h = \frac{k_B T}{6\pi\eta D} \tag{2.17}$$

where k_B is the Boltzmann constant, T is the absolute temperature and η is the viscosity of the solvent. For our calculations, $T = 293$ K and $\eta = 8.90 \times 10^{-4}$ Pa s are used, corresponding to water at 25 °C. The polydispersity index of the vesicles is calculated as:

$$\mathrm{PDI} = \frac{\mu_2}{\Gamma^2} \tag{2.18}$$

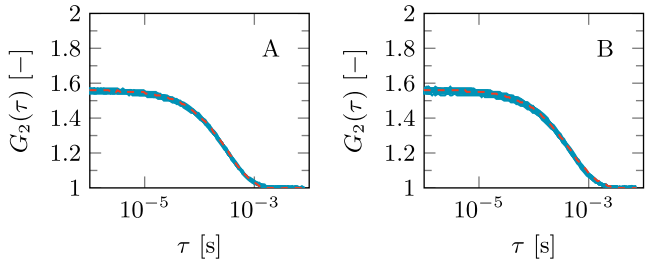

Figure 2.10: The first twenty autocorrelation curves for NBD-0.2% vesicles without added streptavidin (A) and with added streptavidin ($N_s/N_b = 1/25.6$) (B) as obtained using DLS. A single fit is optimized for all autocorrelation curves (red dashed line).

The first 5 fits of the second cumulant analysis of the DLS results in table 1 in the main article are shown in figure 2.10.

For our data analysis, we assume the vesicles to be spherical, which is actually not true for vesicle pairs and higher forms of aggregation. For a simple model of vesicle pairs and how it relates to the Stokes-Einstein radius of single vesicles, we refer back to section 2 of this document.

CONTIN Analysis

The cumulant method is valid provided that we are dealing with a Gaussian distribution around a single population. To check this, we performed a CONTIN analysis [52, 53] on our DLS data. This method uses a multi exponential fit with n fractions with n up to about 100 fractions:

$$G_1(\tau) = \frac{1}{n}\sum_{i=1}^{n} w_i(\Gamma_i)e^{-\Gamma_i\tau} \tag{2.19}$$

with $w_i(\Gamma_i)$ the weighting function showing how much the particles in size range i contribute to the intensity of the scattered light. We subsequently plotted the acquired data as an "equal area representation" [54], giving $w_i(\Gamma_i) \cdot \Gamma_i$ normalized to the maximum weight, as a function of R. An overview of this analysis for representative aggregation experiments using all three different linkers is found in figure 2.11

Figure 2.11 shows that a distribution around a single particle size is found for all aggregation experiments. In addition, the radii obtained at the peak values of these size distributions are similar to those obtained from the cumulant method. We therefore conclude that the cumulant method is sufficient to analyse the DLS results obtained during the aggregation experiments.

We also found a significant broadening of the vesicle size distribution for PG vesicles upon

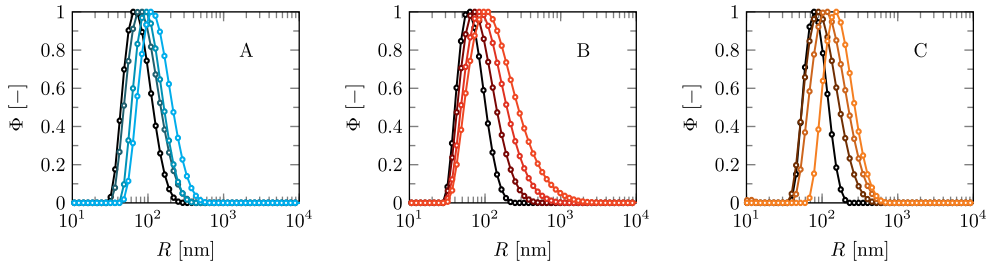

Figure 2.11: Particle size distribution curves obtained using a CONTIN analysis on DLS data for different aggregation experiments. (A) Aggregation of biotinylated vesicles ($f_b = 0.0004$) using streptavidin. From dark to light blue: $N_s/N_b = 0$, $N_s/N_b = 1/102.4$, $N_s/N_b = 1/12.8$, $N_s/N_b = 1/1.6$. (B) Aggergation of PG vesicles ($f_{\mathrm{DOPG}} = 0.1$) using PLL at 10 mM NaCl. From dark to light red: $N_{\mathrm{PLL}}/N_v = 0$, $N_{\mathrm{PLL}}/N_v = 0.75$, $N_{\mathrm{PLL}}/N_v = 1.5$, $N_{\mathrm{PLL}}/N_v = 2.12$. (C) Aggregation of S-0 vesicles using C18-pNIPAm. The graphs contain data as measured at 40 °C. From dark to light orange: $f_{\mathrm{C18-pNIPAm}} = 0$, $f_{\mathrm{C18-pNIPAm}} = 0.02$, $f_{\mathrm{C18-pNIPAm}} = 0.04$, $f_{\mathrm{C18-pNIPAm}} = 0.16$. The graphs are plotted as an "equal area representation", i.e. $\Phi = w_i\Gamma_i \times \Gamma_i / \left(w_i\Gamma_i \cdot \Gamma_i\right)_{\max}$ as a function of R (logarithmic scale).

addition of PLL. This suggests that at an average aggregation of 2, a broad distribution between single vesicles, vesicle pairs, trimers etc is obtained. In contrast, for both the biotin-streptavidin and C18-PNIPAM linker systems the peaks in the size distributions shift to higher radii as a result of aggregation. This is because of the migration of biotinylated lipids or PNIPAM-C18 to the contact zones which causes vesicle pairs to form more selectively during the aggregation experiment.

Guinier analysis from SLS data

In a Guinier analysis the natural logarithm of the Rayleigh scattering, $\ln(\mathrm{R}_\theta)$, is plotted as a function of the wave factor squared (q^2) as obtained through multi-angle measurements. For a homogeneous, stable particle solution, the curve follows a linear relationship. See figure 2.12 for some representative results for the B-0.4% vesicles at different stages of the aggregation experiment.

Each curve is a linear relationship according to the following equation:

$$\ln(R_\theta) = \ln(K_R C M) - \frac{R_g^2}{3} q^2 \tag{2.20}$$

with K_R a constant (see equation below) and C the mass concentration of our sample which is known (generally $C = 0.075$ kg/m^3) and also constant. The molar mass (M_w) can be calculated from the intercept and the radius of gyration (R_g) is calculated from

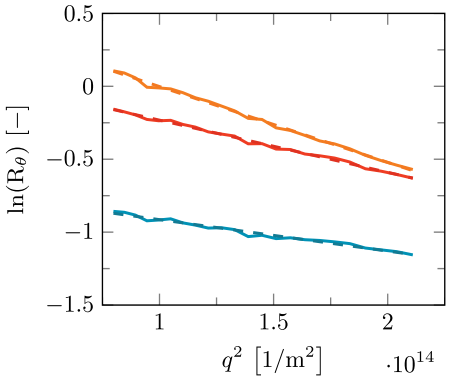

Figure 2.12: Guinier plots of the multi-angle SLS measurements at different stages of the aggregation experiment of B-0.4% with subsequent addition of streptavidin. Representative curves are shown for conditions at $N_s/N_b = 0$ (blue), $N_s/N_b = 1/12.8$ (red) and $N_s/N_b = 1/1.6$ (orange). Both the measurements (solid lines) as the linear fit (dashed lines), representing equation (19), are shown.

the slope.

$$K_R = \frac{4n_m^2\pi^2}{\lambda_0^4 N_{Av}}\left(\frac{\mathrm{d}n}{\mathrm{d}C}\right)^2 \tag{2.21}$$

Here n_m is the refractive index of the solvent, λ_0 is the wavelength of the light in vacuum, and $\frac{\mathrm{d}n}{\mathrm{d}C}$ is the refractive index increment)

The mean aggregate number (M) is calculated by dividing the average molar mass of the aggregates by the average molar mass of the single vesicles: (M_0):

$$M = \frac{M_w}{M_0} \tag{2.22}$$

Fitting of the form factor

When examining a dispersion of particles using light scattering, light that emits from different parts of a particle can lead to interference of the scattered light. This interference partially extincts the scattered light, resulting in a lower Rayleigh ratio (R_θ). The reduction of R_θ is described by the form factor (P), which is a function of the wave vector (q) and the radius of the particle (R). By fitting the form factor to the static light scattering data (R_θ as a function of q) we can obtain the radius (R) of our vesicles. While the fitting of the form factor is an alternative way to calculate the radius of particles, in our aggregation experiments this method is not very suited as the form factor equation needs to be adapted to the shape of the particles, which differs between vesicles, vesicle-pairs and higher forms of aggregation, and is not accurately known. For this data analysis, we assumed all particles to consist of spherical hollow shells for which the thickness of the

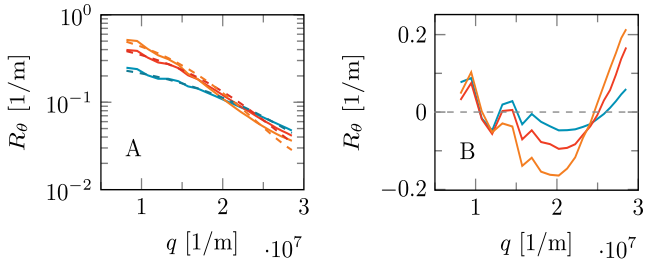

Figure 2.13: Form factor fits, fitted according to equation (22), of our multi-angle SLS experiments are shown (A), including the residuals of the fit (B). The measurement was performed at scattering angles ranging from 30° to 130°. Measurements are shown corresponding to three conditions during our aggregation experiment with B-0.4% vesicles with subsequent addition of streptavidin: $N_s/N_b = 0$ (blue), $N_s/N_b = 1/25.6$ (red) and $N_s/N_b = 1/1.6$ (orange). Both measured data (solid lines, A) and the form factor fits (curved lines, A) are shown. The fits are optimized to that the sum of residuals is minimal.

shell (i.e. the membrane) is infinitely thin. The form factor can then be simplified to the following equation:

$$P(qR) = \left(\frac{\sin(qR)}{qR}\right)^2 \tag{2.23}$$

The results of this fit for 3 stages during our aggregation experiment with biotin and streptavidin can be found in figure 2.13.

As can be seen from the figure, we can fit the data of individual vesicles much better compared to the data obtained at conditions in which we have vesicle pairs or higher forms of aggregation, reflected by much higher residuals for these conditions compared to individual vesicles. While we cannot accurately estimate the correct radius of our particles using this approach, the results indicate that vesicles during the aggregation experiments do not fuse to form larger vesicles, since if that was the case, fits of the form factor of a hollow spherical shell would hold better.

2.7.2 FCS data analysis

In this section we provide a short overview of the equations used to fit the correlation curves obtained from FCS measurements. The approaches used to calculate the main properties of our system, like the average number of fluorescent particles in the confocal volume $\langle N \rangle$ and the diffusion coefficient (D), can be found in literature [47, 50].

The fluorescence intensity as obtained with FCS can be described as a constant average fluorescence intensity I with a time-dependent part $I(t)$. The autocorrelation function $G(t)$, correlating the fluorescence intensity at time t with the intensity at time $t + \tau$, can be described as:

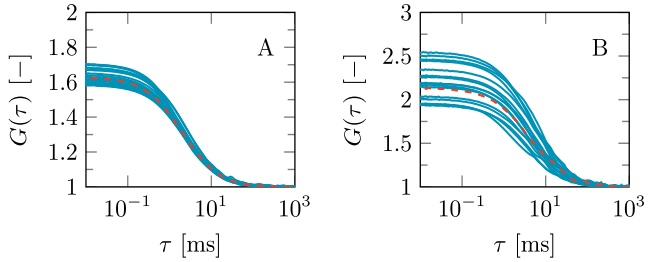

Figure 2.14: FCS autocorrelation curves for NBD-0.2% vesicles without added streptavidin (A) and with added streptavidin ($N_s/N_b = 1/25.6$) (B). A single fit according to equation (24) is optimized for all autocorrelation curves (red dashed line).

$$G(\tau) = \frac{\langle I(t) \cdot I(t+\tau) \rangle}{\langle I(t) \rangle^2} = \frac{\langle I \rangle^2 + \langle \Delta I(t) \cdot \Delta I(t+\tau) \rangle}{\langle I \rangle^2} \tag{2.24}$$

The autocorrelation curves that are obtained can be fitted with

$$\begin{aligned} G(\tau) = 1 + \frac{1}{\langle N \rangle} \left(1 + \frac{F_{\text{trip}}}{1 - F_{\text{trip}}} \right) \cdot e^{-t/T_{\text{trip}}} \\ \cdot \sum_{i=1}^{n} \frac{F_i}{(1 + t/\tau_{\text{diff,i}}) \cdot \sqrt{1 + (\omega_{xy}/\omega_z)^2 \cdot t/\tau_{\text{diff,i}}}} \end{aligned} \tag{2.25}$$

Properties in this equation not yet described are F_{trip}, which accounts for the fraction of molecules in the triplet state and T_{trip} which is the average time a molecule resides in the triplet state. The last part of the equation describes the diffusion behavior of the molecules, where F_i is the fraction of species, i, with diffusion time $\tau_{\text{diff,i}}$; ω_{xy} and ω_z are the equatorial and axial radii of the detection volume, respectively. See figure 2.14 for the fit of the correlation curves corresponding to the results as displayed in table 1 in the main article.

The diffusion coefficient D_i of species i is directly related to the observed diffusion time $\tau_{\text{diff,i}}$, according to

$$D_i = \frac{\omega_{xy}^2}{4 \cdot \tau_{\text{diff,i}}} \tag{2.26}$$

The hydrodynamic radius (R_h) for the vesicles, can be calculated using the Stokes-Einstein equation for spherical particles, see equation 2.17.

The mean aggregate number (M) for FCS is calculated by dividing the average number

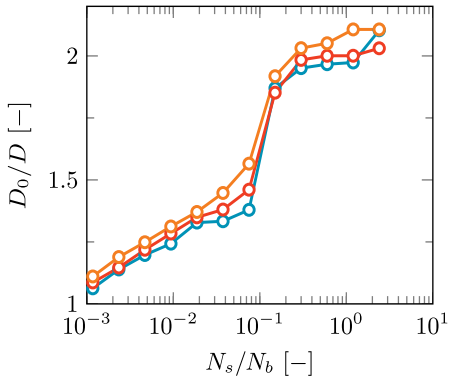

Figure 2.15: Normalized hydrodynamic radius of vesicles with $f_b = 0.01$ as a result of stepwise adding streptavidin. Results for various vesicle concentrations are shown: $C_v \sim 2.0\text{e}{-10}$ M (blue), $C_v \sim 5.0\text{e}{-10}$ M (red) and $C_v \sim 2.5\text{e}{-9}$ M (orange).

of single vesicles in the confocal volume ($\langle N_0 \rangle$) by the actual average number of particles in the confocal volume ($\langle N \rangle$).

$$M = \frac{\langle N_0 \rangle}{\langle N \rangle} \tag{2.27}$$

For our data analysis, we assume the vesicles to be spherical, which is actually not true for vesicle pairs and higher forms of aggregation. For a simple model of vesicle pairs and how it relates to the Stokes-Einstein radius of single vesicles, we refer back to section 2.6.2 of this document.

2.7.3 Effect of vesicle concentration on aggregation of vesicle pairs using biotin and streptavidin

The aggregation of the vesicles as a function of N_s/N_0 is independent of the vesicle concentration: see figure 2.15. From this result it can be concluded that our experiments are in the regime where the collision time between vesicles is much higher than the diffusion time of biotin-bound streptavidin to existing contact zones: if the collision time would be comparable or smaller than the lipid diffusion time, aggregation beyond vesicle pairs would increase with increasing vesicle concentration, until eventually uncontrolled aggregation would occur, as found by Kisak et al [30].

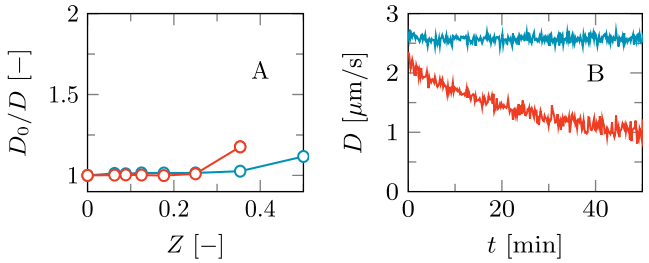

Figure 2.16: Normalized diffusion coefficient of vesicles as a function of Z, the ratio between positive charges, due to polylysine, and negative charges, due to DOPG (A). The experiment is performed for PG-5% vesicles (red), and for PG-10% vesicles (blue). Small polylysine (M_n of 1 - 5 kg/mol) are subsequently added to the vesicle solution. The diffusion coefficient as measured with DLS is shown as a function of time after adding small polylysine to the solution (B). Here, results of PG-5% vesicles are shown at a $Z = 0.35$ (blue) and a $Z = 0.5$ (red). Note that the blue curve in B represents the last data point of the red curve in A.

2.7.4 Vesicle aggregation for small polylysine

Controlled aggregation of vesicles using small PLL molecules (M_n of 1 - 5 kg/mol) was practically not achieved. Adding a small amount of PLL did not lead to any aggregation, see figure 2.16A. Increasing the amount of PLL in the solution, had no effect until uncontrolled complete aggregation occurred. This is illustrated in figure 2.16B by the progressive decline of the diffusion coefficient when $Z = 0.5$ (red curve), while for $Z = 0.35$ (blue curve) (represents the last data point of the red curve of figure 2.16A) the diffusion coefficient D remained stable.

We assume that the cause for this behaviour is related to the gradual adsorption of small PLL molecules to the vesicle surface. In low concentrations they absorb only a little as the conformational and translational entropy penalty upon binding to a vesicle is too high, while the entropy gain of released counterions compensates only just for this. The adsorption increases slowly with concentration and as soon as they do adsorb significantly so that they can induce bridging, the concentration of freely dispersed PLL molecules is sufficiently high so that these can replenish the chains that are lost in the contact zones. In contrast, for large PLL molecules strong adsorption already occurs at very low PLL concentrations such that the adsorption and subsequent bridging results in a decline of the PLL concentration in the bulk. This depletion of freely dispersed chains prevents further adsorption on the freely exposed vesicle surfaces, simply because the PLL chains are not available: for large PLL chains all chains are adsorbed and virtually no chains remain in the bulk. In other words, short PLL chains with a finite bulk concentration have a buffering capacity for adsorption, while longer chains with a vanishing bulk concentration lack this buffering capacity. In this explanation the surface-to-volume ratio is

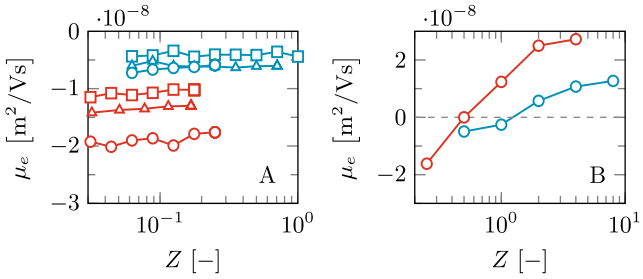

Figure 2.17: Electrophoretic mobility results for the aggregation experiments involving PG vesicles and PLL. Aggregation experiments with stepwise addition of PLL, up until uncontrolled aggregation occurred (A) (corresponding to the DLS data of figure 3 in the main document), as well as aggregation experiments in which PLL is added in one go (B) are shown. Blue: vesicles with a DOPG lipid fraction $f_{\mathrm{DOPG}} = 0.025$. Red: $f_{\mathrm{DOPG}} = 0.1$. Measurements were performed at three NaCl concentrations: 10 mM (circles), 50 mM (triangles) and 100 mM (squares).

essential.

2.7.5 Electrophoretic mobility of PG vesicles

In addition to DLS and SLS, the electrophoretic mobility (μ_e) was measured to check for potential neutralization of DOPG vesicles by PLL addition. See figure 2.17 for the results.

As can be seen from figure 2.16A, μ_e remains constant with increasing Z ($N_{\mathrm{PLL}}/N_{\mathrm{DOPG}}$). This could mean that no PLL adsorbs to the vesicle surface at all, leading to no aggregation of vesicles. This is the case for $f_{\mathrm{DOPG}} = 0.025$ and $C_{\mathrm{NaCl}} = 100$. However, for other conditions, our DLS and SLS measurements clearly show an increase in aggregate size, indicating that for these conditions PLL does adsorb onto the surface of the vesicles. We anticipate that PLL is completely enclosed within the contact area of vesicle pairs or aggregates. It is therefore not present in the slipping plane of the aggregates and thus has practically no effect on μ_e.

The mobility μ_e is depending on the salt concentration (C_{NaCl}) or vesicle charge density (σ) though. A higher σ, caused by an increasing fraction of DOPG in the vesicles, increases the absolute mobility ($|\mu_e|$) of vesicles, while a higher C_{NaCl} decreases it. Interestingly, $|\mu_e|$ is still higher at high σ with a high C_{NaCl}, compared to low σ at low C_{NaCl}, which supports the notion that the electrostatic interaction between PLL and vesicles is still very high for high σ with a high C_{NaCl} and thus the effect of salt concentration on the extent of vesicle aggregation is not yet visible.

Although we observed a continuous increase in aggregate size for $Z \approx 1$ and size measurements are therefore unreliable, electrophoretic mobility measurements still gives us

much insight. It is expected that μ_e changes sign at $Z \approx 1$, as was previously reported [62]. To confirm this, we performed additional zeta potential measurements of vesicles in which a substantial amount of PLL is added in one go, see figure 2.16B. We indeed observe a change in sign, which indicates that for $Z \approx 1$ PLL is not fully enclosed in contact areas.

References

[1] Christian Sohlenkamp and Otto Geiger. Bacterial membrane lipids: diversity in structures and pathways. *FEMS microbiology reviews*, 40(1):133–159, 2016.

[2] Làszló Vigh, Pablo V Escribá, Alois Sonnleitner, Max Sonnleitner, Stefano Piotto, Bruno Maresca, Ibolya Horváth, and John L Harwood. The significance of lipid composition for membrane activity: new concepts and ways of assessing function. *Progress in lipid research*, 44(5):303–344, 2005.

[3] Ilian Simidjiev, Virginijus Barzda, László Mustárdy, and Gyözö Garab. Role of thylakoid lipids in the structural flexibility of lamellar aggregates of the isolated light-harvesting chlorophyll a/b complex of photosystem ii. *Biochemistry*, 37(12):4169–4173, 1998.

[4] Barry R Lentz, Vladimir Malinin, Md Emdadul Haque, and Kervin Evans. Protein machines and lipid assemblies: current views of cell membrane fusion. *Current opinion in structural biology*, 10 (5):607–615, 2000.

[5] Guru V Betageri and Milton B Yatvin. Liposome drug delivery, July 13 2004. US Patent 6,761,901.

[6] ET Kisak, B Coldren, CA Evans, C Boyer, and JA Zasadzinski. The vesosome-a multicompartment drug delivery vehicle. *Current medicinal chemistry*, 11(2):199–219, 2004.

[7] Marc Michel, Mathias Winterhalter, Laurent Darbois, Joseph Hemmerle, Jean Claude Voegel, Pierre Schaaf, and Vincent Ball. Giant liposome microreactors for controlled production of calcium phosphate crystals. *Langmuir*, 20(15):6127–6133, 2004.

[8] Vincent Noireaux and Albert Libchaber. A vesicle bioreactor as a step toward an artificial cell assembly. *Proceedings of the national academy of sciences of the United States of America*, 101(51): 17669–17674, 2004.

[9] Daniel T Chiu, Clyde F Wilson, Frida Ryttsén, Anette Strömberg, Cecilia Farre, Anders Karlsson, Sture Nordholm, Anuj Gaggar, Biren P Modi, Alexander Moscho, et al. Chemical transformations in individual ultrasmall biomimetic containers. *Science*, 283(5409):1892–1895, 1999.

[10] Susanne Franziska Fenz, Ana-Sunčana Smith, Rudolf Merkel, and Kheya Sengupta. Inter-membrane adhesion mediated by mobile linkers: effect of receptor shortage. *Soft Matter*, 7(3):952–962, 2011.

[11] Bettina van Lengerich, Robert J Rawle, Poul Martin Bendix, and Steven G Boxer. Individual vesicle fusion events mediated by lipid-anchored dna. *Biophysical journal*, 105(2):409–419, 2013.

[12] Thomas C Südhof and James E Rothman. Membrane fusion: grappling with snare and sm proteins. *Science*, 323(5913):474–477, 2009.

[13] BV Derjaguin and L Landau. Theory of the stability of strongly charged lyophobic sols and of the adhesion of strongly charged particles in solution of electrolytes. *Acta Physicochim: USSR*, 14: 633–662, 1941.

[14] Evert Johannes Willem Verwey. Theory of the stability of lyophobic colloids. *The Journal of Physical Chemistry*, 51(3):631–636, 1947.

[15] Qian Chen, Sung Chul Bae, and Steve Granick. Directed self-assembly of a colloidal kagome lattice. *Nature*, 469(7330):381, 2011.

[16] Stefano Sacanna, WTM Irvine, Paul M Chaikin, and David J Pine. Lock and key colloids. *Nature*, 464(7288):575, 2010.

[17] Yufeng Wang, Yu Wang, Dana R Breed, Vinothan N Manoharan, Lang Feng, Andrew D Hollingsworth, Marcus Weck, and David J Pine. Colloids with valence and specific directional bonding. *Nature*, 491(7422):51, 2012.

[18] Daniela J Kraft, Ran Ni, Frank Smallenburg, Michiel Hermes, Kisun Yoon, David A Weitz, Alfons van Blaaderen, Jan Groenewold, Marjolein Dijkstra, and Willem K Kegel. Surface roughness directed self-assembly of patchy particles into colloidal micelles. *Proceedings of the National Academy of Sciences*, 109(27):10787–10792, 2012.

[19] Katherine M Buettner, Claudia I Rinciog, and Steven E Mylon. Aggregation kinetics of cerium oxide nanoparticles in monovalent and divalent electrolytes. *Colloids and Surfaces A: Physicochemical and Engineering Aspects*, 366(1-3):74–79, 2010.

[20] Frank von der Kammer, Stephanie Ottofuelling, and Thilo Hofmann. Assessment of the physico-chemical behavior of titanium dioxide nanoparticles in aquatic environments using multi-dimensional parameter testing. *Environmental Pollution*, 158(12):3472–3481, 2010.

[21] Chad A Mirkin, Robert L Letsinger, Robert C Mucic, and James J Storhoff. A dna-based method for rationally assembling nanoparticles into macroscopic materials. *Nature*, 382(6592):607, 1996.

[22] Kadir Aslan, Claudia C Luhrs, and Víctor H Pérez-Luna. Controlled and reversible aggregation of biotinylated gold nanoparticles with streptavidin. *The Journal of Physical Chemistry B*, 108(40): 15631–15639, 2004.

[23] Marie-Pierre Valignat, Olivier Theodoly, John C Crocker, William B Russel, and Paul M Chaikin. Reversible self-assembly and directed assembly of dna-linked micrometer-sized colloids. *Proceedings of the National Academy of Sciences of the United States of America*, 102(12):4225–4229, 2005.

[24] Yin Zhang, Angus McMullen, Lea-Laetitia Pontani, Xiaojin He, Ruojie Sha, Nadrian C Seeman, Jasna Brujic, and Paul M Chaikin. Sequential self-assembly of dna functionalized droplets. *Nature Communications*, 8(1):21, 2017.

[25] Michael A Boles, Michael Engel, and Dmitri V Talapin. Self-assembly of colloidal nanocrystals: From intricate structures to functional materials. *Chemical reviews*, 116(18):11220–11289, 2016.

[26] Lucia Parolini, Bortolo M Mognetti, Jurij Kotar, Erika Eiser, Pietro Cicuta, and Lorenzo Di Michele. Volume and porosity thermal regulation in lipid mesophases by coupling mobile ligands to soft membranes. *Nature communications*, 6:5948, 2015.

[27] Ulla Jakobsen, Adam C Simonsen, and Stefan Vogel. Dna-controlled assembly of soft nanoparticles. *Journal of the American Chemical Society*, 130(32):10462–10463, 2008.

[28] Maik Hadorn and Peter Eggenberger Hotz. Dna-mediated self-assembly of artificial vesicles. *PLoS One*, 5(3):e9886, 2010.

[29] Scott A Walker and Joseph A Zasadzinski. Electrostatic control of spontaneous vesicle aggregation. *Langmuir*, 13(19):5076–5081, 1997.

[30] ET Kisak, MT Kennedy, D Trommeshauser, and JA Zasadzinski. Self-limiting aggregation by controlled ligand- receptor stoichiometry. *Langmuir*, 16(6):2825–2831, 2000.

[31] Shivkumar Chiruvolu, Scott Walker, Jacob Israelachvili, Franz-Josef Schmitt, Deborah Leckband, and Joseph A Zasadzinski. Higher order self-assembly of vesicles by site-specific binding. *Science*, 264(5166):1753–1756, 1994.

[32] Tereza Pereira de Souza, Guilherme Volpe Bossa, Pasquale Stano, Frank Steiniger, Sylvio May, Pier Luigi Luisi, and Alfred Fahr. Vesicle aggregates as a model for primitive cellular assemblies. *Physical Chemistry Chemical Physics*, 19(30):20082–20092, 2017.

[33] Guilherme Volpe Bossa, Tereza Pereira de Souza, and Sylvio May. Adhesion of like-charged lipid vesicles induced by rod-like counterions. *Soft matter*, 14(19):3935–3944, 2018.

[34] Hideyuki Minami, Tohru Inoue, and Ryosuke Shimozawa. Aggregation kinetics of dimyristoylphosphatidylglycerol vesicles induced by divalent cations. *Journal of colloid and interface science*, 158 (2):460–465, 1993.

[35] A Di Biasio, F Bordi, and C Cametti. Salt-induced aggregation in cationic liposome suspensions. In *Trends in Colloid and Interface Science XVI*, pages 78–82. Springer, 2004.

[36] S Chiruvolu, JN Israelachvili, E Naranjo, Z Xu, JA Zasadzinski, EW Kaler, and KL Herrington. Measurement of forces between spontaneous vesicle-forming bilayers. *Langmuir*, 11(11):4256–4266, 1995.

[37] Doris A Noppl-Simson and David Needham. Avidin-biotin interactions at vesicle surfaces: adsorption and binding, cross-bridge formation, and lateral interactions. *Biophysical Journal*, 70(3):1391–1401, 1996.

[38] Stef AJ van der Meulen and Mirjam E Leunissen. Solid colloids with surface-mobile dna linkers. *Journal of the American Chemical Society*, 135(40):15129–15134, 2013.

[39] Thomas E Kodger and Joris Sprakel. Thermosensitive molecular, colloidal, and bulk interactions using a simple surfactant. *Advanced Functional Materials*, 23(4):475–482, 2013.

[40] Jiajie Diao, Yuji Ishitsuka, Hanki Lee, Chirlmin Joo, Zengliu Su, Salman Syed, Yeon-Kyun Shin, Tae-Young Yoon, and Taekjip Ha. A single vesicle-vesicle fusion assay for in vitro studies of snares and accessory proteins. *Nature protocols*, 7(5):921, 2012.

[41] Yee-Hung M Chan, Bettina van Lengerich, and Steven G Boxer. Lipid-anchored dna mediates vesicle fusion as observed by lipid and content mixing. *Biointerphases*, 3(2):FA17–FA21, 2008.

[42] Harke Pera, Tom M Nolte, Frans AM Leermakers, and J Mieke Kleijn. Coverage and disruption of phospholipid membranes by oxide nanoparticles. *Langmuir*, 30(48):14581–14590, 2014.

[43] Nelson GO Júnior, Marlon H Cardoso, Elizabete S Cândido, Daniëlle van den Broek, Niek de Lange, Nadya Velikova, J Mieke Kleijn, Jerry M Wells, Taia MB Rezende, Octávio Luiz Franco, et al. An acidic model pro-peptide affects the secondary structure, membrane interactions and antimicrobial activity of a crotalicidin fragment. *Scientific reports*, 8(1):1–11, 2018.

[44] Wyn Brown. *Light scattering: Principles and development*. Clarendon Press Oxford, 1996.

[45] Bruce J Berne and Robert Pecora. *Dynamic light scattering: with applications to chemistry, biology, and physics*. Courier Corporation, 2000.

[46] Dennis E Koppel. Analysis of macromolecular polydispersity in intensity correlation spectroscopy: the method of cumulants. *The Journal of Chemical Physics*, 57(11):4814–4820, 1972.

[47] Antsje Nolles, Adrie H Westphal, Jacob A de Hoop, Remco G Fokkink, J Mieke Kleijn, Willem JH van Berkel, and Jan Willem Borst. Encapsulation of gfp in complex coacervate core micelles. *Biomacromolecules*, 16(5):1542–1549, 2015.

[48] A Guinier and G Fournet. Small-angle scattering of x-rays, 1955.

[49] Douglas Magde, Elliot L Elson, and Watt W Webb. Fluorescence correlation spectroscopy. ii. an experimental realization. *Biopolymers: Original Research on Biomolecules*, 13(1):29–61, 1974.

[50] Victor V Skakun, Mark A Hink, Anatoli V Digris, Ruchira Engel, Eugene G Novikov, Vladimir V Apanasovich, and Antonie JWG Visser. Global analysis of fluorescence fluctuation data. *European Biophysics Journal*, 34(4):323–334, 2005.

[51] BWM Kuipers, MCA Van de Ven, RJ Baars, and AP Philipse. Simultaneous measurement of rotational and translational diffusion of anisotropic colloids with a new integrated setup for fluorescence recovery after photobleaching. *Journal of Physics: Condensed Matter*, 24(24):245101, 2012.

[52] Stephen W Provencher. Contin: a general purpose constrained regularization program for inverting noisy linear algebraic and integral equations. *Computer Physics Communications*, 27(3):229–242, 1982.

[53] Stephen W Provencher. A constrained regularization method for inverting data represented by linear algebraic or integral equations. *Computer Physics Communications*, 27(3):213–227, 1982.

[54] P Stepanek. Data analysis in dynamic light scattering. *The Method and Some Applications*, pages 177–241, 1993.

[55] Joyce Wong, Ashutosh Chilkoti, and Vincent T Moy. Direct force measurements of the streptavidin–biotin interaction. *Biomolecular engineering*, 16(1-4):45–55, 1999.

[56] Paolo Carrara, Pasquale Stano, and Pier Luigi Luisi. Giant vesicles "colonies": a model for primitive cell communities. *ChemBioChem*, 13(10):1497–1502, 2012.

[57] Patrick S Stayton, Stefanie Freitag, Lisa A Klumb, Ashutosh Chilkoti, Vano Chu, Julie E Penzotti, Richard To, David Hyre, Isolde Le Trong, Terry P Lybrand, et al. Streptavidin–biotin binding energetics. *Biomolecular engineering*, 16(1-4):39–44, 1999.

[58] Claire E Chivers, Apurba L Koner, Edward D Lowe, and Mark Howarth. How the biotin–streptavidin interaction was made even stronger: investigation via crystallography and a chimaeric tetramer. *Biochemical Journal*, 435(1):55–63, 2011.

[59] A Yekta, J Duhamel, H Adiwidjaja, P Brochard, and MA Winnik. Association structure of telechelic associative thickeners in water. *Langmuir*, 9(4):881–883, 1993.

[60] Ann-Charlotte Hellgren, Peter Weissenborn, and Krister Holmberg. Surfactants in water-borne paints. *Progress in organic coatings*, 35(1-4):79–87, 1999.

[61] J Sprakel, E Spruijt, MA Cohen Stuart, NAM Besseling, MP Lettinga, and J van der Gucht. Shear banding and rheochaos in associative polymer networks. *Soft Matter*, 4(8):1696–1705, 2008.

[62] Dmitry Volodkin, Vincent Ball, Pierre Schaaf, Jean-Claude Voegel, and Helmuth Mohwald. Complexation of phosphocholine liposomes with polylysine. stabilization by surface coverage versus aggregation. *Biochimica et Biophysica Acta (BBA)-Biomembranes*, 1768(2):280–290, 2007.

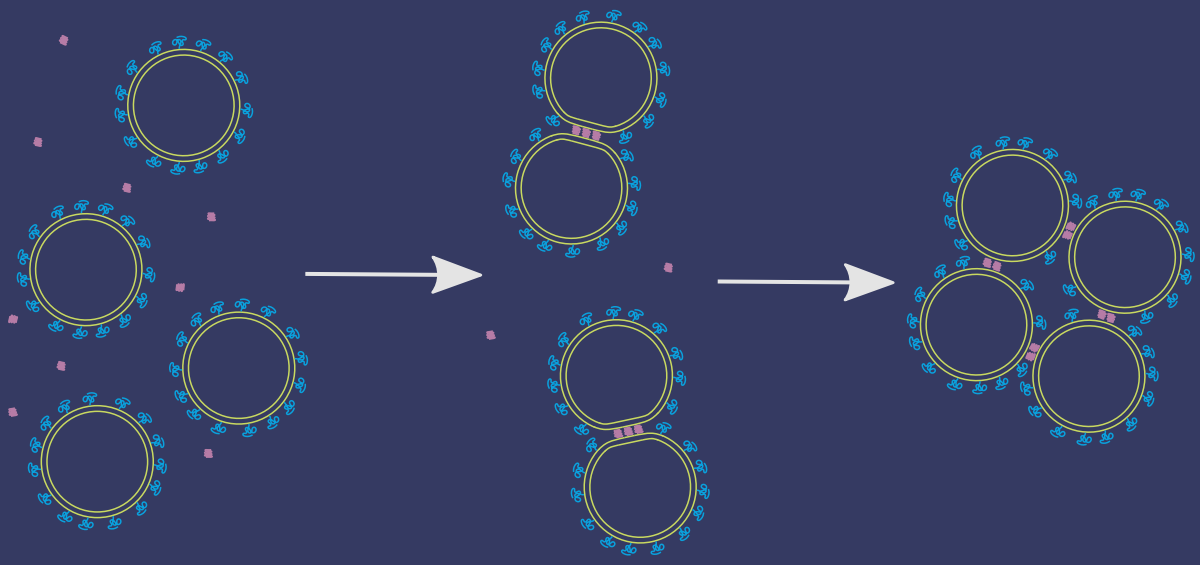

CHAPTER 3

Step-wise linking vesicles by combining reversible and irreversible linkers

Towards total control on vesicle aggregate sizes

Small vesicle aggregates as a model for primitive cellular assemblies or for application as multi-compartment drug delivery systems recently received a lot of interest, yet controlling the aggregation of vesicles to predetermined aggregate sizes remains quite a challenge. We show that this type of control is possible by using a combination of two different linker systems: streptavidin-biotin and C18-pNIPAm. The latter linker is a thermoresponsive surfactant, which below its lower critical solution temperature (LCST) of 32 °C acts as barrier on the outside of the vesicles preventing aggregation, even in the presence of other linkers. Above the LCST however, C18-pNIPAm collapses, becomes sticky and thus acts as a linker inducing aggregation. By working at low vesicle concentrations and tuning the C18-pNIPAm/lipid ratio, the aggregation is by design limited. When the temperature drops below the LCST again, the aggregation is reversed. However, this is not the case if other linkers are present. The collapse of C18-pNIPAm above the LCST provides close contact between vesicles, allowing other linker molecules to connect them. By combining the reversible 'switch-like' aggregation properties of C18-pNIPAm, with the irreversible linkage between biotinylated lipids and streptavidin, it is possible to control the size of the aggregates step by step using a simple temperature program.

This chapter has been published as: de Lange, N., F. A. M. Leermakers, and J. M. Kleijn. *Soft Matter* **16**(29) (2020): 6773-6783.

3.1 Introduction

Aggregation of colloidal particles is a widely popular research field where recently the interests have shifted towards controlled or directed self-assembly into pre-designed structures. Aggregation of liposomes (lipid vesicles) is of special interest as it provides a model system for cell-cell or cell-organelle interactions. Liposomes have been used for various applications like drug delivery [1, 2], bioreactors [3, 4], and to study chemical reactions under confinement and biologically relevant conditions [5]. Controlled assembly of these vesicles into small aggregates further expands the possible applications, for example for multi-compartment drug delivery [2]. More recently, vesicle aggregates have gained much interest as a platform to create synthetic cells [6]. A special challenge is making synthetic cell tissues from vesicles, where they need to be attached together as small aggregates. Successful strategies however are sparse [7].

Control over the aggregation of colloidal particles has been achieved in different ways such as using symmetrically arranged patches [8], specific shapes [9], and surface functionalisation with linkers like DNA [10–13] or biotin and streptavidin [14].

Aggregation of vesicles has been studied extensively as well. Linkers such as biotin and streptavidin [15–17], DNA with sticky ends [18], polyelectrolytes (with charged vesicles) [19–21], and recently a thermosensitive surfactant, C18-pNIPAm [15], have all been used to induce vesicle aggregation. However, control of the size of vesicle aggregates remains limited, or very hard to accomplish. In previous work we achieved to restrict the aggregation to the level of mainly vesicle pairs using either biotin and streptavidin or C18-pNIPAm as the linker system [15]. The key factor allowing such limited aggregation resulting in relatively sharp aggregate size distributions, is that the membrane-bound linker molecules diffuse to the contact area between two vesicles, depleting the rest of the membrane, before collision with another vesicle occurs. We therefore defined this as "self-limiting aggregation". As a prerequisite, the vesicle concentration needs to be low, so that the time scale on which vesicles collide, is much smaller than the typical diffusion time of the linker molecules along the membrane. While this concept of self-limiting aggregation can be applied using C18-pNIPAm or streptavidin-biotin, these two linker systems are very different from one another. Aggregation of biotinylated vesicles using streptavidin is practically irreversible and happens immediately after adding streptavidin. In contrast, addition of C18-pNIPAm stabilizes the vesicles at room temperature, and initiates aggregation only at temperatures above the LCST (32 °C). Upon lowering of the temperature below the LCST again, the collapsed pNIPAm chains take up water again and the vesicles dissociate. The formation of vesicle pairs or other small vesicle aggregates using C18-pNIPAm is thus reversible with respect to temperature [15].

In this paper we show that combining the two linker types, C18-pNIPAm and streptavidin-biotin, and applying temperature cycles (25 °C/40 °C), it is possible to induce a step-wise growth of vesicle aggregates and obtain small aggregates of a predetermined size. In addition, we discuss ways to control the increase in aggregation number, defined as the number of single vesicles per aggregate, that occurs during each temperature cycle. This involves variation of the added amount of linker molecules (biotinylated lipids, streptavidin and C18-pNIPAm) or, in specific cases, changing the time span of the 40 °C step. Throughout this step-wise process of aggregation, individual vesicles remain intact and do not show signs of fusion. We prove this using an assay by which lipid exchange between vesicles is monitored using FRET (Förster resonance energy transfer).

In addition to the relevance for the above-mentioned applications, the ability to create stable, small vesicle aggregates paves the way for investigation of intricate phenomena related to inter-membrane interactions, such as fusion and the formation of membrane handles.

3.2 Materials and methods

3.2.1 Materials

All chemicals are analytical grade and were used without further purification. Chloroform solutions of the phospholipids 1,2-dioleoyl-sn-glycero-3-phosphocholine (DOPC), 1,2-dioleoyl-sn-glycero-3-phosphoethanolamine-N-(cap biotinyl) (DOPE-biotin), 1,2-dioleoyl-sn-glycero-3-phosphoethanolamine-N-(lissamine rhodamine B sulfonyl) (Rhod-PE) and 1,2-dioleoyl-sn-glycero-3-phosphoethanolamine-N-(7-nitro-2-1,3-benzoxadiazol-4-yl) (NBD-PE) were purchased from Avanti Polar Lipids Inc. Streptavidin was purchased from Jackson ImmunoResearch. N-isopropylacrylamide (NIPAm) was obtained from TCI Europe N.V. Other chemicals were acquired from Sigma-Aldrich. This includes 1-octadecatonethiol, 2,2'-azobis(2-methylpropionitrile (AIBN), 0.1% (w/v) poly-L-lysine solution in H_2O ($M_w \approx 1.5 \times 10^5 - 3.0 \times 10^5$ g/mol), poly-L-lysine hydrobromide ($M_w \approx 1000 - 5000$ g/mol) and all chemicals used to make the buffer solutions.

Buffer solutions were prepared using ultrapure water (resistivity > 18 MΩ cm). Unless otherwise mentioned, they contained 10 mM Tris (2-amino-2-(hydroxymethyl)propane-1,3-diol) and 50 mM NaCl. The pH was adjusted to 7.5 using 1 M HCl or 1 M NaOH. All buffer solutions were filtered through 0.2 μm pores before use.

Table 3.1: Composition of the various vesicles and their size and polydispersity index (PDI) in 50 mM NaCl as determinded by DLS.

Vesicle Code	**Molar membrane composition [DOPC/DOPE-Biotin Rhod-PE/NBD-PE]**	**Radius [nm] ± st. dev.**	**PDI [-] ± st. dev.**
B-0.08%	999.2 / 0.8 / 0 / 0	73.6 ± 1.4	0.10 ± 0.04
B-0.4%	996 / 4 / 0 / 0	74.6 ± 2.0	0.11 ± 0.04
B-2%	980 / 20 / 0 / 0	76.9 ± 1.6	0.13 ± 0.05
Rhod-1%	986 / 4 / 0 / 10	70.8 ± 1.5	0.12 ± 0.06
NBD-1%	986 / 4 / 10 / 0	71.3 ± 1.2	0.11 ± 0.04
NBD-Rhod	986 / 4 / 5 / 5	72.1 ± 1.5	0.12 ± 0.05
NBD25-Rhod75	986 / 4 / 7.5 / 2.5	69.1 ± 3.1	0.26 ± 0.04
NBD75-Rhod25	986 / 4 / 2.5 / 7.5	66.5 ± 2.0	0.22 ± 0.04

3.2.2 Vesicle preparation

Large unilamellar vesicles have been prepared by extrusion following the procedure as described by De Lange et al [15]. First, phospholipids dissolved in chloroform were mixed in the right composition in a round-bottom flask and dried in the vacuum oven for two hours. The obtained lipid film was then re-suspended in buffer solution to a final lipid concentration of $C_l \approx 2.0\text{e}{-2}$ M and hydrated for about one hour in a rotary evaporator (no vacuum, 323 K, 100 rpm). The obtained (giant) multilamellar vesicles underwent eight freeze-thaw cycles using liquid nitrogen to freeze and a 40 °C water bath to thaw to gain unilamellar vesicles. Afterwards, the vesicles were extruded 21 times using a mini-extruder (Avanti Polar Lipids, Inc) equipped with a polycarbonate membrane with 0.2 μm pore sizes, which gave vesicles of approximately 75 nm in radius. The vesicles were subsequently collected and stored in the fridge until further use. The maximum storage time was 1 week.

Characterization of the vesicles was performed using dynamic light scattering (DLS) [22, 23]. A cumulant analysis [24], showed the vesicles to be spherical, with a hydrodynamic radius R_h between 65 and 75 nm and a polydispersity index (PDI) of ≈ 0.1. For a detailed overview of the cumulant analysis and the calculated PDI, see the supported information of previous work [15].

See table 3.1 for an overview of the prepared vesicles.

3.2.3 C18-pNIPAm surfactant synthesis

We used the same C18-pNIPAm surfactants as in previous work [15], which were synthesized following the protocol as published by Kodger et al [25]. In short, 1-octadecanethiol (1.03 g, $\sim$ 3.5 mmol), NIPAm (29.36 g, $\sim$ 262.5 mmol) and AIBN (1.14 g, $\sim$ 7.0 mmol) in a molar ratio of 1:75:2 were dissolved in 100 ml THF. After bubbling the solution with nitrogen for 30 minutes, the free radical chain-transfer polymerization was run overnight at 55°C. Purification was done by precipitation into cold hexane, with subsequent centrifugation. The precipitate was dried under vacuum, collected and stored for further use. The average molecular weight $\langle M_n \rangle$ of the surfactant was characterized by gel permeation chromatography (GPC) with HFIP (hexafluoro-2-propanol) as the running solvent; this gave $\langle M_n \rangle$ = 5708 g/mol, with a polydispersity index (PDI) of 2.8 and a degree of polymerization of approximately 50.

3.2.4 Vesicle aggregation experiments

sample preparation

Samples were prepared by diluting the vesicles in buffer to a final lipid concentration $C_l \approx$ 1.0e−4 M, unless otherwise mentioned. Subsequently, a small amount of C18-pNIPAm linkers was added, generally to obtain a fraction of C18-pNIPAm per lipid of 0.05 ($f_{C18-pNIPAm/lipid} = 0.05$). When applicable, streptavidin was added after the addition of C18-pNIPAm.

Light scattering

The aggregation of vesicles was followed using DLS. All light scattering experiments were performed using an ALV5000/60×0 external correlator and a 300 mW Cobolt Samba-300 DPSS laser operating at a wavelength λ = 532 nm.

Standard DLS measurements consisted of continuous measurements of 10 s recorded at a 90° angle. During the recording, the samples underwent a temperature program. Unless otherwise mentioned, this involved an initial 10 minutes at 25 °C, after which several temperature cycles were performed of 45 minutes at 40 °C and subsequently 30 minutes back at 25 °C .

3.2.5 Determination of lipid exchange between vesicles

To check for potential vesicle fusion a simple FRET assay was applied to observe phospholipid exchange between vesicles during aggregation experiments. As FRET pairs, we used fluorescently labeled lipids, NBD-PE as the donor and Rhod-PE as the acceptor.

Aggregation experiments with fluorescently labeled phospholipids

Sample preparation for FRET experiments was similar as described above. Here 1:1 mixtures of NBD-1% vesicles and Rhod-1% vesicles were used (see Table 3.1). After adding C18-pNIPAm and streptavidin, aggregation during the temperature program was monitored with DLS as before, now taking out 1.5 ml of sample at several stages, generally after 0, 1, 5 and 13 temperature cycles, to be measured using fluorimetry. As controls we performed the same experiments adding only C18-pNIPAm, only streptavidin or no linkers at all to the vesicle mixtures.

Fluorimetry

Standard fluorimetry measurements were recorded using a Cary Eclipse Fluorescence Spectrophotometer from Agilent Technologies. The temperature was controlled using a Cary Temperature Controller. Unless otherwise mentioned, measurements involved recording emission spectra from $\lambda_{em} = 470 - 640$ nm with an excitation wavelength $\lambda_{ex} = 460$ nm. The excitation and emission pinhole slit size was set to 5 nm.

Calculating the degree of phospholipid exchange

To calculate the degree of phospholipid exchange between the vesicles during the step-wise aggregation process, we performed some control fluorimetry measurements with the same settings as mentioned above. These included emission spectra of only NBD-1% vesicles, only Rhod-1% vesicles, a 1:1 mixture of NBE-1% vesicles and Rhod-1% vesicles, NBD-Rhod vesicles and a 1:1 mixture of NBD75-Rhod25 with NBD25-Rhod75 vesicles. The emission spectra are shown in figure 3.1.

We calculated the fraction of lipid exchange as follows. First, the FRET efficiency (E) of each sample was obtained from its emission spectrum:

$$E = \frac{I_{583}}{I_{535} + I_{583}} \tag{3.1}$$

I_{535} and I_{583} are the fluorescence intensities measured at $\lambda = 535$ nm and $\lambda = 583$ nm, the wavelengths corresponding to the peak emissions of NBD and Rhod, respectively: see the blue and green spectra in figure 3.1. Subsequently, a calibration curve was drawn between the FRET efficiencies of a 1:1 mixture of NBD-1% and Rhod-1% (orange curve, figure 3.1), of the NBD-Rhod vesicles (purple curve, figure 3.1) and of a 1:1 mixture of NBD75-Rhod25 with NBD25-Rhod75 vesicles (red curve, figure 3.1), which were defined as 0%, 100% and 50% lipid exchange respectively. Using this calibration curve, the lipid exchange was estimated for the samples drawn during the aggregation experiments with

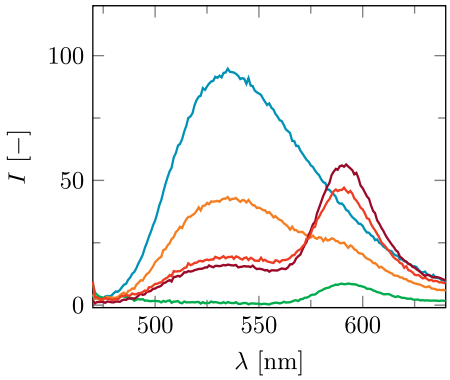

Figure 3.1: Emission spectra of control vesicle mixtures used to calculate the fraction of phospholipid exchange. These include NBD-1% vesicles (blue), Rhod-1% vesicles (green), a 1:1 mixture of NBD-1% and Rhod-1% (orange), NBD-Rhod vesicles (purple) and a 1:1 mixture of NBD75-Rhod25 with NBD25-Rhod75 vesicles (red). The total vesicle concentration was kept at $C_v = 5e{-}10$ M. Excitation wavelength $\lambda_{ex} = 460$ nm.

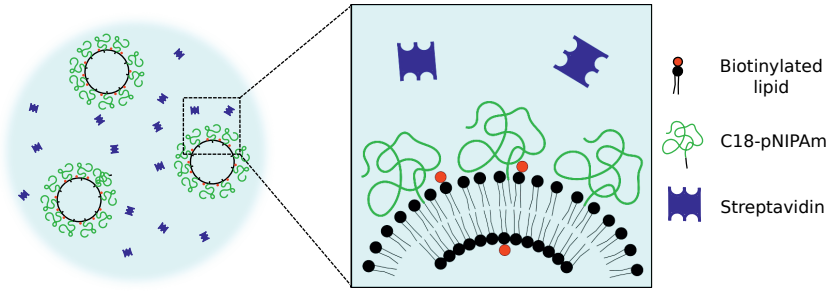

Figure 3.2: Schematic representation of the individual vesicles with added C18-pNIPAm and added streptavidin before the temperature cycle. The carbon tail of the C18-pNIPAm inserts itself into the membrane, while the swollen pNIPAm polymer block forms a corona around the vesicle. Streptavidin is not able to reach the biotin due to steric hindrance of the C18-pNIPAm.

fluorescently labeled phospholipids.

3.3 Results and Discussion

3.3.1 The first temperature cycle

General aggregation behaviour

Biotinylated vesicles with added C18-pNIPAm, with and without streptavidin in solution, were subjected to the standard temperature cycle. See figure 3.2 for a schematic representation of the starting situation.

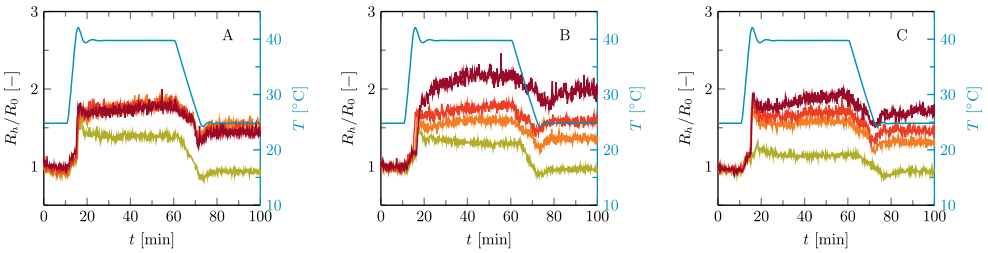

Figure 3.3: Normalized hydrodynamic radius R_h/R_0 over time for A) B-0.08% vesicles, B) B-0.4% vesicles and C) B-2% vesicles. All vesicles underwent a standard temperature cycle of 10 min at 25 °C, 45 min at 40 °C and 20 min back at 25 °C. The C18-pNIPAm/phospholipid fraction is fixed to $f_{C18-pNIPAM/lipid} = 0.05$. The blue curves represent the temperature. The yellow curves show the results for vesicles without added streptavidin. The other curves are for cases where streptavidin is added as well and each color represents a particular amount of streptavidin added. The resulting streptavidin/biotin ratios ($f_{s/b}$) are: A) 1/4 (orange), 1/2 (red) and 1 (purple); B) 1/20 (orange), 1/10 (red) and 1/5 (purple); C) 1/100 (orange), 1/50 (red) and 1/25 (purple).

This first temperature cycle already shows the differences between these two cases, see figure 3.3. In short, vesicles with only C18-pNIPAm added as linkers show reversible self-limiting aggregation triggered by temperature, as was shown before [15], whereas the combination of C18-pNIPAm and streptavidin-biotin linkers leads to self-limiting aggregation upon increasing the temperature as well, but now this process is irreversible. To explain the differences in detail, we will describe the general picture, going chronologically through the three stages of this temperature cycle. These stages are 1) 10 minutes at 25 °C, 2) 45 minutes at 45 °C, and 3) 20 minutes back at 25 °C.

No aggregation occurs during the first stage, regardless of whether streptavidin is present or not. C18-pNIPAm is thus blocking the aggregation that biotin and streptavidin would initiate otherwise [15]. Either the swollen pNIPAm corona around the vesicles prevents streptavidin from binding to the biotin on the vesicles (as illustrated in figure 3.2), or if streptavidin does bind to biotin on individual vesicles, these cannot come in close enough contact to allow streptavidin to connect them. Important to note is that for all experiments reported here, streptavidin is added after addition of C18-pNIPAm. When added in opposite order, some aggregation already takes place before addition of C18-pNIPAm, and *after* adding C18-pNIPAm the measured particle size is stable but higher than that of individual vesicles (data not shown).

In stage 2, aggregation occurs as the temperature is above the LCST of C18-pNIPAm. At this temperature the pNIPAm chains collaps and start to attract each other. All C18-pNIPAm molecules, including those that exist as micelles in the solution, assemble into sticky patches onto the surface of the vesicles. This initiates the aggregation, which happens rapidly and, in case no streptavidin is present, stops abruptly once there are mainly

vesicle pairs in the solution. This self-limiting aggregation has been described in detail in previous work [15]. As explained in the introduction, at relatively low vesicle concentrations as used in the experiments described here, when a vesicle has aggregated with one or two other vesicles, the still remaining linkers diffuse to the formed contact area(s) before collisions with other vesicles happen, so that further aggregation does not occur. With added streptavidin the initial fast aggregation generally leads to somewhat larger aggregates compared to using only C18-pNIPAm. This is simply because the collapse of C18-pNIPAm allows streptavidin to bind to biotin, so more linkers are available and successful collisions between vesicles with subsequent linking happen more often. In most cases, aggregation remains limited to small vesicle aggregates. Based on a simple model describing vesicle pairs as prolate ellipsoids, the hydrodynamic radius of a vesicle pair is about 1.3 times that of a single vesicle, depending on the size of the contact zone [15]. As our current experiments show a R_h/R_0 between 1.5 and 2, we estimate the aggregation number in the order of 2-4 vesicles.

The most outstanding difference between the vesicle aggregation with and without added streptavidin becomes apparent in the third stage. At this stage, the temperature is back below the LCST of C18-pNIPAm, which swells again and is no longer sticky. In the absence of streptavidin therefore the small aggregates fall apart again into individual vesicles. However, when streptavidin was added, the links formed between biotin and streptavidin during the 40 °C step keep the small vesicle aggregates intact. Further aggregation through to biotin and streptavidin is however not possible, due the swollen pNIPAm chains preventing vesicles and small aggregates to come into close contact.

Effect of streptavidin-biotin ratio

To best explain the effect of the ratio of streptavidin and biotin ($f_{s/b}$), we will speak in terms of biotin-limited and streptavidin-limited regimes. As streptavidin has four biotin binding sites and assuming that about half of the available biotin resides in the inward-facing part of the vesicle bilayer, the maximum amount of streptavidin-biotin linkers available for connecting vesicles is at a $f_{s/b} \approx 1/8$ and higher. Below this fraction more biotin is present than biotin binding sites, and thus this is the streptavidin-limited regime. For $f_{s/b} > 1/8$ more biotin binding sites are available than biotin and this region is therefore denoted as the biotin-limited regime. At $f_{s/b} > 1.4$ the excess of streptavidin is large enough to potentially bind and block all biotin on a vesicle before a link with another one is established and as a result practically no links between vesicles would be formed. Without C18-pNIPAm an excess of streptavidin to biotinylated vesicles limits the total aggregation and this effect is well-known in literature [15, 16].

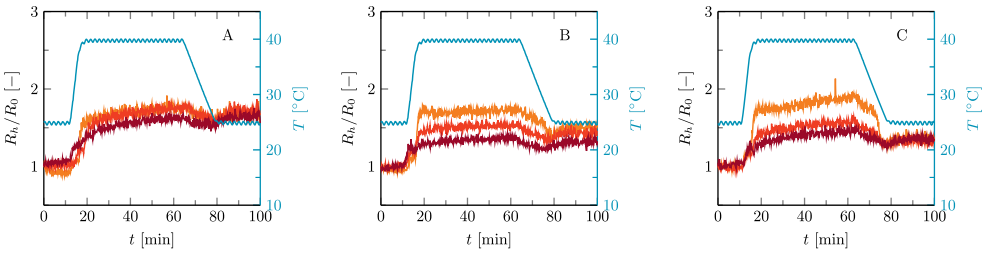

Figure 3.4: Normalized hydrodynamic radius R_h/R_0 over time for B-0.4% vesicles undergoing a standard temperature cycle of 10 min at 25 °C, 45 min at 40 °C and 20 min back at 25 °C. Streptavidin is added to obtain a ratio $f_{s/b} = 1/5$ (A), $f_{s/b} = 1/10$ (B) and $f_{s/b} = 1/20$ (C). The amount of C18-pNIPAm is varied: $f_{C18-pNIPAM/lipid} = 0.05$ (orange), $f_{C18-pNIPAM/lipid} = 0.025$ (red) and $f_{C18-pNIPAM/lipid} = 0.0125$ (purple).

Using streptavidin-biotin in combination with C18-pNIPAm results into similar trends in vesicle aggregation as found without C18-pNIPAm. This means that in the streptavidin-limited regime ($f_{s/b} < 1/8$), adding a higher amount of streptavidin results in higher aggregate sizes after a single temperature cycle, see figures 3.3B and 3.3C. For the biotin-limited regime, the opposite effect is visible: adding more streptavidin slightly lowers the final aggregate size after one temperature cycle, as shown in figure 3.3A. Interestingly, even at a very high streptavidin biotin ratio of $f_{s/b} \approx 1$ (purple curve in figure 3.3A), vesicle aggregates remain intact after a full temperature cycle which shows that still a sufficient amount of streptavidin-biotin links could be established between vesicles. This is a strong indication that during the initial temperature step at 25 °C, the C18-pNIPAm not only hinders vesicles to come in close contact with each other, but also blocks binding of streptavidin to biotin. Otherwise, streptavidin would have covered all available biotin before aggregation started at 40 °C.

Effect of the amount of C18-PNIPAm

The effect on vesicle aggregation of varying the amount of C18-pNIPAM linkers at different $f_{s/b}$ ratios is explored as well and the results are presented in figure 3.4. The effect of adding more C18-pNIPAm is straightforward and can be summarized as follows: the size of the vesicle aggregates during the 40 °C temperature step is dependent on the amount of C18-pNIPAm added, but the size of the vesicle aggregates after one full temperature cycle is not. As can be seen in figure 3.4, an increase in the amount of C18-pNIPAm added generally results in higher aggregate sizes at 40 °C. This effect is most apparent in figure 3.4B and C. Interestingly, the effect of the amount of C18-pNIPAm is smaller for B-0.4% vesicles with a $f_{s/b} = 1/5$, see figure 3.4A. This indicates that in this case streptavidin-biotin binding between vesicles contributes more to the aggregation process

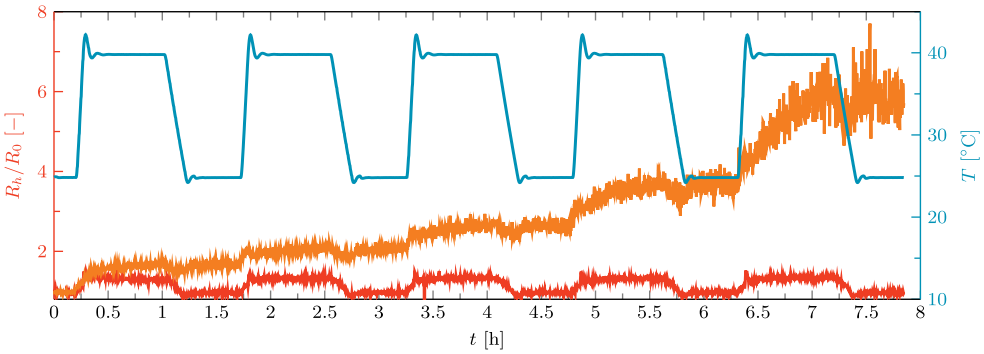

Figure 3.5: Normalized hydrodynamic radius R_h/R_0 of B-0.4% vesicles containing C18-pNIPAM with streptavidin ($f_{s/b} \approx 0.2$, orange), and without streptavidin (red) as they undergo multiple temperature cycles. The blue curve shows the temperature. For the red curve $f_{C18-pNIPAM}/f_{phospholipids} = 0.05$ and for the orange one $f_{C18-pNIPAM}/f_{phospholipids} = 0.0125$.

compared to the cases of $f_{s/b} = 1/10$ and $f_{s/b} = 1/20$, as more streptavidin-biotin linkers are available. As a result, the effect of changing the added amount of C18-pNIPAm is negligible. After a full temperature cycle, vesicle aggregates are linked together solely due to biotin- streptavidin links as the C18-pNIPAm is swollen again and non-attractive to other C18-pNIPAm molecules. In line with this, the size of the aggregates after a full temperature cycle slightly decreases with decreasing $f_{s/b}$ ratios, a trend which is visible in figure 3.3 as well.

3.3.2 Multiple temperature cycles

While tuning the amount of linkers already allows controlling the aggregate size in the first temperature cycle, repeating the temperature cycle a number of times expands the options on obtained aggregate sizes extensively. After the first temperature cycle, aggregates on the level of vesicle pairs or vesicle trimers have been formed (R_h/R_0 generally in the range 1.5 to 2). While the aggregation is triggered by the collapse of C18-pNIPAm at elevated temperature, streptavidin-biotin bonds keep the aggregates intact as the temperature is dropped again. C18-pNIPAm swells and loses its stickiness, and is presumably driven out of the confined contact zones. As such, it is available again on the outside of the vesicle aggregates and can trigger further aggregation when the temperature goes above the LCST again. Provided there are still enough free biotin and streptavidin molecules in the system, newly formed contact zones will again be consolidated. This offers a simple way to increase step by step the aggregate size.

As can be seen in figures 3.5 and 3.6, in the presence of streptavidin the size of the aggregates seems to increase exponentially with the number of temperature cycles. This

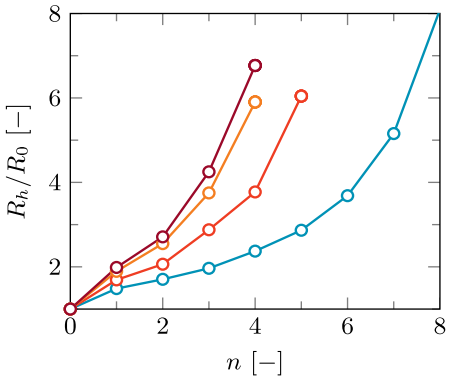

Figure 3.6: Normalised hydrodynamic radius (R_h/R_0) as a function of number of temperature cycles n for B-0.4% vesicles containing $f_{C18-pNIPAm/lipid} = 1/160$ (blue), $f_{C18-pNIPAm/lipid} = 1/80$ (red), $f_{C18-pNIPAm/lipid} = 1/40$ (orange) and $f_{C18-pNIPAm/lipid} = 1/20$ (purple). To all samples, streptavidin was added to a $f_{s/b} \approx 1/5$. R_h was measured at 25 °C after each full temperature cycle (45 min at 40 °C and 30 min back at 25 °C.

reflects that vesicle aggregates start aggregating with each other rather than with single vesicles, which are not abundantly present anymore, and that this aggregation is again self-limiting.

As the size of the aggregates increases step-wise with each temperature cycle, control on the final (average) aggregate size can thus be achieved by tuning the amount of cycles the sample goes through. It should be noted however that after the first temperature cycle the aggregate size distribution is still narrow, but with each cycle it becomes wider, since aggregates of different sizes randomly collide and are linked together. The consequence is that for obtaining aggregates of rather well-defined sizes, one should not apply too many temperature cycles, say up to four or five. We will come back to the aggregate size distributions later in the discussion.

Further control on the increase of aggregate sizes with each temperature cycle can be achieved by optimizing the amount of C18-pNIPAm linkers and the amounts and ratios of streptavidin and biotin. These ways to influence the aggregation process will be explored in the following subsections. In addition, the duration of the 40 °C step in the temperature cycles can be used as control parameter. As visible in figure 3.5, during this step the aggregate size gradually increases, a phenomenon that becomes significant after a few temperature cycles. This may be explained by a reduction in the frequency of the number of successful collisions between aggregates, due to their increasing size (decreasing diffusion coefficient) and declining number concentration. As a result the average aggregate size does not show a fast increase at the beginning of the 40 °C step anymore, but a more

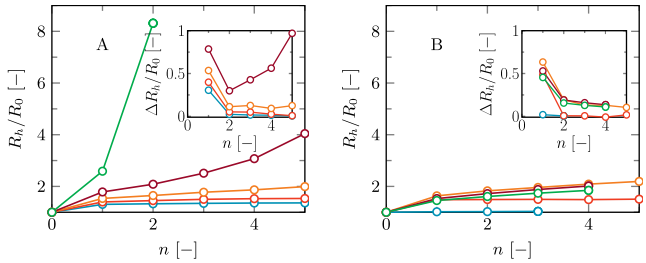

Figure 3.7: Normalised hydrodynamic radius (R_h/R_0) as a function of number of temperature cycles n for B-2% vesicles (A) and for B-0.08% vesicles (B). A) $f_{s/b} = 1/204.8$ (blue), $f_{s/b} = 1/102.4$ (red), $f_{s/b} = 1/51.2$ (orange), $f_{s/b} = 1/25.6$ (purple) and $f_{s/b} = 1/12.8$ (green). B) no streptavidin added (blue), $f_{s/b} = 1/8$ (red), $f_{s/b} = 1/4$ (orange), $f_{s/b} = 1/2$ (purple) and $f_{s/b} = 1$ (green). For all samples $f_{C18-pNIPAm/lipid} = 1/20$. R_h was measured at 25 °C after each full temperature cycle (45 min at 40 °C and 30 min back at 25 °C). The change in the normalized radius with each temperature cycle ($\Delta R_h/R_0$) is shown in the insets of the graphs.

gradual growth during the whole period of elevated temperature. Anyway, it is evident that aggregate sizes can be tuned by changing the time span of this step.

Effect of the amount of C18-pNIPAm

The amount of C18-pNIPAm added to the vesicles affects the aggregation in successive temperature cycles in the same way as in the first one. Adding more C18-pNIPAm enhances the growth in aggregation number occurring at 40 °C. Provided that there is enough biotin and streptavidin to stabilize the contact areas, the exponential increase in aggregate size happens faster at higher amounts of C18-pNIPAm added, as can be seen in figure 3.6.

Effect of the amount of biotin and streptavidin

To observe the effect of the amounts of biotin and streptavidin, we performed experiments on both B-2% and B-0.08% vesicles with varying amounts of streptavidin while keeping the amount of C18-pNIPAm the same ($f_{C18-pNIPAm/lipid} = 1/20$).

In principle, when working in the streptavidin-limited regime ($f_{s/b} < 1/8$), the more streptavidin added, the higher the increase in aggregate size per temperature cycle (figure 3.7A). However, a threshold amount of linkers is needed to obtain further aggregation with more temperature cycles: the red and blue curves in figure 3.7A represent cases below this threshold. Figure 3.7B shows that for vesicles with only 0.08% biotinylated lipids the threshold amount of linkers is hardly reached at $f_{s/b} = 1/8$ (orange curve). In this case, increasing $f_{s/b}$ only lowers the total amount of links that can be formed, because the excess of streptavidin leads to blocking of the limited available biotin. This

aggregation behaviour clearly illustrates that the task of biotin and streptavidin is to keep the aggregated vesicles together through the temperature cycles, rather than to initiate the aggregation. If the amount of streptavidin-biotin linkers is below the threshold, they are effectively used up in the first cycle, which is clearly illustrated by the inset in figure 3.7B.

3.3.3 Lipid exchange between vesicles

During the 40 °C step C18-pNIPAm is in a collapsed form in the contact areas between vesicles and swells again when the temperature drops below the LCST. Biotin and streptavidin however hold the contact areas and consequently the vesicle membranes might be subjected to various stresses as C18-pNIPAm is driven out of these areas. Different scenarios are imaginable for what happens with the vesicles as a result. One such scenario is that vesicles fuse rather than stay intact in the vesicle aggregates. To check this we performed FRET measurements on vesicles in which fluorescently labelled lipids NBD-PE and Rhod-PE were incorporated during preparation. In this FRET pair, NBD is the donor while Liss-Rhod is the acceptor. As shown in figure 3.1, when both NBD-PE and Rhod-PE are incorporated in the same vesicles, the amount of energy transfer between the donor and acceptor is substantial. In contrast, a mixture of vesicles containing only NBD-PE and vesicles containing only Rhod-PE do not show any FRET. Using the latter vesicle mixture in the aggregation experiments, an increase in FRET, i.e. an increase in the intensity at 583 nm with respect to the intensity at 535 nm, is expected if lipid exchange due to vesicle fusion occurs. The results of such an experiment are shown in figure 3.8.

As can be seen from figure 3.8, an increase in FRET is observed for vesicle aggregates undergoing several temperature cycles. However, even after 13 cycles the total amount of FRET is still much lower than the maximum amount of FRET that is expected when vesicles mix completely. Since full-scale vesicle fusion would eventually lead to complete mixing, this is ruled out of the possibilities. Four other scenarios remain plausible: (1) it is well known that lipid exchange occurs more frequently at higher temperatures [26] and bringing the vesicles close together, e.g. by vesicle aggregation, speeds up this process even more; (2) in the contact areas between vesicles the membranes are close enough together to allow FRET to happen between labelled lipids of different vesicles; in each temperature cycle more contact areas are formed, which increases the amount of FRET that occurs; (3) at 40 °C, C18-pNIPAm accumulates in the contact areas, including C18-pNIPAm that exists in micelles in solution. Upon cooling, a fraction of C18-pNIPAm forms micelles again, pulling out with it and solubilizing some of the lipids, which promotes lipid exchange between vesicles in each temperature cycle; (4) C18-pNIPAm allows for the

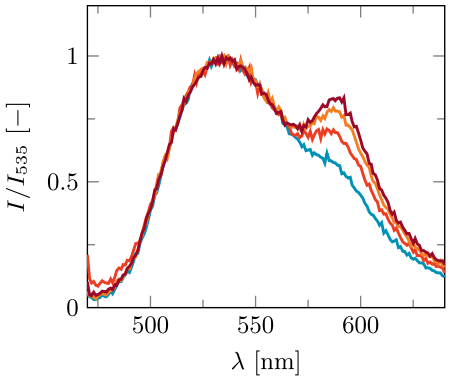

Figure 3.8: Emission spectra for a 1:1 mixture of NBD-1% and Rhod-1% vesicles containing C18-pNIPAm ($f_{C18-pNIPAm} = 0.0125$) and with streptavidin added ($f_{s/b} = 1/5$). The total vesicle concentration is $C_v = 5e{-}10$ M. The spectra were obtained after 0 (blue), 1 (red), 5 (orange) and 13 (purple) temperature cycles of 10 min at 25°C, 30 min at 40 °C and back at 25 °C. Excitation wavelength $\lambda = 460$ nm. The intensities are normalized to the intensity at $\lambda = 535$ nm.

formation of membrane handles between vesicles allowing for mixing of their lipids; this mixing occurs faster as the aggregates become larger. In addition, in a vesicle pair there is only a 50% chance to have both a donor- and an acceptor-containing vesicle, whereas in larger vesicle aggregates, the chances are higher that donor and acceptor vesicles are bound together. As a result, FRET would increase with each successive temperature cycle.

To determine which scenario is most likely, several control experiments were performed in which the amount of FRET was determined after various temperature cycles. The fraction of lipid exchange that occurred with each temperature cycle is presented in figure 3.9. The procedure to calculate the fraction of lipid exchange from the amount of FRET has been described in the materials and methods section.

Figure 3.9 shows that some lipid exchange already happens in the control experiment without added streptavidin or C18-pNIPAm (yellow curve). Additionally, the degree of lipid exchange that occurs during the temperature cycles for vesicles to which only streptavidin is added (green curve), is similar to this control. Adding streptavidin does cause limited aggregation and thus brings vesicles close together, but this apparently does not result into more FRET or lipid exchange. This rules out both scenarios 1 and 2. The figure furthermore shows, that a significant increase in lipid exchange to approximately the same extent is seen in all cases in which C18-pNIPAm is added to the vesicles, with or without streptavidin. However, even after 13 cycles the phospholipids are still far from being mixed completely. Therefore, scenario 4, i.e. the formation of membrane handles, is

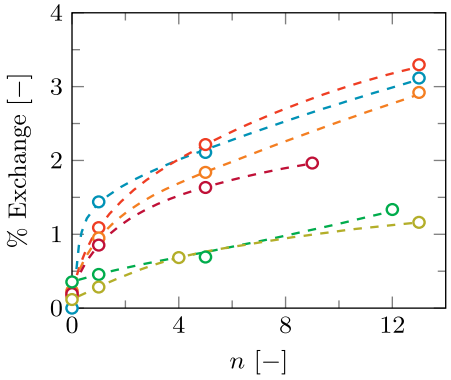

Figure 3.9: Percentage of lipid exchange as a function of n temperature cycles of 10 min at 25 °C, 30 min at 40 °C and back at 25 °C. Samples measured are 1:1 mixtures of NBD-1% and Rhod-1% vesicles, without added linkers (yellow), with streptavidin only (green), with C18-pNIPAm only (purple), and with both streptavidin and C18-pNIPAm (blue, red and orange). The orange curve is a duplicate measurement of the blue curve and the red curve is for the exact same sample as the blue curve after a 2-day incubation period in the fridge. For the cases in which streptavidin is added, $f_{s/b} = 0.2$, and for the cases in which C18-pNIPAm is added, $f_{C18-pNIPAm} = 0.0125$. The dashed lines through the data serve as guidelines.

also unlikely, since that would lead eventually to complete mixing of the lipids. Because this process might be slow, the sample with both streptavidin and C18-pNIPAm was stored in the fridge and measured again after two days. However, even after two full days of incubation, the amount of lipid exchange is still the same (compare the red and blue curves in figure 3.9).

Changes in size distribution during aggregation

To check the size distributions of the aggregates after various temperature cycles, a CONTIN analysis [27, 28] was performed on the DLS data. In figure 3.10 the resulting size distributions are shown for B-0.4% vesicles with $f_{C18-pNIPAm} = 0.00625$ and a $f_{s/b} = 0.2$. For this sample the normalized hydrodynamic radius after each temperature cycle was already presented in figure 3.6 (blue curve).

The CONTIN analysis reveals that besides the expected widening in the size distribution, each temperature cycle caused a clear shift of the peak of the distributions to higher sizes. This confirms that aggregation happens in clear steps, in which self-limiting aggregation takes place by linkers that can diffuse to newly formed contact zones. In comparison, only a widening in the size distribution is seen during vesicle aggregation using linkers for which diffusion to the contact area is not possible, as previously shown for negatively charged vesicles linked by the positively charged polyelectrolyte polylysine [15].

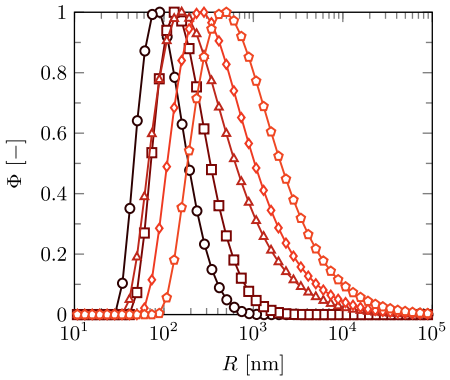

Figure 3.10: Size distributions measured for B-0.4% vesicles with added C18-pNIPAm and streptavidin ($f_{C18-pNIPAm} = 0.00625$; $f_{s/b} = 1/5$) after 0 (circles), 2 (squares), 4 (triangle), 6 (diamond) and 8 (pentagon) temperature cycles (45 min at 40 °C and back at 25 °C.

3.4 General discussion and outlook

While aggregation of vesicles into small aggregates can be achieved using several methods, controlling the size of these aggregates remains a challenge. For some methods the various aggregate sizes that can be produced are very limited [15, 16], while in other methods only the speed of aggregation can be controlled [17], or requires precise timing of the addition of polymer to stop the aggregation process [20]. In addition, on the odd chance previous methods succeed in producing vesicle aggregates of specific sizes, subsequent modifications such as a controlled continuation of the aggregation, is usually not an option [20]. Our approach offers a simple, universal and effective alternative to obtain small vesicle aggregates of sizes to one's choice.

In short, our approach involves a step-wise increase in vesicle aggregate size by using a reversible, temperature triggered linker (C18-pNIPAm) and an irreversible linker system (streptavidin-biotin) to secure the formed contact zones, and applying a number of temperature cycles. We have shown that depending on the number of temperature cycles, stable and fairly monodisperse vesicle aggregates of predetermined sizes up to about eight times the hydrodynamic radius of single vesicles can be prepared. The protocol to obtain small vesicle aggregates of a desired size can be optimized by tuning the amount of linkers added, the amount of temperature cycles, or in some cases the duration of the temperature steps.

Based on the experimental results, we sketch the following picture regarding the details of the aggregation process. See figure 3.11. The starting point is a solution with individual vesicles in which swollen C18-pNIPAm surfactants prevent any vesicle aggregation due to

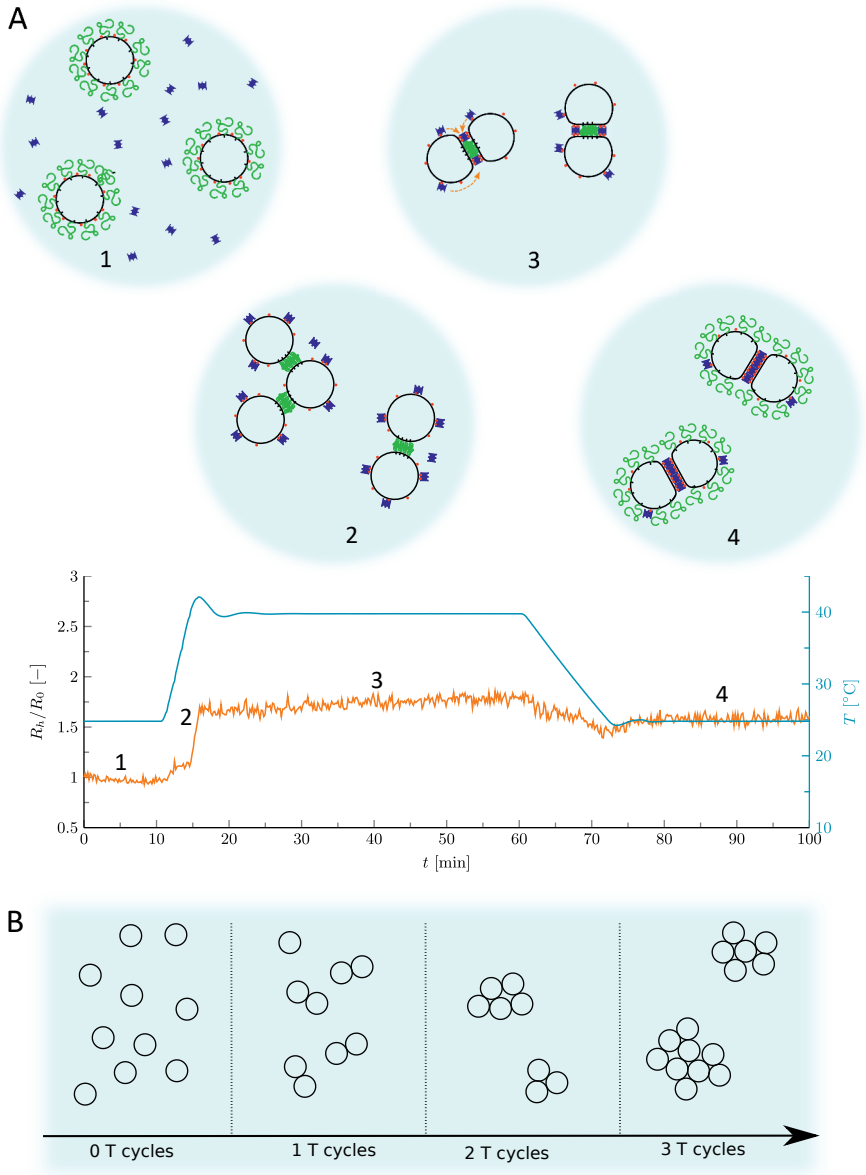

Figure 3.11: Schematic overview of the step-wise vesicle aggregation process using reversible, temperature triggered linkers and irreversible linkers. (A) The first temperature cycle; (B) vesicle aggregate sizes during the first 3 temperature cycles. In the drawings (1-4) biotin is depicted in red, streptavidin in blue and C18-pNIPAm in green. See the text for a detailed explanation.

steric hindrance. At the same time, streptavidin present in solution is not able to bind to biotin on the vesicle surface. During the first temperature cycle, once the temperature rises above the LCST of around 32 °C, C18-pNIPAm collapses into sticky patches onto the vesicle surface. Subsequently, upon a successful collision with another vesicle this causes aggregation. Once a contact area is formed, extra C18-pNIPAm molecules migrate to the contact area, depleting the rest of the vesicle membranes which limits the aggregation to mainly vesicle pairs or trimers, as was previously found [7]. Increasing the amount of C18-pNIPAm added causes larger sticky patches to form, increasing the chance of successful collisions which results into (on average) larger aggregates. Meanwhile, streptavidin is able to reach the surface of the vesicle and bind to the available biotin. At the edges of the already formed contact areas, streptavidin-biotin links can be formed between the two vesicles that consolidate the binding of the two vesicles. If relatively high amounts of streptavidin and biotin are present in the right ratio ($f_{s/b} \approx 1/8$), they also contribute in the aggregation, leading to higher average aggregation sizes during the elevated temperature step. Upon lowering the temperature, C18-pNIPAm swells and forces itself out of the contact area, which are kept intact by the streptavidin-biotin links. Any further aggregation is again prevented by steric hindrance of the swollen C18-pNIPAm on the outside of the vesicle aggregates. Subsequent temperature cycles proceed in a similar way: C18-pNIPAm collapses, becomes sticky and binds a few (two or three) vesicle aggregates together. Given that there is enough biotin and streptavidin, the newly formed contact areas are irreversibly connected. As with each temperature cycle, self-limiting aggregation happens between increasingly larger aggregates, the growth in aggregate size happens in a exponential fashion.

We envision that that the ability to create stable, small vesicle aggregates using our approach will serve as a stepping stone for creating synthetic primitive cellular tissues, for which controlling the vesicle aggregate size is a prerequisite. In addition, our approach will be a useful tool for studying various inter-membrane interactions. With simple changes in for example lipid composition, or by adding membrane targeting molecules such as antimicrobial peptides [29], it can be used to investigate relevant physical properties and typical membrane phenomena. For example, we anticipate our approach provides an ideal tool to study membrane fusion or membrane topology changes such as the formation of stable inter-membrane handles. Furthermore, it can be extended to bind giant vesicles together for which it is possible to visualize the size and shape of the contact zones using confocal microscopy and other microscopy methods. From there, the strength and nature of the membrane adhesion could be determined as well as various physical properties of the membrane, such as bilayer bending rigidities. This is something we aspire to do ourselves in a follow-up study.

References

[1] Guru V Betageri and Milton B Yatvin. Liposome drug delivery, July 13 2004. US Patent 6,761,901.

[2] ET Kisak, B Coldren, CA Evans, C Boyer, and JA Zasadzinski. The vesosome-a multicompartment drug delivery vehicle. *Current medicinal chemistry*, 11(2):199–219, 2004.

[3] Marc Michel, Mathias Winterhalter, Laurent Darbois, Joseph Hemmerle, Jean Claude Voegel, Pierre Schaaf, and Vincent Ball. Giant liposome microreactors for controlled production of calcium phosphate crystals. *Langmuir*, 20(15):6127–6133, 2004.

[4] Vincent Noireaux and Albert Libchaber. A vesicle bioreactor as a step toward an artificial cell assembly. *Proceedings of the national academy of sciences of the United States of America*, 101(51): 17669–17674, 2004.

[5] Daniel T Chiu, Clyde F Wilson, Frida Ryttsén, Anette Strömberg, Cecilia Farre, Anders Karlsson, Sture Nordholm, Anuj Gaggar, Biren P Modi, Alexander Moscho, et al. Chemical transformations in individual ultrasmall biomimetic containers. *Science*, 283(5409):1892–1895, 1999.

[6] Pasquale Stano, Roberto Marangoni, and Fabio Mavelli. Experimental evidences suggest high between-vesicle diversity of artificial vesicle populations: Results, models and implications. In *International Meeting on Computational Intelligence Methods for Bioinformatics and Biostatistics*, pages 171–185. Springer, 2017.

[7] Tereza Pereira de Souza, Guilherme Volpe Bossa, Pasquale Stano, Frank Steiniger, Sylvio May, Pier Luigi Luisi, and Alfred Fahr. Vesicle aggregates as a model for primitive cellular assemblies. *Physical Chemistry Chemical Physics*, 19(30):20082–20092, 2017.

[8] Yufeng Wang, Yu Wang, Dana R Breed, Vinothan N Manoharan, Lang Feng, Andrew D Hollingsworth, Marcus Weck, and David J Pine. Colloids with valence and specific directional bonding. *Nature*, 491(7422):51, 2012.

[9] Qian Chen, Sung Chul Bae, and Steve Granick. Directed self-assembly of a colloidal kagome lattice. *Nature*, 469(7330):381, 2011.

[10] Yin Zhang, Angus McMullen, Lea-Laetitia Pontani, Xiaojin He, Ruojie Sha, Nadrian C Seeman, Jasna Brujic, and Paul M Chaikin. Sequential self-assembly of dna functionalized droplets. *Nature Communications*, 8(1):21, 2017.

[11] Ulla Jakobsen, Adam C Simonsen, and Stefan Vogel. Dna-controlled assembly of soft nanoparticles. *Journal of the American Chemical Society*, 130(32):10462–10463, 2008.

[12] Chad A Mirkin, Robert L Letsinger, Robert C Mucic, and James J Storhoff. A dna-based method for rationally assembling nanoparticles into macroscopic materials. *Nature*, 382(6592):607, 1996.

[13] Marie-Pierre Valignat, Olivier Theodoly, John C Crocker, William B Russel, and Paul M Chaikin. Reversible self-assembly and directed assembly of dna-linked micrometer-sized colloids. *Proceedings of the National Academy of Sciences of the United States of America*, 102(12):4225–4229, 2005.

[14] Stefano Sacanna, WTM Irvine, Paul M Chaikin, and David J Pine. Lock and key colloids. *Nature*, 464(7288):575, 2010.

[15] Niek de Lange, Frans Leermakers, and J Mieke Kleijn. Self-limiting aggregation of phospholipid vesicles. *Soft Matter*, 2020.

[16] ET Kisak, MT Kennedy, D Trommeshauser, and JA Zasadzinski. Self-limiting aggregation by controlled ligand- receptor stoichiometry. *Langmuir*, 16(6):2825–2831, 2000.

[17] Scott A Walker and Joseph A Zasadzinski. Electrostatic control of spontaneous vesicle aggregation. *Langmuir*, 13(19):5076–5081, 1997.

[18] Maik Hadorn and Peter Eggenberger Hotz. Dna-mediated self-assembly of artificial vesicles. *PLoS One*, 5(3):e9886, 2010.

[19] Guilherme Volpe Bossa, Tereza Pereira de Souza, and Sylvio May. Adhesion of like-charged lipid vesicles induced by rod-like counterions. *Soft matter*, 14(19):3935–3944, 2018.

[20] Jingxia Yao, Yuan Feng, Ying Zhao, Zichen Li, Jianbin Huang, and Honglan Fu. Vesicle aggregation in aqueous mixtures of negatively charged polyelectrolyte and conventional cationic surfactant. *Journal of colloid and interface science*, 314(2):523–530, 2007.

[21] Dmitry Volodkin, Vincent Ball, Pierre Schaaf, Jean-Claude Voegel, and Helmuth Mohwald. Complexation of phosphocholine liposomes with polylysine. stabilization by surface coverage versus aggregation. *Biochimica et Biophysica Acta (BBA)-Biomembranes*, 1768(2):280–290, 2007.

[22] Wyn Brown. *Light scattering: Principles and development*. Clarendon Press Oxford, 1996.

[23] Bruce J Berne and Robert Pecora. *Dynamic light scattering: with applications to chemistry, biology, and physics*. Courier Corporation, 2000.

[24] Dennis E Koppel. Analysis of macromolecular polydispersity in intensity correlation spectroscopy: the method of cumulants. *The Journal of Chemical Physics*, 57(11):4814–4820, 1972.

[25] Thomas E Kodger and Joris Sprakel. Thermosensitive molecular, colloidal, and bulk interactions using a simple surfactant. *Advanced Functional Materials*, 23(4):475–482, 2013.

[26] JMH Kremer, MM Kops-Werkhoven, C Pathmamanoharan, OLJ Gijzeman, and PH Wiersema. Phase diagrams and the kinetics of phospholipid exchange for vesicles of different composition and radius. *Biochimica et Biophysica Acta (BBA)-Biomembranes*, 471(2):177–188, 1977.

[27] Stephen W Provencher. Contin: a general purpose constrained regularization program for inverting noisy linear algebraic and integral equations. *Computer Physics Communications*, 27(3):229–242, 1982.

[28] Stephen W Provencher. A constrained regularization method for inverting data represented by linear algebraic or integral equations. *Computer Physics Communications*, 27(3):213–227, 1982.

[29] Nelson GO Júnior, Marlon H Cardoso, Elizabete S Cândido, Daniëlle van den Broek, Niek de Lange, Nadya Velikova, J Mieke Kleijn, Jerry M Wells, Taia MB Rezende, Octávio Luiz Franco, et al. An acidic model pro-peptide affects the secondary structure, membrane interactions and antimicrobial activity of a crotalicidin fragment. *Scientific reports*, 8(1):1–11, 2018.

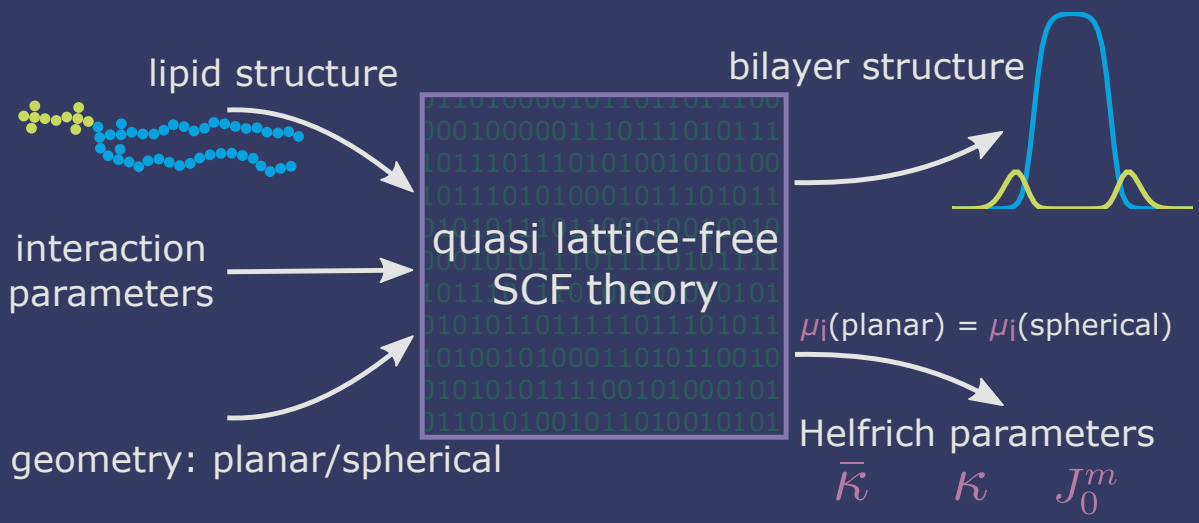
lipid structure
interaction parameters
geometry: planar/spherical
quasi lattice-free SCF theory
bilayer structure
μ_i(planar) = μ_i(spherical)
Helfrich parameters
$\bar{\kappa}$ κ J_0^m

CHAPTER 4

Structural and mechanical parameters of lipid bilayer membranes using a lattice refined self-consistent field theory

The self-consistent field theory of Scheutjens and Fleer is implemented on a grid with (lattice) sites that are smaller than the segment size. In this quasi lattice-free implementation we consider united atom-like molecular models and study bilayer self-assembly of phospholipids in a selective solvent (water). We find structural as well as mechanical parameters for these bilayers. The mean (κ) and Gaussian ($\bar{\kappa}$) bending moduli, as well as the spontaneous curvature of the monolayer (J_0^m), are computed for the first time following a grand canonical ensemble route. Results are in line with previous estimates for mechanical parameters that at the time could not be made following this correct route. This proves that the mean bending modulus is only a very weak function of the membrane tension. We performed a systematic study on the effects of model parameter variations. The mean bending modulus generally grows with increasing bilayer thickness. As expected J_0^m and $\bar{\kappa}$ behave oppositely with respect to each other and for classical phospholipids assumes values near zero. As an example, an increase in the lipophilic to hydrophilic ratio in the lipids, may cause the Gaussian bending rigidity to switch sign from negative to positive, while - not necessarily at the same point - the spontaneous curvature of the monolayer may switch sign from positive to negative. Together with other investigated trends, these results point to mechanisms of how topological phase transitions of the lipid bilayer membranes may be regulated in the biological context, which correlates with known lipid phase behaviour.

This chapter has been published as: de Lange, N., J. M. Kleijn, and F. A. M. Leermakers. *Physical Chemistry Chemical Physics* **23** (2021): 5152-5175.

4.1 Introduction

A spontaneous assembly of lipids and proteins into bilayer membranes is the scene of fascinatingly complex phenomena fundamental to life. The fluid mosaic model of Singer and Nicolson [1], the cornerstone of membrane understanding, still leaves many important questions, e.g., regarding the (in)stability against topological changes, unanswered.

The complexity of the biological membrane is manifest in the many different functions membranes have even inside a single cell. Membranes such as those occurring in mitochondria and chloroplasts, or the membranes of the endoplasmatic reticulum (ER) and nucleus have fascinatingly complex structures and often non-lamellar topologies. Non-lamellar topologies are often associated with proteins or protein complexes, but the role of the lipid composition of the membrane is arguably undervalued. A good example is the double membrane which forms the nuclear envelope. Topologically this double-membrane is in fact a single membrane due to the presence of so-called nucleopores: you may 'walk' along the inner membrane, via the nucleopore to the outer membrane without the need to leave the bilayer. While a large protein complex facilitates this double-membrane pore-like structure [2], the physical nature of the lipid assembly needs to allow for such non-trivial curvatures. In other words: curving the lipid-bilayer itself into a continuous structure connecting both membranes should not cost excessive amounts of energy. To date, the question what lipid mix is needed for such bending properties remains unanswered.

In the field of interfacial structures, bilayer assemblies of lipids are truly exotic. While the vast majority of interfaces have a finite interfacial tension (grand potential per unit area, γ) and thus a tendency to minimize their areas, large freely dispersed lipid bilayer sheets are in first-order free of tension ($\gamma = 0$) and maintain a huge interfacial area essentially proportional to the number of lipids in them. Fundamental to this exotic feature is the solvent symmetry. i.e., the same solvent (mainly water) exists on either side of the bilayer. A finite positive value of the interfacial tension of the membrane, to which we also refer as 'membrane tension' for short, would lead to a decrease of its area (and a concomitant increase of the membrane thickness) and a negative tension would do the reverse. By virtue of the mentioned symmetry, fully equilibrated bilayers will also show no interest in curving in a preferred direction. We say that its spontaneous curvature vanishes, that is, $J_0 = 0$. In other words, the planar tensionless bilayer is the so-called ground state.

We haste to mention that in living cells, membranes are typically constrained in some way and subjected to concentration gradients, i.e. they are kept away from equilibrium. This implies that the symmetry is broken and membranes do become asymmetric, resulting in a spontaneous curvature, and may develop a non-zero tension. As usual in modeling situ-

ations, we however consider bilayers in the equilibrium state. Only after the equilibrium properties are established we can have hopes to understand the more general cases.

Ignoring end-effects, that is considering very large freely dispersed lipids assemblies, membranes are thus free of tension, have a well-defined thickness and no spontaneous curvature. Moreover, the chemical potential of its lipids, as well as the solvent in the system, are also well defined. They furthermore do not depend on the number of lipids in the membrane, or equivalently the membrane area.

Similar to a polymer chain, which assumes a coil shape if the ends are not constrained, bilayer membranes will not remain in a perfectly flat configuration either. For entropic reasons freely dispersed membranes must wander (more or less) around through space. For a linear polymer chain, the tendency to form a coil is controlled by its persistence length. Similarly, in the case of the lipid bilayer, there is a membrane persistence length l_m, which in turn depends on the mean bending rigidity κ of the bilayer. [3] The membrane persistence length grows exponentially with the membrane rigidity $l_m \propto l \exp(\alpha\kappa/k_{\mathrm{B}}T)$, with a coefficient α that does not deviate much from unity and l is a length comparable to the size of a water molecule. This means that when $\kappa \gg k_{\mathrm{B}}T$, which tends to be the typical case for lipid bilayer systems, the membrane is essentially flat on the length scale of, e.g., its thickness. For this reason, it is not too exciting to have a strong focus on the mean bending modulus of phospholipid membranes. Much more interesting is to know how the Gaussian bending modulus ($\bar{\kappa}$ and the spontaneous curvature of the monolayer J_0^m are controlled because these parameters determine the topological (in)stability of lipid bilayer membranes.

Relatively few strong predictions exist for the Gaussian bending rigidity. It is generally accepted that a positive value of this quantity would promote non-lamellar, saddle-like topologies as these exist in bicontinuous triple periodic cubic phases. A negative value of this quantity is needed for the lamellar stability, which is especially important for membranes with a barrier function.

A large non-zero value for the spontaneous curvature of the monolayer may be the second cause of loss of the topological stability of bilayers. An individual monolayer may either curve preferentially towards the tails (as in micelles) and this gives $J_0^m > 0$ or towards the headgroup (as in reversed micelles), that is, $J_0^m < 0$. One expects that the planar bilayer is most stable when the monolayer spontaneous curvature is close to zero, i.e., $J_0^m \approx 0$. It was shown earlier that when J_0^m is strongly positive, the bilayer can perforate and then gives way to cylindrical or spherical micelles. [4] A similar bilayer stability catastrophe may happen when $J_0^m \ll 0$.

The mechanical parameters of the bilayer feature in the Helfrich equation. This is an expansion of the interfacial tension γ (grand potential per unit area) of a membrane in terms of the mean curvature $J = \frac{1}{R_1} + \frac{1}{R_2}$ and Gaussian curvature $K = \frac{1}{R_1 R_2}$ in a grand canonical ensemble. Here, R_1 and R_2 are the two principal curvatures that characterize the shape of the membrane.

$$\begin{aligned} \gamma(J,K) &= \gamma(0,0) + \frac{\partial\gamma}{\partial J}J + \frac{1}{2}\frac{\partial^2\gamma}{\partial J^2}J^2 + \frac{\partial\gamma}{\partial K}K \\ &= \frac{1}{2}\kappa J^2 + \bar{\kappa}K \end{aligned} \tag{4.1}$$

The second line in this equation represents the equilibrium case that the membrane tension of the planar bilayer is zero, $\gamma(0,0) = 0$, and that its spontaneous curvature is zero, $\partial\gamma/\partial J = 0$. This line also defines the mean and Gaussian rigidity parameters in terms of derivatives of the membrane tension with respect to the curvatures. The Helfrich equation typically ignores the higher derivatives with curvature. This is a fairly good approximation because all odd terms in curvature vanish due to symmetry and the first non-zero terms are of the order of $1/R^4$.

Since Helfrich published his membrane elasticity theory in 1973 [5] many researchers have focused on estimating and measuring the membrane bending rigidities. A review published by Dimova et al. [6] provides a good account of existing reports. Because the Gaussian bending rigidity cannot directly be measured experimentally and should be inferred from the phase behavior, experiments were aimed primarily on determining the mean bending rigidity. There are various methods that basically give comparable results. One can, for example, study shape fluctuations of giant vesicles [7–10], pull a tether by a pipette suction [11–14] or study fluctuations of membranes in a lamellar phase by suitable scattering techniques [15, 16]. For lipid bilayer membranes that can form giant vesicles, one typically finds values for the mean bending modulus of order 10 $k_{\mathrm{B}}T$. However, we know that not all lipid mixtures are suitable to create giants and the effective mean bending modulus of the bilayer is then not determinable with the same certainty. It may well be that a too low value for the bending modulus is the reason why they fail to form giants.

The situation concerning the value for the Gaussian bending rigidity is less clear. While topology changes of lipid systems can be observed and recorded in phase diagrams, direct correlations between such changes and $\bar{\kappa}$, in particular following the expected sign switch of $\bar{\kappa}$, remain to some degree in the realm of speculations. Early flawed modeling predictions for the Gaussian bending rigidity (see next section) may have had a negative impact on the trust that such a sign-switch of $\bar{\kappa}$ correlates with a topological transition of the bilayer.

The more recent, and also the current more realistic predictions for $\bar{\kappa}$, should restore this trust. This recovery of confidence may materialize when a deeper understanding is generated in the relation between the molecular constituents of lipid bilayer membranes and the value of the Gaussian bending rigidity.

This paper aims to introduce and apply an improved protocol to predict the mechanical parameters κ, $\bar{\kappa}$ and J_0^m of lipid bilayers using Scheutjens-Fleer self-consistent field (SF-SCF) theory, and to test the trends found as a function of lipid molecular properties against experimentally known phase behavior of lipids. Therefore, in the next sections, we will first review earlier attempts to find bilayer mechanical properties using classical SF-SCF theory, providing the context for moving to a quasi lattice-free model. This is followed by a discussion on the implementation of lattice refinements. After defining our lipid models and a brief introduction of the default parameter set, we will show that lattice refinements not only simplify the protocol to predict the mechanical parameters κ, $\bar{\kappa}$ and J_0^m, but also give access to accurate mean-field values of these parameters. It is this simplified approach that allows us to subsequently implement a systematic survey into the effects of changing the hydrophobic/hydrophilic balance in the lipid molecule and the architecture of the lipid tails on the structural and mechanical properties of the lipid bilayer. This in turn is important in the understanding of how a lipid bilayer membrane can be positioned in the vicinity of a topological transition.

4.2 Finding the lipid bilayer bending moduli using self-consistent field theory

Theoretical approaches to find the bilayer rigidities from molecular models have many intricacies. It is often unclear what exactly is the status of the existing theoretical predictions because the strict rules to compute these quantities, as outlined below, are in many cases not obeyed. A general survey of the literature is beyond the scope of the current paper. Instead, we will review our own track record in Scheutjens-Fleer self-consistent field (SF-SCF) modeling, which unfortunately has also been one with ups and downs. Early predictions were definitely flawed (cf. refs before 2013). [17, 18] The protocols used at that time were based on combining curvature energies of cylindrically and spherically curved bilayers. It was not yet realized that cylindrically curved bilayers are under tension and erroneously the full grand potential of cylindrically curved bilayers was interpreted as curvature energy. This resulted in too large values for κ and too negative values for $\bar{\kappa}$, implying a too high predicted stability of lamellar phases. This was definitely not consistent with experimental phase diagrams.

In a more recent, revised protocol we still made use of the cylindrical geometry [19, 20]. As it turns out the grand potential of the cylindrically curved bilayer consists of two exactly equal contributions. One part is taken up by the stretching energy of the bilayer and the other part is invested in bending. Therefore, the revised protocol assigned only half of the grand potential to the bending energy resulting in a prediction for the mean bending modulus which is twice lower than the early protocols. The spherical vesicle was then used to find the combination of the mean and the Gaussian bending moduli. In this revised protocol definitely more trustworthy results were reported for typical phospholipid membranes: the Gaussian bending rigidity is rather close to zero and the trends that were found correlated well with the known phase behavior of lipid systems. The fact that this revised protocol gave reasonable results must to some extent be seen as a surprise as it violates the important requirement for determining the bending moduli that upon curving the chemical potentials should remain unchanged. More specifically, the cylindrically curved membrane has a finite tension and thus its constituents have a chemical potential that must differ (usually only slightly) from that of the planar bilayer.

As advertised more recently [21, 22], in the ideal route to evaluate the mechanical parameters of bilayer membranes one should consider membrane assemblies in different curvature states with the strong constraint that the chemical potentials of its constituents are identical to the ones found in the planar bilayer (ground state) case: the correct route to evaluate the mechanical parameters must involve the grand canonical ensemble! In physical terms, keeping the chemical potentials of the constituents constant implies allowing flip-flop of the lipids from the inner to the outer monolayer as well as exchange of lipids with the bulk, where high curvatures require (relatively) more exchanges during bending than weak curvatures.

The grand canonical ensemble route combines the planar bilayer membrane system with spherically curved vesicles. In more detail, it is well known that one can compute the Gaussian bending rigidity from the planar bilayer already. For this the grand potential density profile $\omega(z)$ is used. This profile represents (minus) the local lateral pressure in the membrane and we will come back later in this paper on how this quantity is computed in the SCF formalism. In several publications it has been shown and discussed that the Gaussian bending modulus is found from the second moment of the grand potential density profile, [23, 24]

$$\bar{\kappa} = 2 \sum_{z>z_0} (z - z_0)^2 \omega(z) \tag{4.2}$$

provided that the membrane is free of tension, that is $\gamma = \sum_z \omega(z) = 0$. In Eqn 4.2 the symmetry plane of the planar bilayer is at $z = z_0$. By the same token we mention that the corresponding first moment is related to the product of the mean bending modulus

and the spontaneous curvature of the monolayer: [23, 24]

$$-\kappa J_0^m = 2\sum_{z>z_0}(z-z_0)\omega(z) \tag{4.3}$$

In this equation, the factor 2 is included because on the left-hand side the value κ of the full bilayer occurs. Alternatively, when $\kappa_{\text{monolayer}}$ is used one can remove this factor of two because $\kappa = 2\kappa_{\text{monolayer}}$. Next, it is well known that the curvature energy of the spherical vesicle

$$\Omega = 4\pi(2\kappa + \bar{\kappa}) \tag{4.4}$$

independent of the vesicle radius, that is, it is scale-invariant. As the grand potential of the spherical vesicle does not depend on the vesicle radius, the chemical potentials of its constituents are also size-independent and, importantly, identical to the ones found for the planar tensionless bilayer system. With $\bar{\kappa}$ known from the planar bilayer, one can extract the mean bending modulus indirectly. Next, using Eqn 4.3 the spontaneous curvature of the monolayer can be calculated. This route is implemented in the current work.

In the work of Pera and coworkers [19] this correct route has been explored, but was rejected at that time for accuracy reasons. In that study the molecules were represented as strings of discrete segments (coarse grained atoms). Additionally, the space was discretized in a grid of cells (lattice), where each cell had a characteristic size equal to the segment size. The problem was that lattice discretization errors made the value of the thickness of the planar bilayer flawed up to perhaps 0.5 lattice layer. Of course similar lattice artifacts appeared in the cylindrical and spherical geometry calculations, but these could more or less be averaged out by using results from a (laborious) systematic variation of the radii of the vesicles, as will be explained in more detail below. As a result, Pera et al. could only use the formally incorrect route of combining cylindrically curved and spherically curved bilayers to obtain the bending rigidities. They also used an approximate route to estimate the spontaneous curvature of the monolayer. To date, we do not know how reliable the route followed by Pera et al. is in practice. In support of the revised protocol, we can say that when the cylindrical vesicles have a sufficiently large radius R, the deviations of the chemical potentials from the ground state are not very large, and one can always attempt to take the limit of $R \to \infty$. Unfortunately, Pera et al. were restricted to use vesicles with a rather small radius, so the reliability issue is not resolved.

To use successfully the advertised correct (grand canonical) route one should find ways to reduce the lattice artifacts in SF-SCF predictions. It proved necessary to implement

the self-consistent field equations on a finer grit. This is exactly what the technical task presented in the current paper is We discuss in depth a quasi lattice-free implementation of the SF-SCF model, developed along similar lines as the approach pioneered by Romeis et al in the context of polymer brushes. [25] Within the lattice-refined SF-SCF model, the lattice site is smaller by a factor 2, 3 or more than the segment size and the lattice artifacts are reduced correspondingly. The smaller the lattice site in comparison to the segment size, the more accurate we can estimate the membrane structure and the more accurate solutions for, e.g., the Gaussian bending rigidity are obtained. This also improves the accuracy of the indirectly obtained mean bending rigidity and finally allows the evaluation of the preferred curvature of the monolayer with Eqn 4.3.

4.3 Lattice refined SF-SCF

From the above, it is clear that theoretical models for lipid bilayer membranes should, on top of structural information, give access to thermodynamical data so that the mechanical parameters of the bilayers can be computed. The self-consistent field theory can deliver these albeit within a framework that makes use of a mean-field approximation. The mean-field approach has intrinsic limitations and we will point these out below while elaborating the theory. We zoom in on the way the segment potentials (quantities that feature in Boltzmann weights) are computed from the segment densities (volume fractions) and *vice versa*. After obtaining the so-called self-consistent field solution as explained below, we can evaluate the then optimized free energy and corresponding thermodynamical parameters for the system.

At the basis of the SF-SCF theory is a mean-field free energy functional which needs to be optimized. To put this functional in action, one needs to (i) make choices for the chain model, so that one can compute the single-chain partition functions for each type of molecule from (known) potentials, (ii) decide on which interactions are taken into account and how these are evaluated so that one can compute the interaction part of the free energy from (known) segment distributions. With these elements in place, one can evaluate the mean-field free energy functional, which is then expressed in terms of the segment volume fraction profiles $\varphi(\mathbf{r})$ and segment potential profiles $u(\mathbf{r})$, frequently complemented with Lagrange parameters to implement constraint relations.

The extremization of the mean-field free energy functional encompasses three steps. (i) The maximization of this mean-field free energy with respect to the potentials gives the rule on how to evaluate the volume fractions. (ii) The minimization of this free energy with respect to the volume fractions gives an equation for the segment potentials. (iii)

Invariably, there is a compressibility relation to which the above results must obey and when necessary other constraints may be imposed. Each of these constraints will introduce a Lagrange parameter as an extra variable in the free-energy functional. Optimization of the mean-field free energy with respect to these Lagrange parameters effectively imposes these constraints. The extremization of the free energy in these three steps typically involves a numerical scheme with successive guesses. When the saddle point of the free energy functional is found, the segment potentials and volume fractions are mutually consistent with each other and in line with all imposed constraints, and this 'fixed point' is known as the self-consistent field solution.

The SF-SCF method combines a freely-jointed chain (FJC) model, with short-range contact interactions accounted for using the Bragg-Williams mean-field approximation, and an incompressibility constraint with lattice approximations, similarly as in the Flory-Huggins model. The latter is applied in spatially homogeneous systems (typically bulk phases); the SF-SCF method on the other hand focuses on concentration gradients, which are important at interfaces, e.g., for (polymer) adsorption, and for self-assembly, to name a few. Below we will highlight several elements in this protocol and focus on those elements that depend on the discretization scheme. More specifically, we will elaborate on ways to implement the SF-SCF equations on a lattice grit that is finer than the bond length. Such grits are needed to prevent lattice artifacts to dominate the results. For a more systematic discussion of the SF-SCF theory, we refer to the literature. [19, 26]

The single-chain partition functions follow from solving the Edwards equation. [27] Edwards realized that the analogy between a diffusing particle and the path followed by a flexible polymer chain suggests a diffusion-like (or Schrödinger-like) equation for polymer problems, wherein the time t is replaced by a contour length parameter s, and the (dimensionless) diffusion constant has a proposed value of 1/6. On top of this Edwards realized that real chains have a finite volume and he proposed to use a segment potential u to self-consistently account, on a mean-field level, for these 'volume' effects. The Edwards equation implements the Gaussian chain model:

$$\frac{\partial G(\mathbf{r},s)}{\partial s} = \frac{1}{6}\nabla^2 G(\mathbf{r},s) - u(\mathbf{r},s)G(\mathbf{r},s) \tag{4.5}$$

This equation is at the basis of the self-consistent field theory for inhomogeneous polymer solutions, here applied to lipids; yet the SF-SCF variant maps this differential equation on a lattice in such a way that the chain model shifts from a Gaussian chain to the freely-jointed chain (FJC) model. In Eqn 4.5 the coordinate $\mathbf{r} = (x, y, z)$ is typically made dimensionless by a segment size (b), s is a parameter that represents a position along the contour of the chain (dimensionless 'time'). The segment potential $u(\mathbf{r}, s)$ is

the energy required to bring a unit contour (near the value of s) from the bulk (reference phase) to coordinate $\mathbf{r}$. This quantity is normalized by the thermal energy $k_{\mathrm{B}}T$. We will elaborate the Edwards equation using homopolymers for simplicity and discuss extensions to copolymers (relevant for lipids) further on. For homopolymers one can use $u(\mathbf{r}) = u(\mathbf{r}, s)$. In the Edwards equation $G(\mathbf{r}, s)$ represents the statistical weight to find the chain fragment around s near the spatial coordinate $\mathbf{r}$. This quantity invariably depends on the 'initial conditions' applied to Eqn 4.5. Typically, any explicitly mentioned initial conditions are included in the notation and we will follow this habit. For example, the notation for the statistical weight may be extended to $G(\mathbf{r}, s|\mathbf{r}', s')$, which then is the statistical weight to have a chain fragment with the contour point s at coordinate $\mathbf{r}$, when it is - along the contour - connected to s' at coordinate $\mathbf{r}'$. In the SF-SCF formalism one frequently encounters so-called end-point distribution functions $G(\mathbf{r}, s|1)$. Here it is understood that when a spatial coordinate is 'missing' in G, the 'integration' over this coordinate is implemented: $G(\mathbf{r}, s|1) = \sum_{\mathbf{r}'} G(\mathbf{r}, s|\mathbf{r}', 1)$. The physical meaning of the end-point distribution $G(\mathbf{r}, s|1)$ is the statistical weight of all possible walks that start with a chain fragment near $s = 1$ and end at the chain fragment near s at position $\mathbf{r}$. The fragment near $s = 1$ in this case can be near any coordinate in the system, which is compatible with the possible walks of a chain-fragment with length s.

Typically, the SF-SCF formalism is applied to systems with a given 'symmetry'. For example, for adsorption onto a planar surface, the density gradients normal to the surface are of main interest. Then the coordinate $\mathbf{r}$ is typically replaced by z and a mean-field approximation is applied in the x-y direction parallel to the surface. The Laplace operator in Eqn 4.5 for this case reduces to $\nabla^2 = \partial^2/\partial z^2$. Two- and three-gradient extensions (systems with less symmetry) are straightforwardly implemented. One-gradient spherical and cylindrical geometries are also frequently used, e.g. when spherical or cylindrically shaped vesicles are considered, respectively. In this case the coordinate $\mathbf{r}$ is replaced by r and the Laplace operator $\nabla^2 = \frac{\partial^2}{\partial r^2} + \frac{2}{r}\frac{\partial}{\partial r}$ for spherical and $\nabla^2 = \frac{\partial^2}{\partial r^2} + \frac{1}{r}\frac{\partial}{\partial r}$ for cylindrical geometry, respectively.

There are many strategies to numerically evaluate the Edwards equation. In the SF-SCF protocol, a finite element approach is used. We split the (polymer) chain into so-called statistical segments with ranking numbers $s = 1,\ 2,\ \ldots,\ N$. The size of such a segment does not necessarily need to coincide with the chemical notion of a segment, e.g., a polymeric monomer. It is assumed that on the length scale of the segment the chain is flexible. Segments are connected with bonds and the center-to-center distance between connected segments is b, also referred to as 'bond length'. In addition, a discrete set of coordinates is used, which in a one-gradient version has lattice layer number $z = 1,\ 2,\ \ldots,\ M$. Without mentioning otherwise we will consider the one-gradient planar

symmetry. The volume of a lattice site is given by $v = l^3$, where l is the characteristic length of a lattice site. In the classical SF-SCF implementations, it is taken that $b = l$, or in other words, neighboring segments along the chain can only occupy neighboring lattice sites on the lattice. Scheutjens and Fleer used the propagator equation as the discrete variant of the Edward equation. The propagator also features the statistical weight $G(z, s)$ (here the initial conditions are not specified yet and we use the generalized notation) and can be expressed as:

$$G(z, s \pm 1) = G(z)\langle G(z, s)\rangle \tag{4.6}$$

with $G(z) = \exp(-u(z))$, which is the Boltzmann equation featuring the (dimensionless) segment potential $u(z)$. In SF-SCF language this quantity is called the 'free segment distribution function'. The term within angular brackets, in the SF-SCF terminology known as the 'site fraction', represents a three-layer average:

$$\langle G(z, s)\rangle = \lambda G(z-1, s) + (1-2\lambda)G(z, s) + \lambda G(z+1, s) \tag{4.7}$$

where λ is the fraction of contacts that a segment in layer z has with segments in both layer $z-1$ and layer $z+1$. When we assume that segments 'live' on a simple cubic lattice, it seems logical to choose $\lambda = 1/6$, in line with the classical assumption in the Edwards equation. The hexagonal lattice, which, as we will argue below, may have been the better choice, implies $\lambda = 1/4$. Segment s in layer z can only be connected to segments in $z-1$, z or $z+1$, or in other words when $l = b$, neighboring segments along the chain - as mentioned earlier - must sit in a neighboring lattice site. The FJC on the lattice in this case reduces to a three-choice FJC model; there are three terms in the site fraction.

It is instructive to briefly show the link between the propagator and the Edwards equation. We will follow quite heuristic steps. We first rewrite Eqn 4.7 as

$$\begin{aligned}\langle G(z, s)\rangle &= G(z, s) + \lambda[G(z-1, s) - 2G(z, s) + G(z+1, s)] \\ &\approx G(z, s) + \lambda\frac{\partial^2 G(z, s)}{\partial z^2}\end{aligned} \tag{4.8}$$

where in the last line the meaning of z has changed from a lattice layer number to a continuous (dimensionless) coordinate, implying that l is the unit length.

Let us next assume that the segment potential felt by the fragment from s to $s+1$ is small, we may write the Taylor series expansion $G(z) \approx 1-u(z)$. Combining this expansion and Eqn 4.8 with the propagator (Eqn 4.6) leads to

$$G(z, s+1) = (1+u(z)) \times (G(z, s) + \lambda\frac{\partial^2 G(z, s)}{\partial z^2}) \tag{4.9}$$

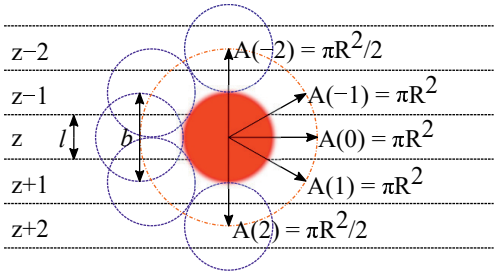

Figure 4.1: Illustration of a lattice refinement with $l = b/2$. The horizontal solid lines demarcate the lattice layers. Shown is a central segment of size b with its center at $z = 0$. On the left five neighboring segments are shown, situated with their centers at $z = -2, \ldots, 2$, respectively. On the right arrows are drawn from the center of the circle (with radius $R = b$) at $z = 0$ to layers $z = -2, \ldots, 2$, representing the directions of the bonds between two neighboring segments, i.e., the five choices in the FJC model. The circle represents a sphere. The total area of the sphere, $A = 4\pi R^2$, is 'distributed' over the five layers with indicated amounts $A(-2), \ldots, A(2)$. The specified areas are used to find the step probabilities used in the site fraction (see text).

We next can write $G(z, s+1) - G(z, s) \approx \partial G(z, s)/\partial s$ where the meaning of s is changed from a ranking number to a contour length variable. Because $u(z)$ is expected to be a small quantity and the second derivative of G to z is for slowly varying G a small quantity, we may subsequently ignore the product $u(z)\ \partial^2 G(z, s)/\partial z^2$. Then we find the one-gradient version of the Edwards equation valid for planar geometries:

$$\frac{\partial G(z, s)}{\partial s} = \frac{1}{6}\frac{\partial^2 G(z, s)}{\partial z^2} - u(z)G(z, s) \tag{4.10}$$

The 'inverse' problem to go from the Edwards equation to the propagator is less trivial, as it is not obvious to use the potential in the Boltzmann weight and to re-introduce the product of the potential and the second derivative of G to z.

In the above, we illustrated that the classical lattice approximations lead to a simple propagator formalism. In many cases, the accuracy of this discretization scheme is sufficient to find reasonable results. However when gradients in G are not small, one can run into problems. These problems are known under the common denominator of 'lattice artifacts'. Lattice artifacts for example occur for lipid membrane modeling when the core-corona or core-water interface is sharp compared to the segment size. The results then depend on, e.g., how exactly the membrane is positioned with respect to the lattice sites. A natural solution to fix this problem is to move to a more refined discretization scheme. In this paper, we implement a quasi lattice-free implementation of the self-consistent field equations inspired by Romeis et al. [25, 28] who used a similar implementation for polymer brushes and generalise the refinement strategy to non-planar geometries. The key idea is to keep the discretisation for the segments the same, that is use the same ranking

numbers $s = 1,\ 2,\ \ldots,\ N$, but to reduce the spatial coordinate, for example, by setting $l = b/2$. To cover the same volume, in case of a planar geometry the number of lattice sites in the z direction has to double with respect to the classical choice $l = b$; in this case, $z = 1,\ 2,\ \ldots,\ 2M$. Here and below, the bond length b is chosen to normalize all lengths in the system.

In the following, we will focus on the case $l = b/2$ and take it that the generalization to even more refined lattices is straightforward. One of the consequences of a refined lattice with respect to the segment size is that neighboring segments along the chain, no longer need to be placed at neighboring coordinates in the lattice. When segment s is in layer $z = z_s$, segment $s-1$ can be positioned in either $z_s - 2,\ z_s - 1,\ z_s,\ z_s + 1$, or $z_s + 2$ as demonstrated in figure 4.1. Hence the FJC model implemented on this refined lattice implies a five-choice propagator and we will refer to this case as the five-choice FJC model:

$$\begin{aligned} G(z, s+1) &= G(z)\langle G(z,s)\rangle \\ &= G(z) \sum_{z'=z-2}^{z+2} G(z', s)\lambda(z, z') \end{aligned} \tag{4.11}$$

To implement this equation, we need transition probabilities $\lambda(z, z')$. Referring to figure 4.1, we have implemented the idea that the transition probabilities $\lambda(z, z')$ should be proportional to the probability that a randomly directed arrow with size $R = b$ starting in layer z has its end in layer z'. This probability is proportional to the area $A(z' - z)$ specified in figure 4.1. The transition probabilities $\lambda(z, z') = \lambda(z' - z) = A(z' - z)/A$ then amount to $\lambda(-2) = \lambda(2) = 1/8$ and $\lambda(-1) = \lambda(1) = \lambda(0) = 1/4$. A similar argument for the classical 3-choice FJC gives the hexagonal values for the transition probabilities $\lambda(-1) = \lambda(1) = \lambda = 1/4$ and $\lambda(0) = 1 - 2\lambda = 1/2$.

A legitimate task is to show how this 5-point stencil relates to the Edwards equation. We can rewrite the site fraction as

$$\begin{aligned} \langle G(z,s)\rangle = G(z,s) + \frac{1}{8}(&G(z-2,s) + 2G(z-1,s) \\ &- 6G(z,s) + 2G(z+1,s) + G(z+2,s)) \end{aligned} \tag{4.12}$$

which can be further decomposed to

$$\begin{aligned}\langle G(z,s)\rangle = G(z,s) \\ + \frac{1}{2}\frac{G(z-2,s)-2G(z,s)+G(z+2,s)}{2^2} \\ + \frac{1}{4}\frac{G(z-1,s)-2G(z,s)+G(z+1,s)}{1^2}\end{aligned} \tag{4.13}$$

which implies that $\langle G(z,s)\rangle = G(z,s) + \frac{3}{4}\partial^2 G(z,s)/\partial z^2$. One should realize that spacing for z is half that for s. The 'effective' diffusion coefficient, which was 1/4 for the three-choice SCF in a hexagonal lattice, is therefore slightly reduced to 3/16 (expressed in units b). This is in line with the expected increase in flexibility of the chain when the lattice sites are reduced in size.

Typically, the propagators need to be supplemented with initial conditions. In the SF-SCF protocol, we start these recurrence relations at the chain ends. Linear polymers have two ends, one at $s = 1$ and the other at $s = N$ and we therefore develop two sets of end-point distribution functions $G(z,s|1)$ and $G(z,s|N)$ (now the extended notation is used). These end-point distributions are generated by the one upward (increase in s) and one downward (decrease in s) running propagator:

$$G(z,s+1|1) = G(z)\langle G(z,s|1)\rangle \tag{4.14}$$

$$G(z,s-1|N) = G(z)\langle G(z,s|N)\rangle \tag{4.15}$$

To start these, one realizes that a walk of one segment long gets the statistical weight given by the free segment distribution function:

$$G(z,1|1) = G(z) \tag{4.16}$$

$$G(z,N|N) = G(z) \tag{4.17}$$

The volume fraction profiles $\varphi(z,s)$, that is, the fraction of sites in coordinate z occupied by segments with ranking number s, are found by the so-called composition law, which combines complementary end-point distribution functions:

$$\varphi(z,s) = C\frac{G(z,s|1)G(z,s|N)}{G(z)} \tag{4.18}$$

The division by the free segment distribution function is needed to prevent double counting of the segment weight for segment number s. In Eqn 4.18 the normalization constant C depends on the ensemble in which the calculations take place. In a grand canonical

ensemble the bulk concentration, φ^b, is specified and $C = \varphi^b/N$. This is easily seen because in the bulk solution all end-point distributions are unity and $\varphi(z,s)N = \varphi^b$. In a canonical ensemble we need to specify the number of chains per unit area: $n = \theta/N$, where $N = \frac{l}{b}\sum_z \varphi(z,s)$. Summing the densities over all segments gives the overall distribution for the polymer $\varphi(z) = \sum_{s=1}^{N} \varphi(z,s)$. The integral over the overall density is the amount $\theta = \frac{l}{b}\sum_z \varphi(z)$. The number of molecules as well as θ is specified on the bond length level. As a result, in the canonical ensemble $C = \theta/(\frac{l}{b}G(1|N))$. We define the chain partition function $q = \frac{l}{b}G(1|N))$.

The Edwards equation must be supplemented with proper boundary conditions and the propagators require these as well. It is easily seen that evaluation of $G(z,s|1)$ or $G(z,s|N)$ in the region $z = 1,\ \ldots,\ 2M$ requires values for end-point distribution functions specified for $z < 0$ and $z > 2M$. We distinguish different boundary conditions, which we will illustrate for $G(z,s|1)$. (i) Neumann boundary conditions or, in SF-SCF language, adsorbing boundary conditions, typically used to model a solid phase at the system boundary. In this case, the chains cannot pass the boundary and we take $G(z,s|1) = 0$ for all $z < 1$ when the Neumann boundary conditions apply near the lower boundary of the system and $G(z,s|1) = 0$ when $z > 2M$ when these conditions apply to the upper boundary. (ii) Dirichlet boundary conditions or, in SF-SCF language, mirror-like boundary conditions. In this case, the target is to have vanishing gradients (gradients are zero) at the boundaries of any spatial distribution in the system. As a consequence, lipid chains are allowed to cross the symmetry plane and there are no entropic restrictions felt by the molecules at the system boundary. Therefore we set $G(z,s|1) = G(1-z,s|1)$ for all $z < 0$ and $G(z,s|1) = G(4M+1-z,s|1)$ for all $z > 2M$. (iii) Periodic boundary conditions are implemented by $G(z,s|1) = G(z+2M,s|1)$ when $z < 1$ and $G(z,s|1) = G(z-2M,s|1)$ when $z > 2M$. It is understood that for $G(z,s|N)$ and for all segment densities $\varphi(z,s)$ and thus also for $\varphi(z)$ similar boundary conditions may be implemented when necessary. In this work, we use the Dirichlet boundary conditions.

The generalization to multiple types of chains in the system is only an organizational issue: the notation in the above equations must be extended to include the chain type $i = 1,\ 2,\ \ldots,\ I$. For example, the volume fraction distribution of molecule i is typically referred to as $\varphi_i(z)$. The polymer chains may be composed of different segments. Let the segment types be scanned by the variable $X = A,\ B,\ \ldots$. When the chain architecture is known from the input, we can define chain-architecture operators $\delta_{i,s}^{X}$. These quantities take the value unity when segment s of chain i is of segment type X and are zero otherwise. Each unique segment type X has its unique potential profile, $u_X(z)$, and thus has its unique free segment distribution function $G_X(z) = \exp(-u_X(z))$. We may generalize the free segment distribution function, $G_X(z)$, to one which depends on the molecule i and

segment ranking number s, $G_i(z,s)$, as follows

$$G_i(z,s) = \sum_X G_X(z)\delta_{i,s}^X \tag{4.19}$$

For example, when segment s of molecule i is of type A, we have $G_i(z,s) = G_A(z)$. This quantity features in the propagator replacing $G(z)$. Typically in the propagator, the end-point distributions will have the extended notation also to avoid confusion with the ranking number dependent free segment distribution. Also in the composition law, Eqn 4.18, $G_i(z,s)$ replaces $G(z)$. After all ranking number dependent volume fraction profiles are computed, one can subsequently collect these in various segment type-dependent ones. For example, the overall volume fraction profile of segments of type A is found by

$$\varphi_A(z) = \sum_i \sum_s \varphi_i(z,s)\delta_{i,s}^A \tag{4.20}$$

The implementation of branching in the propagator formalism is also just a technical one and we refer to the literature for details. [29]

In SF-SCF modeling the Flory-Huggins equation of state is used. Segment interactions are parameterized by Flory-Huggins exchange interaction parameters $\chi_{A-B} = Z/k_{\mathrm{B}}T(2U_{AB} - U_{AA} - U_{BB})/2$, where Z is a lattice coordination number and U is the (potential) energy of the specified pairwise interaction, that is, the depth of the square-well potential for each specified contact. From this definition one can see that for 'like' contacts the FH parameter is zero by definition, i.e., $\chi_{A-A} = 0$. Such 'Archimedes-like' choice for the interaction parameter, is appropriate for systems that are incompressible because in such a system segments cannot 'escape' from interactions. In the Flory-Huggins theory (and also in SF-SCF) the Bragg-Williams approximation is implemented, which means that the probability (per unit area) of having an A-B 'contact' is given by the product of the respective volume fractions $\varphi_A \times \varphi_B$. This is an approximation because segments that like each other will have a higher probability than the average value to be next to each other and *vice versa*. This correlation effect is thus ignored. Optimization of the mean-field free energy within the Flory-Huggins way of accounting for interactions leads to the following rule how to compute the segment potentials

$$u_A(z) = \alpha(z) + \sum_X \chi_{A-X}(\langle\varphi_X(z)\rangle - \varphi_X^b) \tag{4.21}$$

Here $\alpha(z)$, known as the Lagrange field contribution, is the energy needed to generate space to insert the segment at position z. Hence it is related to the compressibility

constraint. The numerical value of $\alpha(z)$ is during the optimization routine adjusted until at coordinate z the sum of the volume fractions equals unity:

$$\sum_X \varphi_X(z) = 1 \tag{4.22}$$

The same equation applies to the bulk and the bulk volume fraction of the solvent is taken such that the sum of the bulk volume fractions is unity. As stated before, in grand canonical calculations all bulk volume fractions are known. Inversely in canonical calculations, one can compute the bulk volume fractions of all chains from the normalization constant C that is used (or computed) in the composition law, Eqn 4.18.

To evaluate the segment potentials (Eqn 4.21) we also need to evaluate the site fraction (cf. Eqn 4.7). This quantity depends on the discretization scheme in the same way as the end-point distributions do. The appropriate boundary conditions must be implemented to evaluate the site fraction near the system boundaries. The use of the site fraction to evaluate the potentials is a unique feature of the SF-SCF theory. In the field of polymer micro-phase segregation, the Edwards equation is typically solved using a finite element scheme that retains the Gaussian chain model, yet it loses the length of the chain as an independent variable. Instead, the product χN is retained. In such an approach it is not natural to account for the site fraction in the potential and typically the approximation is introduced that $\phi(z) = \langle\phi(z)\rangle$. One can say that only the local contribution is used and the non-local contributions, which in a lattice model come in to approximate the second derivative, are ignored. We have shown that such an approach is not without its consequences [22], especially when one is interested in results in the weak segregation limit.

When on top of the short-range contact interactions other interactions exist in the system, one has to extend the free energy functional with the corresponding terms, leading to additional terms in the segment potentials. A well-known example is electrostatic interactions when there are charged species in the system. In this case, we need to take into account the electrostatic potential and for this we need to solve the Poisson equation. Here we will not go into these details because the evaluation of the Poisson equation on a finer grit essentially takes place in the same way as for a less refined grit. [19]

The numerical methods to find the 'fixed point', or the self-consistent solution for the set of equations, do not depend on the discretization scheme and details of this can be found elsewhere. [30] It suffices to mention that routinely the solutions are obtained with 8 to 10 significant digits. This is sufficient to accurately evaluate various thermodynamic potentials and the interfacial rigidities.

Non-planar geometries

Above we have elaborated on the main details of the SF-SCF theory and we have shown how one can use a grit with lattice sites that are twice smaller than the segment size (or equivalently the bond size). It is of significant interest to elaborate further on how one can implement the corresponding strategy in spherical or cylindrical one-gradient coordinate systems. From the above, it is clear that the main challenge is to implement the Laplacian in the five-choice FJC model. In the lattice we have spherical (or cylindrical) lattice layers which we number once again by $z = 1,\ 2,\ \ldots,\ 2M$ and understand that the r-coordinate (units b) takes values $r = (z - 1/2)/2$. In the planar lattice we arrived at transition probabilities $\lambda(z - z')$, where $z - z'$ obtained values $-2,\ -1,\ 0,\ 1,\ 2$. It is clear that for finite r we will need to modify these transition probabilities with an r-dependent function such that in the limit $r \to \infty$ the planar quantities are recovered.

$$\lambda(r, r') = \Lambda(r, r')\lambda(z - z') \tag{4.23}$$

where $\Lambda(r, r')$ contains the lattice geometry information. We define $L(r) = V(r + 1/2) - V(r - 1/2)$, with $V(r) = \frac{4}{3}\pi r^3$ in spherical and πr^2 in cylindrical geometry. Hence, in spherical coordinates $L(r) \approx 4\pi r^2$ and in cylindrical coordinates $L(r) = 2\pi r$. Next we need to make sure that the statistical weight to make steps from r to r' is the same as the weight to make steps from r' to r (so-called inversion symmetry), which requires that $L(r)\Lambda(r, r') = L(r')\Lambda(r', r)$. Similarly as in the classical approach we therefore take the transition probabilities proportional to the area $A(r'')$, where $A(r) = 4\pi r^2$ in spherical and $A(r) = 2\pi r$ in cylindrical geometry, of the plane at r'' halfway between the coordinates r and r':

$$\Lambda(r, r') = \frac{A(\frac{r+r'}{2})}{L(r)} \tag{4.24}$$

As the sum over all transition probabilities need to be unity we take $\lambda(z, z) = 1 - \lambda(z, z - 2) - \lambda(z, z - 1) - \lambda(z, z + 1) - \lambda(z, z + 2)$. It can be shown that these transition probabilities obey to the Laplacian properties in curved geometries, that is, it is not too difficult to show that these transition probabilities give in spherical and cylindrical geometry a term proportional to $2/r$ and $1/r$, respectively, times a term $\frac{1}{8}[G(z+2) + G(z+1) - G(z-1) - G(z-2)] = \frac{3}{4}\frac{\partial G}{\partial z}$. The coefficient $3/4$ is in line with the result from Eqn 4.13 discussed above. Hence, the corresponding Edward equation reads

$$\frac{\partial G(z, s)}{\partial s} = D\left(\frac{b}{l}\right)\nabla^2 G(z, s) - u(z)G(z, s) \tag{4.25}$$

with $D(2) = 3/4$, when the unit length is l is used and $D(2) = 3/16$ when the unit length b is chosen.

The continuous limit

It is possible to repeat this exercise for other lattice refinement factors b/l. Assuming b/l is an integer number we can follow the above strategy to find the transition probabilities. The resulting 'diffusion coefficient' $D(b/l)$ takes the form $D(b/l) = \frac{-(b/l)^2+\sum_{k=1}^{b/l} 2k^2}{4(b/l)^3}$ when the bond length units are used. As the nominator can be shown to be equal to $\frac{2}{3}(b/l)^3+\frac{b/l}{3}$, we find the remarkable result

$$D(b/l) = \frac{1}{6}\left(1 + \frac{1}{2}\frac{1}{(b/l)^2}\right) \tag{4.26}$$

This means that in the continuous limit $D(\infty) = 1/6$ as advertised in the Edwards equation, while for $b/l = 1$ the hexagonal lattice result is recovered, i.e. $D(1) = 1/4$. Indeed this result shows that the link between propagators and the Edwards equation is much more subtle than the heuristic approach used above.

Importantly, in the classical SF-SCF method with $b/l = 1$ it is advised to use a hexagonal lattice rather than the simple cubic lattice. Interestingly, the latter choice has been the default and rarely SF-SCF results have been reported using the hexagonal lattice!

Thermodynamic relations

When the self-consistent field solution is found numerically, we know that we have optimized the mean-field free energy F. Using this quantity we can evaluate the grand potential $\Omega = F - \sum_i \mu_i n_i$, where μ_i is the chemical potential of component i. The grand potential can be written as the sum over the grand potential density $\omega(z)$, i.e. $\Omega = \frac{l}{b}\sum_z L(z)\omega(z)$. Interestingly, there is a closed expression for the grand potential density [30]:

$$\begin{aligned}\omega(z) = &-\sum_i \frac{\varphi_i(z) - \varphi_i^b}{N_i} - \alpha(z) \\ &- \frac{1}{2}\sum_X \sum_Y \left(\varphi_X(z)\langle\varphi_Y(z)\rangle - \varphi_X^b\varphi_Y^b\right)\end{aligned} \tag{4.27}$$

and therefore we can find this quantity in high precision. Subsequently one can execute the protocol to find the bending rigidities of, e.g., membranes or in general interfaces.

4.4 The molecular model, parameter set and approach

4.4.1 Molecular architectures

As mentioned in the introduction a rather long tradition exists in evaluating the structural, thermodynamic, and mechanical parameters of model lipid bilayers using the self-consistent field method. [17, 19, 29, 31–35] Calculations presented in this paper aim to elaborate on and extend the results of Pera et al. [19] Our default system is therefore strongly linked to the one used by these authors. We will introduce this model and reiterate some arguments in support of this model.

Our focus is basically on membranes that are composed of (model) phospholipids in a solvent that aims to represent water. Both of these components bring in modeling challenges by themselves. Water is an associative solvent which forms a hydrogen-bonded network effectively preventing that water units go to the membrane core: it is said that the membrane core is dry. At the same time, the chemical potential of the surfactant should not exceed the value that corresponds to the so-called critical micellization concentration (CMC), which can only be found from complementary calculations. Obtaining satisfying estimates for the experimental CMC with having a dry core is impossible in the Flory-Huggins equation of state when water is modeled as a monomer. We follow Pera et al., who argued that a reasonable way to achieve both aspects, is to represent water as small clusters of 5 W segments. In figure 4.2 we have schematically illustrated such a water component. In the same figure, we present the architecture of the standard lipid that is used. In these lipids, there is a glycerol backbone onto which two tails and one headgroup are connected. The challenge to accurately model the self-assembly of amphiphiles is to represent the size and shape of the molecules at least in first-order correctly. As is illustrated in this figure a united atom description is adopted to realize this. All the individual 'united atoms', here represented by a small filled circle, have a size b. Depending on the discretization scheme this size is a value b/l times larger than the lattice site. Classically $b/l = 1$, however in the present study most of the calculations were done for $b/l = 3$. Here and below we have used $b = 0.35$ nm as an estimate of the size of these segments. We have named the C-segments in the different parts of the molecule differently so that we can vary the 'hydrophobicity' in the three regions, i.e. the tail region, the glycerol region, and the headgroup region, independently. We hope that by doing so we will learn more about how the hydrophobic/hydrophilic balance is reflected correspondingly in the membrane properties. As illustrated in figure 4.2 the default lipid has two fatty acid 'tails' with a tail length (l_t) of 18 carbons. They are attached to

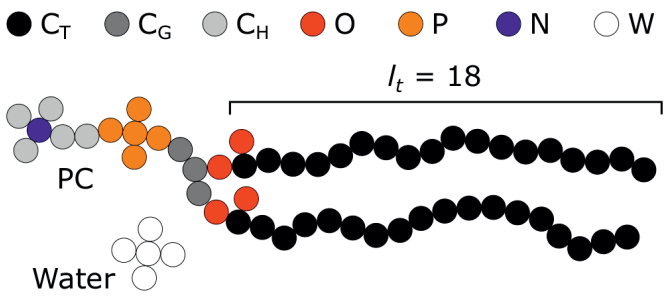

Figure 4.2: Schematic overview of the standard molecules used in this work. All specified united atoms (segments) have equal volume. The lipid contains a PC-like headgroup without explicit charges. In the headgroup we chose a single segment type for the phosphate group and in the choline group we distinguish the nitrogen from the surrounding carbon atoms, which are made more hydrophylic than the other carbon atoms. The two lipid tails have equal length, in this example 18 carbons, that is, $l_t = 18$. The water consists of five equal monomers arranged in a configuration wherein one W is surrounded by four neighboring W units.

the sn_1 and sn_2 position of a glycerol backbone. A phosphatidylcholine (PC) 'head' is attached to the sn_3 position. As double bonds are not implemented in our chain model, this structure could resemble the unsaturated dioleoyl phosphatidylcholine (DOPC) as well as the saturated distearyl phophatidylcholine (DSPC). However as our modeled lipid bilayers remain in the liquid state in all cases, we choose to use DOPC to name our default model lipid. The oxygens of the phosphate group are included in the P-units, the ones in the glycerol moiety (esters connecting the tails) are given by the O's. The quaternary nitrogen (in blue) is surrounded by three methyls and is connected to the phosphate by an ethyl unit. Note that in the SCF model no gel-to-liquid phase transition occurs and therefore we can probe the effects of changes in the tail length without the (experimental) complication that the liquid state of the membrane core is compromised above a certain tail length (e.g. $l_t > 18$).

4.4.2 Interaction parameters

4.4.3 Interaction parameters

We have decided not to follow the model of Pera et al. [19] in the way electrostatic interactions were accounted for. Pera et al. included these types of interactions by solving the Poisson equation in addition to the Edwards equation. This resulted in an extended Poisson Boltzmann-like model with a relatively large number of variables and quite a number of these were linked to the electrostatic effects. To reduce the number of parameters in the model we replaced all electrostatic interactions by effective short-range Flory-Huggins interactions. This is a not too strong simplification because in the biological context the

Table 4.1: The default interaction parameters $\chi_{X-Y} = \chi_{Y-X}$ used to quantify the solvent quality and the intermolecular interactions. The values in the table are the interaction parameters between the monomers X and Y listed in the left column and top row.

	W	$C_{\mathbf{H}}$	**N**	**P**	**O**
$\mathbf{C_T}$ / $\mathbf{C_G}$	1.2	0.5	2	2	2
O	−0.2	1	0	0	
P	−0.2	1	−0.5		
N	−0.2	1			
C_H	0.6				

ionic strength is relatively high and as a result, electrostatic interactions are short-ranged. We do not claim here that electrostatic interactions are irrelevant, but we argue that a full account of all possible electrostatic effects should account for many additional features such as the size and solubility of the ions, the hydration levels of the ions, the concentration, etcetera. We are of the opinion that only a dedicated study towards these effects will do justice to the real effects of electrostatics. The 'idealized' settings as used by Pera and coworkers simplify the matter too much (brushing complicating effects under the carpet so to say) and therefore we feel that at this stage it is better to remove electrostatics completely from our models and replace it with short-range interactions. The downside of our choice to drop the electrostatic interactions is that we cannot generate new insights in how for example the ionic strength modulates the mechanical parameters and phase behaviour of lipid systems.

An overview of the default χ-parameter set used for this simplified model system can be found in table 4.1. As the explicit charges are removed from the model, we have, with respect to the model of Pera et al., slightly modified the interaction parameters to mimic the effect of electrostatics at reasonably high ionic strengths. Since actual PC lipids are zwitterionic, we 'compensated' for this by choosing an attractive interaction parameter between nitrogen and the phosphate, $\chi_{\mathrm{P-N}} = -0.5$. In addition, the carbon groups in the headgroup have been given a slightly lower interaction parameter (less water repellent) with water ($\chi_{\mathrm{C_H-W}} = 0.6$) to represent the somewhat hydrophilic nature of this region and to compensate for the positive charge of the nitrogen group. In combination with χ_{C-N}, χ_{C-P} and χ_{C-O} all set to unity, this caused the choline group to be slightly further away from the core than the phosphate group, consistent with experimental results [36–38]. Other interaction parameters have been kept the same compared to the previous model [19]: $\chi_{\mathrm{W-N,P,O}} = -0.2$ to represent a weak attraction of the headgroup monomers with water; importantly, $\chi_{\mathrm{C_T-W}} = \chi_{\mathrm{C_G-W}} = 1.2$, chosen as this leads to a dependence of the critical micelle concentration (CMC) on the tail length close to experimental results. Finally, $\chi_{\mathrm{C_T-N,P,O}} = \chi_{\mathrm{C_G-N,P,O}} = 2$ and $\chi_{\mathrm{C_H-C_T,C_G}} = 0.5$ are chosen to ensure a strong segregation of the headgroup from the bilayer core.

4.4.4 Systematic variations of interaction parameters and lipid structure

Invariably in a multi-parameter model system for the lipid bilayer membrane, it is relevant to know how sensitive the results are for changes in the parameter set. Unlike in MD simulations in which a particular force field has known pros and cons, the parameter set presented above has a far less established character. In this light, it is timely to find out how the structural and mechanical parameters are subject to change when the Flory-Huggins interaction parameters are varied within reasonable ranges. In the classical SF-SCF theory, the lattice artifacts were seriously limiting such an exercise. However, in a lattice-refined SF-SCF approach such project suddenly becomes of interest not only because it is relevant to know how sensitive parameters determine results, but also because it opens avenues to learn more about the membrane mechanics. For example, by systematically varying the interaction parameters χ_{C_T-W}, χ_{C_G-W} and χ_{C_H-W} we can determine how the hydrophobicity of various regions of the lipid influences structural and mechanical parameters of the bilayer. We can project such results on different classes of lipids. For example, previous studies have shown that varying χ_{C_T-W} effectively influences lipid tail stretching and bilayer thickness [19]. Nature can do so by tuning the degree of unsaturation of the fatty acid tails [14, 39]. Changing the parameterization of the segments of the glycerol moiety of lipids arguable is not only relevant for the understanding of how glycerol-based lipids differ from e.g. sphingolipids, but it also gives generic insight in the role of the polarity gradient from head to tail that characterizes so many lipids. Headgroups of lipids are overall hydrophilic but typically contain not only polar but also apolar groups. Modifying the interaction parameters of (parts of) the headgroup with for example water may influence the readiness to hydrate the headgroup and this will affect the tension in the headgroup region (headgroup overlap) as a stopping force for the membrane formation. Insight into how much these changes can influence the overall membrane properties may lead to a deeper understanding of the relevance of headgroup variations in nature.

Apart from a parametric study on the interaction parameters, we have varied relevant structural features of the lipid tails. These variations comprise lipid tail length (l_t), including tails of different lengths in one lipid molecule, and variations in tail bulkiness by introducing a branching point in the tails.

To structure our results we have divided these into separate sections according to variations of the lipid tails, glycerol backbone, and the headgroups.

4.4.5 Data analysis

The structural features of the lipid bilayer predicted by the SF-SCF calculations can be extracted from the volume fraction distributions of all the segments per molecule. Typically these distributions are added together resulting in the overall lipid volume fraction profile, $\varphi_{\text{lipid}}(z)$. Alternatively, one can group these per segment type, e.g. the P units are grouped in $\varphi_P(z)$. When in a parameter study the interaction parameters are changed it is not productive to show all the changes in the corresponding volume fraction profiles. Instead, we have decided to follow and report on various measures that quantify the membrane structure in some way.

One of these measures is the average z position of the monomers C_G and C_H and the O, P, and N segments in the bilayer configuration. Because of the symmetry, it suffices to determine the average z positions over just one leaflet of the bilayer. These averages follow from the so-called first-moment analysis

$$\langle z \rangle_X = \frac{\sum\limits_{z>z_0} (z - z_0)(\varphi_X(z) - \varphi_X^b)}{\sum\limits_{z>z_0} \varphi_X(z) - \varphi_X^b} \tag{4.28}$$

were $\langle z \rangle_X$ is referred to as the average position of segment type X from the plane of symmetry z_0. Using these averages we can quantify the bilayer thickness, e.g. defined by the twice the distance of the N groups to the center of the bilayer: $d_{NN} = 2\langle z \rangle_N$. Similarly, the bilayer core thickness may be found from twice the distance of the O groups to the center of the bilayer: $d_{OO} = 2\langle z \rangle_O$. The headgroup orientation may be related to the difference in the average positions of the phosphate and the N of the choline in one leaflet of the bilayer, that is, $d_{PN} = \langle z \rangle_N - \langle z \rangle_P$. Another structural parameter of interest is the area per lipid molecule A_0, which is easily computed by

$$A_0 = \frac{N_{\text{lipid}}}{\theta^{\sigma}_{\text{lipid}}} \tag{4.29}$$

where $\theta^{\sigma}_{\text{lipid}} = \sum_{z>z_0}(b/l)(\varphi_{\text{lipid}}(z) - \varphi^b_{\text{lipid}})$ is the excess amount of segments of the lipid molecule per unit area (per leaflet) of the membrane, and N is the number of segments in the lipid molecule (measure for the molar volume). Multiplying A_0 by b^2 results in the area per molecule, a quantity that is known and tabulated for many types of lipids. Frequently this area is referred to as the headgroup area because in the planar geometry the bilayer tails occupy the same area as the heads. This should be distinguished from the headgroup area featuring in the so-called surfactant packing parameter $P = v/(la_0)$. This phenomenological parameter introduced by Israelachvili [40, 41] features an 'exper-

imental' area that a surfactant occupies, e.g. on the air/liquid interface, a_0. Together with theoretical values of the tail volume v and the (average) length of the tail(s), the value of P is indicative of the preferred association shape for self-assembly. If it is near 1/3 one should expect spherical micelles, near 1/2 cylindrical micelles, and for values near 1 bilayers. Often the packing parameter is used in a loose sense to rationalise various trends in phase behaviour for series of surfactants. An example is the prediction that for a given v and l an increase in the value of a_0 will give a trend from lamellar to cylinder to spheres and vice versa. The value of J_0^m is the SCF counterpart of this packing parameter. We may argue that trends predicted from P-changes could also be predicted from J_0^m-changes. Similar arguments practised in surfactant science to discuss trends in P can thus be used to rationalise trends in J_0^m.

4.5 Results and Discussion

This section is split into two parts. In the first one, we will discuss the structural and mechanical properties of the membrane using the default parameter set. The first task that is picked up is to establish the effectiveness of lattice refinement to find numerically accurate values for the bending rigidities. We will do this by focusing on the grand potential of spherically curved vesicles. In principle, the grand potential of spherical vesicles is scale-invariant. However, in the SCF computations this is not strictly the case in particular when lattice artifacts are manifest. The idea here is to show that the variations that are found for this value upon a change of the vesicle radius decreases rapidly when the ratio between segment and grit size, b/l, is increased. For a b/l ratio that gives sufficiently smooth results, we can derive the mechanical parameters of the bilayer from a single vesicle calculation: no laborious averaging is needed anymore. In the second part of this section, we will present results from systematic variations of structural and interaction parameters for the case that the discretization parameter $b/l = 3$. In order, we pay attention to variations in the lipid tails, we introduce changes in the glycerol backbone region and finally, we consider various ways to change the headgroup properties of the lipids. The overall goal of this section is to give insight in the sensitivity of the parameterization, but an important derived target is to learn how structural as well as mechanical parameters of lipid bilayer membranes can be regulated (at least in principle).

Table 4.2: Average values for the effective modulus $\kappa_s = 2\kappa + \bar{\kappa}$ including the maximum deviation from the average ($s_{\max}$) for spherical vesicles of $R \approx 100b$ consisting of the standard lipids (see figure 4.2) at different lattice refinements (b/l).

b/l [-]	$\kappa_s \pm s_{\max}$ $[k_{\mathrm{B}}T]$
1	-17 ± 345
2	6.03 ± 0.03
3	5.507 ± 0.001
4	5.3305 ± 0.0005
5	5.2495 ± 0.0005

4.5.1 The default system

Lattice refinement reduces lattice artefacts

As mentioned in the above section, the previously revised protocol to evaluate the bending rigidities of lipid bilayer membranes involves a large number of calculations wherein the radius of spherically or cylindrically curved vesicles is systematically increased by increasing the number of lipids in the system and the grand potential of these vesicles is recorded. Every time the radius of the vesicle increases by one lattice layer the grand potential goes through a local maximum and a local minimum, oscillating around an average value. Only this averaged value has clear physical interpretations: the oscillations are just a result of the use of a lattice. The amplitude of these sinusoidal variations in the grand potential becomes larger when the vesicle radius increases. When a sufficient number of these oscillations are generated one can find the 'averaged' grand potential. For the spherical vesicle such average is given by $\langle\Omega\rangle = 4\pi\kappa_s$, where the effective bending rigidity $\kappa_s = 2\kappa + \bar{\kappa}$ (cf. Eqn 4.4). Focusing on this spherical lattice we can thus find κ_s as well as $s_{\max} = (\Omega^{\max} - \Omega^{\min})/(4\pi)$ the difference between the maximum and minimum values for the effective bending rigidity along an oscillation (here taken when the radius of the vesicle $R = 100$). Pera et al. used the face-centered cubic (FCC) lattice with $\lambda = 1/3$, which was found to give the smallest value for $s_{\max}$. For obvious reasons, we here focus on the hexagonal lattice ($\lambda = 1/4$) for which $s_{\max}$ is relatively large unless lattice refinement techniques are implemented. The results for the default lipid bilayer are collected in table 4.2.

Inspection of table 4.2 reveals that the deviation $s_{\max}$ is enormous for $b/l = 1$. Indeed $s_{\max}$ is much larger than the average value κ_s. This was one of the challenges using the classical SCF theory to evaluate the mechanical parameters of lipid bilayers. It illustrates that the classical approach truly has a problem. Again, the workaround for this problem

implemented by Pera et al. was to use the FCC lattice ($\lambda = 1/3$) which compared to the hexagonal ($\lambda = 1/4$) or simple cubic lattice ($\lambda = 1/6$) reduces $s_{\max}$ to more or less acceptable values. In addition, Pera et al. used spherical vesicles that were as small as possible so that the oscillations around the mean were not yet overwhelming large. This explains why still reasonable predictions for the bending rigidity could be made. As seen in table 4.2 for the hexagonal lattice $s_{\max}$ is much larger than κ_s and it is clear that the estimates for the average are not very accurate. Already for $b/l = 2$ the value of $s_{\max}$ is significantly smaller than κ_s and one can have confidence in the reported estimate for κ_s at least up to 0.1 unit of $k_{\mathrm{B}}T$. For $b/l > 3$ the error no longer is due to lattice artifacts but merely by the precision in which the SCF solution was generated. As the computational cost increases with increasing lattice refinement, we have chosen to use a lattice refinement of $b/l = 3$ for the remainder of our calculations.

Apart from the reduced deviations, it is found that the average effective modulus κ_s decreases with increasing b/l. This implies that the membranes become slightly easier to bend. This must be attributed to a systematic change in the chain model. In the freely-jointed chain (FJC) model subsequent segments may be placed onto $1 + 2b/l$ different lattice positions. This increase in the number of positions with increasing b/l is reflected in an increase in the conformational entropy in the chain. Apparently, the lipid molecules are intrinsically more flexible with increasing b/l. To prevent a too high internal flexibility of the chains is another reason for choosing $b/l = 3$ over higher lattice refinement calculations. In the FJC model, the excluded volume correlations along a chain further than one segment are ignored. One can implement, e.g. the rotational isomeric state (RIS) scheme [29, 31, 42] wherein short-range correlations of (in this case) three segments are accounted for. In such a model the local stiffness of the chain can be incorporated to compensate for the increased flexibility of the chain when b/l is increased. To construct a RIS scheme in a lattice-refined model will be a task that is high on the agenda in the near future as this may restore the chain model to arguably more realistic ones. Until then, we have to accept the rather high flexibility of the chains as an SCF feature.

The small drift of the chain model with an increasing value of b/l has not only measurable effects on the mechanical parameters of the bilayer membranes but also has structural counterparts. Since the z-coordinate is based on the segment size b rather than on the size of the lattice site (we use b as the unit length), these structural differences are typically rather small and it is not too interesting to elaborate on these in detail. That is why we decided to show and discuss as an example the segment density profiles over the bilayer for the standard lipid and standard parameter set and discuss differences compared to the previous model using overall membrane measures. In figure 4.3 A the full bilayer cross-section is shown and in panel B an enlarged part for the headgroup region is given.

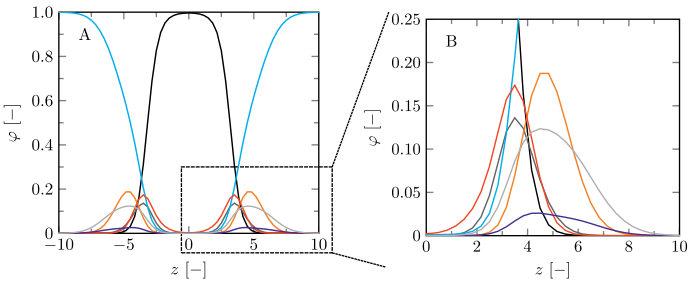

Figure 4.3: Volume fraction profiles of the default lipid bilayer membrane in a planar geometry. Figure A shows the volume fraction profiles for a full bilayer, whereas figure B shows a zoomed-in version, focusing on the headgroup and glycerol parts of a single leaflet of the bilayer. The profiles are presented in colors corresponding to the segment colors used in figure 4.2: C = black, O = red, P = orange, N = blue, C_G = dark grey, C_H = light grey. Water is depicted in light blue. The profiles correspond to SF-SCF calculations using a refined lattice ($b/l = 3$).

We have selected a planar geometry for which both leaflets are identical; $z = 0$ is set at the symmetry plane. In corresponding cross-sections of spherically and cylindrically curved bilayers the symmetry is broken and curvature effects may be seen on segment density profile level. We do not go here in detail and refer to the literature for an analysis of these effects. [33]

The volume fraction profiles shown in figure 4.3 are fully consistent with the generally accepted view of the lipid bilayer membrane. The core of the bilayer is predominantly populated by the tails (C monomers, black curves) and in this region, the water density is less than 1%. This is in line with experimental data and with computer simulations at large. The glycerol moiety sits in between the core and the headgroups. Near the maximum of the O's of the glycerol backbone, the solvent (water) density starts to grow so that in the region of the headgroups water is already the main component. Figure 4.3B gives a closer view of the distribution of the headgroup segments. It is of interest to notice that the width of the distribution of the headgroup region is comparable to the width of the hydrophobic core. This observation can only in part be attributed to the higher density and the flexible nature of the lipid tails in the core. Contributions to the broadening of the distribution of the headgroup segments are conformational fluctuations of the headgroup and protrusion-like fluctuations of lipids as a whole (that is fluctuations in the position of the molecules in the z-direction).

For this case study, the bilayer width as given by d_{NN} amounts to approximately $10.1b$, which translates to about 3.5 nm, and the equilibrium area per lipid molecule $A_0 = 11.5b^2$, corresponding to approximately 0.9 nm^2. These values are comparable to numbers found before with SF-SCF modeling [19] albeit that compared to previous estimates the area

went up by a few percent and the thickness went down by some 10%. Also compared to experimental estimates [14, 15, 43–47] the theoretical result underestimates the thickness and overestimates the area and the current model does this a bit more than the classical result of Pera et al. These differences are not unexpected. As mentioned above, compared to the real lipids we overestimate the chain flexibility. In addition, the mean-field model underestimates excluded volume effects. Both these facts can explain the observed shortcomings. We should also note that in SF-SCF the thickness of the bilayer is the so-called intrinsic thickness. Undulation fluctuations of the bilayer, which broaden the membrane thickness and typically influence experimentally reported membrane widths, are fully ignored. The underestimation of the membrane width and the small overestimation of the area per molecule have a corresponding impact on the mean bending modulus as will be discussed below.

The bilayer core thickness $d_{OO} = 6.72b$ represents about 2/3 of the total bilayer width, fairly consistent with literature [45]. The headgroup orientation can be related to the relative position of the nitrogen with respect to the phosphate group. Our results give a result of $d_{PN} = 0.23b$ indicating that the headgroup lies relatively flat on the surface of the bilayer, with the choline group slightly further outward compared to the phosphate group, similar to previous results [19]. The rather flat average orientation of the headgroups does not imply that all headgroups are parallel to the membrane plane. The rather broad distributions of N and P groups indicate that there are considerable fluctuations in the headgroup orientation. The width of these distributions may increase, and so will the conformational entropy, when the headgroup is on average parallel to the membrane surface compared to the perpendicular orientation. So there is also an entropic argument that disfavors large values for d_{PN}. Strong excluded volume effects in the headgroup region (when the area per lipid is small) will push the choline group to the outside and then larger values are expected for d_{PN}.

The values found for the structural properties of the lipid bilayer membrane are largely in line with all-atom computer simulations [35, 42, 48–51]. There are many ways to coin this result but to us this is remarkable because the CPU-time needed to find the SF-SCF result is on the order of a few CPU-seconds on a single CPU, while for full-atom MD simulations the computational efforts, which obviously scale with the number of lipids in the membrane piece considered and the length of time over which the results have been averaged, are easily 10^4 times longer. As SF-SCF is computationally inexpensive it is doable to conduct a parameter study (see below). Moreover, because the mean-field free energy is available we can evaluate thermodynamic and mechanical parameters for the lipid bilayer membranes. Computing mechanical parameters by MD is even more CPU time consuming so that we are aware of only few attempts for this [52, 53], let alone that

trends in these quantities have been simulated for systematically modified bilayers.

Let us next focus on the mechanical parameters of the default bilayer system as these follow from SCF. Here and below we have used the method of combining results from the planar geometry with a result for a spherical vesicle (the grand canonical route). Typically we used a vesicle with a radius $R \approx 100b$. Alternatively the mean and Gaussian bending rigidities could be evaluated combining the cylindrical and spherical geometries (previously used approach). When for both cylindrical and spherical vesicles a radius of $R \approx 100b$ is used, the tension in the cylindrical vesicle remains sufficiently small so that on the level of the accuracy of the calculations the mean bending rigidity is not affected and both routes give closely the same results. On the one hand this internal consistency check is satisfying and raises confidence in our results. On the other hand, it means that a small membrane tension does not have an impact on the mean bending modulus. Otherwise the method of Pera et al. would have failed. In retrospect, it indicates that the results of Pera et al. are indeed trustworthy, albeit that the numerical noise on their data is considerable. The new approach of combining planar and spherical results is strictly executed in the grand canonical ensemble and is preferred because it is computationally the most efficient and formally the correct route.

We find the bending modulus $\kappa = 2.84\ k_{\mathrm{B}}T$, the Gaussian bending modulus $\bar{\kappa} = -0.17\ k_{\mathrm{B}}T$ and the spontaneous curvature of the monolayer $J_0^m \approx 0.014b^{-1}$, i.e. close to 0. The negative value for $\bar{\kappa}$ and the small value for J_0^m show that the default lipid indeed is rather 'satisfied' with the planar bilayer assembly. Of course, the default parameterization was tuned to give these results as it is expected for a phosphatidylcholine lipid with two tails with length $l_t = 18$. The fact the numerical value of $\bar{\kappa}$ is rather close to zero indicates that the bilayer is not too far from a topological transition, which we consider realistic.

Experimental estimates are available only for the mean bending modulus. For most lipid bilayer membranes, reported values for this quantity are significantly higher, values as high as 10-50 $k_{\mathrm{B}}T$. [54] The largest numerical values may be linked to membranes in or extremely close to the gel-state. It is possible to upgrade the SCF approach to include the gel-to-liquid transition [32] by more accurately accounting for excluded volume effects of densely packed tails. This route, however, was abandoned due to the huge lattice artifacts that presented themselves. In a lattice-refined SCF approach, the ideas to introduce cooperative chain alignment effects may become of interest again. For the time being, however, such an extension of the theory is not available. Within the current lattice-refined SCF theory, the model bilayers are significantly more flexible than their real counterparts. As explained this result must not be coined as a surprise. Above we have seen that the theory underpredicts the membrane thickness, basically because the molecules do not feel

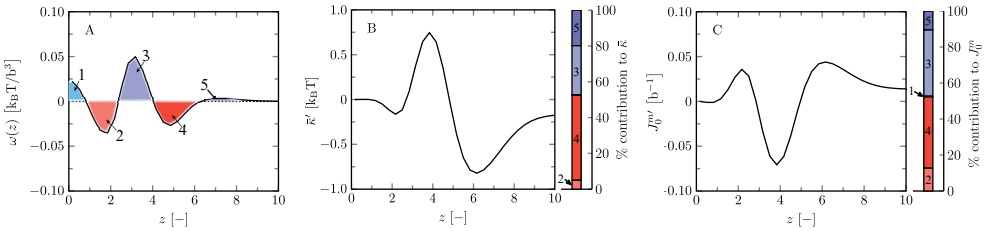

Figure 4.4: The grand potential density profile $\omega(z)$ (A), $\bar{\kappa}'(z)$ (B) and $J_0^{m\prime}(z)$ (C) for the default lipid bilayers in a planar geometry calculated using a refined lattice with $b/l = 3$. The functions $\bar{\kappa}'$ and $J_0^{m\prime}$ give the cumulative contributions to $\bar{\kappa}$ and J_0^m as defined in the text. The positive (in blue) and negative (in red) peaks (1-5) are defined in panel A. The relative contributions of these regions (1-5) to $\bar{\kappa}$ and J_0^m are shown in the bar chart next to the graphs.

sufficient excluded volume correlations and the chains are intrinsically too flexible. On the other hand, it cannot be ruled out that experimental estimates of the mean bending modulus could be on the high side because it is difficult to measure such quantities in a full equilibrium setting. For example, when the bending modulus is measured on time scales for which lipid flip-flop is not possible one must find significantly higher values for the bending modulus than from measurements on larger time scales.

Even though the current mean-field theory underestimates the value of the mean bending modulus, it is not expected that the same systematic underestimations or possible systematic overestimations would occur for $\bar{\kappa}$ and J_0^m. The relative preference for a bilayer to be in the planar state compared to some saddle-shaped configuration may depend more on how the hydrophobic/hydrophilic balance is spread throughout the lipid molecule rather than that it is influenced by the flexibility of the chain and/or the bilayer thickness per se. Furthermore, since similar (flexibility) errors are anticipated in the different geometries, we expect that the trends in $\bar{\kappa}$ and J_0^m that are discussed below are comparatively realistic. To substantiate this argument we continue the analysis of the default bilayer by focusing on the grand potential density profile.

As given by Eqns 4.2 and 4.3, $\bar{\kappa}$ and J_0^m follow from the second and first moment of the grand potential density profile, respectively. It is of more than average interest to pay attention to the grand potential profile. In figure 4.4A such a profile is shown for the default membrane, which is free of tension. This means that $\int_0^\infty \omega(z) = 0$. In this profile, we have identified five regions. The regions 1, 3, and 5 give a positive contribution to the membrane tension and are given colors from light to dark blue. The regions 2 and 4, colored light, and dark red give a negative contribution to the membrane tension. The total area for the red regions equals that of the blue regions because the membrane tension is zero. The positive contributions imply a tendency of the membrane area to

decrease while a negative contribution indicates a tendency to increase the membrane area. Positive excursions may be identified as 'driving forces' for membrane formation, while the negative ones contribute to the 'stopping forces'. Typically the hydrophobic tails that are in contact with the solvent at the core-corona interface invoke a positive local tension (region 3), and this is seen as the important driving force for the assembly of the membrane. The negative tension of region 2 results from stretching of the tails in the normal direction. This is a known but not often mentioned stopping mechanism for self-assembly. The negative tension in region 4 is referred to as the headgroup pressure, which is related to headgroup overlap, a stopping force as well. The positive contribution near the center of the bilayer (region 1) is often found for lipid bilayer membranes. A physical implication of this local positive tension is that the tails of the two leaflets of the bilayer attract each other so that no density dip occurs in the membrane core. This also permits the interdigitation of the tails into opposite monolayers which are known to happen to some extent. [32] Sometimes region 5 occurs at the periphery of the membrane surface. When this local positive tension is large we expect that membranes are mutually attractive. So a large positive contribution in region 5 is indicative of the loss of the colloidal stability of freely dispersed bilayers. In the default case, the colloidal stability is not compromised. When electrostatics are accounted for, one usually will find a small attraction due to dipole-dipole attraction of the PC headgroups.

For the impact of the various contributions of regions 1-5 to the Gaussian bending rigidity and the spontaneous curvature of the monolayer, not only the absolute values are important but also the precise location is relevant. In this case the local maxima occur at $z = 0$, at $z \approx 3.2$ and at $z \approx 7$ (regions 1, 3 and 5). The minima occur around $z \approx 1.8$ and $z = 4.8$ (region 2 and 4).

To further quantify how regions 1-5 contribute to the Gaussian bending rigidity and the spontaneous curvature of the monolayer, it is instructive to introduce cumulative functions that collect respective contributions up to layer z to $\bar{\kappa}$ and $J_0^m(z)$:

$$\bar{\kappa}'(z) = \sum_{z'=0}^{z} (z' - z_0)^2 \omega(z') \tag{4.30}$$

to $\bar{\kappa}$ and

$$J_0^{m\prime}(z) = \frac{-1}{\kappa} \sum_{z'=0}^{z} (z' - z_0) \omega(z') \tag{4.31}$$

These functions are presented in figures 4.4B and C, respectively. Note that in the limit of $z \to \infty$ the value of $\bar{\kappa}'(z)$ goes to the Gaussian bending rigidity $\bar{\kappa}$, and the similar limit for $J_0^m(z)$ is identical to J_0^m. The charts next to figures 4.4B and C give the fractional

contributions of the integrated parts of regions 1-5.

As $\bar{\kappa}$ is associated with the second moment of the grand potential density profile, contributions at larger z, i.e. regions 3 and 4, are more relevant then regions 1 and 2. For the spontaneous curvature of the monolayer, which is linked to the first moment, all regions are more equally important. These features are recognized in figure 4.4B and C. The fact that $\bar{\kappa} < 0$ can be attributed to the dominance of region 4. The positive value for J_0^m is traced to the relatively large contribution of the tension generated in region 3.

We anticipate that details in the glycerol backbone region may influence region 3, whereas an increment of the chain length will position all the regions 1-5 to somewhat larger z-values, with concomitant changes in $\bar{\kappa}$ and J_0^m. Below we will not present all the details of the grand potential density profiles, but in order to rationalize why particular changes in the mechanical parameters are found, we have made use of this type of information. In the supplementary information, more information can be found on how the grand potential density changes for a selected number of parameter variations. For example, the minimum in region 4 generally becomes less deep when it is found at larger values of z. Therefore it is likely that J_0^m will become less positive but the effect on $\bar{\kappa}$ is less clear because the weighting with z^2 may compensate for the reduced amplitude.

4.5.2 Parameter variation for the lipid tails

Several parameters can be varied for the lipid tails. We will start with varying the tail length (l_t) and the hydrophobicity of the tails by changing χ_{C_T-W}. In nature lipids with different tail lengths are frequently found in different types of biomembranes, and the hydrophobicity of the tails is altered by the degree of unsaturation of the fatty acids. It is expected that a higher degree of unsaturation decreases the hydrophobicity of the tails, as an increased solubility in water is observed [14, 39]. In addition, we will consider the effect of a difference in length between tails on sn_1 and sn_2 positions in the lipid molecule. Finally, we pay attention to the effect of branching of the lipid tails. For all these variations we will first present changes of structural parameters of the bilayers and then pay attention to the corresponding mechanical parameters.

Effect of tail length and tail hydrophobicity

The effects of tail length and tail hydrophobicity have been explored in previous work [19] and this is repeated here in support of the current and previous work. We present the bilayer core width d_{OO}, the orientation of the headgroups d_{PN} and the area per lipid A_0 in figure 4.5 as a function of the value of χ_{C_T-W} for lipids with tails $l_t = 12, \ldots, 20$. The larger χ_{C_T-W}, the stronger is the repulsion between the tails and water (the C's in the

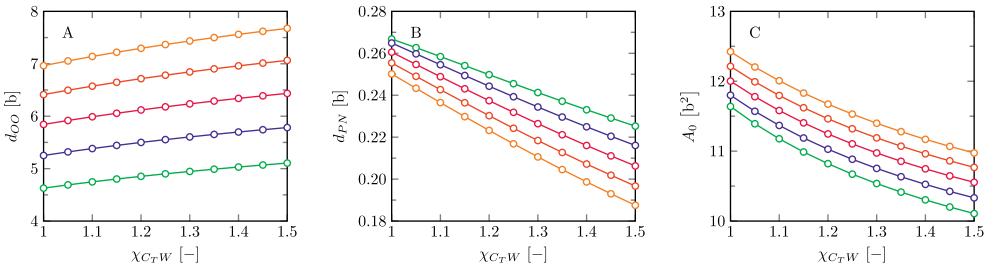

Figure 4.5: Structural parameters of bilayer membranes of lipids with different tail length as a function of the interaction parameter between tail carbons and water, χ_{C_T-W}. A) Bilayer core width, d_{OO}, B) headgroup orientation, d_{PN}, and C) area per lipid, A_0. Green: $l_t = 12$ C segments, blue: 14 segments, purple: 16 segments, red: 18 segments, orange: 20 segments.

glycerol backbone and in the heads remain unaltered). We varied this parameter around the default value of 1.2. It relates to the amount of water in the hydrophobic core. When $\chi_{C_T-W} = 1$ the water content is unacceptably high (above 1%). It also relates to the freely dispersed lipid concentration in the solvent (CMC). When $\chi_{C-W} \approx 1.5$, the CMC is much lower than the experimental estimates. We should keep this in mind when we discuss the trends, which are to some extent non-trivial. One would expect that with increasing driving force for assembly (longer or more hydrophobic tails) the two stopping forces would become stronger, that is, the area per molecule should go down and the stretching in the tails should increase. We see these trends for the increase in the hydrophobicity of the tails, but not for the increase in the tail length. When the tails are repelled stronger by water, the tension at the core-corona interface increases somewhat and this triggers both a stronger stretching of the tails and a reduced area per molecule. When for a given strength of the repulsion between tails and water the tail length is increased the area per molecule goes up. This is only possible when the stretching of the tails is becoming a more dominant stopping mechanism. Experimentally the area per lipid in the membrane was found to depend on whether or not the tails were saturated or not. [55] For lipids with unsaturated bonds the ordering of lipid tails in the core is expected to be less than for the saturated tails and for these less ordered bilayers, the increase in membrane area with increasing tail length is indeed reported. [55]

The core size d_{OO} increases with both increasing tail hydrophobicity χ_{C_T-W} and tail length l_t. The overall thickness of the bilayer d_{NN} follows the trend of d_{OO} as shown in the supplementary information. This trend is consistent with experimental results [55]. The headgroup orientation (as deduced from d_{NP} tends to become more parallel to the membrane surface when the tails become more hydrophobic as well as when the tails become longer. When χ_{C_T-W} is increased the tension between core and corona increases somewhat and this triggers the choline group to be closer to the core: it becomes stronger

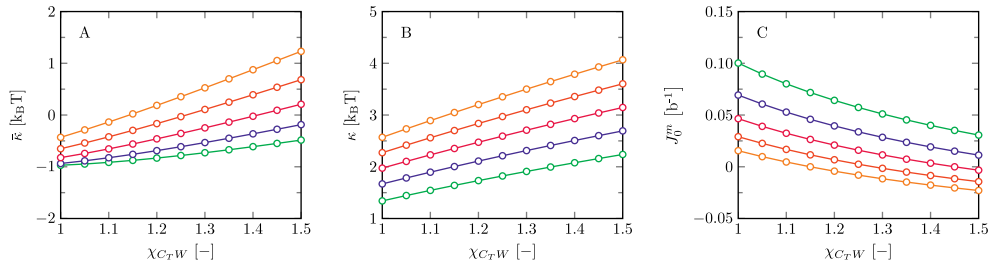

Figure 4.6: SCF predictions for the bending rigidities $\bar{\kappa}$ (A) and κ (B), and preferred curvature of the monolayer J_0^m (C) as a function of χ_{C_T-W} for different tail lengths (l_t). Green: $l_t = 12$ C segments, blue: 14 segments, purple: 16 segments, red: 18 segments, orange: 20 segments.

adsorbed at this interface at the expense of water. Such an adsorption effect goes against the natural response that a decrease in area per molecule leads to a larger tilt of the headgroup. This shows that the headgroup orientation is the result of a complex interplay of effects.

Referring to figure 4.6 we find increases in $\bar{\kappa}$ and κ and a decrease in J_0^m for both increasing l_t and χ_{C_T-W}. These trends are in good agreement with previous work [19]. Pera et al. argued that the mechanical parameters of the bilayers can be rationalized using structural arguments: both $\bar{\kappa}$ and J_0^m can be correlated with the shape of the lipid, which for amphiphilic molecules is generally described by the critical packing (surfactant) parameter [40, 41] and κ could be correlated to the overall bilayer thickness. We will also use similar arguments and try to deepen the insight where possible.

As with respect to the mean bending modulus (panel B) we find a strong correlation between this parameter and the membrane thickness d_{NN} (see also SI figure 4.16B). A thicker bilayer is simply harder to bend. Interestingly, we find a rather weak dependence with l_t. To a reasonable approximation κ grows linearly with l_t. The increase in the area per molecule which also takes place with increasing l_t must have contributed to this weak dependence.

The Gaussian bending modulus as well as the spontaneous curvature of the monolayer are expected to correlate to the topological stability of the bilayers. However, the corresponding effects on the topological stability of the self-assembled bilayers are subtle and hard to rationalize. More specifically, the sign-switch of $\bar{\kappa}$ that is predicted both for relatively hydrophobic tails and in the limit of long tails, tells us that both these trends destabilize the lamellar topology in favor of phases with saddle shapes, e.g. a cubic phase of some sort. The spontaneous curvature of the monolayer tends to become negative for long tails and/or very hydrophobic tails. This means that 'inverted' assemblies gradually should become the more favorable aggregation state. Pera et al. reasoned using surfactant pack-

ing parameter arguments. A hurdle in this approach is that we do not know exactly how the surfactant packing parameter responds to the changes in the parameters and there is some arbitrariness in it. Alternatively, to explain these trends we could relate them to the changes of the grand potential density profiles. However, it goes too far to show all these profiles individually. In addition, a formal 'explanation' of trends in terms of how the grand potential density profile changes, should be accompanied with arguments why the particular grand potential density profile did change as a response to variation of some parameter. This in turn is a challenging task in itself. In the following, we will combine both approaches to understand and qualitatively explain the trends.

It is known that relatively small headgroup sizes promote Gaussian curvatures and/or inverted assemblies. Alternatively for fixed headgroup properties, increasing the size of the tails or the hydrophobicity of the tails should induce the same trend. Indeed these expectations, based on 'geometric' arguments, are supported by the analysis of the grand potential density profiles, shown in supplementary figure S1A: the peaks for regions 2-5 shift to larger values of z both with increasing l_t and increasing $\chi_{\mathrm{C_T-W}}$, consistent with an increase in bilayer thickness. Peaks at higher z tend to have a reduced amplitude and therefore it is hard to see how the first or second moment of these profiles is changing in a particular way. In this case, the relative contribution of region 3 (driving force) overshadows the other contributions, and $\bar{\kappa}$ increases as well as J_0^m decreases. The relative increase in the importance of the tail stretching to the stopping force may have contributed to this trend. The negative grand potential in the headgroup region is less pronounced and the Gaussian bending rigidity is not receiving a concomitant negative contribution of the heads so that it can become positive. The same argument can be made for the trend of J_0^m.

Lipid with tails of unequal length

Many phospholipids within biomembranes have two tails with unequal tail lengths, or tails that differ in degree of unsaturation [56]. Why this is the case is not fully understood. In this light, it is of interest to know if and how much membrane properties depend on the acyl chain length difference. The effects on the bilayer structure and mechanical parameters remain largely unexplored, presumably because it is thought to be a secondary effect. From a surfactant packing parameter perspective, no changes are expected because it assumes that only the average tail length is important.

To investigate the effects of different tail lengths within one lipid, we have chosen to consider lipids with a fixed total of 32 carbons in their tails. Hence, when we choose a tail length of 14 carbons on the $\mathrm{sn_1}$ position ($l_{\mathrm{sn_1}} = 14$), the lipid tail on the $\mathrm{sn_2}$ position

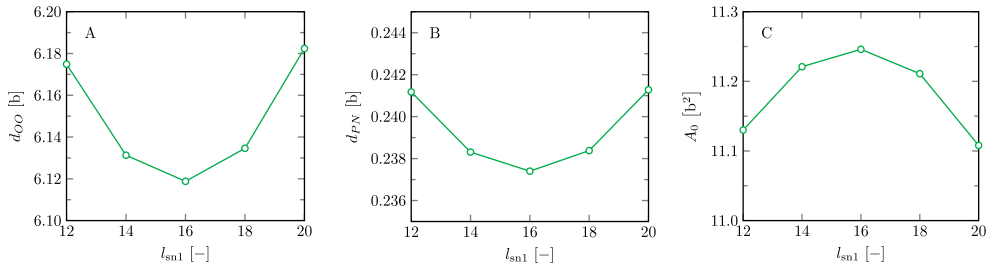

Figure 4.7: Structural analysis of lipid bilayers as a function of lipid tail length on the sn_1 position (l_{sn_1}). The total amount of carbon segments in both tails was fixed to 32; hence the tail on the sn_2 position has a length $l_{\mathrm{sn}_2} = 32 - l_{\mathrm{sn}_1}$. A) Bilayer core width, d_{OO}; B) headgroup orientation, d_{PN}; C) area per lipid, A_0. Parameters have the default values.

will thus have 18 carbons ($l_{\mathrm{sn}_2} = 18$), and so on. The structural membrane properties of the lipid bilayer are shown in figure 4.7 as a function of the length of the sn_1 tail.

Inspection of this figure proves that there are noticeable differences in whether the lipids have equally long tails or not, yet the magnitude of these differences is much smaller compared to changing the length of both tails l_t or $\chi_{\mathrm{C_T-W}}$. In general, the SCF theory predicts that tails of equal lengths, in this case with two C_{16} tails, have a smaller d_{OO} and d_{PN} and a higher A_0 compared to a lipid with two unequal tails. When the lengths of the two tails are different, the lipid can position the long tail more to the membrane center, while the shorter one can remain closer to the head (the lipid tails can split tasks). This degree of freedom allows for further optimization of the free energy which subsequently leads to slightly more lipids per unit area (reduced headgroup size) compared to the case that both tails are equally long and behave similarly. We may also argue that the membrane core size scales with the longest tail, which obviously is the case in the limit that all tail segments are in a single tail. As the longest tail increases with increasing asymmetry between the tail lengths, it is natural to expect that the core size increases with increasing difference in lengths. The minimum in the area per molecule, when the two tails have equal length, reflects in a maximum in the headgroup area and the headgroup orientation is most parallel to the membrane surface (d_{PN} goes through a minimum).

Close inspection of the curves proves that there is a slight asymmetry in the values whether or not the sn_1 tail is the longest. The reason for this is that the headgroup is closer to the sn_2 tail than to the sn_1 tail. As a result, the sn_1 tail is buried slightly deeper in the bilayer than the sn_2 (when both tails are equally long). Increasing the tail length of sn_2 has therefore less impact than increasing the sn_1 tail because it has first to catch up with sn_1 before it can be the tail that can go deepest in the bilayer.

Interestingly, while the changes in bilayer structure seem very subtle, the effect on $\bar{\kappa}$,

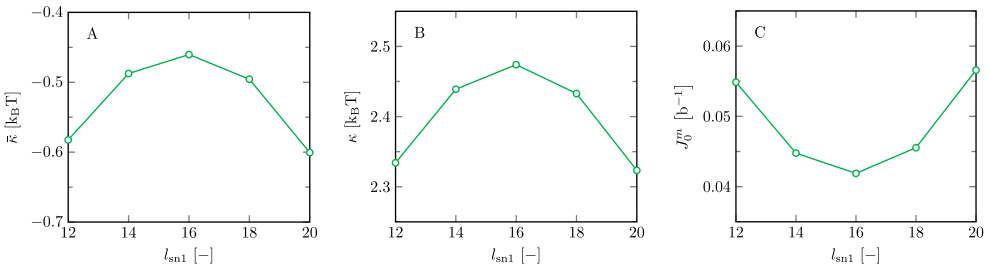

Figure 4.8: Estimation of the bending rigidities $\bar{\kappa}$ (A) and κ (B), and J_0^m (C) as a function of the lipid tail length on the sn_1 position (l_{sn_1}). The total amount of tail segments was chosen to be 32. Parameters similar as in figure 4.7

κ and J_0^m are surprisingly large: the relative increase in κ for lipids with tails of equal lengths over unequal tail lengths, is in the order of 10%, see figure 4.8.

One of the reasons why we present the effect of chain length variation within one lipid is that from a packing parameter point of view no differences are expected. Nevertheless, significant variations are found. The mean bending modulus in this case does not follow the trend that a thicker bilayer is harder to bend. Just the opposite is found! Clearly, when the tails are of unequal length, the lipid can target one tail to the center and the other tail more towards the corona. In this way, the bilayer can deal better with an imposed membrane curvature. This is reflected in a more flexible bilayer even with its thickness is slightly increased.

The Gaussian bending rigidity for the default lipid is close to zero and understandingly when the structure of the lipids is varied, small changes in the Gaussian bending rigidity can have large effects. The Gaussian bending rigidity deviates more from zero when the chains are more asymmetric in length. The stopping mechanism is distributed slightly less in the tail stretching and more in the headgroup overlap and therefore, region 4 becomes more important for the Gaussian bending rigidity. The trend for the spontaneous curvature of the monolayer can be rationalized in the same way.

Effect of branching of the lipid tails

The effects of chain branching are expected to follow trends suggested by the surfactant parameter arguments. Clearly, for a fixed amount of C monomers in the tails, branching reduces the average length of the tails. This 'naturally' leads to an increase in the value of the surfactant packing parameter. The larger value of the surfactant packing parameter then suggests a more negative spontaneous curvature of the monolayer and a tendency for a positive Gaussian bending rigidity.

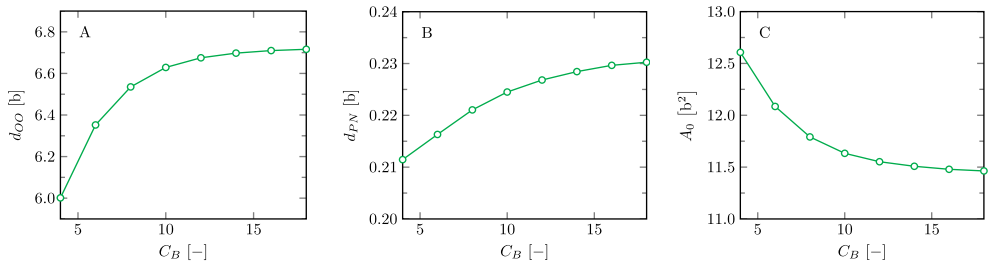

Figure 4.9: Structural analysis of bilayers consisting of lipids with a branching point in both tails at the same position. Each tail has a fixed number of carbon segments of 18 and splits into two equal branches at position C_B. A lipid with branching point $C_B = 4$, thus has two tails that split at the fourth C segment into two C_7 branches. A) Bilayer core width, d_{OO}; B) headgroup orientation, d_{PN}; C) area per lipid, A_0. The results were calculated using a lattice refinement of $b/l = 3$.

To test these expectations we introduce a systematic change of the bulkiness of the tails by introducing a branching point in each lipid tail while keeping the total number of carbon monomers per tail the same, here 18 per tail. For example, by introducing a branching point on the fourth carbon from the glycerol ($C_B = 4$), we subsequently have two smaller tail fragments each with a length of 7 carbon monomers. As such by varying the position of the branching point in the lipid tail, we can tune the effective bulkiness of the tails. The structural properties of the membrane as a function of the positions of the branching point are presented in figure 4.9. The core thickness is smallest for the lipids with the branching point closest to the backbone and it grows to the value of the unbranched chain when the branching point occurs at large values of C_B. At the same time, the area per molecule is largest when the branching point is near the headgroup. The larger the headgroup area is, the smaller is the z distance between N and P (d_{PN}), corresponding with the smallest angle between the headgroup and the plane of the bilayer. This trend is in line with the expectations sketched above. There is a strong nonlinear dependence on C_B. As expected the effects of branching near the backbone have a stronger effect than branching near the tail ends.

The consequences for the mechanical parameters of the lipid bilayer membranes are presented in figure 4.10. As can be seen from figure 4.10B, the mean bending modulus follows the membrane thickness: the thicker the bilayer, the stiffer it is. In line with the trend of the surfactant packing parameter, the Gaussian bending rigidity is clearly positive for the lipid with tail branching near the glycerol backbone and approaches the value for the default lipid (a small but negative value) when the tail branching occurs far towards the tail ends. The spontaneous curvature of the monolayer also follows the surfactant packing parameter prediction. It is negative (meaning that inverted assemblies are promoted) when the branching is close to the heads and shifts to the value for the default lipid (which

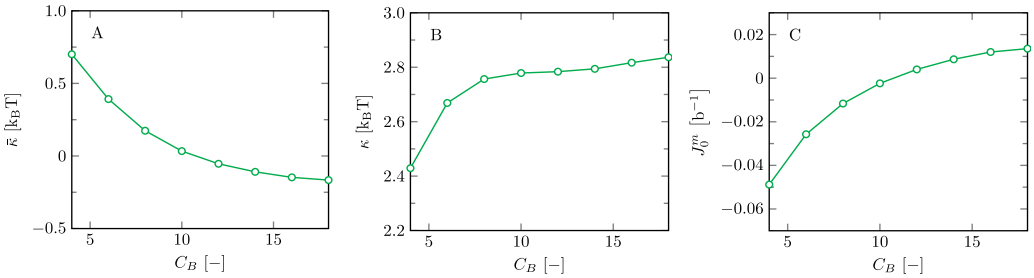

Figure 4.10: SCF predictions of Gaussian bending rigidity $\bar{\kappa}$ (A), mean bending rigidity κ (B) and J_0^m (C) as a function of branching point (C_B) for the same bilayers with branched lipids as in figure 4.9.

is slightly positive) for lipids with branching near the tail ends.

It is clear that bilayers consisting of lipids with shorter and bulkier tails have a higher tendency to form cubic phases compared to lipids with fewer and longer tails. Depending on the goal, varying the bulkiness of the tails can be a systematic strategy to obtain self-assembled structures of a desired topology. We do not know of experimental counterparts to substantiate this prediction. For the way in which we varied the lipid branching, SCF theory predicts that the Gaussian bending rigidity changes sign almost simultaneously with the change of sign of the spontaneous curvature of the monolayer. For the desired change of phases, it may well be relevant which of the two quantities changes sign first.

4.5.3 Parameter variation for the glycerol backbone

The role of the polarity of the glycerol backbone is the next focus of our parameter variation study. In the study to understand lipid bilayer properties one typically considers the effects of tails and the effects of headgroups of the lipids, but the role of the transition between heads and tails, for phospholipids the glycerol backbone, is generally neglected. Nature, however, does consider lipids of various sorts which do differ in how the tails and the headgroups are linked to each other, cf. phospholipids versus sphingolipids. The difficulty in understanding the role of variations in the region between heads and tails is that when the structure is changed, also the gradients from polar to apolar are affected. Here we decided to keep the architecture of the lipids the same and only modify the interaction parameters in this region of the molecule. In this way, we hope to generate a more clear picture of what happens to structural as well as mechanical parameters of the membranes when the gradient from polar to apolar in the lipids occurs relatively abruptly or more gradually.

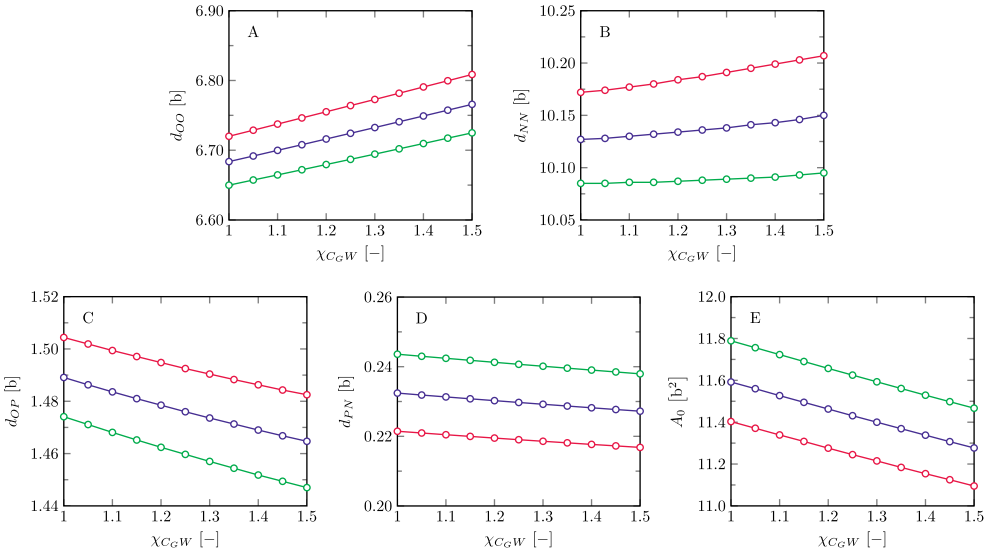

Figure 4.11: Effect of glycerol backbone hydrophobicity ($\chi_{\mathrm{C_G-W}}$ and $\chi_{\mathrm{O-W}}$) on various bilayer properties: A) bilayer core width d_{OO}; B) overall thickness of the bilayer d_{NN}; C) distance between P and O in the glycerol backbone d_{OP}; D) headgroup orientation d_{PN}; E) area per lipid A_0. Green: $\chi_{\mathrm{O-W}} = -0.4$, blue: $\chi_{\mathrm{O-W}} = -0.2$, purple: $\chi_{\mathrm{O-W}} = 0$.

We have varied the hydrophobicity of the glycerol backbone in two ways. The first one is by varying the repulsion between water and the hydrocarbons from the glycerol backbone, $\chi_{\mathrm{C_G-W}}$, and the second one is by changing the attraction of water to the O's, $\chi_{\mathrm{O-W}}$. The results regarding the structural effects of the lipid bilayers are collected in figure 4.11. Besides reporting on the headgroup area A_0, the orientation of the headgroup d_{PN} and the core size d_{OO}, we also show the effects on the overall membrane thickness d_{NN}, and the distance between the phosphate group and the O in the glycerol backbone d_{OP}. We note that increasing χ_{C_G-W} as well as making χ_{O-W} less negative implements two complementary ways to make the glycerol backbone region overall more hydrophobic. Making χ_{O-W} more negative implies a wider gradient in polarity from head to tail within the lipid molecule, but not necessarily implies a wider region of polarity in the lipid bilayer as the conformations of the molecules respond to the imposed interactions.

As there are only a few O's per lipid and also the number of hydrocarbon units in the glycerol backbone is small, we cannot expect huge effects on the overall membrane properties. The modest changes that do occur are as follows. The d_{OO} thickness increases with increasing glycerol hydrophobicity, the headgroup orientation flattens, i.e. d_{PN} goes down, and the area per lipid A_0 decreases. This smaller headgroup area implies that the glycerol backbone contributes to some extent to the stopping force for self-assembly:

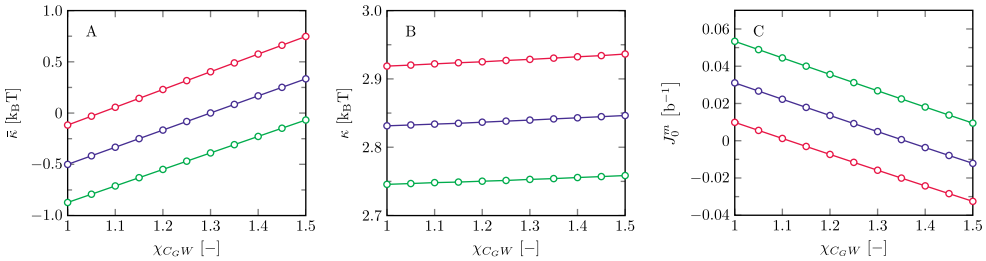

Figure 4.12: SCF predictions for the bending rigidities $\bar{\kappa}$ (A) and κ (B), and J_0^m (C) as a function of the hydrophobicity of the glycerol backbone (χ_{C_G-W} and χ_{O-W}). Green: $\chi_{O-W} = -0.4$, blue: $\chi_{O-W} = -0.2$, purple: $\chi_{O-W} = 0$.

reduction of the hydrophilicity of the glycerol backbone requires a stronger overlap of the headgroups to make the membranes free of tension. Just as with varying χ_{C_T-W}, the decrease in A_0 is accompanied with a flatter headgroup orientation, probably due to water being pushed out of the headgroup region. In other words, the choline group is pulled towards the core at the expense of water molecules being in contact with tails (adsorption effect). Interestingly, although their general effects are comparable, small differences exist between varying χ_{C_G-W} and χ_{O-W}, in particular in the strength of their effects. This is best seen in the bilayer thickness d_{NN}, where almost no change is observed when varying χ_{C_G-W}, while a clear increase in d_{NN} is observed increasing χ_{O-W}. The distance between the phosphate and the O of the glycerol decreases when χ_{C_G-W} is increased at a fixed polarity of the O-groups. It is also decreased when at fixed χ_{C_G-W} the O's are made more polar. This means that the conformations of the glycerol backbone, especially of the part in contact with the headgroups, can be modified to bring hydrophilic O's near the polar groups of the head and close to water.

The corresponding effects on the bending rigidities and spontaneous curvature of the monolayer are collected in figure 4.12. Again one would have expected just modest changes, but surprisingly large effects are found for the Gaussian bending rigidity and the spontaneous curvature of the monolayer, proving that the region connecting the headgroup and the tails is not unimportant for the topological stability of lipid bilayer membranes.

In line with the reported changes in the membrane thickness d_{NN}, it is found that the mean bending modulus slightly increases with the hydrophobicity of the hydrocarbons of the glycerol backbone and somewhat stronger with the polarity of the O's.

With respect to the Gaussian bending modulus and the spontaneous curvature of the monolayer, the trends follow the same patterns as for χ_{C_T-W} and l_t. That is, the increase in $\bar{\kappa}$ and decrease in J_0^m correlate with a decrease in A_0.

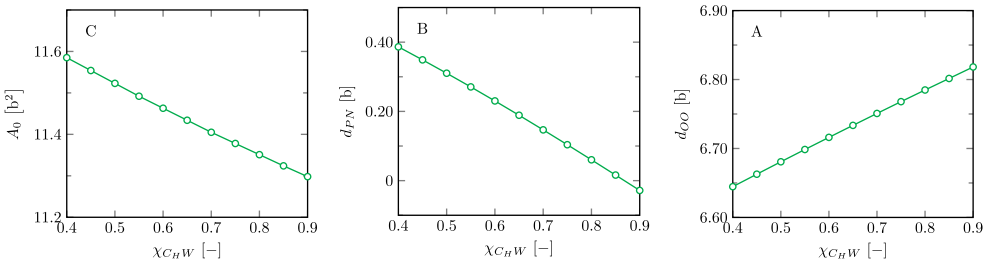

Figure 4.13: Structural analysis of lipid bilayers as a function of hydrophilicity of the headgroups, $\chi_{\mathrm{C_H-W}}$. A) Bilayer core width d_{OO}; B) headgroup orientation d_{PN}; C) area per lipid A_0.

4.5.4 Parameter variation for the head groups

In nature, many different lipid headgroups have evolved. The headgroup is the water-loving part of the lipids. Frequently this water-solubility is enhanced by charged groups. Again, one can vary the headgroup architecture, and several parameters will vary simultaneously. For example, in a phosphatidylethanolamine (PE) headgroup the methyl groups on the nitrogen present in the PC headgroup are replaced by hydrogen atoms, making the headgroup significantly more hydrophilic and less bulky. With respect to charge, headgroups vary from zwitterionic to nonionic or completely ionic. Following the same pattern as for the lipid tails and glycerol backbone, we vary the hydrophilicity of the headgroups by changing the interaction parameter of the carbon monomers with water $\chi_{\mathrm{C_H-W}}$. Variations in headgroup polarity have been explored before [19] albeit using a slightly different strategy, and as we found similar effects here, we will keep this part of the study short.

In figure 4.13 we focus once again on the core thickness, the headgroup orientation, and the area per lipid. In short, with increasing hydrophobicity of the headgroup (increasing $\chi_{\mathrm{C_H-W}}$) tail stretching is enhanced, manifested as a slight increase in d_{OO}. The distance between P and N in the headgroup, d_{PN}, is a strong function of $\chi_{\mathrm{C_H-W}}$ and it turns negative for $\chi_{\mathrm{C_H-W}} > 0.8$, meaning that the choline groups are oriented with respect of the phosphate group towards the core. Even though the core thickness increases, the overall thickness, d_{NN}, decreases because of the changing orientation of the choline group. As also reported by Pera et al. [19], the area per molecule A_0 decreases with increasing d_{OO}, which occurs when the hydrophilicity of the headgroup decreases.

The effects on the mechanical parameters follow the generic rules: κ decreases as the bilayer thickness decreases; $\bar{\kappa}$ increases and J_0^m decreases in line with smaller headgroup areas, see figure 4.14.

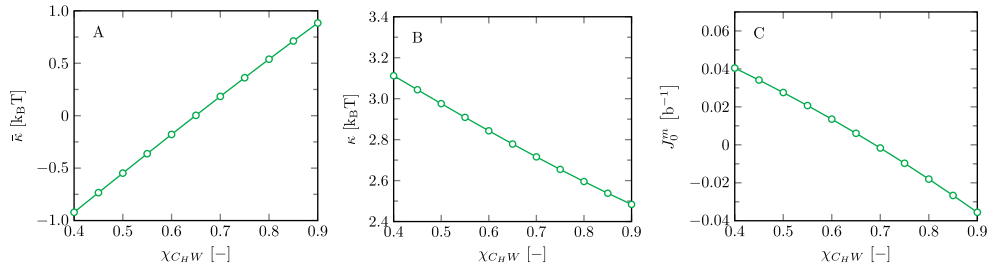

Figure 4.14: Estimation of the bending rigidities $\bar{\kappa}$ (A), κ (B) and J_0^m (C) as a function of hydrophilicity of the headgroups, $\chi_{\mathrm{C_H-W}}$.

4.6 Outlook

The self-assembly of lipids in aqueous solution is of fundamental research interest. One- two- and three-dimensional mesophases can be found depending on the spontaneous curvature of the monolayer and the values of the mean and Gaussian bending rigidity. Transitions between the lamellar phase and, for example, bicontinuous triple periodic phases, such as the primitive (P, Im3m), the diamond (D, Pn3m), and the gyroid (G, Ia3d) cubic phases, are thought to be driven by a transition from negative to positive Gaussian bending rigidity and are usually induced by adding amphiphilic additives. In our modeling study we have explored an unusual route in which the transition from lamellar to, e.g., a bicontinuous cubic phase is inferred by parameter changes in the model. This route not only helps us to identify for our model lipid the proper range of parameters consistent with the lamellar topology, but it also gives insight into the properties that provide other types of lipids, like monogalactosyl diacylglycerol (MGDG) lipids as a main component in the thylakoid membrane, the tendency to assemble in non-bilayer topologies. As it is progressively clear that in nature besides the lamellar topology, which is essential for the barrier function of biomembranes, also bicontinuous phases are relevant [57–59], there is an urgent need to know more about the phase behavior of lipids in the biological context.

Self-assembly of lipid molecules in bilayer membranes is a complex phenomenon, which we have shown can be captured by SF-SCF models when molecularly detailed models are used. The complex interplay between the various types of interactions and the corresponding conformational changes of the lipids in the tensionless bilayers makes it hard to come up with simple arguments to support the predicted trends for the mechanics of lipid bilayer membranes. This is unfortunate because we are definitely in need of simple guidelines. However, we can count our blessings and be happy that a computationally inexpensive SCF machinery does provide us with interesting dependencies, which appear

consistent with experimentally known phase behavior of lipids in general. We know that the current approach is still very approximate and therefore it is not yet the time to bring theory and experiments one-to-one together. For this, further improvements on the lattice-refined SCF theory is required, including an optimization (tuning) of the parameter set to correlate the mechanical parameters better to experimental data. Nevertheless, we consider the trends that we have investigated to be stepping stones for membrane understanding.

We have varied the polarity of the lipid molecules in various ways. We changed the hydrophobicity of the tails, we varied the polarity in the glycerol backbone, and made polarity changes in the headgroup region. The default lipid, resembling DOPC, and the default parameters were selected so that the lipid bilayer was stable (negative Gaussian bending rigidity and a spontaneous curvature of the monolayer close to zero). We found that when the lipid molecules are made somehow more hydrophobic than our default lipid it is possible to induce a sign switch of either $\bar{\kappa}$ or J_0^m or both. These sign-switches do not necessarily take place at the same set of parameters, because the Gaussian bending rigidity follows from the second moment of the grand potential density profile, while the spontaneous curvature of the monolayer is proportional to the first moment. Experimentally, when the spontaneous curvature of the monolayer becomes sufficiently negative before the saddle splay modulus becomes positive, there is a window for which the inverted hexagonal phase is expected. However, when $\bar{\kappa}$ turns positive while the preferred radius is still positive or close to zero, we expect a bicontinuous cubic topology in a concentrated lipid system.

For all membranes, we have seen that the mean bending modulus is positive and small changes in this parameter were expected to be of little consequence. However, the lower the mean bending modulus is, the more prominent membrane undulations will be. When in a bicontinuous phase the mean bending modulus is large, there will be a natural tendency that a minimal surface develops. For a minimal surface, the mean curvature is zero everywhere and there is no effect of the mean bending modulus. However, when the mean bending modulus is not very large, we can expect phases for which the mean curvature can locally deviate from zero. The smaller this value the larger are the undulations and eventually, a periodic bicontinuous cubic phase will melt in favor of a sponge phase in which long-range order is not present. Above we have seen that it is possible to reduce the mean bending modulus while the Gaussian bending rigidity becomes positive and the spontaneous curvature is close to zero. This happens for example when the lipid tails are branched in the limit that one phospholipid has effectively four short tails compared to the classical two long ones. Small molecular weight additives are expected to do the same. [60]

Above, we have considered model bilayer membranes composed of just one type of lipid. In the biological context however, membranes are composed of many different types of amphiphilic compounds. It is known that when there are two or more lipids the mean bending modulus can be lower than the computational average of the bending modulus of the two individual bilayers. [19, 61] This is because, in mixtures, the individual lipids can take different average positions in the curved bilayer so that the bending of the bilayer is facilitated. Similar effects may influence the Gaussian bending modulus as well as the spontaneous curvature of the monolayer. In the lattice-refined SCF model, the evaluation of mechanical parameters of mixed bilayer membranes becomes more feasible than in the classical approach and therefore such a study should be high on our scientific agenda.

The lattice-refined SF-SCF theory is far from completely developed. The chain model that is adopted is of the freely-jointed chain type. This implies that the chain is very flexible and the flexibility increases with increasing the lattice refinement b/l value. In the past, extensions of the SF-SCF route were considered in which the chain model was more realistic. For example, the rotational isomeric state (RIS) scheme has been used to model lipids with a higher rigidity along the chain. [31] It is feasible to combine the lattice-refinement approach and the RIS scheme so that the semi-flexibility of the tails can be restored. This more elaborate approach will lead to thicker and more stiff bilayers. In addition, we reckon that a better account of the excluded volume effects is needed for a more realistic description of densely packed lipids. Again in combination with the lattice-refinement technique explored in this paper, we expect that improved excluded volume correlations can be introduced, similarly as in earlier work. [32] Hence, the lattice-refinement approach reopens old and opens new avenues in the modeling of lipid bilayer membranes.

4.7 Conclusions

By implementing a lattice refinement in the SF-SCF approach, we were able to significantly reduce lattice artifacts which in turn enabled us to implement the grand canonical route to predict mechanical parameters such as $\bar{\kappa}$, κ, and J_0^m. An accurate estimation of these parameters can now be established from the evaluation of the tensionless planar bilayer and a corresponding bilayer curved in the spherical geometry (vesicle). This method replaces a previous, computationally more expensive route, which combined cylindrically curved bilayers and spherically curved ones, to estimate the mean bending κ and indirectly the Gaussian bending rigidity. [19] This previous route is formally flawed because it used bilayers for which the lipids were not at the chemical potential equal to that of the planar ground state. We traced the problem to the cylindrical vesicles which invariably

balance bending energy with stretching energy and therefore have a finite tension and cannot exist at the chemical potential equal to that of the planar one. Fortunately, we found that the mean bending modulus of bilayer membranes did not depend much on the membrane tension and this explains why the current predictions for the mechanical parameters of lipid bilayer membranes are in good agreement with the ones found by the previously used route.

In the lattice-refined SCF approach, we are able to numerically accurately predict mean-field values for the mechanical characteristics as well as structural parameters of tensionless bilayers. Unfortunately in this approach, the lipids have rather high chain flexibility which renders the bilayer to be relatively thin and correspondingly has a too low mean bending rigidity. [14, 54] Further extension of the SF-SCF scheme is envisioned to correct for this shortcoming. The rotational isometric state scheme as well as an improved account for the excluded volume effects, which cause densely packed tails to cooperatively align [32], are now high on the to-do list to be incorporated in lattice-refined self-consistent field theory.

The default parameter set used for model DOPC bilayers gives a membrane for which the Gaussian bending rigidity is slightly negative and a slightly positive spontaneous curvature of the monolayer. This is consistent with the observation that for such lipids the bilayer has a lamellar topology. When we deviate from the default parameter set, we can find bilayers for which the lamellar topology no longer is stable. More specifically, an increase in hydrophobicity, by increasing either the repulsion between the hydrocarbon segments of the tails with water, or the hydrophobicity of the glycerol backbone or that of the headgroup, leads to a sign-switch of both the Gaussian bending modulus and the spontaneous curvature of the monolayer. For such a system we may expect, for example, a bicontinuous cubic phase, or an inverted hexagonal phase. These types of computations help us to understand the relation between the composition, topology, and function of lipid membranes in the biological context and how lipid phase behavior may be modified, e.g. by using lipids with different hydrophobic/hydrophilic balances or by using additives.

4.8 Supplementary Information

4.8.1 Grandpotential density variations

In this section, we provide a quick overview of the changes found in the grand potential density (GPD) profiles upon a select few parameter variations. Find below in figure 4.15 the GPD profiles of our model lipid bilayer with various variations in χ_{C-W} parameters.

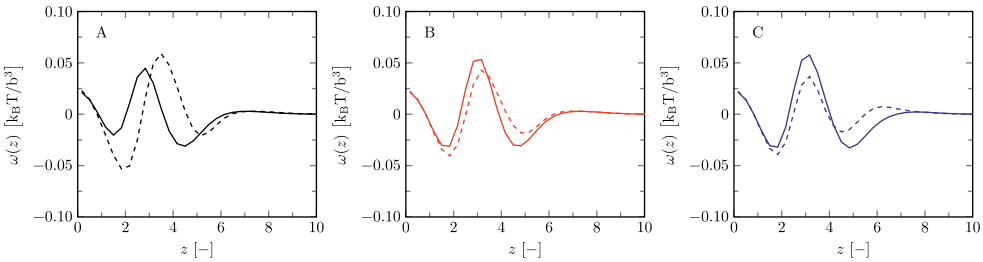

Figure 4.15: Grandpotential density profiles for lipid bilayers with variations in χ_{C_W-T} (A), in χ_{C_G-W} (B) and in χ_{C_H-W} (C). Solid black line: $\chi_{C_T-W} = 1.0$; Dashed black line: $\chi_{C_T-W} = 1.5$; Solid red line: $\chi_{C_G-W} = 1.0$; Dashed red line: $\chi_{C_G-W} = 1.5$; Solid blue line: $\chi_{C_H-W} = 0.4$; Dashed blue line: $\chi_{C_H-W} = 0.9$;

While discussing these results, we will be speaking in terms of various regions of this GPD profile, i.e. regions 1 to 5, which have been defined in the main article. We will first discuss the general GPD profile changes after which we will shortly discuss the consequences for the mechanical parameters $\bar{\kappa}$ and J_0^m.

As can be seen in figure 4.15, the effect of χ_{C-W} is quite substantial, whether the interaction parameter change occurs in the tails, glycerol backbone, or in the headgroup. In the figure, the solid line represents a more hydrophilic tail, glycerol, or headgroup compared with the dashed line. The negative regions (regions 2 and 4) represent a stopping force for self-assembly, and positive regions (regions 1, 3, and 5) represent a driving force. A discussion on each region is given in the main text. As we are looking at a tensionless bilayer, the driving forces and stopping forces are equally balanced, but we observe a change in the ratio of the two stopping forces when varying the χ parameters. For all cases, we observe a decrease in region 2 and an increase in region 4. This suggests that tail stretching (region 2) becomes a more important stopping force compared to the headgroup overlap (region 4) as the lipid becomes more hydrophobic. The main driving force occurs in region 3 (the large positive peak), and it represents the hydrophobic-hydrophilic interface. The height of this peak is effectively dependent on how strong the repulsion of the hydrophobic and hydrophilic region is. The stronger the repulsion, the larger the peak. When increasing χ_{C_T-W}, we observe an increase in region 3, see figure 4.15A, while increasing χ_{C_G-W} and χ_{C_H-W}, a decrease in region 3 is observed, see figure 4.15B and C. In short, more hydrophobic tails increase the repulsion of the hydrophilic-hydrophobic interface, whereas an increased hydrophobicity of the glycerol backbone or the headgroup, which are generally more hydrophilic in nature, decreases this repulsion.

Some individual effects are also visible and worth mentioning. For the case of varying χ_{C_T-W} (figure 4.15A), in addition to the changes in $\omega(z)$, we observe a shift to higher z as

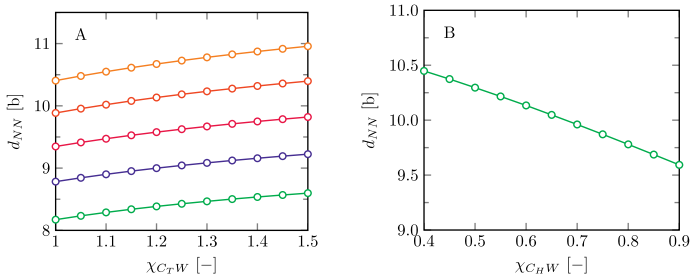

Figure 4.16: d_{NN} as a function of χ_{C_T-W} (A) and χ_{C_H-W} (B). For (A) we display the results for various tail lengths: Green: $l_t = 12$ C segments, blue: 14 segments, purple: 16 segments, red: 18 segments, orange: 20 segments.

well. This is consistent with a significant increase in the bilayer core width (d_{OO}) due to tail stretching, see main figure 5A. A different effect is seen when changing χ_{C_H-W} (figure 4.15C) where we find a significant positive peak in region 5. For these circumstances, we expect that the bilayers are mutually attractive, as is explained in the main article.

Also discussed in the main article is that an increase in hydrophobicity of the lipid, no matter the region, leads to an increase in $\bar{\kappa}$ and a decrease in J_0^m. As these parameters directly follow from the GPD profiles, it seems like the clue to understanding these effects can thus be found in the GPD profile. Changes in $\bar{\kappa}$ and J_0^m occur when ω changes as well, and as $\bar{\kappa}$ scales with z^2 and J_0^m scales with z, increases or decreases to ω at higher z have substantially more effect compared to at lower z. Taking this into account, it thus seems like the change in ratio of the two stopping forces, are the main instigators to the changes in $\bar{\kappa}$ and J_0^m. As a lot of questions remain concerning the GPD profiles and the immense amount of information it contains, we abstain from going into too much detail. A more in-depth study is required.

4.8.2 Bilayer thickness results

The most important structural results are provided in the main article, yet for a few arguments, other structural parameters, such as the bilayer thickness (d_{NN}) are useful. Find results of d_{NN} in figure 4.16. As can be seen from the figure, d_{NN} increases with increasing χ_{C_T-W} or tail length (figure 4.16A), and decreases with increasing χ_{C_H-W} (figure 4.16B). The discussion on these results can be found in the main chapter.

References

[1] S Jonathan Singer and Garth L Nicolson. The fluid mosaic model of the structure of cell membranes. *Science*, 175(4023):720–731, 1972.

[2] Sanjay K Vasu and Douglass J Forbes. Nuclear pores and nuclear assembly. *Current opinion in cell biology*, 13(3):363–375, 2001.

[3] Pierre-Gilles De Gennes and Pierre-Gilles Gennes. *Scaling concepts in polymer physics*. Cornell university press, 1979.

[4] H Pera, JM Kleijn, and FAM Leermakers. On the edge energy of lipid membranes and the thermodynamic stability of pores. *The Journal of chemical physics*, 142(3):01B614_1, 2015.

[5] Wolfgang Helfrich. Elastic properties of lipid bilayers: theory and possible experiments. *Zeitschrift für Naturforschung C*, 28(11-12):693–703, 1973.

[6] Rumiana Dimova. Recent developments in the field of bending rigidity measurements on membranes. *Advances in colloid and interface science*, 208:225–234, 2014.

[7] Julia Genova, Victoria Vitkova, and Isak Bivas. Registration and analysis of the shape fluctuations of nearly spherical lipid vesicles. *Physical Review E*, 88(2):022707, 2013.

[8] Philippe Méléard and Tanja Pott. Overview of a quest for bending elasticity measurement. In *Advances in planar lipid bilayers and liposomes*, volume 17, pages 55–75. Elsevier, 2013.

[9] Andrew F Loftus, Sigrid Noreng, Vivian L Hsieh, and Raghuveer Parthasarathy. Robust measurement of membrane bending moduli using light sheet fluorescence imaging of vesicle fluctuations. *Langmuir*, 29(47):14588–14594, 2013.

[10] C Monzel and K Sengupta. Measuring shape fluctuations in biological membranes. *Journal of Physics D: Applied Physics*, 49(24):243002, 2016.

[11] Jonas Rosager Henriksen and John H Ipsen. Measurement of membrane elasticity by micro-pipette aspiration. *The European Physical Journal E*, 14(2):149–167, 2004.

[12] Volkmar Heinrich and Wiesława Rawicz. Automated, high-resolution micropipet aspiration reveals new insight into the physical properties of fluid membranes. *Langmuir*, 21(5):1962–1971, 2005.

[13] Thomas Portet, Sharona E Gordon, and Sarah L Keller. Increasing membrane tension decreases miscibility temperatures; an experimental demonstration via micropipette aspiration. *Biophysical journal*, 103(8):L35–L37, 2012.

[14] W Rawicz, K Cc Olbrich, T McIntosh, D Needham, and E Evans. Effect of chain length and unsaturation on elasticity of lipid bilayers. *Biophysical journal*, 79(1):328–339, 2000.

[15] Jianjun Pan, Stephanie Tristram-Nagle, Norbert Kučerka, and John F Nagle. Temperature dependence of structure, bending rigidity, and bilayer interactions of dioleoylphosphatidylcholine bilayers. *Biophysical journal*, 94(1):117–124, 2008.

[16] G Pabst, N Kučerka, M-P Nieh, MC Rheinstädter, and J Katsaras. Applications of neutron and x-ray scattering to the study of biologically relevant model membranes. *Chemistry and Physics of Lipids*, 163(6):460–479, 2010.

[17] MMAE Claessens, BF Van Oort, FAM Leermakers, FA Hoekstra, and MA Cohen Stuart. Bending rigidity of mixed phospholipid bilayers and the equilibrium radius of corresponding vesicles. *Physical Review E*, 76(1):011903, 2007.

[18] RA Kik, JM Kleijn, and FAM Leermakers. Bending moduli and spontaneous curvature of the monolayer in a surfactant bilayer. *The Journal of Physical Chemistry B*, 109(30):14251–14256, 2005.

[19] H Pera, JM Kleijn, and FAM Leermakers. Linking lipid architecture to bilayer structure and mechanics using self-consistent field modelling. *The Journal of chemical physics*, 140(6):02B606_1, 2014.

[20] F A M Leermakers. Bending rigidities of surfactant bilayers using self-consistent field theory. *J. Chem. Phys.*, 138(15):04B610, 2013. URL `https://doi.org/10.1063/1.4801327`.

[21] F A M Leermakers. Direct evaluation of the saddle splay modulus of a liquid-liquid interface using the classical mean field lattice model. *The Journal of Chemical Physics*, 138(12):124103, 2013.

[22] Ramanathan Varadharajan and Frans A M Leermakers. Sign switch of gaussian bending modulus for microemulsions: A self-consistent field analysis exploring scale invariant curvature energies. *Physical Review Letters*, 120(2):028003, 2018.

[23] S M Oversteegen and F A M Leermakers. Thermodynamics and mechanics of bilayer membranes. *Phys. Rev. E*, 62(6):8453, 2000. URL `https://journals.aps.org/pre/abstract/10.1103/PhysRevE.62.8453`.

[24] Avinoam Ben-Shaul and William M Gelbart. Statistical thermodynamics of amphiphile self-assembly: structure and phase transitions in micellar solutions. In *Micelles, Membranes, Microemulsions, and Monolayers*, pages 1–104. Springer, 1994.

[25] D. Romeis, Merlitz H., and J.-U. Sommer. A new numerical approach to dense polymer brushes and surface instabilities. *J. Chem. Phys.*, 136:044903, 2012.

[26] Gerard Fleer, M A Cohen Stuart, J M H M Scheutjens, T Cosgrove, and B Vincent. *Polymers at interfaces*. Springer Science & Business Media, 1993. URL `http://www.springer.com/gp/book/9780412581601`.

[27] Sam F Edwards. The statistical mechanics of polymers with excluded volume. *Proceedings of the Physical Society*, 85(4):613, 1965.

[28] A Egorov, D. Romeis, and J.-U. Sommer. Surface instabilities of minority chains in dense polymer brushes: A comparison of density functional theory and quasi-off-lattice self-consistent field theory. *J. Chem. Phys.*, 137:064907, 2012.

[29] Lucas A. Meijer, Frans A. M. Leermakers, and Johannes Lyklema. Modeling the interactions between phospholipid bilayer membranes with and without additives. *J. Phys. Chem.*, 99(47):17282–17293, 1995. doi: 10.1021/j100047a037. URL `http://dx.doi.org/10.1021/j100047a037`.

[30] O. A. Evers, J. M. H. M. Scheutjens, and G. J. Fleer. Statistical thermodynamics of block copolymer adsorption. 1. formulation of the model and results for the adsorbed layer structure. *Macromolecules*, 23(25):5221–5233, 1990.

[31] FAM Leermakers and JMHM Scheutjens. Statistical thermodynamics of association colloids. i. lipid bilayer membranes. *The Journal of chemical physics*, 89(5):3264–3274, 1988.

[32] FAM Leermakers and JMHM Scheutjens. Statistical thermodynamics of association colloids. iii. the gel to liquid phase transition of lipid bilayer membranes. *The Journal of chemical physics*, 89(11): 6912–6924, 1988.

[33] F A M Leermakers and J M H M Scheutjens. Statistical thermodynamics of association colloids. 2. lipid vesicles. *J. Phys. Chem.*, 93:7417–7426, 1989.

[34] Richard A Kik, Frans A M Leermakers, and J Mieke Kleijn. Molecular modeling of proteinlike inclusions in lipid bilayers: Lipid-mediated interactions. *Phys. Rev. E*, 81(2):021915, 2010. URL `https://journals.aps.org/pre/abstract/10.1103/PhysRevE.81.021915`.

[35] F A M Leermakers, A L Rabinovich, and N K Balabaev. Self-consistent-field modeling of hydrated unsaturated lipid bilayers in the liquid-crystal phase and comparison to molecular dynamics simulations. *Physical Review E*, 67(1):011910, 2003.

[36] K Gawrisch, D Ruston, J Zimmerberg, V A Parsegian, R P Rand, and N Fuller. Membrane dipole potentials, hydration forces, and the ordering of water at membrane surfaces. *Biophysical journal*, 61(5):1213–1223, 1992.

[37] Joachim Seelig, Peter M MacDonald, and Peter G Scherer. Phospholipid head groups as sensors of electric charge in membranes. *Biochemistry*, 26(24):7535–7541, 1987.

[38] Leonor Saiz and Michael L Klein. Electrostatic interactions in a neutral model phospholipid bilayer by molecular dynamics simulations. *The Journal of chemical physics*, 116(7):3052–3057, 2002.

[39] Perttu S Niemelä, Marja T Hyvönen, and Ilpo Vattulainen. Influence of chain length and unsaturation on sphingomyelin bilayers. *Biophysical journal*, 90(3):851–863, 2006.

[40] Jacob N Israelachvili, D John Mitchell, and Barry W Ninham. Theory of self-assembly of hydrocarbon amphiphiles into micelles and bilayers. *Journal of the Chemical Society, Faraday Transactions 2: Molecular and Chemical Physics*, 72:1525–1568, 1976.

[41] J N Israelachvili, S Marčelja, and Roger G Horn. Physical principles of membrane organization. *Quarterly reviews of biophysics*, 13(2):121–200, 1980.

[42] A L Rabinovich, P O Ripatti, N K Balabaev, and F A M Leermakers. Molecular dynamics simulations of hydrated unsaturated lipid bilayers in the liquid-crystal phase and comparison to self-consistent field modeling. *Physical Review E*, 67(1):011909, 2003.

[43] L J Lis, D M McAlister, N Fuller, R P Rand, and V A Parsegian. Interactions between neutral phospholipid bilayer membranes. *Biophysical journal*, 37(3):657, 1982.

[44] Barbara A Lewis and Donald M Engelman. Lipid bilayer thickness varies linearly with acyl chain length in fluid phosphatidylcholine vesicles. *Journal of molecular biology*, 166(2):211–217, 1983.

[45] John F Nagle and Stephanie Tristram-Nagle. Structure of lipid bilayers. *Biochimica et Biophysica Acta (BBA)-Reviews on Biomembranes*, 1469(3):159–195, 2000.

[46] Norbert Kučerka, Stephanie Tristram-Nagle, and John F Nagle. Closer look at structure of fully hydrated fluid phase dppc bilayers. *Biophysical journal*, 90(11):L83–L85, 2006.

[47] Norbert Kučerka, John F Nagle, Jonathan N Sachs, Scott E Feller, Jeremy Pencer, Andrew Jackson, and John Katsaras. Lipid bilayer structure determined by the simultaneous analysis of neutron and x-ray scattering data. *Biophysical journal*, 95(5):2356–2367, 2008.

[48] Marzieh Saeedimasine, Annaclaudia Montanino, Svein Kleiven, and Alessandra Villa. Role of lipid composition on the structural and mechanical features of axonal membranes: a molecular simulation study. *Scientific reports*, 9(1):1–12, 2019.

[49] Leonor Saiz and Michael L Klein. Structural properties of a highly polyunsaturated lipid bilayer from molecular dynamics simulations. *Biophysical journal*, 81(1):204–216, 2001.

[50] See-Wing Chiu, Eric Jakobsson, Shankar Subramaniam, and H Larry Scott. Combined monte carlo and molecular dynamics simulation of fully hydrated dioleyl and palmitoyl-oleyl phosphatidylcholine lipid bilayers. *Biophysical Journal*, 77(5):2462–2469, 1999.

[51] Roger S Armen, Olivia D Uitto, and Scott E Feller. Phospholipid component volumes: determination and application to bilayer structure calculations. *Biophysical journal*, 75(2):734–744, 1998.

[52] ES Boek, JT Padding, Wouter K den Otter, and Willem J Briels. Mechanical properties of surfactant bilayer membranes from atomistic and coarse-grained molecular dynamics simulations. *The Journal of Physical Chemistry B*, 109(42):19851–19858, 2005.

[53] Richard M Venable, Frank LH Brown, and Richard W Pastor. Mechanical properties of lipid bilayers from molecular dynamics simulation. *Chemistry and physics of lipids*, 192:60–74, 2015.

[54] John F Nagle, Michael S Jablin, Stephanie Tristram-Nagle, and Kiyotaka Akabori. What are the true values of the bending modulus of simple lipid bilayers? *Chemistry and physics of lipids*, 185: 3–10, 2015.

[55] N kučerka, M-P Nieh, and J. Katsaras. Fluid phase lipid areas and bilayer thicknesses of commonly used phosphatidylcholines as a function of temperature. *Bioch. Biophys. Acta.*, 1808:2761–2771, 2011.

[56] S Ali, J M Smaby, M M Momsen, H L Brockman, and R E Brown. Acyl chain-length asymmetry alters the interfacial elastic interactions of phosphatidylcholines. *Biophys J.*, 74:338–348, 1998.

[57] M Rappolt. The biological relevant lipid mesophases as "seen" by x-rays in: Leitmannova-liu a, ed. advances in planar lipid bilayers and liposomes, 2006.

[58] A Tamayo Tenorio, EWM De Jong, CV Nikiforidis, RM Boom, and AJ Van Der Goot. Interfacial properties and emulsification performance of thylakoid membrane fragments. *Soft matter*, 13(3): 608–618, 2017.

[59] Ingvar Brentel, Eva Selstam, and Göran Lindblom. Phase equilibria of mixtures of plant galactolipids. the formation of a bicontinuous cubic phase. *Biochimica et Biophysica Acta (BBA)-Biomembranes*, 812(3):816–826, 1985.

[60] Leonie van't Hag, Sally L Gras, Charlotte E Conn, and Calum J Drummond. Lyotropic liquid crystal engineering moving beyond binary compositional space–ordered nanostructured amphiphile self-assembly materials by design. *Chemical society reviews*, 46(10):2705–2731, 2017.

[61] MMAE Claessens, BF Van Oort, FAM Leermakers, FA Hoekstra, and MA Cohen Stuart. Charged lipid vesicles: effects of salts on bending rigidity, stability, and size. *Biophysical journal*, 87(6): 3882–3893, 2004.

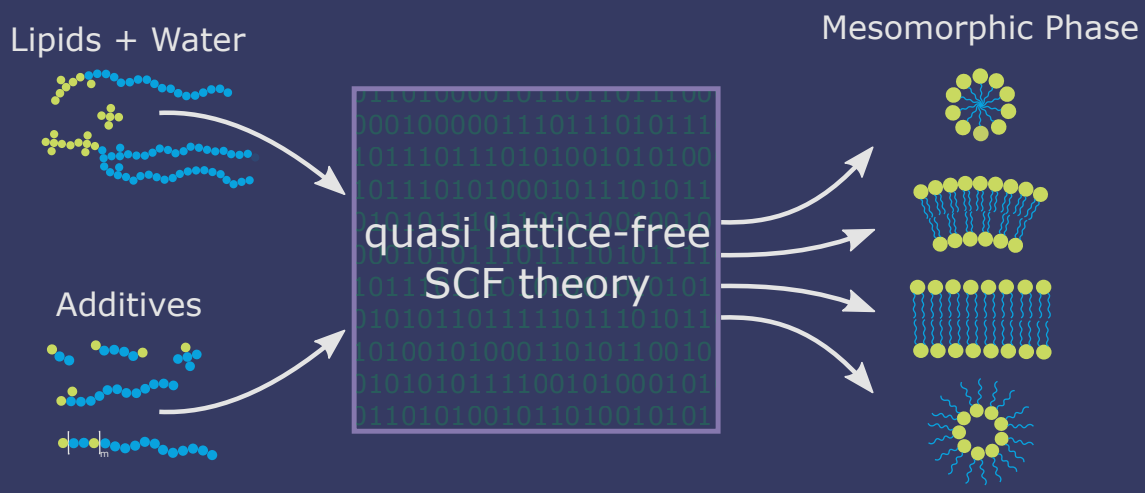
Lipids + Water
Additives
quasi lattice-free
SCF theory
Mesomorphic Phase

CHAPTER 5

Self-consistent field modelling of mesomorphic phase changes of monoolein and phospholipids in response to additives

Mapping the topological phase behaviour of lipids in aqueous solution is time consuming and finding the ideal lipid system for a desired application is often a matter of trial and error. modelling techniques that can accurately predict the mesomorphic phase behaviour of lipid systems are therefore of paramount importance. Here, the self-consistent field theory of Scheutjens and Fleer (SF-SCF) in which a lattice refinement has been implemented, is used to scrutinize how various additives modify the self-assembled phase behaviour of monoolein (MO) and 1,2-dioleoyl-phosphatidylcholine (DOPC) lipids in water. The mesomorphic behaviour is inferred from trends in the mechanical properties of equilibrium lipid bilayers with increasing additive content. More specifically, we focus on the Helfrich parameters, that is, the mean and Gaussian bending rigidities (κ and $\bar{\kappa}$, respectively) supplemented with the spontaneous curvature of the monolayer (J_0^m). We use previously established interaction parameters that position the unperturbed DOPC system in the lamellar L_α phase ($\bar{\kappa} < 0$, $\kappa > 0$ and $J_0^m \approx 0$). Similar interaction parameters position the MO system firmly in a bicontinuous cubic phase ($\bar{\kappa} > 0$). In line with experimental data, a mixture of MO and DOPC tends to be in one of these two phases, depending on the mixing ratio. Moreover we find good correlations between predicted trends and experimental data concerning the phase changes of MO in response to a wide range of additives. These correlations give credibility to the use of SF-SCF modelling as a valuable tool to quickly explore the mesomorphic phase space of (phospho)lipid bilayer systems including additives.

Chapter 5 has been submitted to *Physical Chemistry Chemical Physics*.

5.1 Introduction

The self-assembly of lipids in aqueous solutions yields a wide variety of structures of various shapes and morphologies. Relatively polar lipids can, for example, self-assemble into structures with a positive interfacial curvature, like spherical and cylindrical micelles. Phospholipids with their two hydrophobic tails typically form bilayers. Although this is not often emphasised, such bilayers can reside in various topological states. These may be lamellar, like the L_α phase, which dispersed in solution forms vesicles, or with saddle-shaped curvatures such as the L_3 sponge phase, or cubic phases (Q_{II}) such as the primitive (P, $Im3m$), diamond (D, $Pn3m$) and gyroid (G, $Ia3d$) cubic phases. Lastly, very apolar lipids may exhibit large negative interfacial curvatures and form an inverted hexagonal phase (H_{II}) or even inverted micelles. An overview of all types of lipid phases is readily available in literature [1, 2].

The intriguing phenomenon of lipid self-assembly and the richness in resulting structures has garnered a lot of interest from academic researchers and companies alike, as the applications are vast. Lipid vesicles can be applied as drug delivery systems and bioreactors [3–6], whereas cubic mesophases can be used in other applications, such as biosensors and biofuel cells [7–9]. Many different phases can also be found in nature. While the outer membrane of the cell and of various organelles exists in lamellar form for obvious reasons, the endoplasmic reticulum and inner membranes of mitochondria have been shown to contain cubic phase-like topologies as well [10]. Additionally, saddle-shaped membranes arise during various cellular processes such as membrane fusion [11] and occur in nuclear pores, the 'holes' in the double membrane of the nuclear envelope [12].

While large protein complexes are associated with the formation of saddle-shaped membranes, for example for the formation of nuclear pores [13], the impact of the mechanical properties of the lipid bilayer itself is often overlooked. After all, if bending the bilayer would cost an excessive amount of energy, the formation of bilayer handles would not occur. It is clear that the packing of lipids within the bilayer affects its mechanical properties, including its resistance to stretching and bending, and that these properties determine what shape the bilayer can adopt. In other words, each mesomorphic state of the bilayer, e.g. lamellar, sponge or cubic, has its own range of mechanical parameter values for which it is the stable configuration. Many questions such as what this range is, and what bilayer composition is required to obtain these specific properties still remain to be answered.

A theoretical model that is able to accurately model a lipid bilayer and predict the corresponding mechanical properties is greatly needed. Recently, we forwarded a quasi lattice-

free Scheutjens-Fleer self-consistent field (SF-SCF) approach, which delivers this information for molecularly detailed models with unprecedented (numerical) accuracy (chapter 4). We applied this so-called lattice-refined method to model a phospholipid bilayer containing DOPC (dioleoyl phosphatidylcholine) in an aqueous solution and investigated the effects of several model parameter variations on the mechanical properties of the bilayer. We used the predicted trends to parametrize DOPC. The default parameter set that resulted from this study positions the DOPC bilayer to be, in accordance to experimental data, in a stable lamellar phase.

While the SF-SCF method is able to predict the mechanical properties of lipid bilayers, the theory continues to be under construction to better deliver on this promise and any validation of its predictions is welcomed to guide the development process. Therefore, predictions should be compared with experimental measurements.

In the current paper we follow how the mechanical parameters of model bilayers respond to the addition of a series of additives. In addition to DOPC, we model bilayers formed by the lipid monoolein (MO)because the response of the MO system to many additives is well documented in a recent review on this topic. [14] Thus, we can correlate the obtained trends for the mechanical parameters directly to experimentally observed mesoscopic phase behaviour. The main idea behind this approach is not to just verify the obtained trends but to show that from these trends one can consistently predict the mesomorphic phase behaviour of lipids in response to different types of additives.

The self-assembly of MO is very different from that of DOPC. MO is one of the few lipids that readily forms Q_{II} mesophase bilayers, which makes this an ideal lipid in applications that utilize bicontinuous cubic phases such as membrane protein crystallization. [15, 16] In combination with additives, MO has shown a high versatility in the self-assembled topologies it can form [14]. Addition of DOPC to MO, for example, causes the Q_{II} phase to swell after which it transitions into a lamellar bilayer phase [17]. Apart from this lipid mixture, we have chosen to model both lipids in combination with a selection of additives. Criterion for this selection was that we could (as a first approximation) make use of the same parameter set so that no new uncalibrated parameters were needed. Fortunately we can do so and obtain additives that can direct the model systems (DOPC and MO) into different directions in phase space as we will see below. We have used models for additives aiming to represent ethanol, butanediol and *t*-butanol, three fatty acids (FA) with a C_8, C_{12} and C_{16} tail, respectively, and a surfactant with a C_{12} tail and a polyethylene oxide headgroup ($C_{12}E_m$ with $m = 4$, 5 or 10).

In this paper we will first review the membrane elasticity theory that links mechanical parameters to the corresponding topological state. This is followed by an introduction of

the basic principles of the lattice-refined SF-SCF theory. For a detailed overview of the lattice-refined SF-SCF theory, we refer to our previous work. In the methods section, we sketch the routes used to determine the bending properties and structural properties of the bilayer and present the input specifications used in this work. These include the molecular architecture of the molecules and the default parameter set. In the results section we will first show a systematic survey into the effects of parameter variation for MO and the various additives to validate the chosen default parameters, as done previously for DOPC in chapter 4. Next, we will present results of the mechanical parameters of DOPC/MO mixed lipid bilayers, and of both DOPC and MO bilayers in combination with various additives. We will show how the results for MO correlate with the known phase behaviour of these lipids and subsequently discuss in turn how MO and the other additives influence the phase behaviour of DOPC. At the end of this article we discuss the direction future work may take us.

5.2 Linking mechanical parameters of bilayers to the corresponding topological state

The notion that mechanical parameters govern the physics of tensionless interfaces, such as membranes, stems from the work of Helfrich [18]. He introduced the now famous Helfrich equation which expands the interfacial tension γ (grand potential per unit area) of a membrane as a function of the mean curvature $J = \frac{1}{R_1} + \frac{1}{R_2}$ and Gaussian curvature $K = \frac{1}{R_1 R_2}$ in a grand canonical ensemble. Here, R_1 and R_2 are the two principal curvatures that characterize the shape of the membrane.

$$\begin{aligned} \gamma(J,K) &= \gamma(0,0) + \frac{\partial\gamma}{\partial J}J + \frac{1}{2}\frac{\partial^2\gamma}{\partial J^2}J^2 + \frac{\partial\gamma}{\partial K}K \\ &= \frac{1}{2}\kappa J^2 + \bar{\kappa}K \end{aligned} \tag{5.1}$$

In the absence of curvature ($J = 0$ and $K = 0$), the tension of a freely dispersed bilayer vanishes: $\gamma(0,0) = 0$. The term $\partial\gamma/\partial J$ defines the spontaneous curvature of the interface (J_0) which for symmetry reasons is zero as well. Note that when the analysis is restricted to an individual monolayer, the spontaneous curvature of this monolayer (J_0^m) does not have to be zero. Next to the preferential curvature, the Helfrich equation introduces important mechanical parameters such as the mean bending modulus ($\kappa \equiv \partial^2\gamma/\partial J^2$) and the Gaussian bending modulus ($\bar{\kappa} \equiv \partial\gamma/\partial K$).

Of the introduced mechanical parameters, the spontaneous curvature of the monolayer and the Gaussian bending rigidity are of particular interest, as these control the topological

(in)stability of the bilayer (chapter 4). For lipids to form bilayers, the value of J_0^m, should be close to 0, i.e. indicating that the single leaflet of lipids does not have a strong preferred curvature. As such the interpretation of J_0^m conveniently follows the ideas behind the well-known (phenomenological) critical packing parameter $P = v/la_0$ (with v the tail's volume per molecule, a_0 the area of the lipid molecule at the core-corona interface and l the (average) length of the lipid tails) [19]. Clearly, $J_0^m = 0$ correlates with a packing parameter $P = 1$. In the limit where $J_0^m \approx 0$, i.e. with the bilayer as the favourable state, $\bar{\kappa}$ governs the topology of the bilayers. More specifically, the phase transition between bilayers without saddle-shaped curvatures (vesicles, planar bilayers) to bilayers with saddle-shaped curvatures (sponge phases and cubic phases) are linked to the sign-switch of $\bar{\kappa}$ from negative to positive values [20, 21].

The mean bending modulus κ determines the membrane persistence length l_m of the bilayer, which for example controls the size of thermodynamic stable vesicles or the inter-bilayer undulation repulsion, but has little to do with the topological state of the bilayer. Its value is necessarily positive, because negative values for this quantity would imply that the planar bilayer is at a maximum of the interfacial free energy.

As mentioned, using SCF theory it is possible to numerically accurately predict the mechanical properties of lipid bilayers, however for a correct parameterisation of the system, predictions should be compared and verified with existing experimental data. Unfortunately, while numerous experimental methods exist to determine κ [22–31], experimental methods to estimate $\bar{\kappa}$ or J_0^m are scarce. A quantitative indication of $\bar{\kappa}$ can only be obtained by carefully investigating membrane processes that involve topology changes, such as membrane fusion or fission [32]. As such, only a handful experimental results [11, 33, 34] are known to us and their accuracy is (debatable) uncertain, also because of a lack of molecularly detailed theoretical guidance. To date the only reliable experimental feedback to substantiate model predictions is the established topological phase behaviour of these lipids. The relation between theoretical predictions of mechanical properties of bilayers and their experimental phase behaviour is however only qualitative and consequently rather coarse.

5.3 Basic principles of lattice-refined SF-SCF theory

Computer simulations are the tool per excellence to find structural information on molecularly complex assemblies such as the lipid bilayer membrane. All we want to know on the nanometre length scale and the nanosecond time scale can be obtained from molecu-

lar dynamics (MD) simulations. However, to unravel lipid phase behaviour requires very long simulation times and extremely large system sizes and to date it seems not possible to execute a systematic MD study in this direction. As usual in such situations one turns to approximate modelling methods. Invariably these routes make use of mean-field approximations. This precisely is the case for the method used in this paper, which is an extension of the self-consistent field theory of Scheutjens and Fleer. [35, 36] The key point of the mean-field route is that it is 'free-energy' based and as such it is delivering both structural and thermodynamic/mechanical parameters, and it is doing so at a (tiny) fraction of the MD computation time.

The method of Scheutjens and Fleer extends mean-field approaches such as the regular solution and Flory-Huggins theory by allowing for concentration gradients. The molecules in the system are assumed to be composed of strings of equally sized segments. The free energy functional, which is written in terms of volume fraction (density) profiles and corresponding potential profiles for each segment type, is evaluated on a grid of lattice sites. The usually adopted chain model requires that the segments fit on the lattice sites and that neighbouring segments in the molecules occupy neighbouring sites on the lattice. In such a discretised world the account of conformational degrees of freedom for the chain molecules is facilitated. Accounting for fully self-avoiding chains would be ideal, but is computationally (still) extremely expensive. That is why a freely-jointed chain (FJC) model is adopted, which ignores the positional correlations along the chain that are more than two segments apart. The chain backfolding which in this approach is not excluded, is counteracted by an incompressibility constraint. Hence only on average backfolding is forbidden as each lattice site is on average filled exactly once. The 'averaging'-range is implemented in layers of lattice sites.

The classical approach of Scheutjens and Fleer uses one length scale to discretise both the space and the molecules, that is, the segments of the molecules fit exactly on the lattice sites. Such an approach works well as long as the gradients in density are not too sharp. However, for a typical oil-water interface the interfacial width is comparable to the size of a water molecule and such coarse approach leads to so-called lattice artifacts. To alleviate these we recently implemented a lattice refinement (chapter 4), making the grid (lattice) size l smaller than the segment size b. The lattice-refinement value b/l takes integer values larger than 1. Typically the segment size is the unit length in the calculations and thus the lattice sites are half or a third, etc of the size of a segment. The FJC model now can position neighbouring segments onto a larger set of nearby lattice sites and this leads of course to a model wherein the chains have a somewhat higher conformational entropy compared to the classical SF-SCF model.

Within the FJC model, even in the lattice-refined version, it is rather inexpensive to compute the statistical weight of all possible and allowed conformations of the chain molecules, but it requires the knowledge of so-called segment potentials $u_X(\mathbf{r})$ (where X is a segment type). Through these potentials the segments 'feel' each other: they represent the work per segment required to bring a segment X from the bulk to the coordinate $\mathbf{r}$. Interactions in these potentials are parameterized by Flory-Huggins interaction parameters and contacts are evaluated using the Bragg-Williams mean-field approximation. [37] The segment potentials serve as Boltzmann-like statistical weights $G_X(\mathbf{r})$. For a given conformation c we can add up all corresponding segment potentials and evaluate the statistical weight G_c. The sum of the statistical weights over all conformations are collected in so-called single molecule partition functions q_i (i refers to a molecule type). This seemingly complex procedure is for the FJC model straightforwardly implemented in the propagator formalism. [38] Knowing all statistical weights also allows the evaluation of relevant volume fraction profiles.

It turns out that one can compute the segment potentials only once the segment volume fractions are available. Hence, the segment potentials and the segment volume fractions mutually depend on each other. Fortunately this problem can be solved routinely using a numerical iteration scheme. The result of such a solution is referred to as the self-consistent field (SCF) result. The SCF solution is characterized by volume fraction profiles that both determine the potentials and follow from these and vice versa for the potentials. [39]

5.4 Methods

5.4.1 Data analysis

The calculation of both mechanical and structural parameters that characterise the bilayers is performed in the same way as in chapter 4. In short, the lattice-refined SF-SCF machinery provides various types of outputs. First of all there are the volume fraction profiles per molecule type $\varphi_i(\mathbf{r})$ as well as per segment type $\varphi_X(\mathbf{r})$. Based on these volume fraction profiles, various structural properties can be calculated. Next to the volume fraction profiles, we can evaluate the mean-field free energy F, which can be expressed in terms of the set of volume fraction and segment potential profiles. Moreover, we can extract the so-called grand potential $\Omega = F - \sum_i \mu_i n_i$, where μ_i is the chemical potential of component i and n_i is the number of molecules of type i in the system. Further, the

grand potential can be written as a sum (integral) over the grand potential densities

$$\Omega = \sum_{\mathbf{r}} \omega(\mathbf{r}) \tag{5.2}$$

The grand potential density can be evaluated explicitly when the segment potentials and volume fractions are available. The numerical accuracy of all these quantities is sufficiently high, at least eight significant digits for the underlying profiles.

Mechanical parameters

The interfacial tension as well as some Helfrich parameters can be extracted from the grand potential density profiles: [40, 41]

$$\gamma = \int_{-\infty}^{\infty} \omega_0(z)\mathrm{d}z \tag{5.3}$$

$$-\kappa_m J_0^m = \int_{0}^{\infty} z\omega_0(z)\mathrm{d}z \tag{5.4}$$

$$\bar{\kappa} = \int_{-\infty}^{\infty} z^2\omega_0(z)\mathrm{d}z \tag{5.5}$$

where $z = 0$ is positioned at the symmetry-plane of the bilayer. The sub-index '0' refers to the planar (ground) state of the bilayer.

Eqn 5.3 shows that the membrane tension follows from the zeroth moment over the (planar) grand potential density profile. In the SCF machinery the number of lipids per unit area will always be adjusted such that $\gamma = 0$ to a good approximation. Obviously, in order for the tension to vanish the grand potential density profile must have locally positive and negative contributions. Typically, negative contributions are connected to 'stopping' forces for membrane formation (chain stretching in the tail region and headgroup repulsion in the corona). The most important positive contribution, i.e. the main driving force for membrane self-assembly, is due to the 'tension' along the core-corona interface where the hydrophobic tails come in contact with the solvent. For phospholipid bilayers, this occurs in the region of the glycerol backbone of the lipid.

Eqn 5.4 encompasses the first moment over the grand potential density profile. The integral starts at the symmetry plane of the bilayer $z = 0$ and extends over just one of the leaflets and provides insight in the spontaneous curvature of the monolayer provided that the mean bending modulus $\kappa = 2\kappa_m$ is known. Eqn 5.5 shows that the Gaussian bending rigidity is found by the second moment over the full grand potential density profile of the planar interface. When comparing eqns 5.4 and 5.5, the negative sign in eqn 5.4 and

the fact that $\kappa > 0$ indicates that J_0^m tends to become negative when $\bar{\kappa}$ tends to become positive and vice versa. However, because of the different weighting (first moment vs second moment) a sign switch of $\bar{\kappa}$ and J_0^m is not completely synchronized.

As is clear from eqn 5.4, the grand potential density profile does not give a direct evaluation of κ or J_0^m. As such, we invariably have to involve the use of different geometries in order to compute these values. An important prerequisite for the comparison between different geometries is that the chemical potential of the components, i.e. lipids, water (and possible additives), are equal to that of the (tensionless) planar bilayer. In other words, comparing mechanical parameters within different geometries can only be done in the grand canonical ensemble. We can do so by evaluating the spherical vesicle. Here, the overall curvature energy of a spherical vesicle (Ω_v) can be written as a function of κ and $\bar{\kappa}$ using the Helfrich equation (eqn 5.1):

$$\Omega_v = \int_A \gamma(J,K) = 4\pi R^2 \gamma(J,K) = 4\pi(2\kappa + \bar{\kappa}) \tag{5.6}$$

The equation shows that Ω_v does not depend on the vesicle radius R. This feature is known as 'scale invariance' and implies that the chemical potential of the lipids does not depend on the size of the vesicle. Hence the lipids must have the same chemical potential as those in an infinitely large vesicle, equivalent to the planar bilayer. Knowing this, we may use the value for $\bar{\kappa}$ as found by eqn 5.5 to extract the value for κ in eqn 5.6, and subsequently extract J_0^m with eqn 5.4.

In the classical approach, that is, in the SCF method before the lattice refinement implementation was available, discretisation artifacts prevented the evaluation of the grand potential density profiles for the tensionless planar bilayer. Instead, the only route available made use of the cylindrical geometry, despite the fact that lipids in cylindrical vesicles with a finite radius R do not have the same chemical potential as lipids in the corresponding planar or spherical bilayer. [42, 43]. In retrospect the error that was introduced by using the cylindrical geometry was found to be sufficiently small so that results generated by the method of Pera et al. [42] are indeed trustworthy. Older predictions however systematically overestimated the mean bending modulus and underestimated the Gaussian bending rigidity. [44–46].

Structural parameters

As mentioned, various structural features of the lipid bilayers may be extracted from the volume fraction distributions of each segment as these occur in the tensionless planar bilayer system. More specifically, we can evaluate the average z position (along the axis

perpendicular to the bilayer plane) of all lipid segments types for a single leaflet following a so-called first-moment analysis:

$$\langle z \rangle_X = \frac{\sum_{z>z_0} (z - z_0)(\varphi_X(z) - \varphi_X^b)}{\sum_{z>z_0} \varphi_X(z) - \varphi_X^b} \tag{5.7}$$

where $\langle z \rangle_X$ is the average position of segment type X and $\varphi_X(z)$ is the volume fraction of segment X at position z. Using these averages we can quantify various structural properties such as the bilayer thickness, defined for DOPC as twice the distance of the average position of the choline (nitrogen) group in the headgroup (see figure 5.1) from the center of the bilayer: $d_{NN} = 2\langle z \rangle_N$. We can define the bilayer core thickness in a similar way, using the average position of the O groups in the glycerol backbone: $d_{OO} = 2\langle z \rangle_O$. For an MO bilayer without DOPC, $d_{O_{MO}O_{MO}}$ can be regarded as the bilayer thickness. The headgroup orientation of DOPC in the bilayer can be quantified by the average z distance between the phosphate and choline: $d_{PN} = \langle z \rangle_N - \langle z \rangle_P$. The closer this value is to zero, the flatter the average headgroup orientation. The last structural parameter of interest is the area per lipid molecule A_0, which can be computed by

$$A_0 = \frac{N_{\text{lipid}}}{\theta^\sigma_{\text{lipid}}} \tag{5.8}$$

where $\theta^\sigma_{\text{lipid}} = \sum_{z>z_0} l/b(\varphi_{\text{lipid}}(z) - \varphi^b_{\text{lipid}})$, i.e. the excess amount of segments of the lipid molecule per unit area (per leaflet) of the membrane, and N is the number of segments in the lipid molecule (measure for the molar volume).

5.4.2 Input parameters

The input required for SF-SCF modelling of lipid bilayers includes of course the molecular architectures of the lipids, the additives as well as the solvent(s). Secondly we need to specify all interaction parameters. Thirdly the method requires specification of the lattice geometry. In the lattice-refined version of course also a value for the discretisation b/l is needed.

Molecular architectures

A schematic representation of the various types of molecules that feature in our systems can be found in figure 5.1. This figure shows that all molecules are represented on the united atom level. The united atoms or segments are represented by small filled or patterned circles and all have a segment length b. In this study we use two lipids: dioleoyl

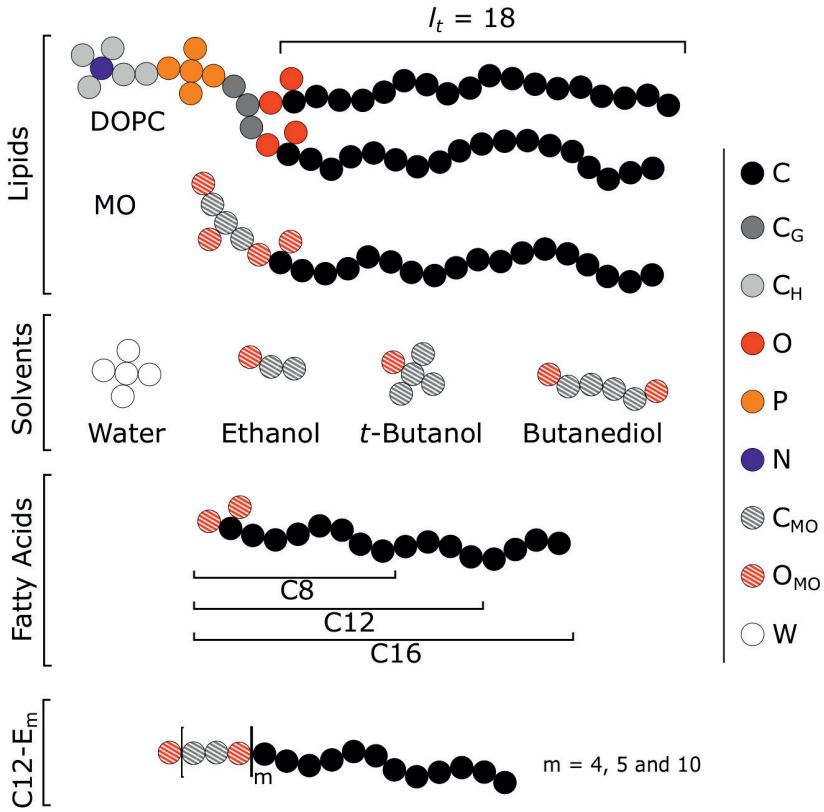

Figure 5.1: Schematic overview of the molecular architectures used in this work. All specified united atoms (segments) have equal volume. We use two lipids: DOPC (without explicit charges) and MO. Both lipids have a hydrophobic tail of 18 carbons ($l_t = 18$). We chose a single segment type for the phosphate group of DOPC and distinguish the carbon atoms surrounding the nitrogen, which are made more hydrophylic than the other carbon atoms. The segments of the glycerol group of MO are distinguished from those of DOPC and are made more hydrophylic. Apart from the two lipids, we use various additives such as solvents (ethanol, *t*-butanol and butanediol), fatty acids and $C_{12}E_m$ surfactants. The main solvent in our system is always water, which in this model (and as in our previous study) consists of five equal monomers arranged in a configuration wherein one W is surrounded by four neighbouring W segments. For the additives we use the same χ values for all O groups, similar to C_{MO}. We differentiate two χ values for the C groups of the additives. One for the tails, similar to C, and one representing the headgroups, comparable to C_{MO}.

phosphatidylcholine (DOPC) and monoolein (MO). The phospholipid DOPC is modelled in the same way as done in our previous work. That is, two fatty acid 'tails' with a tail length $l_t = 18$ carbons, are attached to the sn_1 and sn_2 position of a glycerol backbone. The sn_3 position is attached to a phosphatidyl choline (PC) 'head'. The oxygens of the phosphate group are included in the P-units. We distinguish between the carbon groups of the tails, the glycerol backbone and the headgroup: C_T, C_G and C_H respectively. The monoglyceride MO is modelled as a C18 tail attached to the sn_1 position of a glycerol group. The glycerol carbon and oxygen groups in MO differ from those in DOPC as we expect the glycerol group in MO to be slightly more hydrophilic.

Calculations start with two-component systems where a lipid (by convention $i = 1$) in excess water ($i = 0$) forms a bilayer. Water normally forms an associative hydrogen-bonded network with other water molecules. This effectively prevents water to penetrate the bilayer core, which therefore can be regarded as 'dry'. By modelling water as a small star-shaped cluster of five water segments, we can mimic this feature in first order. In our quest to understand how additives ($i = 2$) modify the bilayer's mechanical characteristics we introduce different molecules in the two-component systems: ethanol, *t*-butanol and butanediol; three fatty acids with different tail length (C_8, C_{12} and C_{16}); and $C_{12}E_m$ surfactants with different amounts of ethylene oxide units ($m = 4$, 5 and 10). Apart from the longer tail carbon groups, we estimate the carbon and oxygen monomers of these additives to be relatively in the same order of hydrophilicity as the glycerol group of MO and have therefore modelled them with the same segments.

Interaction parameters

The Flory-Huggins interaction parameter (χ_{X-Y}) quantifies the interactions between segments X and Y or, when Y equals W, the hydrophobicity/hydrophilicity of segment X. Even though this interaction parameter is well known especially in the polymer community, it remains essential to mention that it is of an Archimedes type: $\chi_{X-Y} = \frac{Z}{k_B T}(2U_{XY} - U_{XX} - U_{YY})$, where Z is the co-called lattice coordinate number. As soon as the average of the 'like'-contacts $(U_{XX} + U_{YY})/2$ is more favourable (more negative) than the unlike contacts U_{XY}, we have a positive χ and this signals the tendency to cluster segments of the same type, leading to phase separation. Of course whether or not this happens depends also on the (mixing) entropy in the system. By definition the Flory-Huggins interaction parameter between similar segments is zero, i.e. $\chi_{X-X} = 0$. The χ between different segments in general may deviate from 0, i.e. have an effective repulsive potential ($\chi_{X-Y} > 0$) or an attractive one ($\chi_{X-Y} < 0$). An overview of the default interaction parameters used in this work can be found in table 5.1.

Table 5.1: Overview of the default interaction parameters $\chi_{X-Y} = \chi_{Y-X}$ used to quantify the solvent quality and the intermolecular interactions. The values in the table are the interaction parameter between the monomers X and Y that are listed to the left and on top.

	W	**O_{MO}**	**C_{MO}**	**C_H**	**N**	**P**	**O**
C/C_G	1.2	2	0	0.5	2	2	2
O	−0.2	0	2	1	0	0	
P	−0.2	0	2	1	−0.5		
N	−0.2	0	2	1			
C_H	0.6	1	0.5				
C_{MO}	1.0	2					
O_{MO}	-0.5						

The hydrophobicity of the lipid tails is represented by a higher interaction parameters of tail segments with water compared to glycerol and headgroup segments.

In chapter 4 the default interaction parameters were chosen such that SCF calculations on the DOPC-water system resulted in a bilayer with structural and mechanical characteristics in agreement with experimental data (e.g. a lamellar topology, and a relative flat headgroup orientation). We use an identical parameter set for DOPC in this paper and for a detailed explanation refer to chapter 4.

One would expect that MO could simply be modelled with the same parameter set as for DOPC, since MO also combines a hydrophobic tail with a 'glycerol'-like headgroup. However, it was found important to tune the parameters in such a way that the physics of the MO bilayer is in accordance with experimental data. A short survey how the mechanical parameters of the MO bilayer depends on some of the interaction parameters is given in the first part of the results section below. More specifically, we have varied the parameters for the glycerol moiety to find out how to provide the MO bilayer with a slightly positive Gaussian bending rigidity. The default parameters that we ended up with differ slightly from the interaction parameters used for DOPC. While the interaction parameter of the tails with water is kept the same ($\chi_{C-W} = 1.2$), the glycerol segments are slightly more hydrophilic ($\chi_{C_{MO}-W} = 1$ and $\chi_{O_{MO}-W} = -0.5$, compared to ($\chi_{C_G-W} = 1.2$ and $\chi_{O-W} = -0.2$ for DOPC. We can rationalize this as the glycerol backbone of MO contains two OH groups, and is therefore able to form hydrogen bonds with water.

All our 'additives' are molecules that combine C with O segments, each with their own specific interaction parameters. However, it is not practical to tune these for each of these additives individually. We thus decided to use the MO-parameterisation for all other additives. Hence long hydrocarbon stretches (e.g. the fatty acids tails) are taken as hydrophobic as the tail of MO (or the tails of DOPC) and the interaction parameters for hydrocarbons near O groups are as for the glycerol moiety of MO. For the oxygen groups of the additives we used the same interaction parameter values as for the glycerol groups

of MO, i.e. $\chi_{C_{MO}-W} = 1$ and $\chi_{O_{MO}-W} = -0.5$.

Lattice specifications and general work flow of the lattice-refined SF-SCF model

As in chapter 4 we have used the hexagonal lattice and used a lattice refinement such that the lattice site was three times smaller than the segment size, that is $b/l = 3$. Within this discretisation setting the numerical noise of many of the quantities that are computed is not resulting from lattice artefacts, but is determined by the accuracy of the self-consistent field solution, which in all cases was at least eight significant digits.

As already mentioned, we can only compute all bending rigidities when using two different geometries, the planar bilayer and a spherical vesicle, for which we use one-gradient planar and spherical coordinate systems, respectively. In the planar coordinate system all quantities are evaluated per unit area. Here the **r**-coordinate as used in eqn 5.2 is implemented as a z-coordinate: $z = 1,\ 2,\ \ldots,\ M_z$ and the number of lattice sites at each coordinate z is independent of z (and can be formally set to unity). On both sides of the system we implement reflecting (mirror-like) boundary conditions. In the simulation volume there is just a single lipid layer near the lower boundary; this layer interacts with its mirror image forming a symmetric bilayer. [47] We choose an appropriate number of molecules per unit area n_i and initiate the iterations by introducing a guess for the bilayer density (or potentials) near the lower boundary. After the SCF solution is found we evaluate the interfacial tension from $\omega(z)$ using eqn 5.3.

In general this tension will not be zero and therefore we choose a new value for the number of (lipid) molecules per unit area n_1 for the membrane constituents and a next loop of the iteration process is performed. The successive adjustment of the number of lipids per unit area continues until the membrane is free of tension (seven or more significant digits can routinely be reached). From this result the grand potential density profile $\omega_0(z)$ is recorded (here the sub index 0 refers to the planar tensionless case). With this result we can evaluate eqns 5.4 and 5.5.

In the spherical geometry case we have a radial coordinate $r = 1,\ 2,\ \cdots,\ M_r$ (in units b) where each layer r has $L(r) \propto r^2$ lattice sites. For a spherically shaped bilayer (vesicle) with a radius R (typically $R = 100b$ is used) we fix the number of lipid molecules to $n_1 = 4\pi R^2 n^0_{\text{lipid}}$, with n^0_{lipid} the number of lipid molecules per unit area in the planar bilayer. After an initial guess for the segment density or potential profile near $r = R$, the SCF iterations are resumed. Importantly, during these iterations the distribution of the additives is normalised using the bulk volume fractions φ^b_2 identical to the ones found in the planar tensionless bilayer calculation. During the calculations the bilayer positions itself optimally in the spherical coordinate system such that for the converged

SCF solution the grand potential $\Omega = \sum_r L(r)\omega(r)$ of the vesicle only contains curvature energy. This means that $\Omega = 4\pi(2\kappa + \bar{\kappa})$. [18, 43] Using this result in combination with eqns 5.4 and 5.5 leads to the mechanical parameters. Importantly, the lipid component ($i = 1$) in the spherical vesicle system has the same bulk volume fraction as in the planar tensionless bilayer case. The same is true for the additive (enforced by the normalisation) and then necessarily the solvent also has a chemical potential that corresponds to the value found for the planar bilayer system (Gibbs-Duhem relation). Hence the vesicle system is exactly in the same thermodynamic state as the tensionless planar bilayer, that is, all components in the two systems have the same chemical potentials, and thus the two systems are in equilibrium.

5.4.3 Limits to the additive-to-lipid ratio

There are limitations to the maximum amount of additives that can be included in the bilayers. In some cases these limitations are set by the system itself. For example, when hydrophobic additives are introduced in the MO bilayers, the system tends to go to inverted phases. It then may become impossible to find the tensionless state of the planar bilayer and this obviously frustrates the protocol to find the mechanical parameters. We therefore have set our own limits in such a way that the concentration of additives in the systems always is below their bulk binodal value. This does not pose major restrictions, because our primary interest is in predicting (initial) trends in how additives push a membrane system towards potential phase changes, rather than to pinpoint a critical composition for such a mesomorphic transition or a concentration at which the membrane falls apart (something which happens for example when large amounts of Triton are used). For surfactant-like additives their critical micelle concentration (CMC) is a threshold that we will not pass. In most cases we estimate the bulk binodal value of the additive from adsorption isotherms, that is the amount of additive that is absorbed in the membrane per unit area θ^σ as a function of its bulk concentration. The maximum amount of additives used does not depart far from the Henri regime, that is the initial linear part of the adsorption isotherm; see the supplementary information (SI) for more information. Important to note is that we do not take into account any lateral phase separation (i.e. lipid rafts) that could occur when working with lipid mixtures. However, as we keep the additive as a minority component in the membrane, we do not expect lateral phase separation to occur.

5.5 Results and Discussion

In the following we will first consider how the mechanical properties of the MO bilayer vary upon (small) changes in the parameters that characterise the way water interacts with the glycerol-like headgroup. This part of the work has been performed to obtain the default parameter set presented above. After this we will present, for illustration purposes, some structural properties of equilibrium DOPC and MO bilayers and a DOPC/MO mixed bilayer as these follow from using the default parameter setting. In the second part of the results section we will elaborate on how a mixed bilayer composed of DOPC and MO has some intermediate values for its mechanical parameters $\bar{\kappa}$, κ and J_0^m). In the third and final topic of the results section we will show how DOPC and MO bilayers respond to additives. Furthermore, we correlate the results of MO with published experimental phase behaviour, and discuss the biological relevance of the response of similar additives on DOPC bilayers.

5.5.1 Parametric study for MO bilayers

Our first priority was to properly model MO bilayers and find a suitable parameter set in line with its mesomorphic phase behaviour. Variation of the interaction parameters for the glycerol headgroup causes significant changes in both structural and mechanical parameters of MO bilayers, see figure 5.2. Figures 5.2A and B show a decrease in bilayer (core) thickness ($d_{O_{MO}O_{MO}}$) and an increase in the area per lipid (A_0) with increasing hydrophilicity of the glycerol backbone (i.e. with more negative $\chi_{C_{G-MO}-W}$ and $\chi_{O_{MO}-W}$). Such effects are in line with expectation and it is reassuring to see that the results are sensitive to these parameters.

For the bending rigidities (Figures 5.2C, D and E) we observe a decrease in $\bar{\kappa}$ and increases in κ and J_0^m, respectively with increasing glycerol backbone hydrophilicity. These trends are relatively similar as found when changing the hydrophobicity of the glycerol backbone of DOPC, see chapter 4. For an explanation of these trends we refer to this previous work; here, we focus on obtaining the interaction parameter set for MO that is in accordance experimental data.

As mentioned already it is well known that pure MO bilayers form cubic phases [14]. This topological state limits the window for $\bar{\kappa}$ and J_0^m. To be precise, the value of $\bar{\kappa}$ is expected to be positive, and the value of J_0^m slightly negative, but relatively close to zero as we obtain bilayers rather than (inverted) micelles. The value of κ is relatively insignificant for cubic phases as the mean curvature in these structures is not expected to be large ($\langle J \rangle \approx 0$). Based on this information, we chose $\chi_{C_{G-MO}-W} = 1.0$ and $\chi_{O_{MO}-W} = -0.5$ as

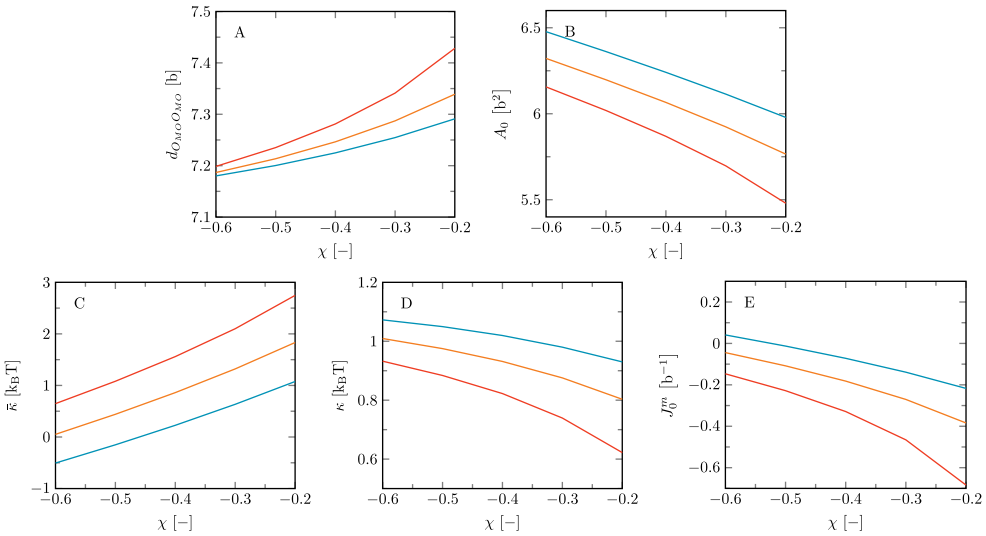

Figure 5.2: Structural and mechanical properties as a function of $\chi_{O_{MO}-W}$ for MO bilayers with different $\chi_{C_{G-MO}-W}$. A) $d_{O_{MO}O_{MO}}$, representing the bilayer core thickness; B) A_0, representing the area per lipid in the bilayer; C) $\bar{\kappa}$; D) κ; E) J_0^m. Red: $\chi_{C_{G-MO}-W} = 1.2$; orange: $\chi_{C_{G_MO}-W} = 1.0$; blue: $\chi_{C_{G-MO}-W} = 0.8$

the interaction parameters for MO, as these values result into bilayers with $\bar{\kappa}$ and J_0^m in the expected range. As in this setting the Gaussian bending rigidity is not extremely far from zero, we may anticipate phase changes towards the lamellar phase in response to additives that induce a more positive preferential curvature of the leaflets of the bilayer.

For the interaction parameters chosen, we find κ to be close to 1 k$_B$T, $d_{O_{MO}O_{MO}} \approx 7.2b$ and $A_0 \approx 6.2b^2$, corresponding to 2.52 nm and 0.76 nm^2 respectively. In our previous study on DOPC bilayers we found that the current model tends to underestimate the value for this latter quantity at least when we may trust corresponding experimental estimates. We expect that κ found for the MO bilayers is also a lower estimate. We argued earlier that the FJC model, which gives the lipid molecule a high flexibility, is partly responsible for this. In addition the mean-field approximation may underestimate the excluded volume correlations between neighbouring lipids in the bilayer and this also may lead to a too soft bilayer. In the same token we expect the membrane thickness of MO-bilayers, here estimated as twice the average position of the O's from the bilayer center $d_{O_{MO}O_{MO}}$, to be an underestimation of the real value and correspondingly the area per lipid may be too high [48, 49]. The underestimation of the mean bending modulus κ is unfortunate. Typically we would like to argue that when the value is of order unity, regularly ordered bicontinuous cubic phases should give way to less ordered L$_3$ phases. We still expect that

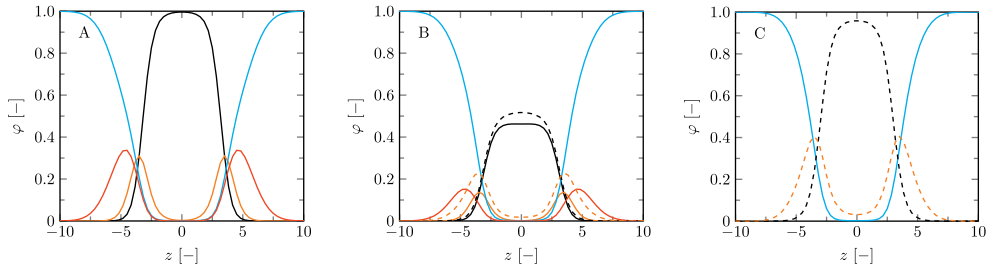

Figure 5.3: Volume fraction profiles for A) a pure DOPC bilayer, B) a mixed DOPC/MO bilayer ($f_{MO} = 0.5$), and C) a pure MO bilayer. Solid blue lines represent water, other solid lines represent DOPC and dashed lines represent MO. Black: lipid tails; orange: glycerol backbone of the lipids; red: lipid headgroups.

when κ is sufficiently small that the L_3 phase is preferred (that is when $\bar{\kappa} > 0$) but that the threshold for such transition in the mean-field 'world' happens at values of κ lower than unity.

5.5.2 Structural and mechanical properties of DOPC and MO bilayers and mixtures thereof

With the parameter set in place a logical next step is to consider bilayers composed of more than one type of lipid. The phase behaviour of MO with added DOPC is well documented [17, 50], which makes this lipid mixture an exciting starting point to verify our method to predict lipid phase behaviour. Here we present the bilayer properties as a function of the fraction MO (f_{MO}). This fraction is calculated as a weight fraction assuming each monomer has equal mass:$f_{MO} = \theta^{\sigma}_{\mathrm{MO}}/(\theta^{\sigma}_{\mathrm{MO}} + \theta^{\sigma}_{\mathrm{DOPC}})$. To provide some insight into the structures formed for pure DOPC, pure MO and a 50/50 wt% lipid mixture, we have plotted the volume fraction profiles in the planar geometry (figure 5.3. The center of the bilayers is set at $z = 0$. As expected the core of these bilayers is dry ($\phi_W = 0$ at $z = 0$); water penetrates only up to the glycerol backbone. An in depth study on the properties of the DOPC bilayer is published in chapter 4 and many of the MO bilayer properties are surprisingly similar. Close inspection reveals that the MO bilayers are a little bit thinner than DOPC ones, which is traced to the fact that DOPC simply has a larger headgroup. The average position of the glycerol backbone is similar in the two membranes and also in the mixed bilayer (figure 5.3B). However, in the MO bilayer the glycerol has a wider distribution than in the DOPC bilayer. We can come up with two reasons for this. Firstly, the glycerol backbone of DOPC is oriented more parallel to the bilayer plane than that of MO, due to the extra tail attached to the sn_2 position of the glycerol. Secondly, since the glycerol backbone of MO is more hydrophilic, we have a more gradual hydrophobic-hydrophilic transition.

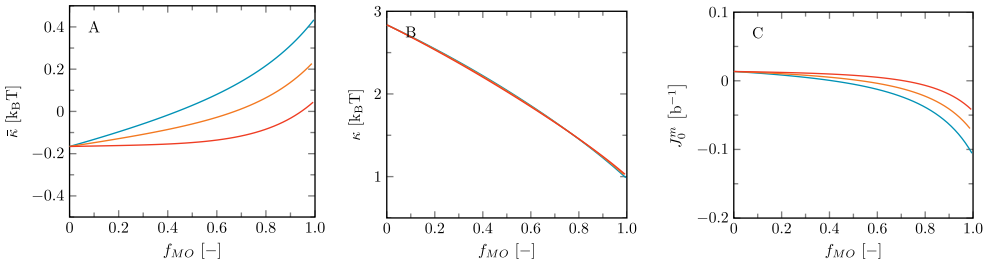

Figure 5.4: Mechanical parameters $\bar{\kappa}$, κ and J_0^m for DOPC bilayers as a function of fraction of MO with different $\chi_{O_{MO}-W}$. Blue: $\chi_{O_{MO}-W} = -0.5$; orange: $\chi_{O_{MO}-W} = -0.55$; red: $\chi_{O_{MO}-W} = -0.6$.

5

The differences in structural properties between the MO and DOPC bilayers are reflected in their different natural topological states. As mentioned before, DOPC bilayers naturally occur in a lamellar topology while MO bilayers occur in cubic phases. The mechanical parameters reflect these states: $\bar{\kappa}$ is negative and J_0^m is very close to zero, even slightly positive, for DOPC, while these parameters are respectively positive and slightly negative for MO bilayers. See also figure 5.4 at $f_{MO} = 0$ (pure DOPC bilayer) and at $f_{MO} = 1$ (pure MO bilayer).

Figure 5.4 reports the mechanical parameters for the mixed DOPC/MO bilayers as a function of the fraction MO. The trends in these parameters can be translated into expected changes in the mesomorphic state of these bilayers with increasing fraction of MO. In particular we foresee a transition from a lamellar phase to a phase with saddle-shape topologies as signalled by the change of sign of $\bar{\kappa}$. For the default χ-parameters chosen, we expect this to occur around 40 wt% ($f_{MO} \approx 0.40$): see the blue line in figure 5.4A. In reality this transition occurs around 50-55wt% [17, 50]. This difference does not alarm us too much as the trend is in line with experimental data. Furthermore, small optimizations in the χ parameters can certainly improve these results as the sign-switch is highly dependent on the χ values chosen. This is showcased by the orange and red curves in figure 5.4, for which the interaction parameters for the MO glycerol moiety were chosen slightly different. In short, when the glycerol moiety of MO is made a bit more hydrophilic, $\bar{\kappa}$ decreases for the pure MO bilayers, and as a consequence, the transition point for which $\bar{\kappa} = 0$ shifts to higher MO fractions in the mixed bilayer.

Next to the increase in $\bar{\kappa}$, we observe a decrease in J_0^m with increasing fraction of MO. This trend seems to agree with the experimentally observed phase transition as well. J_0^m goes from slightly positive values, as expected for lamellar bilayer topologies, to slightly negative values, more expected for cubic phases. Like for $\bar{\kappa}$, the sign-switch of J_0^m occurs at higher MO fractions as the glycerol moiety of MO is made more hydrophilic.

Small changes in the hydrophobicity of the glycerol moiety do not have an effect on κ, which remains above $1k_BT$ for all DOPC/MO ratios. As κ thus remains relatively high, the modelling predicts a direct transition from lamellar to cubic without the L_3 or sponge phase as an intermediate mesophase. This corresponds nicely to experimentally observed phase behaviour [17, 50]. Below we will argue that indirect transitions are expected for the addition of some solvents.

5.5.3 Effect of additives

Here we discuss the effects of adding various substances to pure MO or pure DOPC bilayers. We will not go into much detail regarding the structural parameters of the bilayer, but focus on (trends of) the mechanical parameters and aim to correlate these to known lipid phase behaviour in particular for the MO- but also for the DOPC system.

Addition of solvents

We will start with the addition of alcoholic solvents to the bilayer systems. We have chosen to use ethanol, butanediol and *t*-butanol, as it has been found that these solvents affect the MO phase behaviour in different ways [14], although the differences are especially manifested at high volume fractions. To be specific, the addition of all these solvents initially causes a transition from the MO Q_{II} phase into a sponge phase [51, 52]. At high volume fractions ($> 50\%$(v/v)) butanediol changes the sponge phase into a lamellar liquid crystal phase, while t-butanol dissolves the bilayer in a fluid isotropic phase of inverted micelles. [52]

The effect of these alcohols on the phase behaviour of DOPC bilayers is not documented. However, in several studies short alcoholic solvents have been added to lamellar bilayers [53–56]. In some of these studies a few mechanical properties were measured, such as the mean bending modulus κ, using the micropipette aspiration technique [53, 54]. In general, it was observed that the addition of small alcohols largely lowers κ as the bilayers become much more flexible.

The effects of the alcohols on the mechanical properties of the lipid bilayers according to our SCF predictions are shown in figure 5.5.

Let us first consider the MO system and discuss these results in light of the experimental results described above. In figure 5.5A we find that the Gaussian bending rigidity $\bar{\kappa}$ of the MO system decreases with the addition of ethanol and butanediol, albeit that the changes are modest. The response to *t*-butanol is very weak, so apparently there are competing effects that balance each other in this case. The spontaneous curvature of

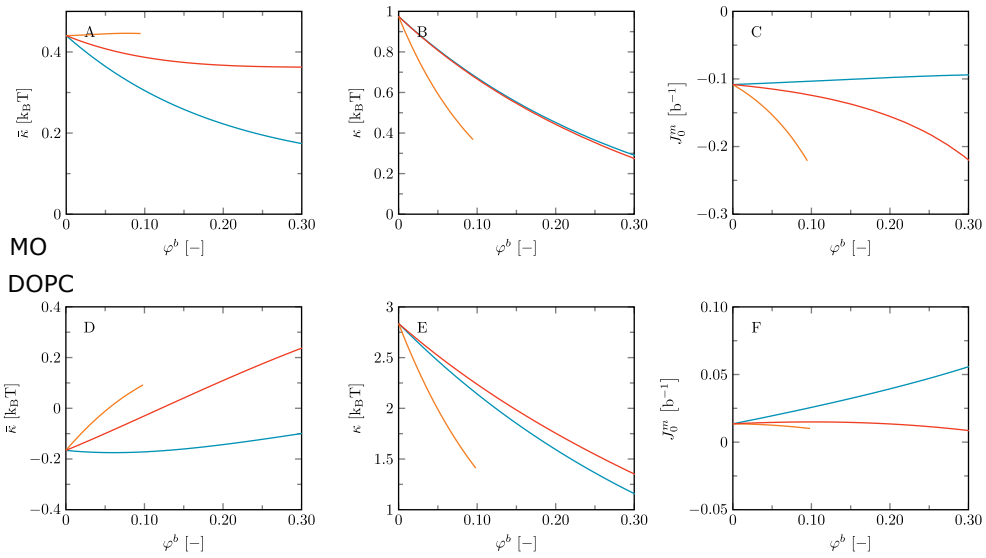

Figure 5.5: Mechanical parameters $\bar{\kappa}$, κ and J_0^m as a function of bulk volume fraction φ^b of added 'solvent' for MO bilayers (top, A-C) and DOPC bilayers (bottom, D-F). Blue: added solvent is ethanol (C_2O); orange: *t*-butanol (*t*-C_4O); red: butanediol (C_4O_2).

the monolayer (figure 5.5C) shows an opposite trend where addition of ethanol gives the smallest effect. The changes in $\bar{\kappa}$ and J_0^m upon addition of small amounts of ethanol, *t*-butanol or butanediol are not sufficient to point to phase changes. However, at high volume fractions of t-butanol inverted phases are likely, since for this case J_0^m is expected to be strongly negative. Figure 5.5B shows that all three solvents tend to make the MO bilayers extremely flexible, since the mean bending modulus drops to sub-unity values rather dramatically. As explained above, this indicates the formation of less ordered phases such as the sponge or L_3 phase. Indeed, as mentioned before this is what has been found experimentally. [51].

The corresponding results for the mechanical parameters for the DOPC bilayer system are presented in figures 5.5D-F. Figure 5.5D shows that upon significant addition of ethanol as well as *t*-butanol and butanediol the Gaussian bending rigidity turns more positive and eventually changes sign. This suggests that this type of additive may destroy the lamellar topology of pure DOPC bilayers. The spontaneous curvature of the monolayer (figure 5.5F) increases both for addition of ethanol and butanediol, but decreases and may become negative for *t*-butanol. As the spontaneous curvature does not become extremely negative we expect that eventually at high volume fractions the alcohols may push DOPC bilayers towards bicontinuous cubic phases rather than the inverted hexagonal phase, although in experimental systems this transition may be hard to reach. Similar to the

MO bilayer, the small alcohols make the DOPC bilayer more flexible (cf figure 5.5E, but typically κ remains larger than unity and therefore transition into the sponge phase is very unlikely. The fact that small alcohols soften phospholipid bilayers has been reported in literature. [53, 54].

Fatty Acids

Experimentally it has been found that addition of fatty acids (FAs) to MO cubic phases induces various phase changes as well, depending on the tail length [57]. The addition of FAs with relatively small tails (C_8) induces transition of MO cubic phases to inverse hexagonal (H_{II}) phases and finally an emulsified microemulsion (EME). Interestingly, the window in which H_{II} phases have been observed is relatively small. Similar behaviour is observed for C_{12} FA, without the formation of an EME phase. The addition of long tail FA (C_{16}) did not show a transition to HII phases. Instead, at high FA to MO molar ratios phase separation occurred into the cubic lipid phase and a separate lamellar crystal phase (L_c) of the FA.

There is much literature on the effect of fatty acids on lamellar (e.g. phospholipid) bilayers, yet on an experimental level almost all data concern long-chain fatty acids like oleic acids [58, 59]. From these, we only found one (very recent) article on fatty acid containing bilayers in the context of phase behaviour. [58] It reported that the long chain fatty acids used, oleic acid (OA) and elaidic acid (EA) , increased the mean bending rigidity of a DOPC bilayer. No topological phase transition was observed. In the few articles we found regarding the addition of medium-chain fatty acids (C6-C14) to lipid bilayers, interest was limited to general features, such as how much FA was incorporated [60] or the effect on flip-flopping and transport across membranes [61–63].

In our model calculations, above some threshold loading of FAs no longer tensionless bilayers could be found, indicating that inverted structures are dominating the phase space. The maximum amount of FA that could be incorporated was in the order of 20 wt% for MO bilayers and 30wt% for DOPC bilayers. To provide a direct comparison for MO and DOPC bilayers we have chosen to show results up to 20 wt% FA ($f_{FA} = 0.2$).

The effects of FA addition on the bending rigidities are shown in figure 5.6. From the figure we immediately observe that the effects of incorporating FA in MO bilayers or in DOPC bilayers are very similar. In general, we see $\bar{\kappa}$ increasing and both J_0^m and κ decreasing with addition of FA. The longer the tail of the FA, the more hydrophobic the FA is: this results into a stronger effect on $\bar{\kappa}$ and J_0^m, but a weaker change in the mean bending modulus κ.

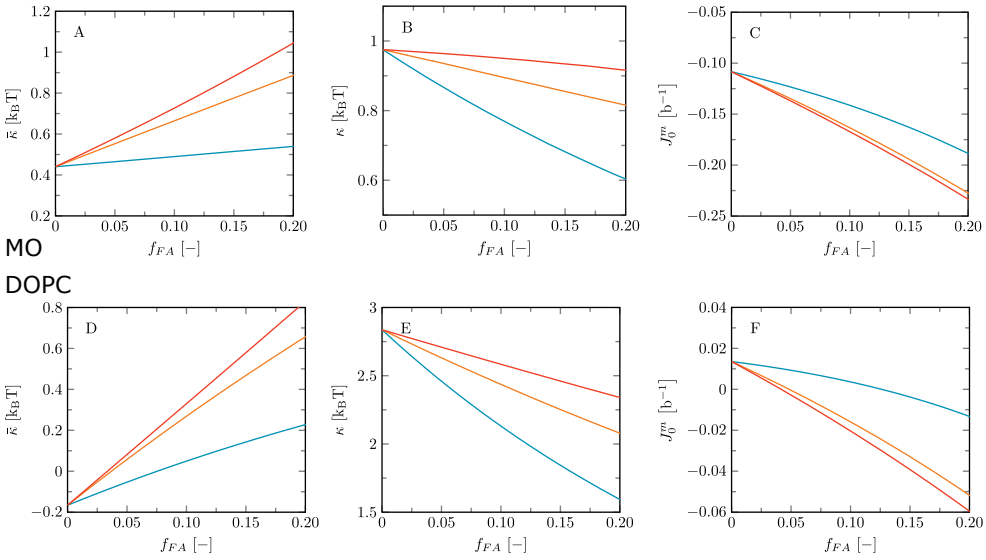

Figure 5.6: Mechanical parameters $\bar{\kappa}$, κ and J_0^m as a function of added fraction of fatty acid, for MO bilayers (top, A-C) and DOPC bilayers (bottom, D-F). Blue: C_8O_2; orange: $C_{12}O_2$; red: $C_{16}O_2$.

Without additives the MO system is in a bicontinuous cubic phase. With increasing loading with FA the Gaussian bending modulus becomes more positive, implying that the system moves away even further from a lamellar state. In addition, the spontaneous curvature of the monolayer becomes significantly negative, implying that the system may well enter an inverted hexagonal phase (H_{II}). This is especially expected for long-tail FA additives. The predictions are in this respect again in line with the experimental data. Experimental results that indicate the relative preference of inverted phases for long tail FA additives, were associated with a critical packing parameter $P > 1$ [14]. This is in accordance with our finding that J_0^m becomes strongly negative. Addition of FAs decreases the mean bending modulus a bit. The softening is much less than for the small molecular weight solvents discussed above. Hence the sponge phase is not expected in this case, especially not for the longer tail FA's. Short tail fatty acids (C3-C6) however may have a softening effect comparable to the small molecular weight solvents.

For DOPC bilayers $\bar{\kappa}$ switches sign as a function of FA loading (figure 5.6D) and we therefore anticipate that FAs will induce a transition from lamellar bilayers to saddle-shaped bilayers. The longer FA's are more effective in this respect than the shorter ones. As usual a strong positive response of the Gaussian bending modulus is mirrored by a strong negative response of the spontaneous curvature of the monolayer. As shown in figure 5.6F the value of the latter becomes significantly negative indicating that transition

into an inverted hexagonal phase (H_{II}) is a realistic scenario. In any case a sponge phase is not in sight because the mean bending modulus remains well above unity (figure 5.6E). This means that if a phase rich in saddle shapes is formed, it will be a bicontinuous cubic arrangement with long-range order.

We further note that the longer the FA tail, the smaller is the decrease in κ with f_{FA}. This trend may suggest that a fatty acid with a tail length ¿ 16 could also increase the value of κ. This would be consistent with the experimental observation that the addition of oleic acid increases κ for DOPC bilayers [58].

$C_{12}E_m$ surfactants

Another interesting class of additives are non-ionic surfactants. These molecules generally have large headgroups and are known to form (spherical) micelles. This usually is rationalised by arguing that they have a critical packing parameter $P \approx 1/3$. The incorporation of micelle-forming surfactants to lipid bilayers forces the transition towards structures with more positive interfacial curvatures, such as micelles. It is thus not surprising that the addition of various detergents to MO lipids induces a transition from the cubic phase to lamellar phases that have no interfacial curvature [14].

At high concentration, micelle-forming surfactants can even completely dissolve the bilayer into mixed micelles containing both lipids and surfactant molecules. A prime example is the addition of the non-ionic polyoxyethylene detergent Triton X-100 to phospholipid bilayers [64–66]. This solubilization of lipid membranes is widely used to isolate, extract and characterize integral membrane proteins [67].

In Triton X-100 the hydrophobic moiety features a benzene ring. In the modelling context this is not ideal because it definitely needs additional parameterisations. That is why we here chose to use $C_{12}E_m$ surfactants to represent the class of surfactants. By varying the amount of ethylene oxide (E) units we can play with the size of the hydrophilic 'head' and thereby mimic both pure micelle-forming surfactants ($C_{12}E_{10}$) and surfactants for which additionally lamellar and even sponge phases have been observed ($C_{12}E_4$ and $C_{12}E_5$) depending on temperature and pressure [68, 69]. We further note that these surfactants can exhibit different lamellar phases such as the fluid lamellar (L_α) and liquid crystalline (L_C) phases [70, 71], between which we make no distinction in this work.

In particular, the phase behaviour of $C_{12}E_5$ is interesting as at high volume fractions at room temperature lamellar bilayers are observed, and at higher temperatures even the transition from lamellar to sponge phases is seen [72]. This suggests that for pure $C_{12}E_5$ bilayers $\bar{\kappa}$ is close to zero at room temperature and positive at higher temperatures. This

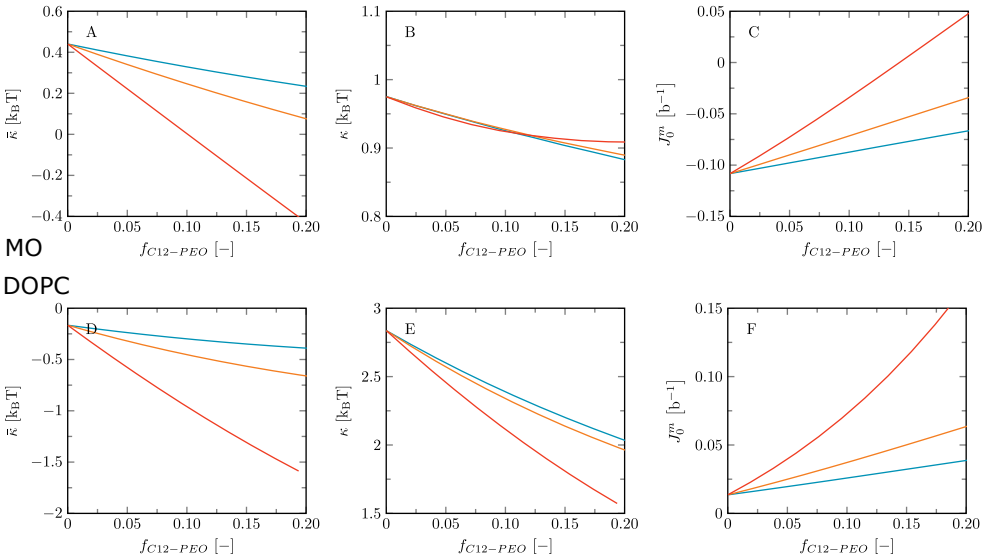

Figure 5.7: Mechanical parameters $\bar{\kappa}$, κ and J_0^m as a function of added fraction $C_{12}E_m$ surfactants, for MO bilayers (top, A-C) and DOPC bilayers (bottom, D-F). Blue: $C_{12}E_4$; orange: $C_{12}E_5$; red: $C_{12}E_{10}$.

can be captured in the model by making the interaction parameters for the ethylene oxide part of the molecule temperature dependent [73] such that the headgroup becomes less water soluble with increasing temperature. In the present paper we ignore this temperature dependence.

When we use the default parameters (table 5.1) to model $C_{12}E_5$ bilayers, we find a Gaussian bending rigidity that is slightly negative $\bar{\kappa} = -0.52$. Consistent with expectations, we observe an increase in $\bar{\kappa}$ when increasing χ_{C_D-W} (not shown). For example, $\bar{\kappa} = 1.4$ is obtained already for $\chi_{C_D-W} = 1.2$, which combined with a low mean bending modulus ($\kappa = 0.34$) indeed suggests the formation of the sponge phase at higher temperatures (i.e., for a more positive value for χ_{C_D-W}).

Although the phase behavior of the pure surfactants is of interest, we here focus on the effect of surfactants as additives to MO and DOPC systems. We chose for this study two surfactants with a small headgroup ($C_{12}E_5$ and $C_{12}E_4$) and a surfactant with larger headgroup ($C_{12}E_{10}$).

The predicted mechanical parameters with increasing added amounts of $C_{12}E_m$ surfactants to DOPC and MO bilayers are presented in figure 5.7. As with the addition of fatty acids, we observe similar trends for the DOPC and MO bilayers with the addition of $C_{12}E_m$ surfactants. In line with expectation and the trends found for the fatty acids,

i.e., an increase in $\bar{\kappa}$ and a decrease in J_0^m with increasing tail length, we now find the opposite effects with increasing surfactant headgroup size. We thus observe that with added fraction surfactant $\bar{\kappa}$ decreases while J_0^m increases and that these effects become more pronounced with increasing number of ethylene oxide units.

For MO bilayers this means we expect transition of the bicontinuous cubic phase towards a lamellar phase. For the addition of $C_{12}E_{10}$ such a transition seems to occur already at about 10 wt% loading, as can be seen from figure 5.7A. As κ remains relatively close to unity, we do not expect the formation of an intermediate sponge phase. This phase behaviour corresponds closely to known phase behaviour of other MO/surfactant (or detergent) mixtures, which also shows a direct transition of the bicontinuous cubic phase to the lamellar L_α phase [14]. The addition of $C_{12}E_4$ and $C_{12}E_5$ causes similar, but weaker, trends in $\bar{\kappa}$ and J_0^m. The decrease in κ with $C_{12}E_{4,\,5}$ fraction seems to suggest that at high fractions the formation of a sponge phase, which requires a low value of κ, is possible. This is most likely for $C_{12}E_4$.

As expected, addition of these surfactants to DOPC bilayers induces the formation of micellar structures at high surfactant/lipid ratios. This follows mainly from the sharp increase in J_0^m to large positive values. The larger the polyethylene oxide headgroup the quicker, i.e. at lower molar fractions, this happens.

5.6 General Discussion

In the previous sections we have shown that the lattice-refined SF-SCF theory can be used to estimate the mechanical parameters of MO and DOPC bilayer systems. We argue that we can use the trends in these parameters to consistently predict the mesomorphic phase behaviour of these lipids in response to a wide range of additives. More specifically, the phase transition from lamellar bilayer topologies to saddle-shaped topologies can be attributed to the sign-switch of $\bar{\kappa}$. Additionally, the formation of micelles or inverted micelles follow from a large positive or large negative value of J_0^m respectively. The transitions between different saddle-shaped bilayer phases, i.e. various cubic phases and eventually the sponge phases, arguably are rather subtle. Invariably these phases can only be stable when the Gaussian bending modulus is positive. When the mean bending modulus is in addition much less than unity, we argue that the system loses its long-range order and forms a sponge phase. Bicontinuous triple periodic phases are likely to have a higher bending modulus compared with sponge phases. The higher the value for κ, the more the triple periodic cubic phase will go to a minimal surface, that is a surface on which the total curvature vanishes everywhere in the unit cell. This is the way the system can

nullify the influence of the (relatively high) bending modulus. We cannot imagine that a strong preferential curvature of the monolayer, which typically is negative in this regime, is consistent with the bicontinuous cubic phase and this parameter should be responsible for the transitions towards the inverted hexagonal or inverted micelle systems. A strong criterion for this transition we do not yet have.

Now that we have established these rules, some general trends can be identified. In short, we observe that the inclusion of additives that are mainly hydrophobic and partition in the bilayer core, drive the bilayer towards a topological state of increased negative interfacial curvature and saddle shape configurations. That is, the DOPC system may lose the lamellar topology in favour of the inverted hexagonal phase or bicontinuous cubic phases and MO tends to go towards an inverted micellar phase. Micelle-forming surfactants do the opposite. The inclusion of small additives, both hydrophilic (i.e. 'solvents') or hydrophobic, generally decreases the mean bending modulus of the bilayers and thus makes bilayers more flexible. This may take a lipid system from a bicontinuous cubic phase closer to an L_3-phase or decreases the persistence length of the bilayers and increase the undulation repulsion. These rules are highly complementary to the general rules for lipid self-assembly as outlined by van 't Hag et al [14].

It should be stressed that small changes in the set of interaction parameters may have a relatively large impact on the results. This not necessarily is a bad property of the approach because in reality small variations in surfactant properties can also result in large shifts in phase behaviour. However, it means that the exact values of $\bar{\kappa}$, κ and J_0^m as provided by the SF-SCF modelling should not be given too much weight. To arrive at our conclusions with respect to the effect of additives on the DOPC and MO bilayers mesomorphic phase behaviour, we only took into account the predicted trends in these mechanical quantities. It remains true that in order to provide more accurate estimates on the mechanical properties, a more detailed and structured parameterisation of each molecule used is required.

5.7 Conclusions

The self-assembly of lipids in aqueous solution yields a wide variety of structures of various shapes and morphologies. From an application perspective, it is of utmost importance to know the topological behaviour of the lipid system, in order to find relevant functionalities. With time, the experimental techniques used to follow this behaviour are becoming more accurate and more precise. However, mapping the topological phase behaviour can still be time consuming and finding the ideal lipid system for the desired application is a matter of

trial and error. modelling techniques that can accurately predict the mesomorphic phase behaviour of lipid systems are therefore in high demand. However when the computation time exceeds the experimental time scale, which still seems the case for all-atom molecular dynamics simulations, they are in this respect of little extra value. Only computationally inexpensive routes can map out a large parameter space needed to feed our intuition regarding the mesomorphism of lipids and lipid mixtures. Computationally inexpensive routes are approximate and we can only start trusting these routes if good correlations with experiments are produced.

In this work, we used the lattice-refined self-consistent field theory of Scheutjens and Fleer (SF-SCF) which is computationally inexpensive. It can be fed with molecularly detailed models (on a united atom level) and come up with structural, thermodynamic and mechanical data that can be interpreted in terms of the preferred mesomorphic phase state of the system of interest. We have illustrated this by predicting the phase behaviour of MO and DOPC bilayers in response to a wide range of additives. For mixtures of MO and DOPC, and for the addition of various additives to MO bilayers, the obtained mechanical parameters clearly correlate with known phase behaviour. These correlations give credibility to the predicted phase behavior of DOPC in response to these additives. Importantly, this analysis can be readily extended to other lipid systems as well.

However, we should emphasise that the lattice-refined SF-SCF approach is by far not yet developed to the best of its possibilities. For example, the chain model that is currently implemented is the freely-jointed chain. This chain model can be upgraded to the rotational isomeric state (RIS) scheme, implementing the chain flexibility more realistically [74]. In addition the mean-field approximation is not suitable to account for thermotropic phase changes such as the gel-to-liquid phase transitions in bilayers. Solutions to overcome these shortcomings are in principle known [75] but currently not implemented. Finally, and this is particularly important for lipid mixtures, we have not yet considered the possibility of lateral segregation of lipids in bilayer membrane (formation of rafts). Again at the expense of CPU time we can improve on this issue as well. [76] We therefore conclude that the lattice-refined SF-SCF model has a great potential to predict mesomorphism of lipids and lipid mixtures and we can already use the approach to sharpen our intuition regarding the many possible phase changes that can occur.

5.8 Supplementary Information

5.8.1 Isotherms

In the three-component systems used in this paper, that is in bilayers in which additives are included, the amount of additive in the system is a free parameter. This means that one can make so-called absorption isotherms, that is the amount of additive that is absorbed in the membrane per unit area θ^σ as a function of the bulk concentration of this additive. Here $\theta^\sigma = \sum_z \varphi_2(z) - \varphi_2^b$. For good reasons we are typically interested in absorbed amounts which keeps the additive as a minority component in the membrane. That is why we in most cases below the isotherms were discontinued as soon as either the bulk concentration or the concentration of the component in the membrane passed some threshold value.

Absorption isotherms are informative about (hidden) solubility limitations that might pop up in cases where the additive my have some solubility gap with the aqueous solution. In such a case the absorption isotherms will feature some type of Van der Waals loop. Below we avoid these regions and always keep the amount of additive below the bulk binodal value. These constraints do not pose major restrictions, because our primary interest is in predicting (initial) trends in how additives may push a membrane system towards potential phase changes, rather than to pinpoint a threshold composition for such mesomorphic variation or where the membrane falls apart (e.g. something which happens when large amounts of Triton is used). The slope of this absorption isotherm can be related to a membrane partition coefficient [77], but we will not dwell on this quantity.

The absorption isotherms for the three alcoholic solvents used in this study are given in figure 5.8.

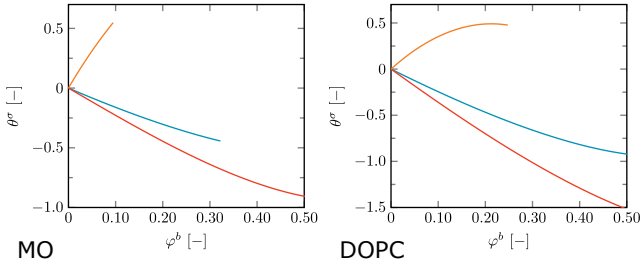

Figure 5.8: Isotherm (θ^σ as a function of φ^b) for MO bilayers (left) and DOPC bilayers (right) with added ethanol C_2O (blue), added t-butanol tC_4O (orange) or added butanediol (C_4O_2) (red). A) $\bar{\kappa}$; B) κ; C) J_0^m.

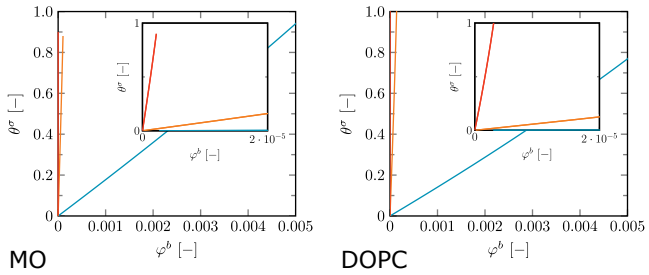

Figure 5.9: Isotherm (θ^σ as a function of φ^b) for MO bilayers (left) and DOPC bilayers (right) with added fatty acids. blue: C_8O_2; orange: $C_{12}O_2$; red: $C_{16}O_2$. The inset provides the same graph but in which the x-axis is zoomed

Intuitively one would expect isotherms to show positive accumulated amounts as a function of the concentration of the additive. However for rather hydrophilic compounds that accumulate weakly in the head group or glycerol-backbone region, may show a strong depletion in the core region, rendering the overall absorption to be negative. Inspection of Fig. 5.8 this is the case for butanediol and for ethanol for both bilayers. Only for t-butanol modest positive absorbed amounts are predicted. For the MO system, we could not exceed the limit of $\varphi^b = 0.1$ for butanol, as no bilayer could be formed anymore, consistent with experimental facts that butanol may easily destroy a bilayer and put the system into a fluid isotropic phase (L_2) [52]. For DOPC we could reach higher levels of φ^b and see the curve reaching a plateau before the same happens. Again our interest is not in the disintegration of bilayers and therefore we have set the limit in added butanol for the remainder of our calculations at $\varphi^b = 0.1$.

In figure 5.9 we have plotted the absorption isotherms of all FA used. As can be seen from the figure, we observe relative linear positive trends. This indicates that FA inserts themselves into the bilayer and that we managed to stay away from the solubility limit or CMC of the fatty acids. Clearly FA partition strongly in the bilayers. This must of course be attributed to the hydrophobic tails that have a high affinity for the core. This preferential partitioning of the FA in the membrane is a strong function of the length of the tail and therefore the adsorption isotherms show an increase in adsorbed amount at progressively lower bulk concentrations the longer is the tail length.

References

[1] RNAH Lewis and Ronald N McElhaney. The mesomorphic phase behavior of lipid bilayers. *The structure of biological membranes*, 2, 1992.

[2] MW Tate, EF Eikenberry, DC Turner, E Shyamsunder, and SM Gruner. Nonbilayer phases of membrane lipids. *Chemistry and physics of lipids*, 57(2-3):147–164, 1991.

[3] Guru V Betageri and Milton B Yatvin. Liposome drug delivery, July 13 2004. US Patent 6,761,901.

[4] ET Kisak, B Coldren, CA Evans, C Boyer, and JA Zasadzinski. The vesosome-a multicompartment drug delivery vehicle. *Current medicinal chemistry*, 11(2):199–219, 2004.

[5] Marc Michel, Mathias Winterhalter, Laurent Darbois, Joseph Hemmerle, Jean Claude Voegel, Pierre Schaaf, and Vincent Ball. Giant liposome microreactors for controlled production of calcium phosphate crystals. *Langmuir*, 20(15):6127–6133, 2004.

[6] Vincent Noireaux and Albert Libchaber. A vesicle bioreactor as a step toward an artificial cell assembly. *Proceedings of the national academy of sciences of the United States of America*, 101(51): 17669–17674, 2004.

[7] Ewa Nazaruk, Renata Bilewicz, Göran Lindblom, and Britta Lindholm-Sethson. Cubic phases in biosensing systems. *Analytical and bioanalytical chemistry*, 391(5):1569, 2008.

[8] Ewa Nazaruk, Sławomir Smoliński, Marta Swatko-Ossor, Grażyna Ginalska, Jan Fiedurek, Jerzy Rogalski, and Renata Bilewicz. Enzymatic biofuel cell based on electrodes modified with lipid liquid-crystalline cubic phases. *Journal of Power Sources*, 183(2):533–538, 2008.

[9] Jijo J Vallooran, Stephan Handschin, Samyuktha M Pillai, Beatrice N Vetter, Sebastian Rusch, Hans-Peter Beck, and Raffaele Mezzenga. Lipidic cubic phases as a versatile platform for the rapid detection of biomarkers, viruses, bacteria, and parasites. *Advanced functional materials*, 26(2):181–190, 2016.

[10] Zakaria A Almsherqi, Sepp D Kohlwein, and Yuru Deng. Cubic membranes: a legend beyond the flatland* of cell membrane organization. *The Journal of cell biology*, 173(6):839–844, 2006.

[11] David P Siegel. The gaussian curvature elastic energy of intermediates in membrane fusion. *Biophysical journal*, 95(11):5200–5215, 2008.

[12] Mehdi Torbati, Tanmay P Lele, and Ashutosh Agrawal. Ultradonut topology of the nuclear envelope. *Proceedings of the National Academy of Sciences*, 113(40):11094–11099, 2016.

[13] Susan R Wente and Michael P Rout. The nuclear pore complex and nuclear transport. *Cold Spring Harbor perspectives in biology*, 2(10):a000562, 2010.

[14] Leonie van't Hag, Sally L Gras, Charlotte E Conn, and Calum J Drummond. Lyotropic liquid crystal engineering moving beyond binary compositional space–ordered nanostructured amphiphile self-assembly materials by design. *Chemical society reviews*, 46(10):2705–2731, 2017.

[15] Hong Qiu and Martin Caffrey. The phase diagram of the monoolein/water system: metastability and equilibrium aspects. *Biomaterials*, 21(3):223–234, 2000.

[16] Chandrashekhar V Kulkarni, Wolfgang Wachter, Guillermo Iglesias-Salto, Sandra Engelskirchen, and Silvia Ahualli. Monoolein: a magic lipid? *Physical Chemistry Chemical Physics*, 13(8):3004–3021, 2011.

[17] Vadim Cherezov, Jeffrey Clogston, Yohann Misquitta, Wissam Abdel-Gawad, and Martin Caffrey. Membrane protein crystallization in meso: lipid type-tailoring of the cubic phase. *Biophysical journal*, 83(6):3393–3407, 2002.

[18] Wolfgang Helfrich. Elastic properties of lipid bilayers: theory and possible experiments. *Zeitschrift für Naturforschung C*, 28(11-12):693–703, 1973.

[19] Jacob N Israelachvili, D John Mitchell, and Barry W Ninham. Theory of self-assembly of hydrocarbon amphiphiles into micelles and bilayers. *Journal of the Chemical Society, Faraday Transactions 2: Molecular and Chemical Physics*, 72:1525–1568, 1976.

[20] David P Siegel and MM Kozlov. The gaussian curvature elastic modulus of n-monomethylated dioleoylphosphatidylethanolamine: relevance to membrane fusion and lipid phase behavior. *Biophysical journal*, 87(1):366–374, 2004.

[21] Ramanathan Varadharajan and Frans A M Leermakers. Sign switch of gaussian bending modulus for microemulsions: A self-consistent field analysis exploring scale invariant curvature energies. *Physical Review Letters*, 120(2):028003, 2018.

[22] Julia Genova, Victoria Vitkova, and Isak Bivas. Registration and analysis of the shape fluctuations of nearly spherical lipid vesicles. *Physical Review E*, 88(2):022707, 2013.

[23] Philippe Méléard and Tanja Pott. Overview of a quest for bending elasticity measurement. In *Advances in planar lipid bilayers and liposomes*, volume 17, pages 55–75. Elsevier, 2013.

[24] Andrew F Loftus, Sigrid Noreng, Vivian L Hsieh, and Raghuveer Parthasarathy. Robust measurement of membrane bending moduli using light sheet fluorescence imaging of vesicle fluctuations. *Langmuir*, 29(47):14588–14594, 2013.

[25] C Monzel and K Sengupta. Measuring shape fluctuations in biological membranes. *Journal of Physics D: Applied Physics*, 49(24):243002, 2016.

[26] Jonas Rosager Henriksen and John H Ipsen. Measurement of membrane elasticity by micro-pipette aspiration. *The European Physical Journal E*, 14(2):149–167, 2004.

[27] Volkmar Heinrich and Wiesława Rawicz. Automated, high-resolution micropipet aspiration reveals new insight into the physical properties of fluid membranes. *Langmuir*, 21(5):1962–1971, 2005.

[28] Thomas Portet, Sharona E Gordon, and Sarah L Keller. Increasing membrane tension decreases miscibility temperatures; an experimental demonstration via micropipette aspiration. *Biophysical journal*, 103(8):L35–L37, 2012.

[29] W Rawicz, K Cc Olbrich, T McIntosh, D Needham, and E Evans. Effect of chain length and unsaturation on elasticity of lipid bilayers. *Biophysical journal*, 79(1):328–339, 2000.

[30] Jianjun Pan, Stephanie Tristram-Nagle, Norbert Kučerka, and John F Nagle. Temperature dependence of structure, bending rigidity, and bilayer interactions of dioleoylphosphatidylcholine bilayers. *Biophysical journal*, 94(1):117–124, 2008.

[31] G Pabst, N Kučerka, M-P Nieh, MC Rheinstädter, and J Katsaras. Applications of neutron and x-ray scattering to the study of biologically relevant model membranes. *Chemistry and Physics of Lipids*, 163(6):460–479, 2010.

[32] Mingyang Hu, John J Briguglio, and Markus Deserno. Determining the gaussian curvature modulus of lipid membranes in simulations. *Biophysical journal*, 102(6):1403–1410, 2012.

[33] Tobias Baumgart, S Das, Watt Wetmore Webb, and James Thomas Jenkins. Membrane elasticity in giant vesicles with fluid phase coexistence. *Biophysical journal*, 89(2):1067–1080, 2005.

[34] Stefan Semrau, Timon Idema, Laurent Holtzer, Thomas Schmidt, and Cornelis Storm. Accurate determination of elastic parameters for multicomponent membranes. *Physical review letters*, 100(8): 088101, 2008.

[35] JMHM Scheutjens and GJ Fleer. Statistical theory of the adsorption of interacting chain molecules. 1. partition function, segment density distribution, and adsorption isotherms. *Journal of Physical Chemistry*, 83(12):1619–1635, 1979.

[36] J M H M Scheutjens and G J Fleer. Statistical theory of the adsorption of interacting chain molecules. 2. train, loop, and tail size distribution. *J. Phys. Chem.*, 84(2):178–190, 1980. URL `http://pubs.acs.org/doi/abs/10.1021/j100439a011`.

[37] William Lawrence Bragg and Evan James Williams. The effect of thermal agitation on atomic arrangement in alloys. *Proceedings of the Royal Society of London. Series A, Containing Papers of a Mathematical and Physical Character*, 145(855):699–730, 1934.

[38] Gerard Fleer, M A Cohen Stuart, J M H M Scheutjens, T Cosgrove, and B Vincent. *Polymers at interfaces*. Springer Science & Business Media, 1993. URL `http://www.springer.com/gp/book/9780412581601`.

[39] O. A. Evers, J. M. H. M. Scheutjens, and G. J. Fleer. Statistical thermodynamics of block copolymer adsorption. 1. formulation of the model and results for the adsorbed layer structure. *Macromolecules*, 23(25):5221–5233, 1990.

[40] VS Markin, MM Kozlov, and SL Leikin. Definition of surface tension at a non-spherical interface. *Journal of the Chemical Society, Faraday Transactions 2: Molecular and Chemical Physics*, 84(8): 1149–1162, 1988.

[41] Samuel Safran. *Statistical thermodynamics of surfaces, interfaces, and membranes*. CRC Press, 2018.

[42] H Pera, JM Kleijn, and FAM Leermakers. Linking lipid architecture to bilayer structure and mechanics using self-consistent field modelling. *The Journal of chemical physics*, 140(6):02B606_1, 2014.

[43] F A M Leermakers. Bending rigidities of surfactant bilayers using self-consistent field theory. *J. Chem. Phys.*, 138(15):04B610, 2013. URL `https://doi.org/10.1063/1.4801327`.

[44] RA Kik, JM Kleijn, and FAM Leermakers. Bending moduli and spontaneous curvature of the monolayer in a surfactant bilayer. *The Journal of Physical Chemistry B*, 109(30):14251–14256, 2005.

[45] Richard A Kik, Frans A M Leermakers, and J Mieke Kleijn. Molecular modeling of proteinlike inclusions in lipid bilayers: Lipid-mediated interactions. *Phys. Rev. E*, 81(2):021915, 2010. URL `https://journals.aps.org/pre/abstract/10.1103/PhysRevE.81.021915`.

[46] Tamiki Umeda, Yukio Suezaki, Kingo Takiguchi, and Hirokazu Hotani. Theoretical analysis of opening-up vesicles with single and two holes. *Physical Review E*, 71(1):011913, 2005.

[47] F A M Leermakers, J M H M Scheutjens, and J Lyklema. On the statistical thermodynamics of membrane formation. *Biophysical chemistry*, 18(4):353–360, 1983.

[48] James P Dilger and Roland Benz. Optical and electrical properties of thin monoolein lipid bilayers. *The Journal of membrane biology*, 85(2):181–189, 1985.

[49] R Fettiplace, DM Andrews, and DA Haydon. The thickness, composition and structure of some lipid bilayers and natural membranes. *The Journal of membrane biology*, 5(3):277–296, 1971.

[50] V Chupin, JA Killian, and B de Kruijff. Effect of phospholipids and a transmembrane peptide on the stability of the cubic phase of monoolein: Implication for protein crystalization from a cubic phase. *Biophysical journal*, 84(4):2373–2381, 2003.

[51] S Engström, K Alfons, M Rasmusson, and H Ljusberg-Wahren. Solvent-induced sponge (l 3) phases in the solvent-monoolein-water system. In *The Colloid Science of Lipids*, pages 93–98. Springer, 1998.

[52] Vadim Cherezov, Jeffrey Clogston, Miroslav Z Papiz, and Martin Caffrey. Room to move: crystallizing membrane proteins in swollen lipidic mesophases. *Journal of molecular biology*, 357(5): 1605–1618, 2006.

[53] Hung V Ly and Marjorie L Longo. The influence of short-chain alcohols on interfacial tension, mechanical properties, area/molecule, and permeability of fluid lipid bilayers. *Biophysical Journal*, 87(2):1013–1033, 2004.

[54] Hung V Ly, David E Block, and Marjorie L Longo. Interfacial tension effect of ethanol on lipid bilayer rigidity, stability, and area/molecule: a micropipet aspiration approach. *Langmuir*, 18(23): 8988–8995, 2002.

[55] Shao-Yu Chen, Bing Yang, Ken Jacobson, and Kathleen K Sulik. The membrane disordering effect of ethanol on neural crest cells in vitro and the protective role of gm1 ganglioside. *Alcohol*, 13(6): 589–595, 1996.

[56] Peter Westh, Christa Trandum, and Yoshikata Koga. Binding of small alcohols to a lipid bilayer membrane: does the partitioning coefficient express the net affinity? *Biophysical Chemistry*, 89(1): 53–63, 2001.

[57] Nhiem Tran, Adrian M Hawley, Jiali Zhai, Benjamin W Muir, Celesta Fong, Calum J Drummond, and Xavier Mulet. High-throughput screening of saturated fatty acid influence on nanostructure of lyotropic liquid crystalline lipid nanoparticles. *Langmuir*, 32(18):4509–4520, 2016.

[58] Arwen II Tyler, Jake Greenfield, Nicholas J Brooks, John M Seddon, et al. Coupling phase behaviour of fatty acid containing membranes to membrane bio-mechanics. *Frontiers in Cell and Developmental Biology*, 7:187, 2019.

[59] Jeffrey R Simard, Frits Kamp, and James A Hamilton. Measuring the adsorption of fatty acids to phospholipid vesicles by multiple fluorescence probes. *Biophysical journal*, 94(11):4493–4503, 2008.

[60] M Langner, T Isac, and SW Hui. Interaction of free fatty acids with phospholipid bilayers. *Biochimica et Biophysica Acta (BBA)-Biomembranes*, 1236(1):73–80, 1995.

[61] Frits Kamp, David Zakim, Fengli Zhang, Noa Noy, and James A Hamilton. Fatty acid flip-flop in phospholipid bilayers is extremely fast. *Biochemistry*, 34(37):11928–11937, 1995.

[62] James A Hamilton. Fatty acid transport: difficult or easy? *Journal of lipid research*, 39(3):467–481, 1998.

[63] Frits Kamp and James A Hamilton. How fatty acids of different chain length enter and leave cells by free diffusion. *Prostaglandins, leukotrienes and essential fatty acids*, 75(3):149–159, 2006.

[64] Robert J Robson and Edward A Dennis. Mixed micelles of sphingomyelin and phosphatidylcholine with nonionic surfactants: Effect of temperature and surfactant polydispersity. *Biochimica et Biophysica Acta (BBA)-Lipids and Lipid Metabolism*, 573(3):489–500, 1979.

[65] Erwin London and Deborah A Brown. Insolubility of lipids in triton x-100: physical origin and relationship to sphingolipid/cholesterol membrane domains (rafts). *Biochimica et Biophysica Acta (BBA)-Biomembranes*, 1508(1-2):182–195, 2000.

[66] Hasna Ahyayauch, Banafshe Larijani, Alicia Alonso, and Félix M Goñi. Detergent solubilization of phosphatidylcholine bilayers in the fluid state: influence of the acyl chain structure. *Biochimica et Biophysica Acta (BBA)-Biomembranes*, 1758(2):190–196, 2006.

[67] Ari Helenius and KAI Simons. Solubilization of membranes by detergents. *Biochimica et Biophysica Acta (BBA)-Reviews on Biomembranes*, 415(1):29–79, 1975.

[68] D John Mitchell, Gordon JT Tiddy, Loraine Waring, Theresa Bostock, and Malcolm P McDonald. Phase behaviour of polyoxyethylene surfactants with water. mesophase structures and partial miscibility (cloud points). *Journal of the Chemical Society, Faraday Transactions 1: Physical Chemistry in Condensed Phases*, 79(4):975–1000, 1983.

[69] Gordon JT Tiddy. Surfactant-water liquid crystal phases. *Physics reports*, 57(1):1–46, 1980.

[70] B Mädler, G Klose, A Möps, W Richter, and C Tschierske. Thermotropic phase behaviour of the pseudobinary mixture dppc/c12e4 at excess water. *Chemistry and physics of lipids*, 71(1):1–12, 1994.

[71] Helge Pfeiffer, G Klose, Karel Heremans, and Christ Glorieux. Thermotropic phase behaviour of the pseudobinary mixtures of dppc/c12e5 and dmpc/c12e5 determined by differential scanning calorimetry and ultrasonic velocimetry. *Chemistry and physics of lipids*, 139(1):54–67, 2006.

[72] Reinhard Strey, Reinhard Schomäcker, Didier Roux, Frederic Nallet, and Ulf Olsson. Dilute lamellar

and l 3 phases in the binary water–c 12 e 5 system. *Journal of the Chemical Society, Faraday Transactions*, 86(12):2253–2261, 1990.

[73] Bong-Seop Lee. Pressure, temperature and concentration effects on hydrogen bonding in poly (ethylene oxide) aqueous solution. *Journal of Molecular Liquids*, 262:527–532, 2018.

[74] FAM Leermakers and JMHM Scheutjens. Statistical thermodynamics of association colloids. i. lipid bilayer membranes. *The Journal of chemical physics*, 89(5):3264–3274, 1988.

[75] FAM Leermakers and JMHM Scheutjens. Statistical thermodynamics of association colloids. iii. the gel to liquid phase transition of lipid bilayer membranes. *The Journal of chemical physics*, 89(11): 6912–6924, 1988.

[76] FAM Leermakers, M Ballauff, and OV Borisov. On the mechanism of uptake of globular proteins by polyelectrolyte brushes: A two-gradient self-consistent field analysis. *Langmuir*, 23(7):3937–3946, 2007.

[77] LA Meijer, FAM Leermakers, and J Lyklema. Self-consistent-field modeling of complex molecules with united atom detail in inhomogeneous systems. cyclic and branched foreign molecules in dimyristoylphosphatidylcholine membranes. *The Journal of chemical physics*, 110(13):6560–6579, 1999.

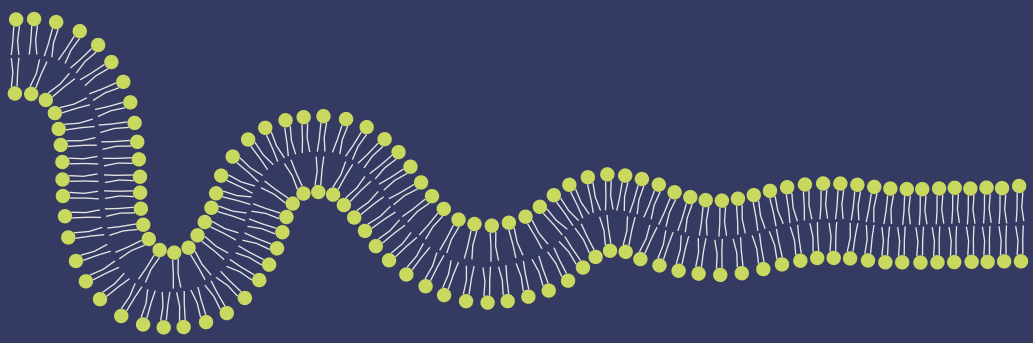

CHAPTER 6

General Discussion

In the introduction I showed an image of a biological cell and noted that when looking at such a picture, most of what you see is membranes. The basic model of the biological membrane, the so-called fluid mosaic model by Singer and Nicolson [1], correctly depicts the membranes as a double layer of lipids in which protein molecules float around. However, it does not explain how the bilayer on a mesoscopic scale takes on many different shapes and forms, as is visualized in such an image of a biological cell. The example I presented in the introduction was the nucleopores present in the nuclear envelope, but many other examples exist as well. One such example is the thylakoid membrane present in chloroplasts of plant cells. It is in these thylakoid membranes that photosynthesis takes place. Important for this process is the large membrane surface area and that the membrane separates two volumes, one enclosed by the thylakoid bilayer (lumen) and one on the outside (stroma). The thylakoid membrane itself can be separated in two different domains, each with its own distinct structure and morphology: grana lamellae and stroma lamellae. The grana thylakoid structure can be seen as multiple flat vesicles stacked on top of each other, similar to a stack of coins and the stroma membranes effectively forms the connection between the different flat vesicles and between different grana. How these two are connected to form a continuous lamellar bilayer system is, to this day, not completely elucidated and various models, such as the helical model [2–4], the bifurcation model [5] and the folded-membrane model [6], still exist. What remains certain is that in order to interconnect all bilayers into a continuous phase, the formation of saddle-shaped bilayer structures is inevitable. It is therefore not surprising that the main lipid found in thylakoid membranes is monogalactosyldiacylglycerol (MGDG). The structure of this lipid molecule is effectively that of a single sugar group attached to a glycerol and two lipid tails. When dispersed in water, this lipid forms cubic or inverse hexagonal (H_{II}) phases [7, 8]. It has the general shape of a cone (form factor $P > 1$) and, as the molecule bears

no charges, it is relatively hydrophobic compared to phospholipids such as DOPC. As such I can't help but speculate, also based on the general rules obtained in chapters 4 and 5, that the inclusion of MDGD would transition lamellar bilayers towards bilayers with a positive Gaussian curvature ($\kappa > 0$) and negative spontaneous curvature of the monolayer ($J_0^m < 0$), and could very well be instrumental in giving the thylakoid membrane its complex morphology. This was recently proposed in literature as well [9].

Clearly, many questions remain regarding the structure and topology of biological membranes on the mesoscale in relation to their function. For example, how can we induce and stabilise the formation of a membrane handle? What bilayer composition is required for this? In this thesis we deliver tools that may contribute to tackle such questions. In short, we developed an experimental method to bring bilayers together in a controlled manner in the form of vesicle pairs and small vesicle aggregates (chapter 2 and 3). The obtained double bilayer in the contact areas is an ideal starting point to induce processes involving a mesomorphic phase change such as vesicle fusion or the formation of membrane handles. Such processes can be monitored using for example fluorescent techniques such as FRET, as shown in chapter 3. In addition, we have extended the SF-SCF theory with a lattice refinement to better describe and predict the mechanical properties of lipid bilayers, and thus their mesomorphic phase behaviour. In chapter 4 we used this to map out the effect of several lipid properties on the bending rigidities of bilayers that govern their curvature properties. And lastly, in chapter 5 we made predictions, based on the lattice-refined SF-SCF model, about the effect of additives on the mechanical properties of lipid bilayers.

In the following paragraphs I will put the work described in the previous chapters in a wider perspective and provide an outlook of future research directions that can be taken. In doing so I will also show and discuss some of my preliminary experiments that were not addressed or shown in previous chapters.

6.1 Self-limiting aggregation of lipid vesicles

As I have mentioned, we managed to find routes that allow to limit the aggregation of vesicles to stable vesicle pairs or other small vesicle aggregates of specific size. This is important because to induce vesicle fusion or the formation of membrane handles through the use of a specific additive, these molecules should be able to reach the contact areas between vesicles. We succeeded in this objective mainly by making use of the natural tendency of bilayer vesicles with added linkers to self-limit their aggregation. The notion "self-limiting" implies that a natural stopping mechanism exists for the aggregation pro-

cess. This stopping mechanism results from the accumulation of linkers in the contact areas of the vesicles, depleting the rest of the vesicle surface of linkers. While this latter phenomenon has been reported before using biotin and streptavidin [10], it was (remarkably) never exploited to limit vesicle aggregation to only small aggregates or vesicle pairs. In chapters 2 and 3 we managed to do just that with two types of linker systems (biotin/streptavidin and the thermoresponsive surfactant C18-pNIPAm) and anticipate this method can be applied as well using other linkers, such as conjugated DNA pairs. Of the various linker systems that we used, the C18-pNIPAm surfactant is the most versatile in its function. Not only does it meet the requirements for a linker to induce self-limiting aggregation, the thermoresponsiveness of the pNIPAm block makes it possible to trigger this aggregation with a temperature switch. On top of that, the aggregation can be reversed as well. By combining this linker with other linkers it is possible to create new types of behaviour: in combination with biotin and streptavidin, we managed to take self-limiting aggregation one step further and designed a stepwise process to obtain stable small vesicle aggregates of predetermined size.

There are however limitations to the experimental conditions for self-limiting aggregation and not all linker systems are suitable. We described these limitations in chapter 2, however here I would like to elaborate on our work using telechelic (triblock) copolymers and our efforts to control vesicle aggregation using such linkers a bit more. The telechelic copolymer used combines a hydrophilic middle block (polyethylene oxide, PEO) with two C_{18} tails at both ends. The difference in the aggregation behaviour induced by this linker compared to "self-limiting linkers" is perhaps most clearly illustrated in figure 6.1, in which we record the vesicle aggregate size as a function of time for biotin/streptavidin and our telechelic polymer. From this data, we observe an increase in aggregation size over time in both cases, yet for the sample with telechelic polymers this happens linearly, whereas the increase in radius using biotin and streptavidin linkers levels off and stops over time. This indicates two distinctly different types of aggregation. The main cause for the difference is that telechelics partition in the system as flower-like micelles in solution as well as components of the bilayer, and that these flower-like micelles can replenish the depleted telechelics on the bilayer during aggregation. This buffering capacity thus allows the aggregation to continue. While my efforts to use telechelics as linkers for self-limiting aggregation was not a success, various changes to the telechelic polymers can be made to potentially allow self-limiting aggregation. For this, the telechelics need to induce vesicle aggregation before formation into flower-like micelles occurs. In other words, the critical micelle concentration (CMC) of the telechelic polymers needs to be increased. This can be realised either by increasing the length of the hydrophilic middle block, or by reducing the length of the hydrophobic tails

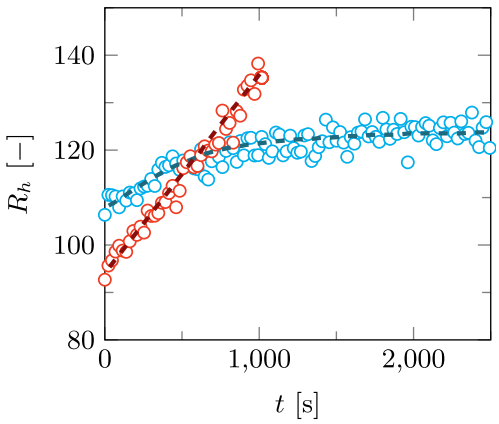

Figure 6.1: Vesicle aggregation observed using biotin and streptavidin (blue) and C18-PEO-C18 telechelic block copolymers ($M_w \approx 35000$ g/mol) (red). The hydrodynamic radius R_h is followed over time using DLS, similar as in chapters 2 and 3. The sample with biotin and streptavidin contained a fraction $f_b \approx 0.015$ of biotinylated lipids, and a streptavidin/biotin ratio $N_s/N_b \approx 0.05$. In the sample with telechelics, the telechelic/lipid fraction $N_{\text{tel}}/N_{\text{lipid}} \approx 0.002$. The dashed lines serve as guidelines through the data.

6.2 Supported double lipid bilayer formation

The method of bringing bilayers closely together using linkers can be used as well to prepare two bilayers on top of each other at solid substrate, a so-called supported double lipid bilayer (SDLB). During my PhD I managed to form such a SDLB using the procedure described by Murray et al. [11]. In this method, the first bilayer is formed through adhesion and subsequent collapse of small lipid vesicles containing biotinylated lipids on a substrate such as glass or silica. In the second phase, streptavidin is added to the system and binds to the biotin on the first bilayer. After washing, a second solution of biotinylated lipid vesicles is introduced, which then attach to the streptavidin and under the right conditions forms a second bilayer on top of the first one. A schematic overview of this process is given in figure 6.2. We followed this process using reflectometry.[12] Here, the adsorbed amount Γ of material on a silica wafer is recorded over time. An example is given in figure 6.3. In the figure we observe a sharp increase in Γ upon adding a vesicle solution and a plateau value of ≈ 3.8 mg/m^2 is reached (step 1). From the molar mass of a DOPC phospholipid ($M_{DOPC} = 786.1$ g/mol) and the area per lipid ($A_L = 0.64$ nm^2 [13]), a simple calculation shows that a DOPC bilayer corresponds to approximately $\Gamma_{bilayer} = 4.08$ mg/m^2. The plateau value at the end of step 1 is relatively close to this, suggesting that indeed a complete DOPC bilayer has formed. This adsorbed layer is not washed away when switching back to a buffer solution (step 2). Upon adding streptavidin

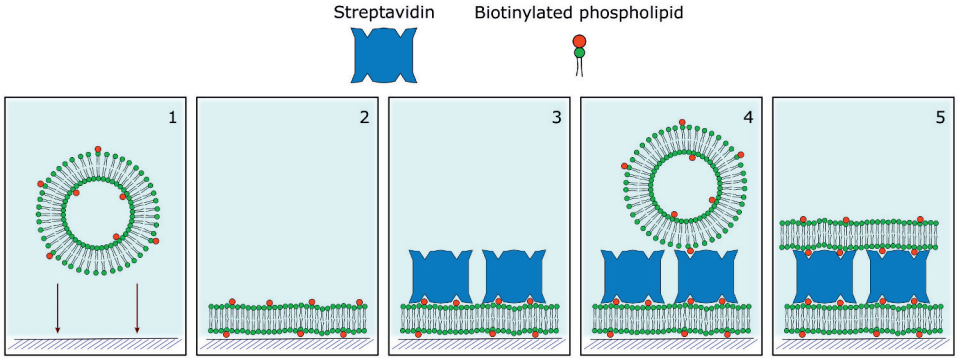

Figure 6.2: Schematic overview of SDLB formation using biotin and streptavidin. In step 1 a vesicle solution containing biotinylated lipids is supplied to a cleaned silica surface. Through adhesion a supported lipid bilayer (SLB) is formed (step 2). After washing, a buffer solution with streptavidin is added to the surface (step 3). In the 4th step the same vesicle solution as in step 1 is added and a second bilayer is formed.

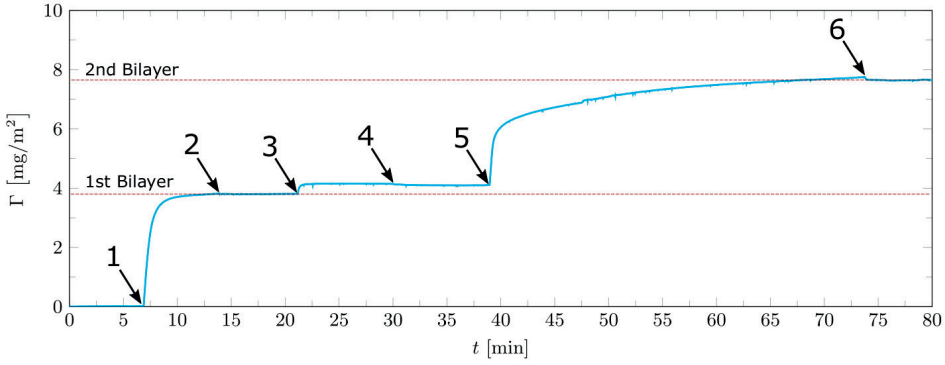

Figure 6.3: Formation of a supported double lipid bilayer (SDLB) as followed by reflectometry. Γ is the adsorbed amount of material on a cleaned silica surface. This experiment is performed in a flow cell where three different solutions are added in turn. A buffer solution (200 mM NaCl, 10 mM Tris, pH 7.5) with biotinylated lipid (DOPC) vesicles ($c_{\text{lipids}} = 0.2$ mM, biotinylated lipid fraction $f_{\text{biotin}} = 0.004$) is added in steps 1 and 5. In steps 2, 4 and 6 we add only the buffer solution without vesicles and in step 3 the buffer solution with streptavidin ($c_{\text{strep}} = 0.01$ mg/ml) is added.

(step 3) we again observe a small increase in Γ, indicating that streptavidin attaches to the biotinylated lipids in the bilayer. After washing (step 4) we again add our vesicle solution (step 5) which subsequently causes another sharp increase in Γ. The plateau level in Γ is however reached much slower, but seems to reach a value approximately twice the value of the first bilayer ($\Gamma = 7.7$ mg/m^2), suggesting the formation of a second bilayer on top of the first one: a SDLB. It however remains possible that we are looking at adsorbed vesicles on top of the first bilayer instead of a SDLB. This could be verified by conducting a similar experiment using a quartz crystal microbalance (QCM) [14]. With this instrument the oscillation frequency of a quartz crystal resonator is followed over time. When material adsorbs on the surface of the resonator, this frequency changes. The change in frequency is linear in first order with the adhered mass [15] and therefore different for adsorbed lipid vesicles than for a lipid bilayer as the mass of the solution in the vesicles also counts. However, in light of the results of Murray et al., we assume that a second bilayer has indeed formed.

Interestingly, similarly to our attempts to obtain small vesicle aggregates using telechelics, SDLB formation using these block copolymers also failed. Rather than the attachment of a second bilayer, we observe a continuous change in the adsorbed amount over time. This suggests we have continued aggregation of more and more vesicles on top of the first lipid bilayer. Similar as with the vesicle aggregation, we think that the cause is in the buffering capacity of the flower-like micelles in solution. The micelles constantly provides telechelic linkers to the bilayer so that newly arriving vesicles can continuously be bound.

With methods to bring bilayers closer together in place, a plethora of opportunities for further research becomes available. For example, the self-limiting aggregation method could be exploited to create synthetic primitive cellular tissues. For this, the content of the vesicles should be altered to mimick the content of cells, for semi-synthetic minimal cells these can include incapsulation of nucleic acids, enzymes, ribosomes and more. [16, 17] Also in the context of this thesis, we envision future work to go in various directions, of which I will mention a few.

6.3 Self-limiting aggregation of giant vesicles

Firstly, the aggregation of vesicles can be extended to giant vesicles ($R > 10$ µm). So far, our experiments were performed with small vesicles in the order of 100 nm in radius. Therefore, the vesicles and small vesicle pairs are not visible under the light, fluorescent or confocal microscope. With giant vesicles, many processes that are involved with the aggregation of vesicles can be directly visualized and characterized with much more detail.

For example, the depletion of linkers towards the contact area can be followed either through the increase in size of the contact area, but also directly when using fluorescently labelled linkers. In such an experiment, the fluorescent signal from individual vesicles will be homogeneously spread, however upon binding with another vesicle, linker depletion will cause the fluorescent signal to gradually accumulate in the contact area. Apart from this, we anticipate that the size of the contact area can be correlated to both the total adhesion strength of the vesicles and the mean bending modulus κ. If the adhesion strength can be measured independently, this thus provides another tool to determine κ, and vice versa. We anticipate that the adhesion strength between two (supported) bilayers due to linkers can be measured using atomic force microscopy (AFM) as done in literature [18]. Alternatively, knowing the individual adhesion strength between linkers such as biotin and streptavidin and the total amount of these linkers present in the contact areas, one can accurately estimate the total adhesion strength as well.

To properly perform such experiments, the giant vesicles should be of approximately the same size. Producing giant (unilamellar) vesicles of approximately the same size can be a challenge however, as simple and conventional methods for giant vesicle preparation, such as the gentle hydration method [19, 20] or electroformation [20, 21] generally produce polydisperse (and multilamellar) giant vesicles. Perhaps most promising is the recently developed method of "dubbed octanol-assisted liposome assembly" (OLA) by Deshpande et al. [22]. With this method, giant unilamellar and monodisperse vesicles are produced on-chip using a microfluidic device. It is perhaps best described as "bubble-blowing on a microscopic scale" [22].

6.4 Triggering mesomorphic phase changes

As mentioned before and indicated by the title of this thesis, our main interest is in triggering and controlling mesomorphic phase changes of lipid bilayers. As such, focus for future research should be in fact trying to do just that. For small vesicle aggregates this entails inducing vesicle fusion or the formation of bilayer handles. As we have shown, phase transitions of these kinds involve saddle-shaped bilayer curvatures, which implies that the Gaussian bending rigidity $\bar{\kappa}$ would have a huge influence. More specifically, as we have indicated in the introduction chapter and verified in chapters 4 and 5, saddle-shaped curvatures arise when $\bar{\kappa}$ is positive. As the value of $\bar{\kappa}$ is ultimately inherent to the bilayer composition, the primary way forward is to alter the bilayer composition through the addition of specific additives that increase $\bar{\kappa}$. As shown in chapter 4 and 5, an increase in $\bar{\kappa}$ can be obtained by making the bilayer more hydrophobic, i.e. with the inclusion of relative hydrophobic additives that partition (mainly) in the bilayer core. Based on

chapter 5, prime candidates for this would be long-tail fatty acids and monoolein lipids. We anticipate that the inclusion of purely hydrophobic molecules such as tetradecane and hexadecane will have similar effects, based on our modelling results and on the reported experimental phase behaviour of these additives with monoolein and monolinolein bilayers [23–25].

Next to triggering membrane fusion or the formation of bilayer handles, it is important to determine whether such an event actually has occurred. This is the main reason that I have developed an assay to monitor lipid exchange between vesicles using Förster resonance energy transfer (FRET). To this end we use a mixture of vesicles containing lipids labelled either with the donor or the acceptor of a FRET pair. When vesicle fusion or formation of handles occurs, lipids will readily exchange which subsequently causes an increase in FRET. For the vesicle aggregation experiments performed in chapter 2 and 3, no lipid exchange was observed, implying that in these cases the primary vesicles remain intact. Alternatively, a fluorescence assay can be developed that is based on exchange of vesicle content. For this, one can again think of using a (soluble) FRET pair, but perhaps a simpler option is to use a self-quenching fluorophore such as calcein or sulphorhodamine B. In such an assay, vesicles with a self-quenching concentration of fluorophores as content would be mixed with vesicles containing no fluorophores. Upon fusion or handle formation, the contents of these vesicles would be mixed, which would dilute the concentration of fluorophores and increase the fluorescent signal. The concept of such an assay is similar to a leakage assay where the leakage of fluorophores out of the vesicles and into the solution triggers the dilution of the self-quenching polymer and causing an increase in fluorescent signal [26]. While not described in this thesis, we reported on such a leakage assay in the work of Júnior et al. [27]. In this study we followed the leakage of DOPC/DOPG vesicles upon binding of fragments of the antimicrobial peptide (AMP) crotalicidin (Ctn).

Interestingly, the Ctn fragments we used in that publication clearly caused some level of leakage, indicating a disruption of the bilayer structure. Other work showed that Ctn and Ctn fragments are also able to disrupt the cell membrane of gram-negative bacteria after accumulation on the membrane surface [28]. How such a peptide disrupts the membrane structure is still under debate, yet most probably it makes pores in the membrane. From previous work with SCF modelling, we know that the formation of pores in bilayers can be correlated directly to large positive values of the spontaneous curvature of the monolayer J_0^m [29]. It is therefore interesting to look at the structure of the Ctn fragments used and see whether we can correlate the addition of these fragments to an increase in J_0^m, based on insights obtained chapters 4 and 5. Snapshots of the structures of these fragments as obtained using MD simulations are given in figure 6.4. As we can see from the figure, these fragments have a hydrophobic part, consisting of mainly hydrophobic amino acids,

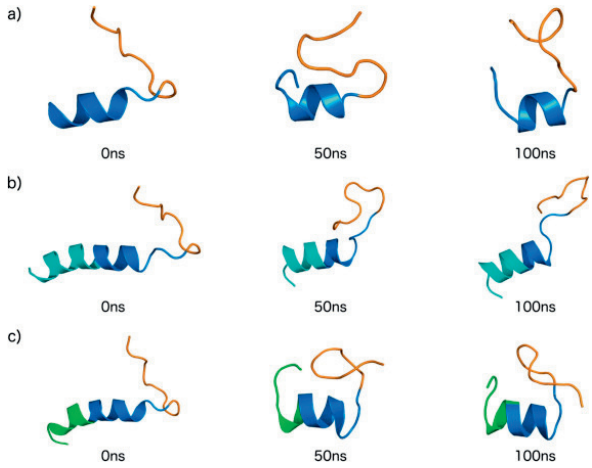

Figure 6.4: Molecular dynamics snapshots of the structures of fragments of crotalicidin. (a) Ctn[15–34], (b) E10-Ctn[15–34] and (c) (GS)4-Ctn[15–34]. Dark blue: basic domain Ctn[15–34], orange: hydrophobic domain Ctn[15–34], light blue: acidic E10 domain, green: control pro-peptide domain (GS)4. Copied from Júnior et al. [27].

and a domain which is generally more hydrophilic. This hydrophilic part is about equally large to quite a bit larger than the hydrophobic domain. As such, these peptides could be effectively modelled as large surfactants with a relatively small hydrophobic tail and a relatively large hydrophilic head. The structure that most closely resembles this resembles in chapter 5 is the C_{12}-E_{10} surfactant, although the size of the Ctn fragments is much larger. Our model calculations clearly showed that J_0^m of a DOPC bilayer increases extensively upon addition of C_{12}-E_{10}, and based on this I would argue pore formation to indeed be a likely mechanism for membrane disruption as a result of addition of Ctn fragments. Further research is required however to substantiate this suggestion.

The lipid and content exchange assays to determine whether vesicle fusion or the formation of bilayer handles takes place, cannot distinguish between these two occurrences. This is where the supported double lipid bilayers may come into play as they allow for various analytical surface techniques that can be used to further clarify what has happened. For example, we anticipate that with atomic force microscopy (AFM) the presence of intermembrane handles in the double lipid bilayer can be visualized, in the same fashion as the formation of membrane pores has been visualized with this technique [30].

6.5 Improvements and outlook of lattice-refined SCF theory for membrane modelling

Our work on SCF modelling, although it ended up being a large portion of this thesis, is ultimately intended to assist the experimental part of the project. To be precise, it can help to specify and narrow the search on which lipid composition and which additives are suitable to potentially trigger vesicle fusion or the formation of membrane handles in double bilayer systems. While our work on the lattice-refined SCF model, described in chapters 4 and 5, meets this objective, further modelling should be performed. Additionally, the lattice-refined SF-SCF approach is but a first step to better model bilayers and by far not yet developed to the best of its capabilities. Several improvements to the model should still be made. In the next paragraphs I will sketch further modelling directions and highlight a couple of improvements that can be made to the lattice-refined SF-SCF model.

In my view the most prominent direction the modelling can take is extension of the theory to capture two dimensions (two gradients). All the lattice-refined SF-SCF modelling so far has been done in 1D. This is highlighted by the many volume fraction (ϕ) profiles and grand potential density (ω) profiles that we show in chapters 4 and 5. Here, ϕ and ω are quantities given only as a function of z. As a consequence, prominent effects on the structure of the bilayer such as raft formation or other types of accumulation of additives are not taken into account. Implementation of two dimensions in the lattice-refinement SF-SCF model will make it possible to visualize and characterize these effects. Additionally, with 2d modelling we could actually describe a membrane handle and research what aspects make such a bilayer structure stable, apart from the bilayer having specific bending rigidities, i.e. with $\bar{\kappa} > 0$. Such a bilayer handle can be modelled in a 2d cylindrical geometry, in the same fashion as Harke et al. [29] have modelled a single membrane pore.

Perhaps even before higher dimensional modelling is attempted, certain aspects of the 1d model can and should be improved. These have been mentioned in chapters 4 and 5 and among these improvements, an upgrade of the chain model is most urgent. In the current lattice-refined model, we use a freely jointed chain (FJC) model in which the next segment of a molecule can be placed on any lattice position, provided that it is adjacent. Without lattice refinement this means three adjacent lattice positions (i.e., layers in which the segment can be placed), but with lattice refinement this number increases considerably. Additionally, in the FJC model excluded volume correlations of segments further than one segment apart are ignored. In other words, the persistence length of the chains is one

segment size in length and cannot be changed. In reality the persistence length of lipid chains is in the order of 3 to 4 segment sizes (≈ 0.5 nm [31]). As a consequence the chain flexibility is very high and this causes the bilayer to be relatively thin and flexible itself, lowering the value for κ. This problem can be resolved by implementing the rotational isomeric state (RIS) scheme [32–34]. In this scheme, the short-range correlations between segments two segments apart are taken into account and as a result the local stiffness of the chain can be incorporated (and increased) in the model. By increasing the energy cost of sharp bond angles, we can bias the system towards smaller angles and thus a stiffer chains. This would thus increase the persistence length of the chain and make the bilayer, in particular the hydrophobic core, thicker than with the existing lattice-refined model. Such a change is typically correlated with an increase in κ, as was seen when increasing the tail length of the lipids (chapter 4).

Next to the upgraded chain model, another change in the model could be implemented which would allow for distinguishing the gel-to-liquid phase transition in a lipid bilayer. For this we have to modify the mean-field approximation and take into account that the anisotropic distribution of the molecules induces a self-consistent anisotropic molecular field (SCAF). In other words: we take the orientation of the bonds in neighbouring chains into account. In previous work this model was successfully used without a lattice refinement to predict a gel-to-liquid phase transition in model phospholipid-like bilayers [35]. Later on however, this model was discarded due to the large lattice artefacts present in the calculations. With our lattice refinement implemented, the SCAF method can be explored again.

6.6 Final remark

The biological cell is fascinatingly complex, and this is also the case for its membranes. One important feature of membranes that remains enigmatic is their mesomorphic phase behaviour. With experimental methods bringing two lipid bilayers together in place and the insight gained on the mechanical properties of bilayers through the lattice-refined SF-SCF model introduced in this thesis, I hope to have made a modest, yet significant contribution towards understanding and controlling the mesomorphic phase behaviour of bilayer membranes.

References

[1] S Jonathan Singer and Garth L Nicolson. The fluid mosaic model of the structure of cell membranes. *Science*, 175(4023):720–731, 1972.

[2] DJ Paolillo. The three-dimensional arrangement of intergranal lamellae in chloroplasts. *Journal of Cell Science*, 6(1):243–253, 1970.

[3] László Mustárdy and Győző Garab. Granum revisited. a three-dimensional model–where things fall into place. *Trends in plant science*, 8(3):117–122, 2003.

[4] Yuval Bussi, Eyal Shimoni, Allon Weiner, Ruti Kapon, Dana Charuvi, Reinat Nevo, Efi Efrati, and Ziv Reich. Fundamental helical geometry consolidates the plant photosynthetic membrane. *Proceedings of the National Academy of Sciences*, 116(44):22366–22375, 2019.

[5] Eyal Shimoni, Ophir Rav-Hon, Itzhak Ohad, Vlad Brumfeld, and Ziv Reich. Three-dimensional organization of higher-plant chloroplast thylakoid membranes revealed by electron tomography. *The Plant Cell*, 17(9):2580–2586, 2005.

[6] Per-Ola Arvidsson and Cecilia Sundby. A model for the topology of the chloroplast thylakoid membrane. *Functional Plant Biology*, 26(7):687–694, 1999.

[7] Ingvar Brentel, Eva Selstam, and Göran Lindblom. Phase equilibria of mixtures of plant galactolipids. the formation of a bicontinuous cubic phase. *Biochimica et Biophysica Acta (BBA)-Biomembranes*, 812(3):816–826, 1985.

[8] Javier Hoyo, Ester Guaus, and Juan Torrent-Burgués. Monogalactosyldiacylglycerol and digalactosyldiacylglycerol role, physical states, applications and biomimetic monolayer films. *The European Physical Journal E*, 39(3):39, 2016.

[9] Christian Wilhelm, Reimund Goss, and Gyözö Garab. The fluid-mosaic membrane theory in the context of photosynthetic membranes: Is the thylakoid membrane more like a mixed crystal or like a fluid? *Journal of Plant Physiology*, page 153246, 2020.

[10] ET Kisak, MT Kennedy, D Trommeshauser, and JA Zasadzinski. Self-limiting aggregation by controlled ligand- receptor stoichiometry. *Langmuir*, 16(6):2825–2831, 2000.

[11] David H Murray, Lukas K Tamm, and Volker Kiessling. Supported double membranes. *Journal of structural biology*, 168(1):183–189, 2009.

[12] JC Dijt, MA Cohen Stuart, and GJ Fleer. Reflectometry as a tool for adsorption studies. *Advances in colloid and interface science*, 50:79–101, 1994.

[13] John C Mathai, Stephanie Tristram-Nagle, John F Nagle, and Mark L Zeidel. Structural determinants of water permeability through the lipid membrane. *The Journal of general physiology*, 131(1): 69–76, 2008.

[14] K Keiji Kanazawa and Joseph G Gordon. Frequency of a quartz microbalance in contact with liquid. *Analytical Chemistry*, 57(8):1770–1771, 1985.

[15] Günter Sauerbrey. Verwendung von schwingquarzen zur wägung dünner schichten und zur mikrowägung. *Zeitschrift für physik*, 155(2):206–222, 1959.

[16] Cristiano Chiarabelli, Pasquale Stano, and Pier Luigi Luisi. Chemical approaches to synthetic biology. *Current opinion in biotechnology*, 20(4):492–497, 2009.

[17] Pasquale Stano and Pier Luigi Luisi. Semi-synthetic minimal cells: origin and recent developments. *Current opinion in biotechnology*, 24(4):633–638, 2013.

[18] Ioana Pera, Rüdiger Stark, Michael Kappl, Hans-Jürgen Butt, and Fabio Benfenati. Using the atomic force microscope to study the interaction between two solid supported lipid bilayers and the influence of synapsin i. *Biophysical journal*, 87(4):2446–2455, 2004.

[19] John P Reeves and Robert M Dowben. Formation and properties of thin-walled phospholipid vesicles. *Journal of cellular physiology*, 73(1):49–60, 1969.

[20] Nicolas Rodriguez, Frédéric Pincet, and Sophie Cribier. Giant vesicles formed by gentle hydration

and electroformation: a comparison by fluorescence microscopy. *Colloids and surfaces B: biointerfaces*, 42(2):125–130, 2005.

[21] Miglena I Angelova and Dimiter S Dimitrov. Liposome electroformation. *Faraday discussions of the Chemical Society*, 81:303–311, 1986.

[22] Siddharth Deshpande and Cees Dekker. On-chip microfluidic production of cell-sized liposomes. *Nature protocols*, 13(5):856–874, 2018.

[23] Leonie van't Hag, Sally L Gras, Charlotte E Conn, and Calum J Drummond. Lyotropic liquid crystal engineering moving beyond binary compositional space–ordered nanostructured amphiphile self-assembly materials by design. *Chemical society reviews*, 46(10):2705–2731, 2017.

[24] Stephanie Phan, Wye-Khay Fong, Nigel Kirby, Tracey Hanley, and Ben J Boyd. Evaluating the link between self-assembled mesophase structure and drug release. *International journal of pharmaceutics*, 421(1):176–182, 2011.

[25] Anan Yaghmur, Liliana De Campo, Laurent Sagalowicz, Martin E Leser, and Otto Glatter. Emulsified microemulsions and oil-containing liquid crystalline phases. *Langmuir*, 21(2):569–577, 2005.

[26] Harke Pera, Tom M Nolte, Frans AM Leermakers, and J Mieke Kleijn. Coverage and disruption of phospholipid membranes by oxide nanoparticles. *Langmuir*, 30(48):14581–14590, 2014.

[27] Nelson GO Júnior, Marlon H Cardoso, Elizabete S Cândido, Daniëlle van den Broek, Niek de Lange, Nadya Velikova, J Mieke Kleijn, Jerry M Wells, Taia MB Rezende, Octávio Luiz Franco, et al. An acidic model pro-peptide affects the secondary structure, membrane interactions and antimicrobial activity of a crotalicidin fragment. *Scientific reports*, 8(1):1–11, 2018.

[28] Clara Pérez-Peinado, Susana Almeida Dias, Marco M Domingues, Aurélie H Benfield, João Miguel Freire, Gandhi Rádis-Baptista, Diana Gaspar, Miguel ARB Castanho, David J Craik, Sónia Troeira Henriques, et al. Mechanisms of bacterial membrane permeabilization by crotalicidin (ctn) and its fragment ctn (15–34), antimicrobial peptides from rattlesnake venom. *Journal of Biological Chemistry*, 293(5):1536–1549, 2018.

[29] H Pera, JM Kleijn, and FAM Leermakers. On the edge energy of lipid membranes and the thermodynamic stability of pores. *The Journal of chemical physics*, 142(3):01B614_1, 2015.

[30] Jian Zhong, Wenfu Zheng, Lixin Huang, Yuankai Hong, Lijun Wang, Yang Qiu, and Yinlin Sha. Prp106–126 amide causes the semi-penetrated poration in the supported lipid bilayers. *Biochimica et Biophysica Acta (BBA)-Biomembranes*, 1768(6):1420–1429, 2007.

[31] W Rawicz, K Cc Olbrich, T McIntosh, D Needham, and E Evans. Effect of chain length and unsaturation on elasticity of lipid bilayers. *Biophysical journal*, 79(1):328–339, 2000.

[32] FAM Leermakers and JMHM Scheutjens. Statistical thermodynamics of association colloids. i. lipid bilayer membranes. *The Journal of chemical physics*, 89(5):3264–3274, 1988.

[33] Lucas A. Meijer, Frans A. M. Leermakers, and Johannes Lyklema. Modeling the interactions between phospholipid bilayer membranes with and without additives. *J. Phys. Chem.*, 99(47):17282–17293, 1995. doi: 10.1021/j100047a037. URL `http://dx.doi.org/10.1021/j100047a037`.

[34] A L Rabinovich, P O Ripatti, N K Balabaev, and F A M Leermakers. Molecular dynamics simulations of hydrated unsaturated lipid bilayers in the liquid-crystal phase and comparison to self-consistent field modeling. *Physical Review E*, 67(1):011909, 2003.

[35] FAM Leermakers and JMHM Scheutjens. Statistical thermodynamics of association colloids. iii. the gel to liquid phase transition of lipid bilayer membranes. *The Journal of chemical physics*, 89(11): 6912–6924, 1988.

Summary

Ever since the invention of the microscope in the 17th century, scientists have studied the structure and behaviour of living cells. The knowledge acquired since then has led to many applications and subsequently improved the quality of our lives immensely, from an improved personal hygiene to healthcare and the availability of many medicines. It should be clear however, that the cell still holds many secrets. In this thesis we focus on one of those secrets, namely how the cell controls the mesomorphic phase behaviour of its lipid membranes. In other words, how come biomembranes of the cell and its organelles come in so many different shapes and forms? As we explain in the introduction of this thesis (chapter 1) the answer ultimately lies in the composition of the lipid bilayer, which is the universal component of all biological membranes. However, how the constituents of the lipid bilayer effect its mesomorphic phase behaviour remains unclear. The main goal of this thesis is to provide the tools and insight necessary to obtain control on the mesomorphic phase behaviour of lipid bilayers. To do so, we have chosen to combine experimental work with theoretical modelling.

In chapters 2 and 3 we describe our experimental efforts to bring bilayers together in close proximity using limited vesicle aggregation. This is important as inducing a mesomorphic phase change in the bilayer such as the formation of membrane handles or inducing vesicle fusion, bringing membranes together is the very first step. In chapter 2 we present three successful strategies that lead to stable finite-sized vesicles aggregates: (i) vesicles containing biotinylated lipids are coupled together with streptavidin, (ii) cationic polymers (polylysine) are used to link negatively charged vesicles, and (iii) temperature as a control parameter is used for the aggregation of vesicles using the thermo-sensitive surfactant C18-pNIPAm, where below a certain temperature (the lower critical solution temperature, LCST) the pNIPAm chains are soluble in aqueous solution, while above this temperature, the chains collapse and become sticky. We show that by tuning the experimental parameters it is possible to limit the aggregation of the vesicles to the vesicle-pair level and provide a detailed analysis on the process of vesicle aggregation under various physico-chemical conditions. We distinguish two routes that lead to limited aggregation

of vesicles: limiting the amount of linkers, or using membrane-bound linkers that upon contact with another vesicle are able to diffuse to the contact area, depleting the rest of the membrane of linker molecules. In particular the latter option, dubbed 'self-limiting aggregation', is found to be effective for the formation of stable vesicle pairs. Amongst the successful strategies, the one involving C18-pNIPAm as a linker molecule shows an additional feature: the limited aggregation of vesicles is completely and repeatedly reversible using temperature as the trigger.

In chapter 3 we build on the work of chapter 2 and combine the biotin/streptavidin linker system with the thermo-sensitive C18-pNIPAm surfactants. In doing so further control over the aggregation of the vesicles is obtained. Due to the presence of C18-pNIPAM no aggregation occurs below the LCST of C18-pNIPAm (32°C), and self-limiting aggregation occurs above this temperature. However, the presence of the biotin/streptavidin linkers makes it that the aggregation is no longer reversible. Instead, repeated temperature cycles cause a step-wise aggregation process that under well-chosen experimental conditions allows for the formation of small vesicle aggregates of predetermined sizes. Additionally, we introduce and apply a lipid-exchange assay to identify whether lipids exchange between vesicles as a result of the linking process, something that will happen if vesicles fuse or form intermembrane handles.

In chapters 4 and 5 we discuss our results on Scheutjens and Fleer self-consistent field (SF-SCF) calculations on lipid bilayers. Our contribution in chapter 4 is two-fold. Firstly, we introduce a lattice refinement to the existing SF-SCF framework. Secondly, we apply the lattice-refined SF-SCF machinery to systematically study bilayer self-assembly of phospholipids in a selective solvent (water). With the lattice refinement implemented it is possible to extract mechanical parameters that govern the mesomorphic phase behaviour of lipid bilayers, such as the mean (κ) and Gaussian ($\bar{\kappa}$) bending moduli, as well as the spontaneous curvature of the monolayer (J_0^m) for the first time following a grand canonical ensemble route. Previous SF-SCF calculations could not follow this correct route due to large lattice artefacts. We predict the abovementioned mechanical parameters in addition to various structural parameters as a function of several lipid properties, such as headgroup hydrophilicity, tail hydrophobicity and tail length. The calculations show that the mean bending modulus generally grows with increasing bilayer thickness. Furthermore, J_0^m and $\bar{\kappa}$ show opposite trends, as expected, and for classical phospholipids both parameters assume values near zero, indicating the planar bilayer is the preferred self-assembled structure. In general we find that increasing the hydrophobicity of the phospholipid (longer tails or more hydrophobic tails/headgroup), leads to larger values for $\bar{\kappa}$, and lower ones for J_0^m. This indicates that, amongst others, the lipophilic to hydrophilic ratio is an important mechanism to control the mesomorphic phase behaviour

of lipid bilayer membranes.

Chapter 5 expands on the work of chapter 4 where we introduce various additives in the system to stimulate changes in the self-assembled phase behaviour of monoolein (MO) and 1,2-dioleoyl-phosphatidylcholine (DOPC) lipids in water. More specifically, we obtain trends in the mechanical parameters (κ, $\bar{\kappa}$ and J_0^m) of equilibrium bilayers as a function of increasing additive content and compare these with known experimental phase behaviour if available. The trends in the mechanical parameters are subsequently correlated to various mesomorphic phase changes in the system. In particular, the phase transition from a lamellar bilayer topology to a saddle-shaped topology is verified to correlate with a sign-switch of $\bar{\kappa}$. Additionally, the formation of micelles or inverted micelles follows from a large positive or a large negative value of J_0^m, respectively. The transitions between different saddle-shaped bilayer phases, such as various cubic phases and sponge phases is more subtle, but invariably needs a positive value for $\bar{\kappa}$ in order to be stable. Our calculations furthermore indicate that if the value for κ is additionally below unity, the system loses its long-range ordering and forms a sponge phase. With these rules established, various groups of additives are subsequently identified that potentially induce mesomorphic phase changes. In agreement with our results in chapter 4, we find that the inclusion of primarily hydrophobic additives that partition in the bilayer core, drives the bilayer towards a topological state of increased negative interfacial curvature and saddle-shape configurations. For DOPC bilayers this entails losing the lamellar topology in favour of an inverted hexagonal phase or a bicontinuous cubic phase, while MO tends to go from a bicontinuous cubic phase towards an inverted micellar phase. Micelle-forming surfactants do the opposite. The inclusion of small additives, both hydrophilic (i.e. 'solvents') or hydrophobic, generally decreases the mean bending modulus of the bilayers and thus makes bilayers more flexible. This may take a lipid system from a bicontinuous cubic phase closer to a sponge phase or decrease the persistence length of lamellar bilayers and increase the undulation repulsion.

In the general discussion of this thesis (chapter 6) I put the results obtained in the previous chapters in a wider context and discuss aspects and results that have not yet been addressed. In particular, we report on the successful preparation of a supported double lipid bilayer (SDLB) using biotin/streptavidin linkers. The general discussion additionally includes an overview of the challenges that still remain and a discussion on the direction future research may take. Most prominently, I envision this should involve inducing a mesomorphic phase change in the small vesicle aggregates causing the vesicles to either fuse together or to form stable membrane handles between them. This can be realized through the addition of additives that cause $\bar{\kappa}$ to switch sign from negative to positive as described in chapter 5, thus using primarily hydrophobic additives such as

long-tailed fatty acids or the lipid monoolein. To properly monitor such changes, the lipid exchange assay developed in this thesis needs to be complemented with other experiments such as a vesicle content exchange assay, or using surface analytical techniques on SDLBs. SCF calculations can further guide and support such experiments by modeling an actual stable membrane handle.

List of Publications

This Thesis

- de Lange, N., F. A. M. Leermakers, and J. M. Kleijn. "Self-limiting aggregation of phospholipid vesicles." *Soft matter* **16**(9) (2020): 2379-2389. **(Chapter 2)**
- de Lange, N., F. A. M. Leermakers, and J. M. Kleijn. "Step-wise linking of vesicles by combining reversible and irreversible linkers–towards total control on vesicle aggregate sizes." *Soft Matter* **16**(29) (2020): 6773-6783. **(Chapter 3)**
- de Lange, N., J. M. Kleijn, and F. A. M. Leermakers. "Structural and mechanical parameters of lipid bilayer membranes using a lattice refined self-consistent field theory." *Physical Chemistry Chemical Physics* **23** (2021): 5152-5175. **(Chapter 4)**
- de Lange, N., J. M. Kleijn, and F. A. M. Leermakers. "Self-consistent field modelling of mesomorphic phase changes of mono-olein and phospholipids in response to additives." *Physical Chemistry Chemical Physics* **(Chapter 5, submitted)**

Other work

- Júnior, N. G., Cardoso, M. H., Cândido, E. S., van den Broek, D., de Lange, N., Velikova, N., ... & de Vries, R. "An acidic model pro-peptide affects the secondary structure, membrane interactions and antimicrobial activity of a crotalicidin fragment." *Scientific reports* **8**(1) (2018): 1-11.

Acknowledgements

At the end of my Master Molecular Life Sciences at the Wageningen University, I was unsure what to do next. As my interests within the molecular world were broad, making my mind up to choose a particular direction was hard. In that period, the offer to start as a PhD candidate within the group of Physical Chemistry and Soft matter (PCC) couldn't have come at a greater time. Even better, the membrane project I would work on was a perfect topic with elements of chemistry, physics and biology. Now, more than 4 years later, I can look back on a successful and enjoyable period of my life, yet this would not have been possible without the help and support of many people.

Frans and **Mieke**, thanks for giving me the opportunity to work on this project and to pursue my PhD. **Frans**, your incredible passion for science and our membrane project is addictive. Your door was always open and the extensive discussions we had about my results and what it meant for future experiments were not only informative and useful, they were highly enjoyable as well. I am very thankful for the time you've set aside for me during the past years. **Mieke**, your input was invaluable and helped to make this project a reality instead of keeping it in the realm of possibilities. Your practical insight in the experiments, and clear and straightforward comments on the articles, in particular during my final year were key to actually finishing my PhD. I sincerely appreciate all the help and support you gave me, even after your retirement.

Besides my (co-)promotors supporting me, I would have never been able to publish all articles without the help of many staff members of PCC and Biochemistry. **Remco**, thanks for all the help and support during my light scattering and reflectometry experiments. **Diane**, whenever I had a question concerning the chemical synthesis of the C18-PNIPAm molecules (used a lot within this thesis), you were there and willing to help, many thanks. **Jan Willem** and **Adrie**, your help on the fluorescent correlation spectroscopy (FCS) experiments was critical for the understanding of what my vesicles do during aggregation. **Joris** and **Thom**, many thanks for the input and comments on the manuscript about the step-wise vesicle aggregation. Thanks to this input it was accepted without much

problems.

To all my (former) colleagues at PCC, thank you for all the fun times/discussions/lunch breaks and more. I utterly enjoyed my time spent at PCC and am saddened that these times have come to an end. There are too many people to mention all by name but I would like to thank a few people in particular.

Mara en **Leonie**, you are the heart of PCC. Thanks for all the help, from administrative issues to the casual chat that I needed. You were always available, even during your free days. **Jasper**, **Renko**, **Joshua**, **Siddarth** and other staff members of PCC, the scientific input and discussions we had during group and other meetings were valuable to me. I never felt unconfortable asking for your help when necessary. I would also like to thank my students, **Daniëlle** and **Siebe**. Although you worked on different topics, it helped me greatly in understanding how to prepare the lipid vesicles and how these interact with specific additives. I highly enjoyed supervising the both of you.

Ram, my crazy office mate! We started our PhD around the same time and we will graduate around the same time, and I am grateful for that. I believe that without you I would not have been able to finish my PhD. Your help with the self-consistent field problems, your relaxed attitude and above all, the crazy conversations we have had about life in general was everything I needed to leave the lab with a smile on my face at the end of the day. Call me selfish, but I am glad that you found another job in the Netherlands, so that we have the opportunity to continue talking and hanging out together. **Sven**, **Huy**, **Ketan**, **Tao** and all other office mates of 6.055 that I have had over the years, thanks for all the fun times we had together. I haven't been in our office lately, but I imagine that the paper target on the window and the toy gun are still present, ready to be shot again! **Lione**, it was a lot of fun organising a PhD weekend with you. I believe we couldn't have done it better. The same can be said about organising the yearly SinteFysko for which I have to thank both **Hanne** and **Inge** for being great co-organisers. **Anton**, **Marco** and all other teammembers, I had great fun with you in the Kollosolex volleyball team. And last but not least, thank you **Justin**, **Ruben**, **Simone**, **Jochem**, **Martijn**, **Dana** and everyone else that participated in fun game nights and drinks, both at PCC, in Utrecht or online. The social activities with you all kept me motivated throughout the years.

Naast collega's wil ik ook graag een aantal vrienden en familieleden bedanken:

Arthur, **Koen**, **Dennis**, en de rest van ons knotsbal team, zonder jullie was mijn studentenleven maar een saaie boel geweest. Ik ben blij dat ik jullie tot mijn beste vrienden kan rekenen. Ondanks dat we inmiddels zijn verspreid over Europa, merk ik dat we, als vanouds, gewoon weer verder gaan waar we gebleven waren, zodra we elkaar weer

ontmoeten. We hebben veel herinneringen gemaakt en ik hoop nog jarenlang met jullie gesprekken te voeren, spelletjes te spelen en te genieten tijdens tripjes naar Frankrijk! **Thessa**, jij verdient een speciale vernoeming. Jij hebt werkelijk waar de mooiste cover ontworpen voor dit boekje en daar ben ik je heel dankbaar voor. Eén van de vrienden van 'vroeger' wil ik hier ook graag noemen. **Michael**, al zien we elkaar nog maar af en toe, ik kijk altijd uit naar onze ontmoetingen. De jaarlijkse LAN-party in december en het dagje pretpark in de zomer zou ik graag nog jaren voortzetten.

Ook wil ik iedereen bedanken die samen met mij Ultimate frisbee heeft gespeeld, met name binnen WAF. Toen ik als kersverse 1e jaars bachelorstudent begon met frisbeeën had ik nooit bedacht hoeveel lol, uitdaging en vriendschappen deze sport mij zou opleveren. Aan iedereen met wie ik samen heb getraind, wedstrijden gespeeld, geborreld, in zowel binnen- als buitenland, dankjulliewel!

Pap, **mam**, **Lies** en **Sanne**, ik kan me geen beter gezin om me heen voorstellen. Op jullie kan ik altijd rekenen, evenals op de rest van mijn familie. Ik voel me dankbaar voor de zorgeloze en veilige omgeving waarin ik ben opgegroeid. Eén familielid wil ik met name noemen. **Opa Kees**, vanaf de eerste kennismaking met de Wageningen Universiteit, was jij betrokken bij alles wat ik ontdekte en meemaakte. Je luisterde met veel geduld en interesse naar al mijn verhalen over vesicles, dubbele membranen en krommingen in dezelfde membranen. Misschien ben ik het lesgeven wel leuk gaan vinden omdat ik het jou uitleggen zo geweldig vindt.

Chloé, it feels only yesterday that we met in San Francisco, yet I can't imagine my life without you anymore. Your unconditional love, support and patience allows me to be myself at any time without judgement. J'espère que nous vivrons beaucoup plus de beaux moments ensemble.

About the author

Niek de Lange was born on the 13th of June 1991 in Wageningen, the Netherlands. He spent the most of his youth living in Middelburg where he received his high school diploma (VWO) in 2009 at the Nehalennia. That same year he started with a bachelor in molecular life sciences at Wageningen University with a minor in food technology. In 2013 he continued with his master in molecular life sciences. During his master, he conducted a thesis on temperature controlled mechanical properties of composite microgel suspensions at the Physical Chemistry and Soft Matter group, which was followed by an internship at the University of California, San Francisco (UCSF) in San Francisco, the United States of America. After a second master thesis on the resistance and expression of beneficial TEM alleles in E. coli, in the laboratory of genetics, he graduated from his master with two specialisations, physical chemistry and biomedical research. He returned to the Physical Chemistry and Soft Matter group at the Wageningen University in September 2016 to pursue a PhD. Under the supervision of Prof. Dr ir. Frans Leermakers and Dr ir. Mieke Kleijn, he worked on the mesomorphic phase behaviour of lipid bilayers. The results of this research is presented in this thesis.

To continue his career, Niek has started as a teacher at the Hogeschool Utrecht (HU) where he will be teaching students following the 'Chemische Technologie' (Chemical Technology) study. He started on the 1st of April, 2021.

Overview of completed training activities

Discipline specific activities

- 4TU Dutch Material Symposia, Netherlands (4TU, 2016)
- Dutch Soft Matter Meeting, Netherlands (2016)
- Statistical Thermodynamics Course, Netherlands (WUR, 2017)
- Han-sur-Lesse Winterschool, Belgium, (WUR, 2017 & 2018)
- 16th Conference of the International Association of Colloid and Interface Scientists, Netherlands (IACIS, 2018)
- 12th International Symposium on Polyelectrolytes, Netherlands (ISP/VLAG, 2018)
- Rheology: The Do's and Don'ts course, Netherlands (VLAG, 2020)

General courses

- Project and Time Management (WGS, 2017)
- Teaching and Supervising Thesis Students (WGS, 2017)
- VLAG PhD week, the Netherlands (VLAG, 2017)
- Efficient Writing Strategies (WGS, 2018)
- Mobilising your - scientific - network (WGS, 2019)
- Career Perspectives (WGS, 2020)

Optionals

- Weekly Work Meetings (PCC, 2016-2020)
- Weekly PCC Group Meetings/Seminars (PCC, 2016-2020)
- PCC Journal Club (PCC, 2016-2020)
- Preparation of Research proposal (2017)
- PhD Day trip to OCÉ (2018)

Cover design by Thessa Blijleven

Printed by Proefschriftmaken.nl